ILMATIETEEN LAITOS
METEOROLOGISKA INSTITUTET
FINNISH METEOROLOGICAL INSTITUTE

121
CONTRIBUTIONS

EMISSION AND DISPERSION MODELLING OF AEROSOLS AND HUMAN EXPOSURE TO PARTICULATE MATTER

JOANA SOARES

FINNISH METEOROLOGICAL INSTITUTE

CONTRIBUTIONS

No. 121

EMISSION AND DISPERSION MODELLING OF AEROSOLS AND HUMAN EXPOSURE TO PARTICULATE MATTER

Joana Soares

Academic dissertation in Physics

To be presented, with the permission of the Faculty of Science of the University of Helsinki, for public criticism in the Auditorium "Brainstorm" at the Finnish Meteorological Institute (Erik Palminén Aukio 1, Helsinki) on May 27th, 2016, at 12 o'clock.

Finnish Meteorological Institute

Helsinki, 2016

Author's address: Joana Soares
Finnish Meteorological Institute
P.O. Box: 503, FI-00101 Helsinki, Finland

Supervisors:

Adjunct Professor, Mikhail Sofiev, Ph.D
Finnish Meteorological Institute

Research Manager, Ari Karppinen, Dr. Tech
Finnish Meteorological Institute

Professor Markku Kulmala, Ph.D
Department of Physics, University of Helsinki

Reviewers:

Professor Ilona Riipinen, Ph.D
Department of Environmental Science and Analytical Chemistry, Stockholm University

Professor Collin O' Dowd, Ph.D
School of Physics, National University of Ireland

Opponent:

Professor Peter Builtjes, Ph.D
Institute of Meteorology, Free University-Berlin,Germany and Netherlands Organization for Applied Scientific Research (TNO-Utrecht)

Custos:

Professor Veli-Matti Kerminen, Ph.D
Department of Physics, University of Helsinki

ISBN I978-951-697-882-9 (paperback)
ISSN 0782-6117
Erweko
Helsinki 2016

ISBN 978-951-697-883-6 (pdf)
http://ethesis.helsinki.fi
Helsingin yliopisto verkkojulkaisut
Helsinki 2016

FINNISH METEOROLOGICAL INSTITUTE

Published by Finnish Meteorological Institute
(Erik Palménin aukio 1), P.O. Box 503
FIN-00101 Helsinki, Finland

Series title, number and report code of publication
Finnish Meteorological Institute
Contributions No. 121, FMI-CONT-121

Date
May 2016

Author
Joana Soares

Title
Emission and dispersion modelling of aerosols and human exposure to particulate matter

Abstract

Atmospheric aerosols are subject to extensive research, due to their effect on air quality, human health and ecosystems, and hold a pivotal role in the Earth's climate. The first focus of this study is to improve the modelling of aerosol emissions and its dispersion in the atmosphere, in different spatial and temporal scales, and secondly, to integrate the dispersion modelling with population activity data to estimate exposure metrics. The mathematical models used in this study are fully or partially developed by the Finnish Meteorological Institute: a regional-to-global scale chemical transport model SILAM, a local-scale point/line-source dispersion model, UDM/CAR-FMI, and a human exposure and intake fraction assessment model, EXPAND.

One of the outcomes of this work was the refinement of the emission modelling for the mesoscale dispersion model. A new parameterisation for bubble-mediated sea salt flux has been developed, taking in to account the effects of wind speed and seawater salinity and temperature. The parameterization is valid for low-to-moderate wind speed, seawater salinity ranging between 0 and 33 ‰, seawater temperature ranging between -2 and 25 °C, and can be applicable to particles with dry diameters raging between 0.01 and 10 μm. The near-real time fire estimation system, IS4FIRES, based on Fire Radiative Power (FRP) measured by the remote sensing instrument MODIS, was refined to reduce the overestimation of particulate matter (PM) emissions by including more vegetation types, improving the diurnal variation, removing misattributed fires from the FRP data, and recalibrating the emission factors. Applying dynamic emission modelling brought more insight to the spatial distribution of these emissions, their contribution to the atmospheric budget, and possible impact on air quality and climate. The modelling shows that sea salt can be transported far over land and contribute up to 6 μg m^{-3} to PM_{10} (at annual level). It also indicates that the Mediterranean Sea has sharp gradients of concentration, becoming an interesting area to analyse regarding the feedbacks to the regional climate. According to the predictions, upward scattering by SSA, at TOA, can be up to 0.5 W m^{-2}, and there will be an overall cooling in the future for the North of Europe and warming for the South, due to SSA. The simulations for wildland fires show how the system improves after calibration and the importance vegetation type for the intensity of the emissions. By including misattributed fires, there will be up to 80% overestimation in aerosol optical depth, close to the misattributed sources.

The emissions for Helsinki Metropolitan Area (HMA) were revised to bring up-to-date the emissions for traffic and energy sectors, for urban-scale applications. The EXPAND model was revised to combine concentrations and activity data in order to compute parameters such as population exposure or intake fraction. EXPAND includes improvements of the associated urban emission and dispersion modelling system, time use of population, and infiltration coefficients from outdoor to indoor air. This refinement showed that $PM_{2.5}$ in HMA is mainly originated from long-range transport, with the largest local contributors being vehicular and shipping (at harbours and its vicinity) emissions. At annual level, the population is mostly exposed to $PM_{2.5}$ indoors (home and work), but the population is acutely exposed while commuting.

Publishing unit
Atmospheric Composition Research

Classification (UDC)	Keywords
504.054, 504.064 551.51, 551.58	Emissions modelling, atmospheric dispersion modelling, exposure modelling, climate change, sea salt, wildland fire, particulate matter

ISSN and series title
0782-6117 Finnish Meteorological Institute Contributions

ISBN	Language	Pages
I978-951-697-882-9	English	114

To the women of my family,
for their strength, wisdom and courage

Às mulheres da minha familia,
pela vossa força, sabedoria e coragem

Acknowledgements

I would like to thank Ari Karppinen for the opportunity of working at FMI for the last 10 years, for entrusting several projects that made me a versatile researcher, and for the supervision throughout my work. I would like to thank Mikhail Sofiev for the scientific guidance, the constant challenge during my work regarding SILAM and so much more. I would like to thank Prof. Markku Kulmala for his support over the course of my studies. I also would like to thank Prof. Jaakko Kukkonen for the guidance and fruitful discussions.

I would like to thank the reviewers, Prof. Collin O'Dowd and Associate Prof. Ilona Riipinen, for accepting reviewing this thesis. I am very grateful to Prof. Veli-Matti Kerminen for being the Custos and being tireless regarding all my questions. I am truly honoured that Prof. Peter Builtjes has accepted to be the Opponent in the public examination of this thesis.

There are too many people that I would like to thank for their support inside and outside of FMI's walls and there are not enough words to express it. I thank the SILAM team for all the discussions, insights, help, laugh and tears: I wouldn't make it without you all. I would like to thank all other colleagues at the Atmospheric Dispersion Modelling group, in particular to the ones I wrote papers and tonnes of reports with. Thank you Joana for being my soulmate. Thank you Edith and Olga for never letting me give up. Thank you Cátia and Pedro for being my family in Finland. Thank you Ella, Jenni, Josephine, Lina, Mari, Marjo, Mikaela, Minna, Juha, Matti, Mikko, Ukko for being who you are in my life. Thank you KRR for the amazing people that keep my head out of the sand. More than thanking for all you have done for me Arto, I am sorry for time that I was not present.

E finalmente à minha familia queria dizer obrigada por me amarem incondicionalmente e por acreditarem em mim, mesmo quando questionam as minhas escolhas. Vocês são uma fonte de inspiração em todos os passos da minha vida e serão sempre o meu porto de abrigo.

Håvard, jeg er klar. Du kan nu forsøde min kaffe med en formiddag kys for en million år.

Helsinki, April 2016,

Joana Soares

Abbreviations and terminology

AQUA	Multi-national NASA scientific research satellite in orbit around the Earth
AIS	Automatic Identification System
AOD	Aerosol Optical Depth
BEM	Biogenic Emission Model
CAR	Road Network Dispersion Model
CTM	Chemical Transport Model
DEHM	Danish Eulerian Hemispheric Model
DMS	Dimethylsulfide
D_p	Particle diameter
DRE	Direct radiative effect
ECHAM5-MPIOM	Atmospheric general circulation model/ocean model developed by the Max Planck Institute
EMEP	Co-operative Programme for monitoring and evaluation of the long-range transmission of air pollutants in Europe
EMME/2	traffic planning model with interactive transportation planning
ESCAPE	European Study of Cohorts for Air Pollution Effects
EXPAND	EXposure model for Particulate matter And Nitrogen oxiDes
FMI	Finnish Meteorological Institute
FRP	Fire radiative power
FORE	Road Suspension Emissions Model
GCM	General circulation models
GLCC	Global Land Cover Characterization
GIS	Geographic Information System
HMA	Helsinki Metropolitan Area
IS4FIRES	Integrated Monitoring and Modelling System for wildland Fires
M03	Mårtensson et al. (2003)

M86	Monahan et al. (1986)
MARGA	Monitor for Aerosol and Gases
MATCH	Multi-scale Atmospheric Transport and Chemistry
MODIS	Moderate Resolution Imaging Spectroradiometer
NASA	National Aeronautics and Space Administration
NEAT	Northeast Atlantic measurement campaign
PM	Particulate matter
SD	Standard deviation
SILAM	System for Integrated modeLling of Atmospheric composition
STEAM	Ship Traffic Emissions Assessment Model
SRES A1B	Emission Scenarios with the assumption that similar improvement rates apply to all energy supply and end-use technologies
SSA	Sea salt aerosol
TERRA	Multi-national NASA scientific research satellite in a Sun-synchronous orbit around the Earth
TOA	top of the atmosphere
Trace gases	Gaseous constituents that comprise less than 1 % of the atmosphere
UDM	Urban Dispersion Modelling System
RCA3	Rossby Centre Regional Climate model, version 3
RMSE	Root mean square error
R	Correlation coefficient.
VOC	Volatile Organic Compounds

Contents

List of publications

Paper I: Sofiev, M., Soares, S., Prank, M., de Leeuw, G. and Kukkonen, J. 2011. A regional-to-global model of emission and transport of SSA particles in the atmosphere. J. Geophys. Res., 116, D21302, doi:10.1029/2010JD014713

Paper II: Soares, J., Sofiev, S., Geels, C., Christensen, J.H., Andersson, C., Tsyro, S., and Langner, J. 2016. Impact of climate change on the production and transport of sea salt aerosol on European seas. Atmos. Chem. Phys. Discuss , doi:10.5194/acp-2015-1056, in review.

Paper III: Soares, J., Sofiev, S., and Hakkarainen, J. 2015. Uncertainties of wild-land fires emission in AQMEII phase 2 case study. Atmos. Environ., 115, 361–370, doi:10.1016/ j.atmosenv.2015.01.068.

Paper IV: Soares, J., Kousa, A., Kukkonen, J., Matilainen, L., Kangas, L., Kauhaniemi, M., Riikonen, K., Jalkanen, J.-P., Rasila, T., Hänninen, O., Koskentalo, T., Aarnio, M., Hendriks, C., and Karppinen, A. 2014. Refinement of a model for evaluating the population exposure in an urban area. Geosci. Model Dev., 7, 1855-1872, doi:10.5194/gmd-7-1855-2014.

Paper V: Loh, M., Soares, J., Karppinen, A., Kukkonen, J., Kangas, L., Riikonen, K., Kousa, A., Asikainen, A., and Jantunen, M. J. 2009. Intake Fraction Distributions for Benzene from Vehicles in the Helsinki Metropolitan Area. Atmos. Environ., 43, 301-310, doi:10.1016/j.atmosenv.2008.09.082.

Review of the papers and Author's contribution

Paper I presents a new analytical formulation for bubble-mediated sea salt spray production for particles with D_p ranging between 0.01 and 10 μm. In this formulation, the production of sea salt aerosol is a function of wind speed and seawater temperature and salinity. This source function was implemented in the dispersion model SILAM and applied to compute the distribution of sea salt aerosol over the North Atlantic and Western Europe, as well as globally. The source function was evaluated by comparing SILAM's predictions with ground-based and remote sensing observations. The author contributed to the validation of the source function, by performing most of the simulations and analysing the results. The author contributed to the writing of the article.

Paper II presents a multi-model comparison of four dispersion models (DEHM, MATCH, EMEP and SILAM) to assess the uncertainty and robustness of the sea spray predictions over Europe, particularly over the European seas. The models were driven by the same global projection climate scenario SRES A1B for past (1990-2009) and future (2040-2059) climate but included different formulations for sea salt aerosol production. In this paper, the impact of climate change on the production and fate of sea salt aerosol was assessed, alongside with the direct radiative effect of this natural aerosol on the regional radiative budget. The author was responsible for the simulations with the SILAM and the radiative transfer (LibRadTran) models, for the collection and standardization of the sea salt aerosol simulations, and for the analysis of the results. The author of this thesis was the leading author of the article.

Paper III discusses the main uncertainties of wildland fires emission estimates used in the AQMEII-II case study, by quantifying the uncertainties of the wildland fire particulate matter emission estimations by IS4FIRES. IS4FIRES converts fire information data from the remote sensing instrument MODIS, to emission fluxes of atmospheric pollutants. It is used for near-real-time and historical evaluation of emissions from wildland fires. The estimation of uncertainties is done by reviewing and refining the fire emission model IS4FIRESv1 to the current version, IS4FIRESv2. The refinement and evaluation was done by comparing SILAM's predictions with remote sensing observations. The author was involved in the refinement and validation of IS4FIRESv2, and was responsible for quantifying the uncertainties for previous and current versions of the fire emission model. The author of this thesis was the leading author of the article.

Paper IV presents an improved version of the exposure model (EXPAND), that estimates the human exposure metrics, in an urban area: population exposure and intake fraction. The paper describes the improvements to emission modelling and exposure estimation. Population exposure to fine particulate matter in Helsinki Metropolitan Area and in Helsinki for 2008 and 2009, respectively, were estimated with EXPAND. These estimations indicate where the population is most affected and which sources are most relevant for the exposure. The author was involved in the gathering and analysis of the results, and was the leading author of the article.

Paper V presents different methods to evaluate intake fractions from benzene emitted by traffic sources in Helsinki Metropolitan Area: a modified version of the exposure model framework EXPAND, for computations in a street canyon; a box-model; and a statistical model relating concentration and time-activity data. The author was responsible for the computations with EXPAND and analysis of the results, and participated in the writing of the article.

Other publications not included in this thesis

Colette, A., Andersson, C., Baklanov, A., Bessagnet, B., Brandt, J, Christensen, J. H., Doherty, R., Engardt, M., Geels, C., Giannakopoulos, C., Hedegaard, G.V.B., Katragkou, E., Langner, J., Lei, H., Manders, A., Melas, D., Meleux, F., Rouil, L., Sofiev, M., Soares, J., Stevensson, D.S., Tombrou-Tzella, M., Varotsos, K.V., Young, P. 2015. Is ozone climate penalty robust for Europe? Environ. Res. Lett. 10, doi:10.1088/1748-9326/10/8/084015.

Hernandez-Ceballos, M. A., Soares, J., Garcıa-Mozo, H., Sofiev, M., Bolivar, J. P., Galan, C. 2013. Analysis of atmospheric dispersion of olive pollen in southern Spain using SILAM and HYSPLIT models. Aerobiologia, doi:10.1007/s10453-013-9324-0

Kollanus, V., Prank, M., Gens, A., Soares, J., Vira, J., Kukkonen, J., Sofiev, M., Salonen, R.O., Lanki, T. 2016. Mortality due to vegetation-fire originated $PM_{2.5}$ exposure in Europe - assessment for the years 2005 and 2008. Environ. Health Prospective

Langner, J., Engardt, M., Baklanov, A., Christensen, J.H., Gauss, M., Geels, C., Hedegaard, G.B., Nuterman, R., Simpson, D., Soares, J., Sofiev, M0., Wind, P., Zakey, A. 2012. A multi-model study of impacts of climate change on surface ozone in Europe. Atmos. Chem. Phys., 12, 10423-10440, doi:10.5194/acp-12-10423-2012

Simpson, D., Andersson, C., Christensen, J., Engardt, M., Geels, C., Nyiri, A., Posch, M., Soares, J., Sofiev, M., Wind, P. and Langner, J.. 2014. Impacts of climate and emission changes on nitrogen deposition in Europe: a multi-model study. Atmos. Chem. Phys., 14, 6995-7017, doi. 10.5194/acp-14-6995-2014

Sofiev, M., Vira, J., Kouznetsov, R., Prank, M., Soares, J., Genikhovich, E. 2015. Construction of the SILAM Eulerian atmospheric dispersion model based on the advection algorithm of Michael Galperin. Geosci.Model Developm. 8, 3497-3522, doi:10.5194/gmd-8-3497-2015.

Tsyro, S., Aas, W., Soares, J., Sofiev, M., Berge, H. and Spindler, G. 2011. Modelling of sea salt pollution over Europe: key uncertainties and comparison with observations. Atmos. Chem. Phys., 11, 10367-10388, doi:10.5194/acp-11-10367-2011

1 Introduction

An atmospheric aerosol is a mixture of liquid and solid particles suspended in air; this mixture can be of different sizes and composition (Warneck, 1988). Atmospheric aerosols can be originated from primary emissions (natural or anthropogenic sources) or formed within the atmosphere through gas-to-particle conversion (Seinfeld and Pandis, 2006). On a planetary scale, the bulk of the total atmospheric burden mainly consist of natural primary aerosol; however, the proportions can be very different if considering urban or industrial areas, where traffic and industrial are the main sources of atmospheric aerosol (Textor et al., 2006). At the source areas, the chemical composition of the aerosol is linked to the prevailing emission sources but throughout the atmospheric life-cycle, concentration and properties of the aerosol change continuously through a series of physical and chemical processes (Kulmala et al., 2004): new particle formation, condensation, evaporation, water uptake, heterogeneous chemistry, dispersion and removal.

Dispersion modelling is a widely used tool to estimate the contribution of aerosols to the atmospheric composition, and infer about its potential impact on human health, ecosystems, and climate. An atmospheric dispersion model is a mathematical simplification of the atmosphere, applied to different space and time scales, depending on the physical and chemical processes that atmospheric species undergo. The process of modelling can be divided in four stages: data input, dispersion calculations, deriving the quantities desired, and analysis. The accuracy and uncertainty of each stage should be known and evaluated to ensure a reliable assessment.

Studies, such as Im et al. (2014) and Prank et al. (2016), show that the misrepresentation of the sources and processes commonly brings under or overestimation of particulate matter (PM) levels by dispersion models. The characterization of PM has many gaps: chemical speciation of the emissions, spatial and temporal distribution of the aerosol emission profile, and misrepresentation of chemical and physical transformation if long periods and large spatial scales are required (Rudich et al., 2007).

PM_X is the term used in air quality and health assessment to define the mass concentration of aerosol with maximum aerodynamic diameter of x μm. PM has been identified as the largest environmental public health risk, being associated with excess morbidity and mortality (Hänninen et al., 2014). Many of the studies that assess the health impact of PM use air quality data directly from models (Amann et al., 2005) or a combination of models and monitoring (Fiala et al 2009) for the estimation of long term population exposure. The assessment of exposure usually requires the application of an integrated model chain starting from estimation of emissions, atmospheric dispersion and transformation of air pollutants (Ashmore and Dimitripoulou, 2009). Finally, the exposure model combines ambient air concentrations of pollutants and population activity data to calculate human exposure. If coupled with time-microenvironment-activity models, exposure will be weighted by the time spent by the population in a particular microenvironment, reflecting the movement of the population and the exposure to existing sources where the population is located.

The overall goal of this thesis is to assess the impact of several major non-anthropogenic aerosol sources on atmospheric composition and air quality, with a downstream application to human health. The work was concentrated on the refinement of mathematical models fully or partially developed by the Finnish Meteorological Institute (FMI): a meso-to-global scale chemical transport model SILAM, a local-scale point/line-source dispersion model UDM/CAR-FMI, and a human exposure and intake fraction assessment model EXPAND, especially regarding the emission modelling of aerosols. The specific objectives considered the development and application of these models to assess the atmospheric composition and human exposure:

- to improve the insight on the contribution of sea salt aerosol (SSA) to the atmospheric composition by developing an unified parameterisation for SSA flux, as a function of wind speed and seawater properties;
- to estimate the climate impact on SSA production and fate over Europe and European Seas and evaluate the feedback to the regional radiative balance due to the presence of SSA;
- to improve the understanding of the impact of PM emissions from wildland fires on atmospheric composition by refining a method for wildland fire emission estimation, IS4FIRES;
- to estimate the contribution from various $PM_{2.5}$ sources to the atmospheric composition and their impact on human exposure in Helsinki and in the Helsinki Metropolitan Area (HMA).

2 Atmospheric dispersion modelling

A dispersion model is a mathematical representation of the transport and diffusion processes that occur in the atmosphere under a set of conditions. The dispersion model intends to represent the complex physical and chemical processes that take plac'e during transport and dispersion of trace gases and particles emitted into the environment, by a set of equations (ordinary, partial differential, parameterised and empirical). The fundamental equations solved by atmospheric dispersion models are the advection-diffusion-reaction equations, describing the evolution of tracers in space and time, considering atmospheric transport, chemical transformation, sources and sinks (Morton, 1996).

Atmospheric problems can be simulated over a variety of spatial scales, depending on the physical and chemical processes to be considered. This thesis addresses dispersion problems taking place at different spatial scales. Papers I, II and III are focused on mesoscale (20 – 100 km) processes, with the resolved time scale ranging from (tens of) minutes up to hours, and Papers IV and V are focused in microscale (< 2 km) processes with a times scale of tens of seconds. Mesoscale modelling tries to capture the diurnal cycle of the circulations, which results in the development of flow gradients and vertical stratification, and the effects of topography; both affect the air quality of a region. These models allow understanding the impact of emissions far away from the sources. Microscale should be able to allow capturing transport and mixing due to local thermal circulations and landscape characteristics. From now on, microscale modelling will be referred as urban scale modelling, since in

this thesis all the computations presented are for an urban area, involving diffusion of individual sources (e.g. power plants) and line-sources (traffic).

2.1 Mesoscale modelling: SILAM

Papers I, II and III have as their main modelling tool the SILAM model, documented in Sofiev et al. (2006, 2008, 2014 and 2015), which includes Eulerian and Lagrangian atmospheric transport descriptions. The system contains a meteorological pre-processor for evaluating the basic features of the boundary layer and the free troposphere, using the meteorological fields provided by numerical meteorological models (Sofiev et al., 2010). The model has several chemical transformation modules, including gas-phase chemistry in the troposphere and the stratosphere (Carbon Bond Mechanism (Gery et al, 1989) with updated coefficients), secondary inorganic aerosol formation (Sofiev, 2000), linearized sulphur oxides chemistry, radioactive nuclides decay, and aerosol dynamics (condensation and coagulation) computed from thermodynamic equilibrium or as dynamic. Aerosol size spectrum is described with sectional approach with user-defined bin distribution. Table 2.1 describes the different aerosols types assumed for the runs in Papers I, II and III, including the numbers of bins and respective size ranges. Depending on the particle size, mechanisms of dry deposition vary from primarily turbulent diffusion driven removal of fine aerosols to primarily gravitational settling of coarse particles (Kouznetsov and Sofiev, 2012). Wet deposition distinguishes between sub- and in-cloud scavenging by both rain and snow (Horn et al., 1987; Smith and Clark, 1989; Jylhä, 1991; Sofiev et al., 2006). The optical properties of aerosols and a selection of trace gases are calculated following Prank (2008). The particle hygroscopic growth is taken into account when deriving gravitational settling, dry deposition and optical properties of the aerosols. Emission models for sea salt (Paper I), wild-land fires (Sofiev et al., 2009, 2012a, Paper III), desert dust, allergenic pollen (Sofiev et al., 2012b, Siljamo et al., 2012, Prank et al., 2013) and volatile organic compounds (VOC) are embedded in SILAM. The bio-VOC can be estimated by MEGAN (Guenther et al., 1995) or BEM (Popkou et al., 2010). The model also includes data assimilation tools for both 3D- and 4D-VAR (Vira & Sofiev, 2010) and ensemble Kalman filter.

SILAM model has been extensively evaluated against air quality observations over Europe and the globe (daily at http://www.gmes-atmoshpere.eu; Solazzo et al., 2012; Huijnen et al., 2010).

Table 2.1 Aerosol types and number of bins and size rages assumed for the runs in Paper I, II and III.

aerosol type	number of bins	size ranges (μm)
anthropogenic/fire	2	[0 2.5] [2.5 10]
dust	4	[0.01–1] [2.5] [2.5 10] [10 30]
sea salt	5	[0.01–0.1] [0.1 1.5] [1.5–6][6 15] [15 30]

2.2 Urban area modelling: UDM-FMI and CAR-FMI

In Paper IV and V, the modelling system applied for evaluating emissions and atmospheric dispersion of pollution in an urban area is a combined application of UDM-FMI and CAR-FMI models. Both models are multiple source Gaussian urban dispersion models and have been addressed in detail by Karppinen et al. (2000a) and Kukkonen et al. (2001). The UDM and CAR-FMI take into account stationary and traffic (vehicular and shipping) sources, respectively.

The dispersion parameters are modelled as a function of Monin-Obukhov length, friction velocity, and boundary layer height, which are computed by the meteorological pre-processing model MPP-FMI (Karppinen et al., 2001). This model has been used with input data from the three nearest synoptic weather stations and the nearest sounding station, to evaluate an hourly meteorological time series for the dispersion modelling computations. Both dispersion models consider inert particles and gaseous compounds where simple chemical transformations, such as conversion between NO, NO_2 and ozone, are included. PM is treated as inert, i.e. no chemical reactions or aerosol processes are included in the calculations. The models include treatment of dry and wet deposition. The system computes hourly time series of concentrations and statistical parameters in each receptor point, which can be directly compared with air quality guidelines. The receptor points are adjustable with intervals ranging from approximately 20 m in the vicinity of the sources to 500 m further from the sources. The regional background concentrations of gaseous compounds are taken from a single measurement or interpolated from several measurements of the monitoring network, or estimated by a regional chemical transport model (CTM).

To include the shipping contribution to $PM_{2.5}$ surface concentrations in Paper IV, CAR-FMI was refined to include emissions from shipping. All shipping emissions were treated as line sources with an injection height of 30m above the sea level.

The CAR-FMI model has been previously evaluated against the measured data of urban measurement networks in HMA and in London, for gaseous pollutants (Karppinen et al., 2000b; Kousa et al., 2001; Hellén et al., 2005) and for $PM_{2.5}$ (Kauhaniemi et al., 2008; Sokhi et al., 2008; Singh et al., 2014). The performance of the CAR-FMI model has also been evaluated against the results of a field measurement campaign and other roadside dispersion models (Kukkonen et al., 2001; Öttl et al., 2001; Levitin et al., 2005). The UDM-FMI model has been evaluated against the measured data of urban measurement networks in HMA (Karppinen et al., 2000b; Kousa et al., 2001) and the tracer experiments of Kincaid, Copenhagen and Lilleström.

3 Exposure modelling

The relationship between a source and the subsequent exposure of a population depends on the ability of the released pollutant to reach individuals. The exposure efficiency is the fraction of material released that penetrates into the human body, depending on the characteristics of the source, pollutant,

environment where the pollutant is released, as well as the receptor (Harrison et al., 1986; Evans et al., 2000).

Since the urban population spends typically 80-95 % of their time indoors (Hänninen et al., 2005; Schweizer et al., 2007), the exposure to pollutants is dominated by indoor exposure. Epidemiological studies based on concentrations (measured at fixed air quality monitoring sites or predicted by land-use regression models) ignore indoor sources, activity patterns of individuals, and fine-scale spatial variability of concentrations. These problems can be overcome by combining concentration of pollutants in air with time-microenvironment-activity models and indoor to outdoor concentration ratios. Microenvironment is defined as a location containing a relatively uniform concentration where the human exposure takes place. The average personal or population exposure is then estimated as a linear combination of concentrations in different microenvironments, weighted by the time spent in each of them. Therefore, exposure can be described as:

$$E_i = \sum_{j=1}^{m} T_{ij}\, C_{ij} \qquad (3.1)$$

where E_i is the total exposure of individual i in various microenvironments m (μg m^{-3} s), T_{ij} is the time spent in microenvironment j by individual i (s) and C_{ij} is the air pollutant concentration that individual i experiences in microenvironment j (μg m^{-3}). This formulation can also be interpreted as a weighted sum of concentrations, in which the weights are equal to the time spent in each environment.

Another concept applied in exposure assessments is intake fraction. This concept has been used in life cycle assessments (Humbert et al. 2011; Apte et al., 2012), for ranking sources (Tainio et al., 2009), and to compare different control policies (Stevens et al., 2005). The intake fraction is defined as a fraction of the pollutant emission that is taken by humans via relevant exposure pathways, e.g. a portion of a source's emissions that is inhaled by an exposed population over a defined period of time. This exposure metric is defined as it follows:

$$iF = \frac{Population\ \ Intake}{Total\ Emissions} = \frac{\int_{T_1}^{\infty} (\sum_{i=1}^{p} C_i(t)\ Q_i(t))\, dt}{\int_{T_1}^{T_2} E(t)\ dt} \qquad (3.2)$$

where iF is the intake fraction for the exposed population, T_1 and T_2 (s) are the starting and ending times of the emission, P is the number of people in the exposed population, Q_i (m^3 s^{-1}) is the breathing rate for individual i at time t, C_i (µg m^{-3}) is the concentration attributable to a specific source at time t in the breathing zone of individual i, and E (g s^{-1}) is the source's emissions at time t. In practice, the integral of the numerator is evaluated until the incremental concentration attributable to the source of interest is negligibly small. For instance, an intake fraction of one in a million (10^{-6}) means that for every tonne of a pollutant emitted, 1 g is inhaled by the exposed population. This allows quantifying

emission-to-intake relations, independently of the emission, location or exposure pathway for non-reactive compounds.

3.1 EXPAND

EXPAND has been used to evaluate the spatial and temporal variation of the average exposure of a urban population to air pollution, in different microenvironments (Kousa et al., 2002). This system combines information on the concentration in ambient air and the population activity and location, utilizing the geographical information system (GIS) MapInfo (Figure 3.1). Papers IV and V are an example of how this modelling framework can be used for health risk assessment. The first paper revises this model to include several improvements related to urban emission estimations, the dispersion module, treatment of the time-use of population, and infiltration coefficients from outdoor to indoor air. The revised model version can also be used for estimating intake fraction; which is then discussed in Paper V. A comparison between the original (Kousa et al. 2002) and the current version (Paper V) is shown is Table 3.1.

Table 3.1 A summary of the refinements of the EXPAND model.

	Original (Kousa et al., 2002)	**Current (Paper IV, V)**
Emissions	Vehicular (exhaust), stationary	Vehicular (exhaust and suspension), shipping, stationary
Pollutants	NO_x, NO_2, ozone	NO_x, NO_2, ozone, $PM_{2.5}$
Time activity data	Working age population, year 2000	All population, year 2010 wider range of activities
Model results	Population exposure, microenvironment- and source-specific	Population exposure and intake fractions, microenvironment-, source-population group-specific
Coordinate systems	Finnish	international and national

The concentration in ambient air for vehicular traffic and shipping are obtained using CAR-FMI, and in case of stationary sources using UDM-FMI. Both models are described in Section 2.2. The emissions serving as input for the models are described in Section 4, and Papers IV and V.

The population activity data is available for four microenvironments: home, workplace, traffic and other activities (shops, restaurants, etc.). The dataset provides the total number, age distribution and geographic information on people living in a particular building, working at a particular workplace, located at a particular road, and spending time at other activities. The methodology for compiling the activity data is described in Papers IV and V.

All the data are interpolated into a rectangular grid defined by the user, then exposure or intake fraction are calculated for the same grid. MapInfo is subsequently utilized in the post-processing and visualization of the results.

4 Emission modelling

Estimating emissions is a key element for assessing air quality. Emissions are typically estimated based on models ranging from simple look-up tables to sophisticated and complex systems. In general, emission models apply methods that combine emissions factors with activity data to calculate emissions; both demanding a variety of parameters which have an impact on the resulting emissions. Emissions can be compiled considering emission totals, derived from aggregated data, then apportioned to smaller areas using proxy data (top-down approach), or using information on emission and activity of single sources to estimate total emissions (bottom-up approach).

Atmospheric models can be driven by a combination of emission inventories and dynamic emission modelling, to estimate the emission of gases and aerosols into the atmosphere. Emission inventories contain the emissions estimates for types of sources (point, area or line), together with complementary data such as location, emission height and sector. These inventories are typically defined for a given time period and with poor time-resolution. Dynamic emission modelling, on the other hand, can be applied to obtain a geographical distribution of individual events and its emissions, reflecting the temporal and spatial variation of the emissions more accurately.

In the sections below, the emission modelling systems for sea spray and wildland fire applied for mesoscale modelling (Paper I, II and II) are presented. Both sources depend on weather conditions and local factors. The dynamic modelling becomes inevitable for accurate assessment of aerosol load, air quality and health impact. Paper III also included the dynamic modelling of wind-blown desert dust and the MACCity emission dataset (Granier et al., 2011) for anthropogenic gases and aerosols. For the urban-scale modelling, Paper IV describes the emission databases compiled for $PM_{2.5}$ originated from traffic and energy production in Helsinki and in HMA. A short description of the methodology to generate those databases is presented in Section 4.3.

4.1 Sea salt aerosol for mesoscale applications

SSA originates from sea spray droplets resulting from waves breaking on the seawater surface, forming whitecaps and causing the entrainment of air into the water. The two main mechanisms responsible for sea spray formation are air bubble bursting during whitecap formation and decay, and direct tearing of droplets from the top of the breaking waves. Therefore, the formation of primary SSA is mainly dependent on wind speed: the emission of SSA is generally considered to be proportional to surface winds cubed (Monahan et al., 1986), suggesting that small changes in surface winds can have a substantial impact on the emission flux. Studies on marine aerosol size distribution (e.g. Covert et

al., 1998; Russell and Heintzenberg, 2001; Bates et al., 2002; Huebert et al., 2003) suggest that for high wind speeds, the production of very coarse SSA (D_p > 20 mm) increases. Other parameters influencing the formation of primary SSA have been identified. Laboratory studies by Mårtensson et al. (2003), hereafter referred as M03, and in situ measurements by Nilsson et al. (2007) show that for nano-sized particles, the aerosol number emission decrease with increasing seawater temperature, and for particles with D_p > 100 nm, the number SSA increase with increasing seawater temperature. These reflect different sea spray formation processes. Seawater salinity also affects the droplet formation, where formation of particles with D_p < 0.2 µm are not affected by salinity, but for larger D_p, salinity impact is substantial: higher salinity contributes to higher production (Mårtensson et al., 2003).

The majority of the CTMs have SSA source based on M03 parameterisation for formation of sub-micron aerosols and white-cap-area parameterisations of Monahan et al. (1986), hereafter referred as M86, for super-micron particles. The idea behind the new parameterisation described in Paper I, was to obtain a unified function that would cover such size ranges and would take into account the temperature and the salinity of seawater. Besides, the numerical implementation of M03 function showed a high sensitivity to the 6th polynomial fit: D_p should range between 0.02 to 2.8 µm of dry diameter, which results in the SSA flux shown in Figure 4.1 (left). If the size ranges are defined differently from the ones tabulated in that study, it can result in a very different outcome.

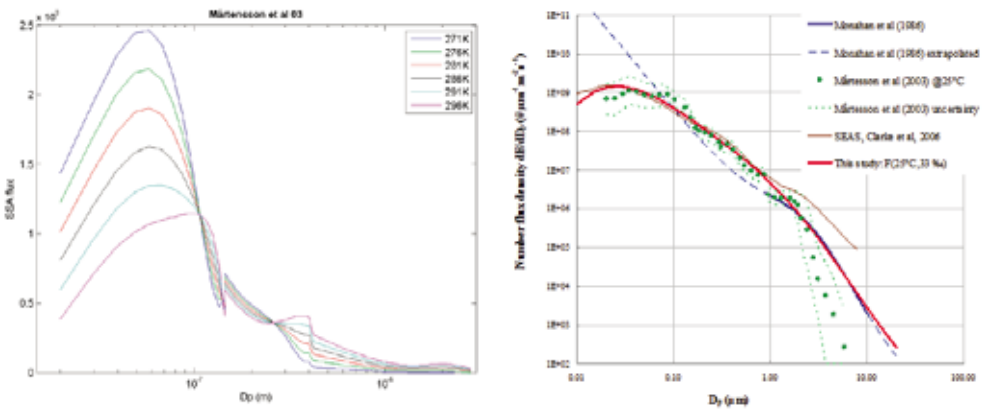

Figure 4.1 SSA number flux density. Left: computed with M03 parameterisation for different seawater temperatures. Right: computed with Paper I parameterisation (red) and with M86 parameterisation (solid blue line) and extrapolated (dashed blue lines), M03 data (green dots) and its uncertainty (light-green dashed line) for Tw=25°C, Sw=33‰, and SEAS data (brown).

The M03 observations for a seawater surface temperature of 25 °C and a seawater salinity of 33 ‰, and the SEAS campaign (Clarke et al., 2006) were used to extrapolate the M86 function to particle sizes down to 20 nm. The M86 function was chosen to be extrapolated because it is widely used, which simplifies the comparison with other models. The function is monotonous and requires few

adjustments to fit into the M03 and SEAS data. All the data and functions used to obtain the SSA flux unified function are show in Figure 4.1 (right). The only significant correction refers to sub-0.1 μm particles, for which an exponential term had to be introduced to reduce the production under 0.03 μm. The resulting curve was then extrapolated from 8 to 10 μm to cover the whole target range of D_p from 0.01 to 10 μm. The resulting sea salt flux function (dF_0/dD_p) for particles with D_p ranging from 0.01 to 10 μm, for seawater temperature of 25 °C and salinity of 33 ‰ is described below and is depicted in red in Figure 4.1 (right):

$$\left(\frac{dF_0}{dD_p}\right)_{33‰,25°} = 1\cdot 10^6 \cdot \frac{\exp\left(\frac{-0.09}{D_p + 3\cdot 10^{-3}}\right)}{2+\exp\left(-\frac{5}{D_p}\right)} \cdot \frac{1+0.05\,D_p^{1.05}}{D_p^3} \cdot 10^{1.05\exp\left(-\left(\frac{0.27-\lg D_p}{1.1}\right)^2\right)} \qquad (4.1)$$

To calculate the SSA production for other seawater temperatures and salinities, correction factors were derived from the M03 experimental data. The correction functions were derived by dividing the M03 observed fluxes for seawater temperatures at 15 °C, 5 °C and -2 °C by the fluxes observed at 25 °C. Figure 4.2 (left) shows that the ratio between the M03 production flux, at these three temperatures and the flux at 25 °C, are smooth and monotonically decreasing with increasing particle size. The correction function for the seawater temperature (F_{TW}) and salinities (F_{SW}) are described below, for D_p in μm.

$$\begin{aligned} F_{T_W=15^0C}(D_p) &= 0.48\cdot D_p^{-0.36} \\ F_{T_W=5^0C}(D_p) &= 0.15\cdot D_p^{-0.88} \\ F_{T_W=-2^0C}(D_p) &= 0.092\cdot D_p^{-0.96} \end{aligned} \qquad (4.2)$$

$$\begin{aligned} F_{S_W=0.0092} &= 0.12\cdot D_p^{-0.71} \\ F_{S_W=0} &= 5.85\cdot 10^{-5}\cdot D_p^{-1.7} \end{aligned} \qquad (4.3)$$

For $D_p \sim$ 0.1-0.2 μm and $D_p \sim$ 2 μm a few outliers appear in two of the correction functions (shown in green and in light blue in Figure 4.2, left). These are related to non-monotonicity of the particle size distributions measured by M03 at different temperatures. Nevertheless, the correction factors for other temperatures seem to be easily obtained by linear interpolation, since water temperature dependency seems to be monotonic.

The effect of salinity is evaluated following the same procedure (Figure 4.2, right). The salinity of 33 ‰ is taken as the reference and for other salinities the correction functions are derived using the ratios of the M03 fluxes for 9.2 ‰ (e.g., Baltic Sea) and 0 ‰ ("fresh" water) to that at 33 ‰ (Atlantic).

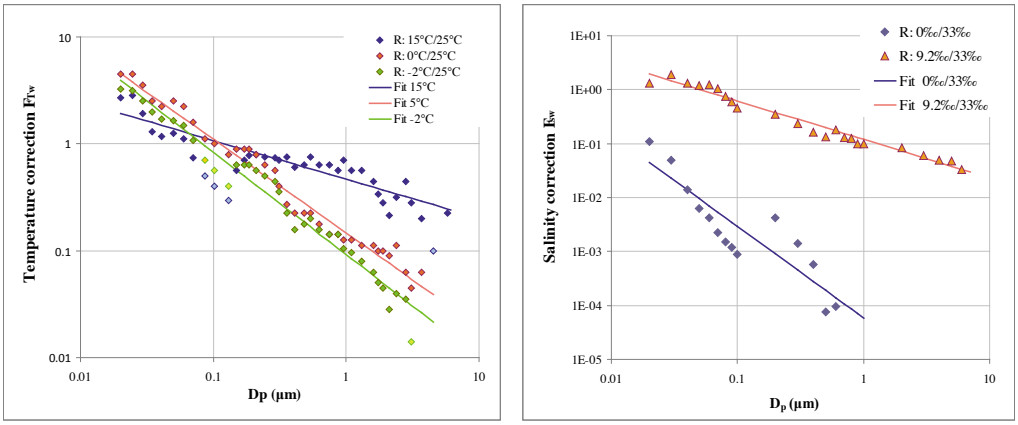

Figure 4.2 Temperature and salinity correction functions. Left: temperature corrections defined as ratios (R) of the SSA production flux at 15 °C, 5 °C, and -2 °C to the flux at 25 °C, and the linear fits for those ratios. Right: salinity corrections defined as ratios (R) of SSA production flux at 0 ‰ and 9.2 ‰ to the flux at 33 ‰, and the linear fits for those rations.

Testing the formulation above has resulted in adjustments to the temperature correction function. The seawater temperature reference for the unified shape function is currently 20 ºC, instead of 25 ºC as referred in Paper I. The changes to the main function are presented in Paper III, section 2.3.4.

4.2 Wildland fires for mesoscale applications

Wildland fires also have strong regional and local contribution, quite often becoming the dominant source and strongly contributing to exceedances of the daily limit value established by air quality directives (Saarikoski et al, 2007). The impact of fire emission on the atmospheric composition depends on the dynamics of the fire and meteorology. The amount of emitted tracer is typically assumed to be proportional to the area affected by the fires (burnt area) and the empirical coefficients characterising the combustion process (Crutzen et al., 1979):

$$E_i = EF_i * BA * BD * CF \qquad (4.4)$$

where E_i (kg) is the total emission of the emitted specie i, EF_i is the emission factor for the emitted specie i (g kg^{-1}) dry matter burned, BA is the size of the burned area (km^2), BD is the biomass density (g kg^{-1} km^{-2}), and CF is the combustion completeness factor reflecting combustion efficiency of the fires.

For large scale applications, emission factors are usually extrapolated from laboratory experiments or field campaigns. Apart from extrapolation errors, variables in Eq. (4.4) also inherit uncertainties, such as the spatial extent and duration of the fires; amount and distribution of available biomass or fuels; and fraction of biomass or fuel consumed from the different carbon reservoirs (French et al., 2004). Kaiser et al. (2012) shows that bottom-up approaches such as these, tend to underestimate PM

emissions. The same study suggests that top-down approaches, based on active-fire remote-sensing observations, could be a better choice. Based on Kaufman et al. (1998) and Ichoku and Kaufman (2005) it is possible to relate the energy of the fire with the rate of biomass consumption and derive a relationship similar to Eq. (4.4), by relating the physical quantities of the biomass burned (BA*BD*CF) with radiant component of the energy release of the fire. This energy release is the so-called fire radiative power.

$$E_i = C_{ia} * FRP \qquad (4.5)$$

where E_i (kg) is the total emission of the emitted specie i, C_{ia} is the emission coefficient (kg MJ^{-1}) for specie i and vegetation type a, and FRP is the fire radiative power (MJ).

IS4FIRES is an operational, near-real-time assessment system for wildland fires based on the active-fire observation products of MODIS (http://modis.gsfc.nasa.gov, Justice et al., 2002; Kaufman et al., 1998) and SEVIRI (Kaiser et al., 2009; Roberts and Wooster, 2008). The system provides PM fire emission compiled from individual-fire FRPs registered daily by MODIS, via Equation 4.5. Temporal evolution of the fire intensity is derived from FRP observation from SEVIRI, for different vegetation classes (Sofiev et al., 2013).The development of the IS4FIRES system for wildland fire emission has been ongoing since 2006. To-date, IS4FIRES has two releases: v1 (Sofiev et al., 2009) and v2 (Paper II). The difference between the versions of IS4FIRES is described in the table 4.2.

For the FRP scaling, the emissions coefficients are obtained offline from the top-down calibration, which is performed once and involves the solution of the inverse dispersion problem for the fire smoke plumes. During the calibration step, SILAM (described in Section 2.1) is used to calculate the atmospheric dispersion of the emitted masses, thus producing both near-surface PM concentrations and aerosol optical density (AOD). The obtained plumes are attributed to the vegetation type prevailing at the location where the fire occurred, based on the Global Land Cover Characterization (GLCC) inventory (Loveland et al., 2000). The emission factor for each land-use type is obtained via fitting the modelled PM concentrations (only IS4FIRESv1) and AOD into the observed ones. The global distribution of AOD is provided by MODIS instruments on-board NASA satellites Aqua and Terra: Level-2 data from Collection 5 (before 2009) and 5.1 (Kaufman et al., 2002; Remer et al., 2008). IS4FIRESv1 calibration is described in Sofiev et al. (2009), Section 4. For IS4FIRESv2, the calibration is based on a long-term comparison (2002-2013) of remote sensing measurements and SILAM results. Both predicted and observed AOD data were projected to a global 1° x 1° grid, on an hourly basis. The MODIS-AOD pixels falling into the same grid cell were averaged; a minimum of 25 pixels per grid-cell were required to avoid biased AOD values. These two steps ensured the maximum possible co-location of the observations and model results, both in space and in time. The calibration used only the fire-dominated cells as predicted by SILAM: daily mean fire-induced AOD was requested to be bigger than combined AOD from all non-fire sources (sea-salt, wind-blown dust, primary anthropogenic and secondary inorganic aerosol). The observed AOD is then corrected by subtracting the non-fire SILAM-AOD. This correction is made under the assumption that fire-induced

AOD over fire-dominated pixels is the most-uncertain part of the total AOD predicted. The final step of the optimisation was to run an unconstrained minimisation of the root mean square error (RMSE) between the SILAM and MODIS AOD by adjusting the C_{ia} for each vegetation type. The optimisation is run independently for each year, maintaining the initial scaling factors as a starting point for the optimisation. A single scaling factor for each vegetation type is attained by averaging the values obtained from every optimisation run.

Upon obtaining the emission factors, the emission bottom-up estimation is performed, resulting in daily biomass-burning emission maps. The daily emissions are then scaled with diurnal variation profiles. Finally, the fire plume is given a prescribed height that can be static, prescribing always the same value or prescribing climatological fields (Sofiev et al., 2013), or dynamic, changing every-time step of the model (Sofiev et al., 2012a).

Elvidge et al. (2013) indicated that some sources, such as gas flares and large industrial installations, could be misinterpreted by MODIS as fires. An effort to mask-out these sources has been undertaken in IS4FIRESv2 by calculating the frequency of fires occurring in each 3*3 km^2 pixel over the globe, based on the MODIS-FRP. Grid-cells burning over 50 days per year, for at least 4 years over the 12-year period, would be flagged as possible highly energetic sources and removed from the FRP database.

Table 4.2 Comparison between previous (v1) and current (v2) versions of IS4FIRES.

	v1 (Sofiev et al., 2009)	**v2 (Paper III)**
emission coefficients	Ichoku & Kaufman (2005)	Ichoku & Kaufman (2005) Akagi et al (2011)
vegetation classes	forest, grass and mixed	boreal, temperate and tropical forests, residual crop, grass, shrub, peat
calibration period	fire cases per vegetation class	2002-2013
calibration data	remote sensing and ground-based measurements vs modelled AOD	remote sensing measurements vs modelled AOD
Plume injection height	Homogeneous from surface up to 1km	Parameterisation derived from MISR fire plume observations (Sofiev et al., 2012).
diurnal variation	night/day-time emissions = ± 50% (Saarikoski et al. 2007)	Parameterized for vegetation classes based on SEVIRI-FRP (Sofiev et al., 2013)
Masked data	-	High-energy sources

4.3 Anthropogenic emissions for urban scale applications

The most relevant PM anthropogenic emissions, for HMA, are traffic and energy production (Niemi et al, 2009). Most widely used methods for heating of residential buildings and domestic water were taken into consideration, with the exception of small-scale combustion, which mainly consists of wood burning. This source can contribute up to 25 % of the national total emission (Karvosenoja et al., 2008) but the spatial distribution of the emission data was not known with sufficient accuracy. Energy

production and other industrial sources emissions were estimated by combining the activity data (Statistics Finland, 2012) and the emission factors (Karvosenoja et al., 2008) available for this sector.

Vehicular traffic emissions were estimated for each link of the HMA using the average speed-dependent functions, determined separately for each vehicle category (Laurikko et al., 2003), and the correspondent emission factors. The traffic information for each line source is obtained by EMME/2 (INRO, 1994). The emission factors are based on the European emission factors and taking into consideration the age distribution of the Finnish vehicle fleet (Laurikko et al., 2003; Kauhaniemi et al., 2011). Cold start and cold driving emissions were taken into account, using coefficients based on laboratory emission measurements (Laurikko, 1998). These emissions are dependent on the ambient air temperature and on the fraction of vehicles using pre-heating of the engine (Kauhaniemi et al., 2008).

Road dust emissions were estimated by FORE (Kauhaniemi et al., 2011). The emission factors for suspension of road dust are a product of the so-called reference emission factors, the reduction factor of the moisture content of the street, and a weighted sum of the contribution of particles from the wear of pavement and traction sand. Emissions from brake, tyre and clutch wear are not included in the model, due to their small contribution compared to suspension and road wear emissions in the Nordic countries. The baseline values for the suspension emission model were set by the reference emission factors that depend on the period (e.g. sanding or not), the mass fraction of particles, and the traffic environment.

Shipping emissions were estimated by STEAM (Jalkanen et al. 2009, 2012). The model combines vessel technical data with the positioning of ship, with a high spatial resolution (typically a few tens of metres), to obtain emission data. This model provides emissions from ships cruising, ships manoeuvring in harbour and while the ship is at berth.

5 Model applications and evaluation

5.1 Sea salt aerosol contribution to the atmospheric composition

SSA contributes from 30 to 75 % of the total production of natural aerosol (Lewis and Schwartz, 2004); with measurements showing SSA as the most important contributor to the total aerosol loading over the Oceans (e.g. Quinn et al., 1999). Understanding the magnitude and spatial variation of SSA is fundamental for assessing anthropogenic and continental impacts, to improve interpretation of satellite retrievals, and to understand the Earth's radiation budget. This understanding has increased substantially, but process-based estimates of the total mass and size distribution of emitted sea spray particles continue to have large uncertainties (de Leeuw et al., 2011). CTMs and general circulation models (GCM) estimates of sea salt burden may vary over 2 orders of magnitude (Textor et al., 2006, Gantt et al., 2012; Grythe et al., 2014).

Paper I describes the development and evaluation of a new SSA parameterisation in order to unify data and existent parameterisations, available for different size ranges and seawater properties. The application of this parameterisation allowed the evaluation of the SSA emission flux and assessment of the SSA impact on the atmospheric composition. The emission module was evaluated by comparing results from simulations with observations: concentration, deposition and AOD. The simulations for this purpose are described below. In these papers, the SSA mass refers to the total mass of dry particles. If sodium (Na^+) concentrations are mentioned instead, it is assumed that Na^+ mass fraction in PM is ~30 % (Seinfeld and Pandis, 2006).

- Paper I: European and Northern Atlantic runs for different time periods: May–October 2003 and years 2000, 2007, 2009 and 2010, driven by meteorological fields from ECMWF-IFS (ECMWF, 2015). The horizontal resolution was 30 km grid spacing and the vertical grid consists of 9 unevenly spaced layers, with the lowest layer being 50 m thick and the top reaching up to the tropopause.
- Paper I: Global runs for the years 2001 and 2008, driven by meteorological fields from ECMWF-IFS (ECMWF, 2015). The horizontal resolution was 1*1 ° grid spacing and the vertical grid as described above was considered.
- Paper II: Europe and Northern Atlantic for a 20-year period (1990-2009), driven by the RCA3 meteorology (Samuelsson et al., 2011; Kjellstrom et al., 2011). RCA3 was driven by the global climate ECHAM5/MPIOM GCM (Roeckner et al., 2006) fields and by emissions from the SRES A1B scenario (Nakićenović, 2000). The horizontal resolution of 50*50 km^2 and vertically similar to Paper I, but the lowest layer being 25 m thick.

The typical spatial distribution for this natural aerosol is depicted in Figure 5.1. Figure 5.1 shows the general pattern of SSA concentration following the emission areas (sea surfaces) with stronger winds and frequent storms. Global runs typically show higher concentration in the Southern Hemisphere, where winds are stronger, and in the equatorial belt due to higher seawater temperature. High resolution runs (Figure 5.1, right) show up to 10-times higher concentrations at open seas than at closed seas e.g. Atlantic vs Baltic Sea. These runs show that the European Seas also have concentrations gradients, e.g. at the Mediterranean Sea, where the model show pronounced maximums at the Balearic Sea and the Levantine Sea. In Figure 5.1, the transport of SSA over land is visible hundreds of km from the coast; near the European coast line it can contribute up to 6 $\mu g\ m^{-3}$ to PM_{10}, at annual level. With dry diameter lower than 1 μm, SSA can easily be transported for long distances in the atmosphere. This is confirmed by measurements campaigns with MARGA instrument (Makkonen et al., 2012), that revealed that PM measurements at continental sites with more than 200 km distance from the sea, such as Hyytiälä, have marine Na^+ contribution. Figure 5.2 (left) shows the predicted contributions of the Atlantic and Baltic Sea on two measurements sites in Finland: Helsinki, close to the Baltic Sea; and Hyytiälä, an inland site (Figure 5.2, right). The results show that, even though the Atlantic Ocean is 700km away from the measurement sites, there is a contribution of the

Atlantic Ocean to these sites. Also, it is important to notice that the contribution is higher when concentrations are high. The latter is explained by the low salinity of the Baltic Sea: as seen in Figure 4.2, right, the amount of SSA produced is highly affected by salinity. But low salinity also allows the emissions of smaller particles that are likely to be transported for longer distances, reaching Hyytiälä measurement site. Table 5.1 shows how the model captured the concentration of Na^+ in aerosol for the two sites. The model performs well for the coarse fraction but overestimates the fine fraction; correlation of daily time series for Na^+ in PM_{10} is good compared to $PM_{2.5}$ daily time series.

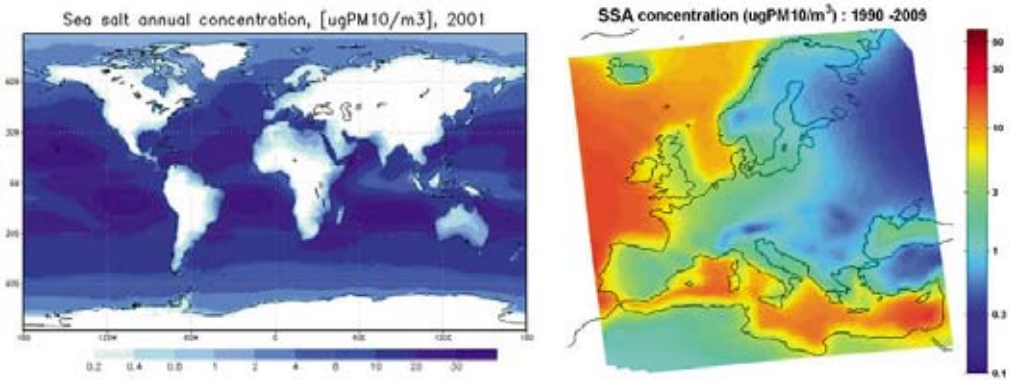

Figure 5.1 SSA near-surface concentrations (μgPM_{10} m^{-3}) for simulations with the actual sea surface temperature. Left: annual mean over the year 2001; right: annual mean over the time period 1990-2009.

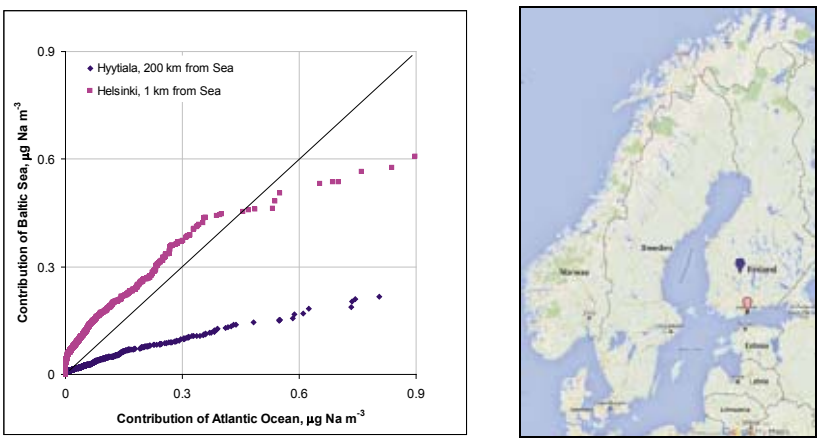

Figure 5.2 Left: predicted impact of Atlantic Ocean and Baltic Sea: Na^+ concentrations (μg Na^+ m^{-3}) originated from Baltic Sea vs those originated from Atlantic Ocean for two measurements sites: Helsinki (pink) and Hyytiälä (blue). Right: location of the measurement sites: Helsinki (pink) and Hyytiälä (blue).

Table 5.1 Comparison of SILAM predictions of Na^+ concentrations in $PM_{2.5}$ and PM_{10} with observation at Hyytiälä (continental) and Helsinki (coastal).

Sites in Finland	substance	Mean Observation	Mean Model	Correlation	RMS
Hyytiälä	Na^+ in $PM_{2.5}$	0.01	0.04	0.20	0.05
Hyytiälä	Na^+ in PM_{10}	0.03	0.05	0.51	0.06
Helsinki	Na^+ in $PM_{2.5}$	0.04	0.07	0.10	0.09
Helsinki	Na^+ in PM_{10}	0.08	0.06	0.41	0.12

To evaluate the sea-salt size distribution inherent in these calculations, eight months in 2009 and 2010 were computed with high spectral resolution (18 bins over a D_p size range from 0.01 to 10 µm range). These calculations were compared with a measurement campaign on a cruise, operating over the Northeast Atlantic, NEAT (O'Dowd et al., 1997), and with the work published by Pierce and Adams (2006). The time period selected for comparison between the model and the observations was different due to unavailability of meteorological data. The results of this comparison are shown in Figure 5.3.

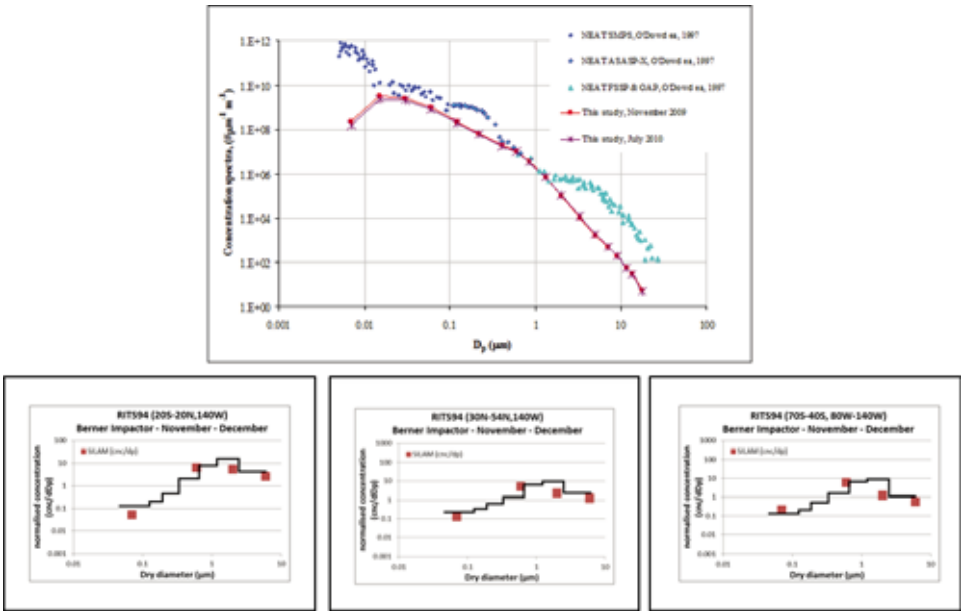

Figure 5.3 Comparison of observed concentrations with predictions by SILAM (µg SSA m^{-3} m^{-1}). Top: observed mean under the NEAT campaign (blue dots) and predicted by SILAM (lines, monthly averages) SSA concentration spectra in the Northeast Atlantic, unit: (# μm^{-1} m^{-3}). Bottom: observed (black lines) published by Pierce and Adams (2006) and SILAM predicted (colour dots) SSA mass concentration over the globe (normalised with the mean diameter of the D_p size range).

The first set of comparisons (Figure 5.3, top) show that the source function applied in SILAM has a close resemblance to the distribution showed by the NEAT campaigns. The closest representations is for the size range from 0.2 to 1 µm, where concentration for the current parameterisation peaks at

approximately 20 nm, then decreasing towards coarser particles. The decrease in concentrations below the 10 nm, contradicting the measurement results, can be a result of the removal of the aerosols due to water uptake or coagulation. The underestimation shown for sizes larger than 2 µm is harder to explain, and probably reflects specific local aerosol formation, such as at the surf-zone, where coarser particles are formed with wave breaking. The same pattern is seen in the work of Pierce and Adams (2006). SILAM's predictions (Figure 5.3, top) shows that November tends to have higher production of SSA due to stronger storms, but coarser particles are emitted less due to low seawater temperature (Figure 4.2). This explains why fine-particle concentration was higher in the winter by few tens of percent, while the coarse-aerosol load remained constant.

Observations available from the EMEP network (Tørseth et al. 2012) were used to evaluate the SSA bulk mass (Figure 5.4). The observations consist of Na^+ concentration in aerosol and ion analysis of precipitation including Na^+. Typically, the surface concentrations are well reproduced by SILAM, the correlation coefficients for all the runs are higher than 0.5 and relatively low bias (0.14) and RMSE (0.71).

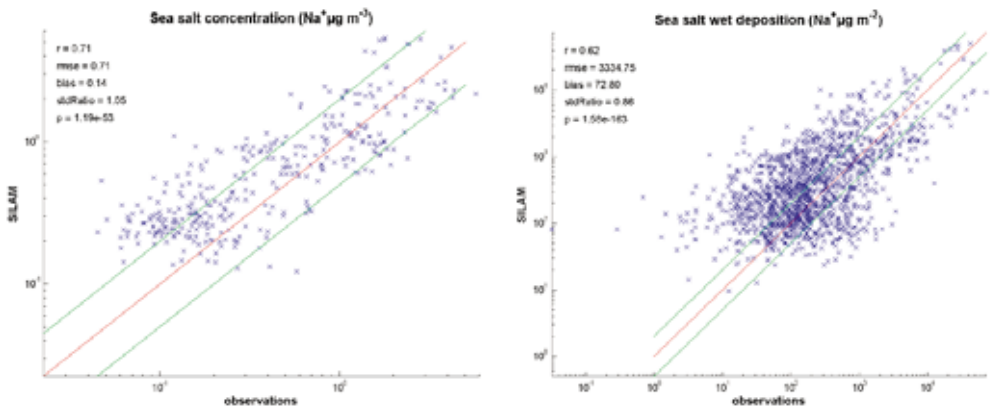

Figure 5.4 Model-measurement comparisons for monthly mean Na^+ concentration (µg m^{-3}) (left) and monthly wet deposition (mg m^{-2}) (right), over the time period 1990-2009. The Pearson correlation (r), root mean square error (rmse), bias, standard deviation ration (stdRatio), p-value (p), 1:1 (red solid), 1:2 (green), and 2:1 (green) lines are shown.

The current model version underestimates wet deposition. This could mean that SSA is strongly scavenged at the source, reducing the availability of the aerosol at the measurement sites. Here is shown the comparison with full size range available (D_p from 0.01 to 30 µm) since the observed wet deposition does not cut-off the size of the particles, i.e. SSA coarser than 10 µm is accounted for, including the SSA produced in the surf zone. Considering the full size range strongly reduced the bias (400 times), correlation improved 1.5 times, and RMSE became slightly smaller. This mostly explains the large negative bias of the models, when reporting PM_{10} only, and, to some extent, the low

correlation. In summer, the scores are slightly better than in winter, but the absolute values and importance of this removal process is smaller in summer time. Nevertheless, wet deposition is harder to evaluate since it depends highly on the quality of the precipitation fields.

The predictions of AOD, due to the presence of SSA in the atmosphere, were evaluated by comparing SILAM's results with satellite observations. The AOD retrievals of MODIS instruments on-board NASA satellites Aqua and Terra (Collection 5, level-2 data), were first pre-processed to remove cloud contaminated pixels (Remer et al., 2008). Then the pixels were projected to the SILAM grid, hourly aggregated, and collocated in time and by grid-cell with the model results. Co-locating the datasets, however, is not enough: the MODIS AOD includes the contribution of aerosols of all types and origin, while the SILAM computations included only SSA. Hence the comparison was restricted to the areas where the SSA load is dominant, i.e. where the AOD is least influenced by non-SSA. These are the oceanic regions at mid-latitudes in the Southern Hemisphere, central part of the North Atlantic and North-Eastern part of the Pacific Ocean (Figure 5.5, black squares). Figure 5.5 shows that AOD predictions are on the same order of magnitude as MODIS, if only the SSA-dominated regions described above are considered. The results also show the regions least affected by the contribution from terrestrial aerosol sources: the Southern and Northern Pacific Oceans. The impact of non-SSA aerosol on AOD over the Northern Atlantic, parts of the Southern Atlantic and the Indian Oceans is noticeable bigger. Both of these findings are confirmed when comparing MODIS and SILAM AOD histograms for the Southern Pacific (area A, in Figure 5.5) and Southern Atlantic and Indian Ocean (area B, in Figure 5.5.) areas. The histograms for SILAM and MODIS for the Southern Pacific area are very similar and the mean-AOD differs by less than 2% (Figure 5.6, top), showing that it is a SSA-dominated area. The same histograms for Southern Atlantic and Indian Ocean show a shift of the predicted SSA AOD to the lower AOD values as compared to MODIS (Figure 5.6, bottom), indicating that other sources are influencing the observations.

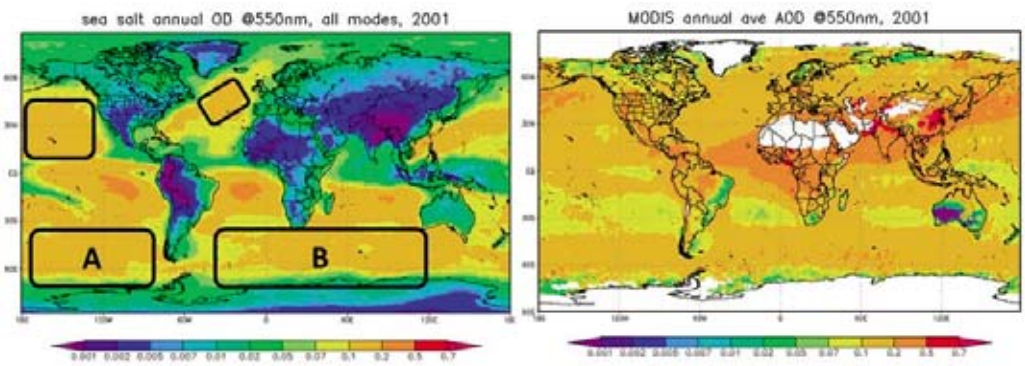

Figure 5.5 Spatial distribution for predicted SSA-AOD by SILAM (left) and by AOD observed by MODIS (right).

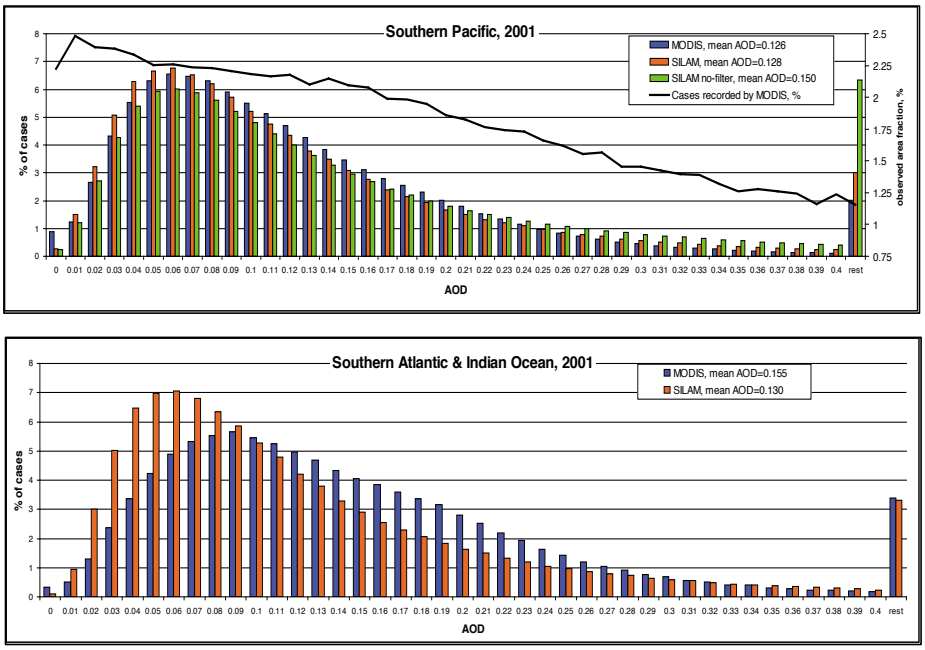

Figure 5.6 AOD histograms for Southern Pacific (area A in Figure 5.5) and Southern Atlantic and Indian Ocean (area B in Figure 5.5) areas. Top: collocated SILAM (red), un-collocated SILAM (green), MODIS (blue), and fraction of SILAM cells observed by MODIS (black line, right-hand axis). Bottom: collocated SILAM (red) and MODIS (blue) data

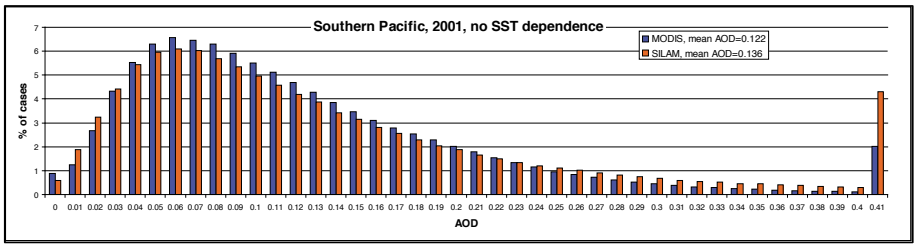

Figure 5.7 AOD histograms for SSA-dominated regions for the 2001 simulations, co-located SILAM and MODIS sets, fixed seawater temperature at 15 °C for Southern Pacific area (area A in Figure 5.5).

The model evaluation showed that the SSA concentration and AOD are reproduced well, especially for the summer period. In winter time, the wind-speed is higher and more prone for coarse particles production. The coarser particles are typically underestimated since the parameterisation is not accounting for spume production. Adding spume droplet formation, for winds higher than 6 m s^{-1} based on the formulation of Andreas (1998), brings the results closer to the ground-based measurements – and further increases the total SSA load.

Finally, predictions of SSA were compared between SILAM and other CTMs widely used in Europe: DEHM, EMEP and MATCH (Paper II). Formally, these models use M86 and M03 parameterisations and differences in SSA emission should be attributed to the temperature and salinity dependencies. To scrutinize this, box-model calculations of the SSA mass flux as a function of temperature were made for seawater salinity of 10 and 35 ‰, representing the Baltic Sea and the Atlantic Ocean, respectively, and with wind-speed fixed at 15 m s^{-1} (Figure 5.8, left).

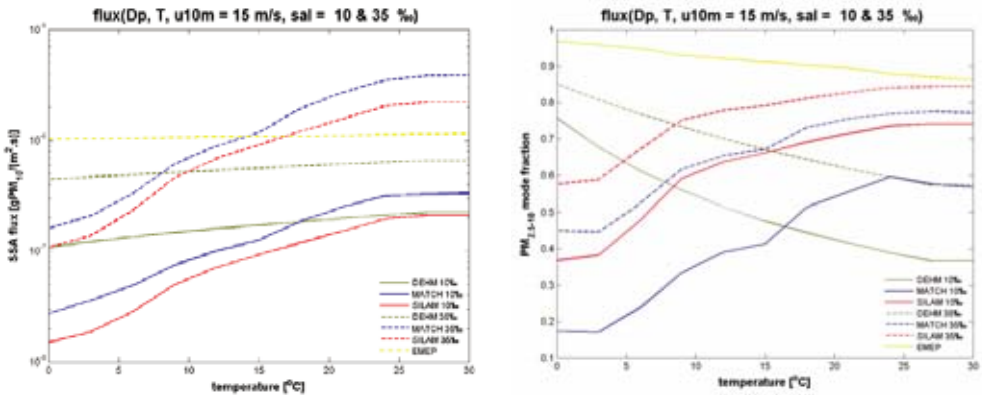

Figure 5.8 SSA mass flux (gPM_{10} m^{-2} s^{-1}) box calculations (left) and coarse mode fraction of the mass flux (right) as a function of radius (dry for DEHM and SILAM and RH = 80 % for MATCH) and temperature, for wind speed 15 m s^{-1} and salinities 10 ‰ and 35 ‰.

In general, the SSA flux can be substantially different between models, for the same seawater properties. All the models show an increase of mass flux of SSA with temperature and salinity, except EMEP that does not apply any correction for salinity. Both DEHM and EMEP mass fluxes show little difference between low and high temperatures; SILAM and MATCH show a substantial dependency of the mass flux on temperature throughout the size ranges. This difference is explained by how the seawater temperature dependency is implemented in each model. In DEHM and EMEP, only $PM_{2.5}$ size range varies with seawater temperature, based on the M03 source function. SILAM has the dependency for all size ranges based on the formulation described in section 4.1 and Paper I. In MATCH, the implementation of seawater temperature correction is done by combining the temperature correction included in the M03 for size-range below D_p = 0.4 µm and the use of the temperature corrections from Paper I for coarser sizes.

Size distribution will affect production of SSA and will possibly affect the removal of SSA from the atmosphere. Figure 5.8 (right) shows how the different models distribute the mass between fine ($PM_{2.5}$) and coarse ($PM_{2.5\text{-}10}$) modes. Again there is a discrepancy between the models. Both DEHM and EMEP assume that the contribution of the coarser mode is reduced with temperature, since more SSA is produced with higher temperatures, for size ranges below 2.5 µm. Temperature-wise, EMEP has always the highest contribution for the coarse mode. For MATCH and SILAM, the contribution to

the coarser mode increases with temperature, though MATCH has a lower coarse mode contribution than SILAM. There is an agreement between the DEHM, MATCH and SILAM for very saline water, where coarser particles are emitted.

For more insight about the unified parameterisation for SSA flux, the reader is referred to Tsyro et al (2011), Grythe et al. (2014), Liora et al. (2015), and Witek et al (2016), where the parameterisation has been used and evaluated.

5.2 Sea salt aerosol and climate change: a European perspective

Roughly 70 % of the Earth's surface is covered by water. Thus, SSA might play a major role for atmospheric processes that govern climate change, especially over remote water surfaces where no other source of aerosols exists. SSA can contribute to changes in cloud albedo and precipitation, since it can lead to cloud formation, and serves as a sink for condensable gases and smaller aerosol particles, changing the size distribution of the marine aerosol (e.g. Korhonen et al., 2010; Wang et al., 2011). Currently, there is an improved understanding regarding the impact of aerosol on global climate than on regional scale (Vogel et al., 2009), with very few studies regarding the European region (Lundgren et al., 2013). The study presented in Paper II fills-in the knowledge gap that currently exists, by studying the climate impact on SSA production and fate over a 40 year period (1990-2009 and 2040-2059) over the European region. The paper also includes considerations about the radiative impact of SSA over sea surface and land. The runs are described in Section 5.1.

This study indicates that, in the future, there will be more emissions of SSA due to changes in wind speed and temperature (salinity was kept constant), see Figure 5.9. For instance, it is expected an increase of emissions over the east of Iceland where temperature is predicted to rise by almost 2 K, and over the Black and Aegean Seas, due to an increase of seawater temperature, supported by higher wind speed. The smallest absolute difference between future and past is predicted for the Baltic Sea; this was expected due to its low seawater salinity. But in relative terms, the model shows an increase up to 20% in Gulf of Bothnia, which is actually higher than the increase predicted for North Sea (5-15%), due to the temperature rise. Therefore, the increase or decrease of SSA emissions needs to be carefully analysed.

SSA directly scatters solar radiation back to space, resulting in a cooling effect on climate by decreasing the amount of radiation absorbed by the water surface. Over land, there can be both cooling over the low-reflectance surfaces, and warming over high-albedo surfaces (e.g., Haywood and Boucher, 2000). The direct radiative effect (DRE) due to SSA is based on the AOD predicted by SILAM for past and future periods. The past period simulation estimates the upward scattering by SSA, at TOA, to be up to 0.5 W m^{-2} over seawater surfaces. This value is within the estimates on upward scattering of radiation by SSA: ranging between 0.08 and 6 W m^{-2}, at wavelengths in the range of 0.3-4 μm (Lewis and Schwartz, 2004). The predicted change in the DRE due to SSA suggests an

overall cooling (negative change) in the future for the Northern and warming for the Southern latitudes. The Mediterranean region is the most sensitive area in this study, where an overall warming was predicted both over sea and over land, and cooling is predicted to happen over the eastern basin of the Mediterranean Sea. The DRE pattern for the whole year is highly influenced by the summer period. The upward scattering in the summer time can be up to 1.7 times higher than in winter (Figure 5.10, left), due to lower cloudiness and prolonged daylight. This can be seen in Figure 5.10 (right), which shows the change between future and past periods but considering only the summer months (June, July and August). This study predicts a substantial seasonal variation for the DRE over the sea surface waters.

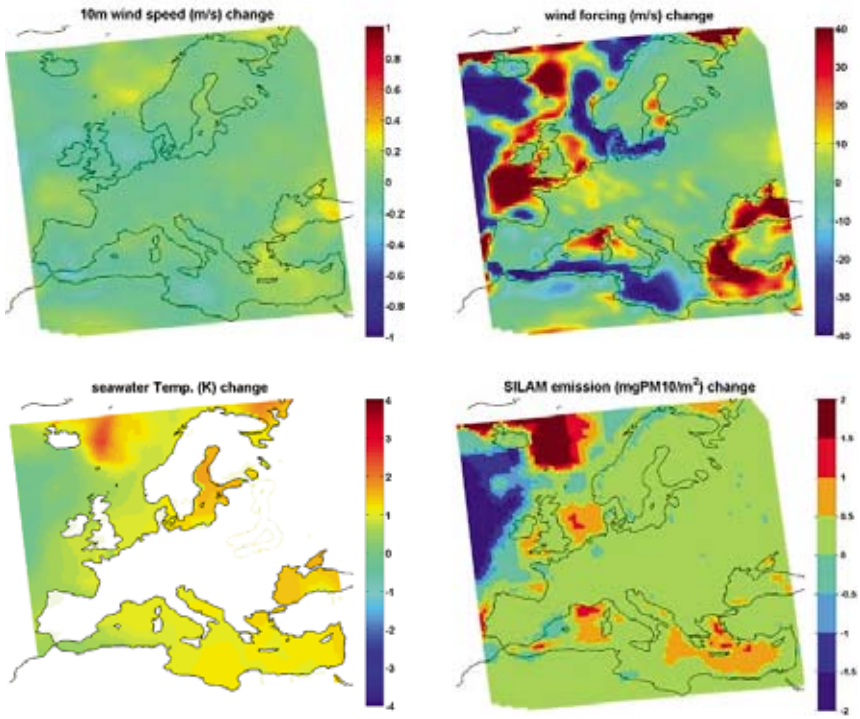

Figure 5.9 Absolute change between future (2040-2059) and past (1990-2009) periods. Top-left: wind speed (m s^{-1}), top-right: wind forcing ($\approx U_{10}^{3.41}$), bottom-left: seawater temperature (K), and bottom-right: SSA emissions ($mgPM_{10}$ m^{-2}).

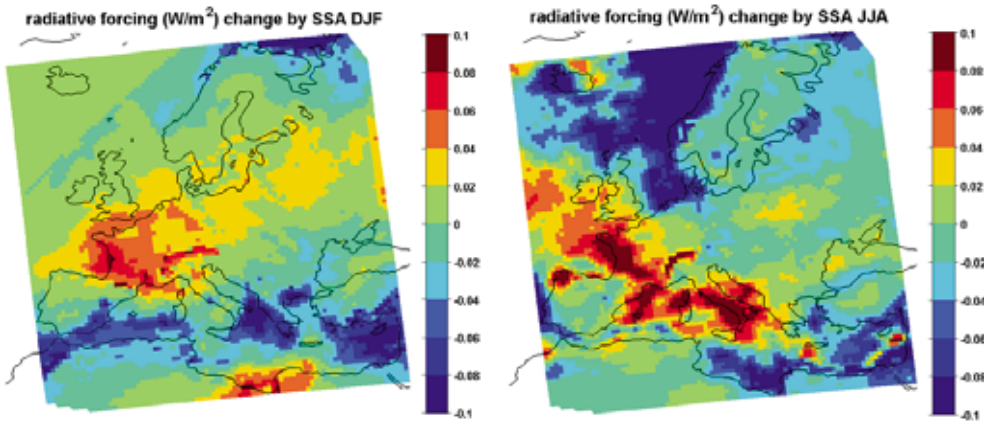

Figure 5.10 Radiative forcing by SSA (W m^{-2}): difference between future (2040-2059) and past (1990-2009) periods. Left: winter (December, January and February); right: summer (June, July and August).

5.3 Fire emission estimation and contribution to atmospheric composition

Wildland fires have been recognised among the most-powerful sources of atmospheric tracers and particles, including precursors for secondary pollutants (Lamarque et al., 2010). Annual estimations of the globally consumed biomass usually range between 5 and 10 Gt (Scholes and Andreae, 2000). However, the estimates of fire emissions are highly uncertain, even if large-scale and long-term averages are considered: inaccuracies of input data and variations in the methodologies employed may lead to an uncertainty in emission estimates of at least 50% (French et al., 2004; Kasischke and Penner, 2004; Schultz et al., 2008).

Estimations for wildland fire emissions for total PM by IS4FIRES are currently on the higher end of the estimations, being at least a factor of 5 higher from other top-down approaches (van der Werf et al., 2010; Kaiser et al., 2012). Figure 5.11 shows the spatial distribution of PM emissions for IS4FIRESv1 and GFASv1 (Kaiser et al., 2012).

Considering the overestimation of the PM emissions by IS4FIRESv1, improvements to the system were undertaken. Section 4.2 and Paper III describe the implementation and optimization of the IS4FIRESv2 and the evaluation of the previous and the current version of the system. A global evaluation of the system was based on AOD. The evaluation considered MODIS AOD at 500 nm (Collection 5, level-2) and AOD predicted by SILAM simulations including primary and secondary inorganic gases and particulates. The simulations for this purpose included sea spray, wildland fire, wind-blown dust and anthropogenic emissions (described in Section 4). The chemical transformation module for secondary inorganic aerosol formation (Sofiev, 2000) was applied together with a bulk mass aerosol dynamics scheme that includes gas phase and heterogeneous oxidation of SO_2 to SO_4, dynamic equilibrium between NH_4NO_3 aerosol and NH_3 and HNO_3 in gas phase, and condensation of HNO_3 to the surface of the sea salt particles. The model was driven by ERA-Interim (Dee et al. 2011)

meteorological data with 3-hour temporal resolution and 0.72 º horizontal resolution. The global simulations were set for a period between 2003 and 2012, with a horizontal resolution of 1*1 ° and the vertical grid consisting of 9 unevenly spaced layers, with the lowest layer being 25 m thick and the top reaching up to the tropopause. All simulations were made with a 15 min internal time-step, while the model results are provided as hourly averages. Observed and predicted AOD were spatially collocated, on an hourly basis, then averaged monthly and annually.

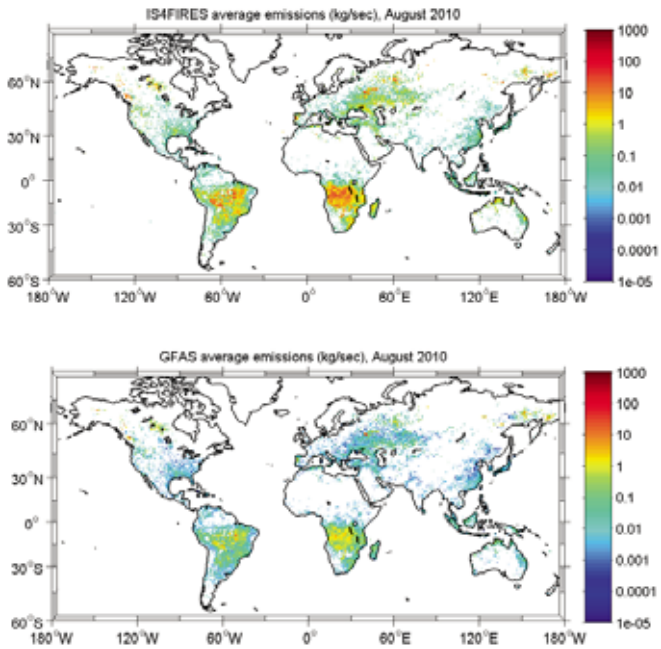

Figure 5.11 Wildland fire total PM emissions fluxes (kg sec^{-1}) for August 2010: IS4FIRESv1 (top) and GFAS v1 (bottom).

When comparing predicted and observed AOD in an annual level, only the mean emission factor for "typical" fires will be obtained. Nevertheless such comparison revealed how the refinement of the IS4FIRESv1 has a significant impact on the AOD estimations. Increasing the number of land-use types from three (IS4FIRESv1) to seven (IS4FIRESv2) improved the prediction scores by reducing the overestimation of the system, and improving mean values and RMSE (Figure 5.12).

Expectedly, the difference is not particularly substantial in Eurasia, since IS4FIRESv1 was initially calibrated for Eurasian fires. The substantial improvements are shown for pro-fire areas such as the African continent: RMSE is reduced by half if the number of land-use types is increased. Further 10% of AOD reduction is obtained by eliminating the misattribution of some specific GLCC land-uses to the selected classes.

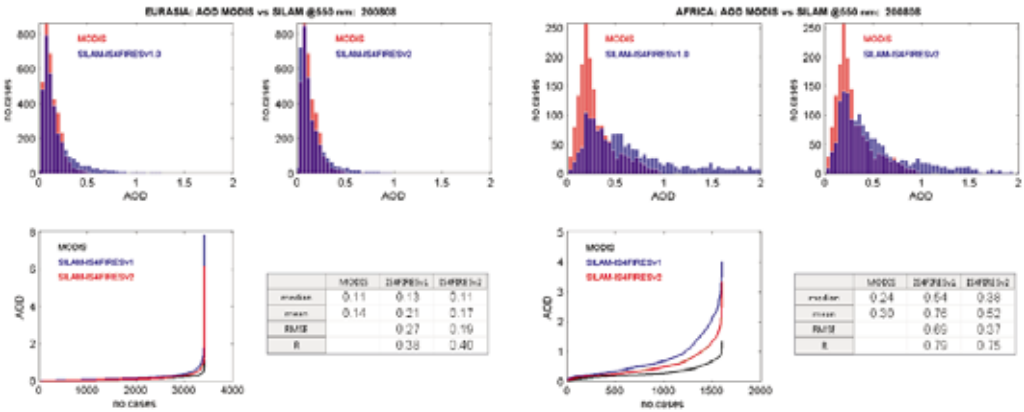

Figure 5.12 Histograms (top), cumulative distribution (bottom-left) and statistical parameters (median, median, RMSE and R, bottom-right) for fire dominating cells (daily averages) for Eurasia and Africa, in August 2008: AOD predicted (MODIS) and computed by SILAM with fire emissions estimated by IS4FIRESv1 (SILAM-IS4FIRESv1) and IS4FIRESv2 (SILAM-IS4FIRESv2).

There are clear cases of MODIS pixels that are persistently reported as fires (Figure 5.13, red crosses), in particular in areas such as Arabian Peninsula. These pixels are currently flagged as highly-energetic sources. The impact of such sources has been simulated with SILAM for August of 2010.

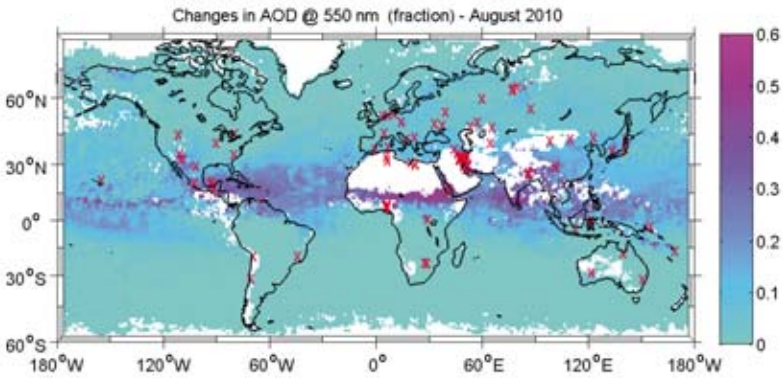

Figure 5.13 Relative AOD reduction due to masking out non-fire pixels (red crosses) from the MODIS database.

Simulations with and without these sources show a substantial impact on AOD values; the fractional difference is shown in Figure 5.13. When highly-energetic sources, such as oil extraction/production plants, are masked-out from the fire emission database, AOD can be reduced by ~80 % in the immediate vicinity of these sources but the effect quickly fades out when the distance from the sources increases. The most-significant difference was predicted for equatorial regions and part of Sahel,

where there is an accumulation of atmospheric aerosol in the Intertropical convergence zone, converging the fire plumes.

5.4 Human exposure to $PM_{2.5}$ in the Helsinki Metropolitan Area

Particulate matter mass concentration has been associated with hospital admissions and mortality for decades (e.g. Pope et al., 1995; Dominici et al., 2006; Kioumourtzoglou et. al., 2016). The World Health Organization suggested that for health effects, the fine fraction is more relevant than PM_{10} and recommends the regulation of $PM_{2.5}$ instead of PM_{10} (WHO, 2006). PM_{10} is less suitable for exposure-response relationships assessment because it includes particles that cannot be inhaled. A comprehensive study on PM phenomenology in Europe was compiled (Putaud et al., 2010). This study shows that there is a clear difference throughout Europe regarding the physical and chemical characteristics of PM, and also when moving from kerbside to rural sites. Helsinki, per se, can be substantially different from other European cities. In Helsinki, the total particle concentration is very low compared to other sites with the same characteristics (e.g. kerbside) and the diurnal variation of local vehicular traffic flows is not always correlated with the $PM_{2.5}$ concentrations (e.g. Pohjola et al., 2002). Karppinen et al. (2005) estimated the contribution from regional and long range transported origins to be less than 50% in Helsinki centre (and nearly 100% in the outskirts of the HMA). This implies that when assessing urban scale atmospheric composition and, consequently, human exposure to $PM_{2.5}$ in HMA, not only local sources should be carefully considered but also accurate estimations for regional background concentrations.

An example of such studies is described in Paper IV. This study assesses the human exposure to $PM_{2.5}$ in the HMA and Helsinki for the years 2008 and 2009, respectively. The HMA comprises four cities; Helsinki, Espoo, Vantaa and Kauniainen. The total population in the HMA is approximately 1.1 million, while the population of Helsinki is about 0.6 million inhabitants. The integrated system EXPAND (Section 3.1) was chosen to perform such assessments. In order to include all the possible contributors to $PM_{2.5}$ surface concentrations, approximately 5000 line sources for vehicular traffic and shipping, and 40 stationary sources (power plants and industrial facilities) were considered. The sources are described in section 4.2.3. Background concentrations where estimated with the LOTOS-EUROS model (Schaap et al., 2008) to include the contribution from regional and long range transport. This contribution is derived from the grid cell including the regional background station Luukki, where the influence of local sources on $PM_{2.5}$ concentrations has been estimated to be on average less than 10 % (Karppinen et al., 2005). Since the exposure estimations included indoor and outdoor activities, an infiltration ratio of 0.57 for home and work microenvironments was applied; both traffic and other activities microenvironments considered that the population is fully exposed to the $PM_{2.5}$ levels (Hänninen et al., 2004, 2005 and 2013). Hourly concentration values were averaged over the whole year of 2008 and 2009. Both concentration and activity data were interpolated to a 50x50 m^2 grid-cell. Though the study for Helsinki represents a smaller area and a different year, it

should still be valid to evaluate how different sources impact the urban atmospheric composition and human exposure in HMA in 2008.

The results for 2008 show that the regional background is the main contributor to $PM_{2.5}$ concentrations in HMA, confirming the previous studies. Figure 5.14. (left) shows the predicted concentrations for vehicular emissions and background contribution for the HMA in 2008. The overall area is dominated by background concentrations, with a maximum of 7 µg$PM_{2.5}$ m^{-3}, with highest concentrations being located in the vicinity of the main roads and streets, and in the centre of Helsinki. Figure 5.14 (right) shows the contribution of anthropogenic sources to the $PM_{2.5}$ emissions in HMA, where vehicular traffic is the most relevant contributor for $PM_{2.5}$ emissions in HMA. The contribution from shipping is as relevant as stationary sources. How these concentrations reflect on human exposure in HMA is show in Figure 5.15 (left and right).

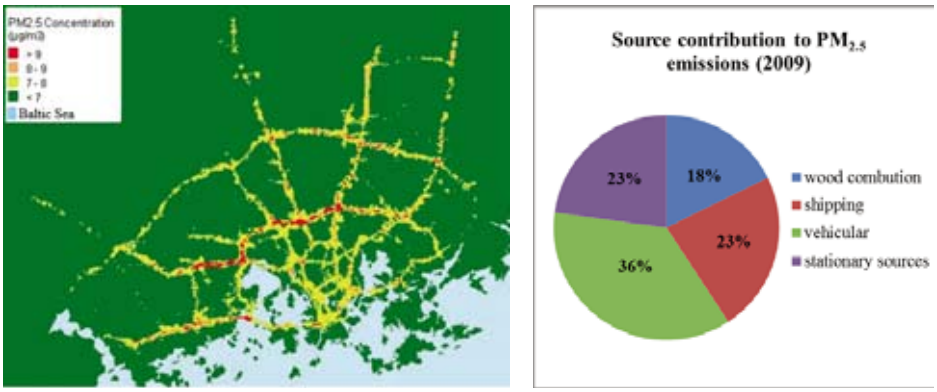

Figure 5.14 Left: predicted annual average concentrations of $PM_{2.5}$ (µg m^{-3}), contribution from vehicular traffic and background for the HMA in 2008. Right: Source contribution to $PM_{2.5}$ emissions for Helsinki in 2009.

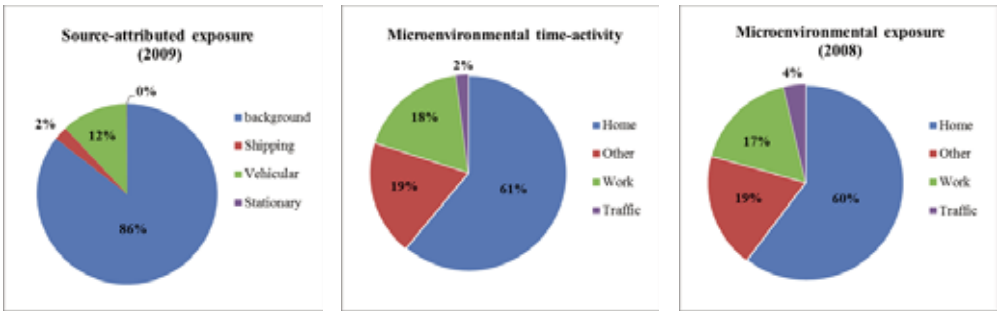

Figure 5.15 Contribution of different sources of $PM_{2.5}$ to exposure (left), and of time-activity (middle) and human exposure in each microenvironment (right).

When exposure is analysed source-wise, it is clear that the background contribution is the most relevant, with vehicular traffic being the second contributor but only with a meagre 12 %. These

results relate to the concentration results discussed above. The exposure originated from major stationary sources is negligible, caused by the dispersion of pollutants to wide regions due to the high stacks for most of these installations. Although the average contribution of shipping to the total $PM_{2.5}$ concentrations within the area considered was a modest 3 %, this contribution can be higher than 20 % in the vicinity of the harbours (within a distance of approximately one kilometre). Figure 5.16 shows how the population exposure to vehicular traffic and shipping emissions can be different due to the spatial distribution of concentrations, which is linked with the predominant sources.

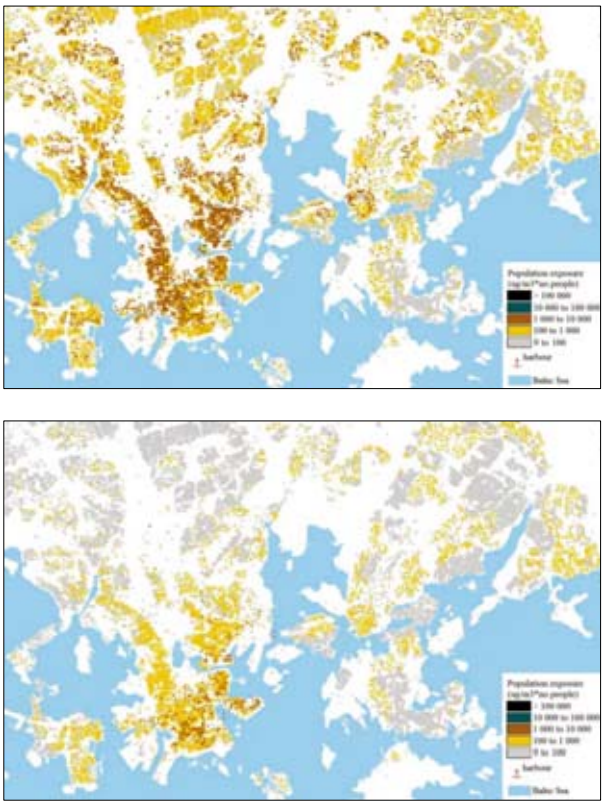

Figure 5.16 Population exposure per year (µg m^{-3} * # persons) to $PM_{2.5}$ in Helsinki in 2009 to emissions from vehicular traffic (right) and emissions from shipping (left).

The microenvironmental population exposure analysis showed that exposure at home is responsible for most of the population's exposure to $PM_{2.5}$, followed by work and other activities. Overall, people are less exposed while commuting, because it is where they spent less time (see activity data, Figure 5.15, middle-panel). Home, work and other activities microenvironments show similar patterns, indicating that there are no major relative differences in the average concentrations prevailing at those microenvironments. However, for traffic, the contribution to exposure is substantially higher than the corresponding contribution to time-activity. This is mainly caused by the relatively higher concentrations on the roads and their vicinity.

The spatial distribution of the predicted annual average population exposures in the HMA, in 2008, for home and work microenvironments, is shown in Figure 5.17. These distributions exhibit characteristics of both spatial concentration and time-activities distributions. There are elevated values in the Helsinki city centre, along major roads and streets, and in the vicinity of urban district centres. The high exposure values at home and work in the centre of Helsinki are caused both by relatively high concentrations and high population densities in the area.

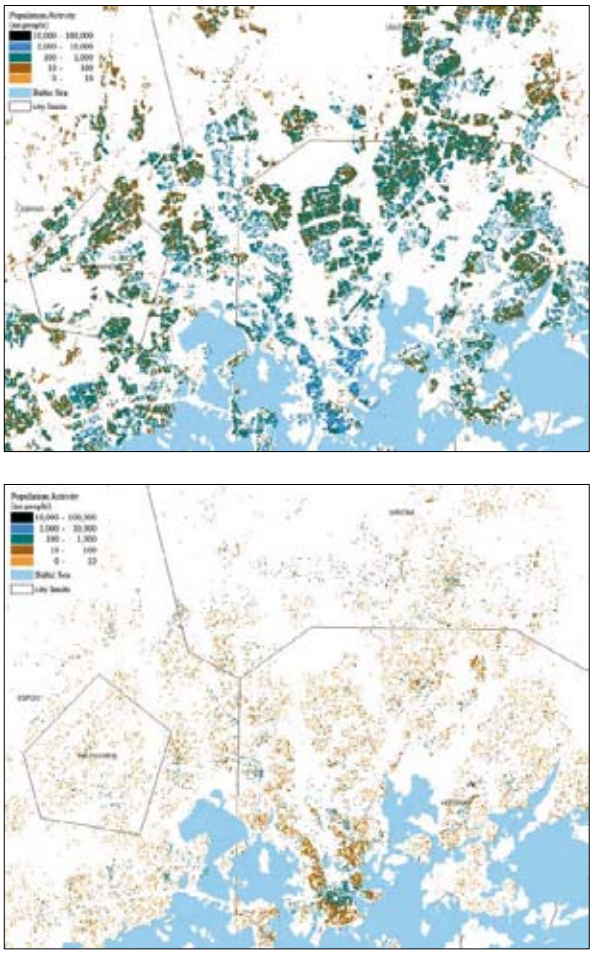

Figure 5.17 Annual average population exposure (µg m^{-3} * # persons) for 2008: home (left) and work (right) microenvironments.

The exposure computations could not be evaluated at the time of this study, since there was no $PM_{2.5}$ personal exposure measurements available. Comparison between modelled personal exposure and monitored personal exposure under the ESCAPE campaign in Finland (Beelen et al., 2015) is currently ongoing at FMI. Paper V describes possible methods to evaluate exposure metrics through box model calculations and personal monitoring data.

6 Conclusions

The main focus of this thesis was to improve the modelling of aerosol emissions and its atmospheric dispersion at different spatial and temporal scales, and to integrate the dispersion modelling with the population activity data to obtain accurate exposure metrics. Emission modelling of SSA and wildland fires in the SILAM model was refined by combining and re-assessing widely used formulations and datasets. Both emission models were thoroughly evaluated with ground-based and remote sensing observations, for several years. Emissions for HMA were revised to bring up-to-date the emissions for traffic and energy sectors in use in urban-scale modelling. The EXPAND model, was revised and applied to bring concentrations and activity data together to compute parameters such as population exposure or intake fraction.

A new parameterisation for bubble-mediated SSA emissions has been developed. It takes into account the effects of wind speed and seawater salinity and temperature, and can be applicable to SSA particles with dry diameters raging between 0.01 and 10 μm. The parameterization is valid for low-to-moderate wind speed, seawater salinity ranging between 0 and 33 ‰ and seawater temperature ranging between -2 and 25 °C. The estimation for SSA emissions with this unified function, 6700-7400 Tg yr^{-1}, are within the range of other global estimates (1000-20000 Tg yr^{-1}, Schulz et al., 2009; Textor et al., 2006). The spatial distribution of SSA has typically higher concentrations where winds are stronger (Southern Hemisphere) and temperatures are high (equatorial belt). Contribution from oceans can be up to 10-times higher than other seas, e.g. the Atlantic vs Baltic Sea, due to higher salinity and stronger wind-gusts. European Seas also have pronounced concentrations gradients, e.g. at the Mediterranean Sea. Transport of SSA over land is significant, even for low salinity waters such as the Baltic Sea, and can contribute up to 6 μg m^{-3} to PM_{10}, at annual level. Wet deposition is more challenging overall, since it relies heavily on the meteorology driving the models. Nevertheless, it is recommended to use full size range available for SSA, to be comparable with the observations.

The first climate impact study related to SSA over Europe was done by applying the unified SSA flux parameterisations. The European climate-change context shows that the difference between the current and future climatic conditions (1990-2009 vs 2040-2059) is driven by the trends in seawater temperature, as the near-surface wind speed is projected to stay nearly the same in the climate scenario used. These results are more accentuated over the Black and the Mediterranean Sea, where the increase of emission and concentration of SSA is significant. Simple calculations for the possible impact of SSA on the DRE show that the North of Iceland, the Norwegian and Baltic Seas are the most affected areas by cooling, and the Mediterranean Area (over land and sea) is mainly affected by warming. The prediction for the upward scattering by SSA, at TOA, can be up to 0.5 W m^{-2}.

The methodology for estimating wildland fire PM emissions under IS4FIRES, shows similar spatial distribution when compared to other top-down methodologies, but can differ by an order of magnitude from the lowest estimation. This methodology shows that fires are very specific concerning vegetation and meteorology, reflecting the local conditions of where the fire is taking place. For this reason, the

number of vegetation types was increased, the diurnal variation per vegetation type was improved, and the emission model was re-calibrated. This reduces the overestimation substantially, especially for fire prone areas such as Africa (~50%). Additionally, FRP retrieved from MODIS should be carefully scrutinized so that the information coming to fire emission models will not take pixels with misleading fire information. Currently, MODIS-FRP classifies highly energetic sources as fires. This misattribution can cause an overestimation in AOD up to 80%, especially close to the misattributed sources. The estimation of fires based on the FRP data should be regularly calibrated with up-to-date remote sensing observations.

The description of regional sources and background contribution is crucial when assessing $PM_{2.5}$ concentrations. According to the study performed, background contribution is the most relevant to the $PM_{2.5}$ concentration in HMA. Traffic is the local source that contributes the most to the $PM_{2.5}$ concentrations (11 %). Although the average contribution of shipping to the total $PM_{2.5}$ concentrations was modest (3 %), this contribution can be higher in the vicinity of the harbours. Energy production does not contribute substantially, since the high stacks allow the dispersion of the emitted PM for longer distances and do not impact the study area. The outcome of this study shows that the population exposure in HMA mostly happens while at home (60%), where people spend most of their time. The lowest exposure will happen while driving or commuting (4%) but comparing the activity data with the exposure results shows that exposure will be more acute while at traffic. Background concentration was responsible the major fraction of the total exposure (86 %), followed by vehicular emissions (12 %). The shipping did not contribute substantially in the whole HMA (2 %) but in harbour areas and their vicinity the contribution can be as high as 20 %. There was no impact of stationary sources on human exposure in the study area.

7 Future of the research field

This study highlights several bottlenecks for emission modelling and what needs to be improved. The SSA parameterisation of SILAM showed high potential for integrated approaches bringing together major factors controlling emission, but also revealed a substantial lack of experimental data describing formation of e.g. coarse particles, strong wind speeds, spume drop formation mechanism, etc. Additionally, surf-zone processes are severely underrepresented. Studies such as Albert et al. (2015), based on satellite observations, claim that the whitecap-area based parameterisation typically used by CTMs is misrepresenting the absolute values, mostly underestimating the production of SSA. Therefore, parameterisations based on Monahan et al. (1986) should be reformulated.

DMS is the dominant volatile biogenic sulphur compound emanating from the ocean (Simó, 2001) and is typically oxidized to form sulfuric and methanesulfonic acids, which contribute to new particle formation and growth, affecting the radiation budget of the Earth (Liss and Duce, 1997). This natural source of aerosol is currently missing or being poorly represented in many CTMs. Global mean surface DMS concentration is quite robust because of the large data set used, but the estimates for

specific regions and seasons remain highly uncertain in many ocean regions where sampling has been sparse (Lana et al, 2011).

Representation of the wildland fire behaviour and emission for regional-to-global scales is still too rudimentary in current available CTMs. A better representation is needed to characterise the fire phase (flaming or smouldering) and relating it to a weighted mass spectrum derived from field studies such as Virkkula et al. (2014), Janhäll et al. (2010), and Chubarova et al. (2012). Representation of the fire relies on the type of vegetation burning, the analysis performed in this study shows that the current emission factors can hardly be used for all the regions with similar land-use type over the globe, and regionalised approaches are needed. More research is needed to identify major factors that influence seasonal and interannual variability in fire occurrence, for different ecosystems, to map the temporal and spatial extent of fires. Hao and Larkin (2014) describes the considerable recent progress in this area, but fires are not easily mapped by satellite-based sensors because they are typically of small size and duration and burn beneath forest canopy. On the other hand, the same sensors are detecting highly-energetic sources, misleading the fire emission estimates.

Small scale combustion is a ubiquitous source during the winter all over Europe, but these emissions have been severely misrepresented in the current inventories (Stohl et al., 2013) and, consequently, in dispersion modelling. As an example, domestic wood combustion in Finland is estimated to contribute around 23% to the $PM_{2.5}$ emitted (Karvosenoja, 2008).

A new challenge for human exposure modelling is the generalization of the approach and upscaling to regional scale. A significant problem for models such as EXPAND, is the lack of activity data of population. More should be done to create generic proxies for the population movements between microenvironments. This could result in an easier link between the dispersion models, such as SILAM, and exposure tools, such as EXPAND, which could be directly used to forecast and assess air quality together with health risk assessment.

There are very few studies that include impact of future air quality directives or climate on human exposure in regional or local scale. Future scenarios for emission and activity data should be compiled to obtain possible human exposure in the near future or climate impact on human exposure.

8 References

Albert, M. F. M. A., Anguelova, M. D., Manders, A. M. M., Schaap, M., and de Leeuw, G. 2015. Parameterisation of oceanic whitecap fraction based on satellite observations. Atmos. Chem. Phys. Discuss., 15, 21219-21269, doi:10.5194/acpd-15-21219-2015.

Amann, M., Bertok, I., Cofala, J., Gyarfas, F., Heyes, C., Klimont, Z., Schöpp, W., and Winiwarter, W. 2005. CAFÉ Scenario Analysis Report Nr. 1, Baseline Scenarios for the Clean Air for Europe (CAFÉ) Programme, Final Report. Contract No B4-3040/2002/340248/MAR/C1, Laxenburg, Austria.

Apte, J.S., Bombrun , E., Marshall, J.D., and Nazaroff, W.W. 2012. Global Intraurban Intake Fractions for Primary Air Pollutants from Vehicles and Other Distributed Sources. Environ. Sci. Technol., 46, 6, 3415-3423, doi:10.1021/es204021h.

Ashmore, M. R. and Dimitripoulou, C. 2009. Personal exposure of children to air pollution. Atmos. Environ., 43, 128–141, doi:10.1016/j.atmosenv.2008.09.024.

Bates, T. S., Coffman, D. J., Covert, D. S., and Quinn, P. K. 2002. Regional marine boundary layer aerosol size distributions in the Indian, Atlantic, and Pacific Oceans: A comparison of INDOEX measurements with ACE-1, ACE-2, and Aerosols99. J. Geophys. Res., 107(D18), 8026, doi:10.1029/2001JD001174.

Beelen, R. Hoek, G., Raaschou-Nielsen, O., Stafoggia,, M. , Andersen, Z. J., Weinmayr, G., Hoffmann, B., Wolf, K. et al. 2015. Natural-Cause Mortality and Long-Term Exposure to Particle Components: An Analysis of 19 European Cohorts within the Multi-Center ESCAPE Project. Environ. Health Perspectives, 123, 6, 525-533, doi:10.1289/ehp.1408095

Chubarova, N., Nezval', Ye., Sviridenkov, I., Smirnov, A., and Slutsker, I. 2012. Smoke aerosol and its radiative effects during extreme fire event over Central Russia in summer 2010. Atmos. Meas. Tech., 5, 557–568, doi:10.5194/amt-5-557-2012.

Clarke, A.D., Qwens, S.R., and Zhou, J. 2006. An ultrafine sea-salt flux from breaking waves: Implications for cloud condensation nuclei in the remote marine atmosphere. J. Geophys. Res., 111, D06202, doi:10.1029/2005JD006565.

Covert, D. S., Gras, J. L, Wiedensohler, A., and Stratmann, F. 1998. Comparison of directly measured CCN with CCN modeled from the number-size distribution in the marine boundary layer during ACE I at Cape Grim, Tasmania. J. Geophys. Res., 103, 16,597-16,608.

Crutzen, P.J., Heidt, L. E., Krasnec, J. P., Pollock, W. H., and Seiler, W. 1979. Biomass burning as a source of atmospheric gases CO, H2, N2O, NO, CH3Cl, and COS, Nature 282, 253-256, doi:10.1038/282253a0

de Leeuw, G., Andreas, E. L, Anguelova, M. D., Fairall, C. W., Lewis, E. R., O'Dowd, C., Schulz, M. and Schwartz, S.E. 2011. Production flux of sea spray aerosol. Rev. Geophys., 49, RG2001, doi:10.1029/2010RG000349.

Dee, D. P., Uppala, S. M., Simmons, A. J., Berrisford, P., Poli, P., Kobayashi, S., Andrae, U., Balmaseda, M. A., Balsamo, G., Bauer, P., Bechtold, P., Beljaars, A. C. M., van de Berg, L., Bidlot, J., Bormann, N., Delsol, C., Dragani, R., Fuentes, M., Geer, A. J., Haimberger, L., Healy, S. B., Hersbach, H., Hólm, E. V., Isaksen, L., Kållberg, P., Köhler, M., Matricardi, M., McNally, A. P., Monge-Sanz, B. M., Morcrette, J.-J., Park, B.-K., Peubey, C., de Rosnay, P., Tavolato, C., Thépaut, J.-N., Vitart, F. 2011. The ERA-interim reanalysis: config

uration and performance of the data assimilation system, Q. J. R. Meteorol. Soc., 137, 553-597.

Dominici, F., Peng, R., Barr, C., and Bell, M. 2010. Protecting human health from air pollution shifting from a single-pollutant to a multipollutant approach, Epidemiology, 21, 187–194, doi:10.1097/EDE.0b013e3181cc86e8.

ECMWF, 2015, www.ecmwf.int/research/ifsdocs/. Last accessed 2015.12.01

Elvidge, C.D., Zhizhin, M., Hsu, F.-C. and Baugh, K.E. 2013.VIIRS nightfire: satellite pyrometry at night. Remote Sens., 5, 9, 4423–4449.

Evans, J.S., Hattis, D., and Thompson, K.M. 2000. Exposure efficiency. Journal of the Air and Waste Management Association, 50, 1700–1703.

Fiala, J., Denby, B., Horálek, J., Kurfürst, P., de Smet, P., de Leeuw, F., and Lükewille, A. 2009. EEA Technical Report No 1/2009: Spatial Assessment of PM10 and Ozone Concentrations in Europe (2005). doi:10.2800/165.

French, N., Goovaerts, P., and Kasischke, E. 2004. Uncertainty in estimating carbon emissions from boreal forest fires, J. Geophys. Res., 109, D14S08, doi:10.1029/2003JD003635.

Fuzzi, S., Baltensperger, U., Carslaw, K., Decesari, S., Denier van der Gon, H., Facchini, M. C., Fowler, D., Koren, I., Langford, B., Lohmann, U., Nemitz, E., Pandis, S., Riipinen, I., Rudich, Y., Schaap, M., Slowik, J. G., Spracklen, D. V., Vignati, E., Wild, M., Williams, M., and Gilardoni, S. 2015. Particulate matter, air quality and climate: lessons learned and future needs, Atmos. Chem. Phys., 15, 8217-8299, doi:10.5194/acp-15-8217-2015.

Gantt, B., Johnson, M. S., Meskhidze, N., Sciare, J., Ovadnevaite, J., Ceburnis, D., and O'Dowd, C. D. 2012. Model evaluation of marine primary organic aerosol emission schemes, Atmos. Chem. Phys.,12, 8553–8566, doi:10.5194/acp-12-8553-2012.

Gery, M. W., Whitten, G. Z. Killus, J. P., and Dodge, M. C. 1989. A Photochemical Mechanism for Urban and Regional Scale Computer Modeling, J. Geophys. Res, 94, 12,925.

Granier, C., Bessagnet, B., Bond, T., D'Angiola, A., van der Gon, H.D., Frost, G.J., Heil, A., Kaiser, J.W., Kinne, S., Klimont, Z., Kloster, S., Lamarque, J.-F., Liousse, C., Masui, T., Meleux, F., Mieville, A., Ohara, T., Raut, J.-C., Riahi, K. Schultz, M.G., Smith, S.J., Thompson, A., van Aardenne, J., van der Werf, G.R. and van Vuuren, D.P. 2011. Evolution of anthropogenic and biomass burning emissions of air pollutants at global and regional scales during the 1980-2010 period. Climatic Change, 109, 163-190, doi:10.1007/s10584-011-0154-1.

Grythe, H., Ström, J., Krejci, R., Quinn, P., and Stohl, A. 2014. A review of sea-spray aerosol source functions using a large global set of sea salt aerosol concentration measurements. Atmos. Chem. Phys., 14, 1277-1297, doi:10.5194/acp-14-1277-2014.

Guenther, A., Hewitt, N., Erickson, D., Fall, R., Geron, C., Graedel, T., Harley, P., Klinger, L., Lerdau, M., McKay, W., Pierce, T., Scholes, B., Steinbrecher, R., Tallamraju, R., Taylor, J.,

Zimmerman, P. 1995. A global model of natural volatile organic compound emissions. J. Geophys. Res. 100, 8873-8892.

Hao, W. M., and Larkin, N. K. 2014. Wildland fire emissions, carbon, and climate: Wildland fire detection and burned area in the United States, For. Ecol. Manage.317, 20–25.

Harrison, K., Hattis, D., and Abbat, K. 1986. Implications of Chemical Use for Exposure Assessment: Development of an Exposure-Estimation Methodology for Application in a Use-Clustered Priority Setting System. MIT Center for Technology Policy and Industrial Development, Report Number CTPID 86-2 to the US EPA.

Haywood, J., and Boucher, O. 2000. Estimates of the direct and indirect radiative forcing due to tropospheric aerosols: A review. Rev. Geophys., 38(4), 513–543, doi:10.1029/1999RG000078.

Hellén, H., Kukkonen, J., Kauhaniemi, M., Hakola, H., Laurila, T., and Pietarila, H. 2005. Evaluation of atmospheric benzene concentrations in the Helsinki Metropolitan Area in 2000–2003 using diffusive sampling and atmospheric dispersion modelling, Atmos. Environ., 39, 4003–4014, doi:10.1016/j.atmosenv.2005.03.023.

Horn, H., Bonka, H., and Maqua, M. 1987. Measured particle bound activity size-distribution, deposition velocity, and activity concentration in rainwater after the Chernobyl accident, J. of Aerosol Science, 18, 681–684, doi:10.1016/0021-8502(87)90096-6.

Huijnen, V., Eskes, H. J., Poupkou, A., Elbern, H., Boersma, K. F., Foret, G., Sofiev, M., Valdebenito, A., Flemming, J., Stein, O., Gross, A., Robertson, L., D'Isidoro, M., Kioutsioukis, I., Friese, E., Amstrup, B., Bergstrom, R., Strunk, A., Vira, J., Zyryanov, D., Maurizi, A., Melas, D., Peuch, V.-H., and Zerefos, C. 2010. Comparison of OMI NO2 tropospheric columns with an ensemble of global and European regional air quality models, Atmos. Chem. Phys., 10, 3273–3296, doi:10.5194/acp-10-3273-2010.

Huebert, B. J., Bates, T., Russell, P. B., Shi, G., Kim, Y. J., Kawamura, K., Carmichael, G., and Nakajima, T. 2003. An overview of ACE-Asia: Strategies for quantifying the relationships between Asian aerosols and their climatic impacts. J. Geophys. Res., 108, D23, 8633, doi:10.1029/2003JD003550.

Humbert, S., Marshall, J. D., Shaked, S., Spadaro, J. V., Yuishioka, Y., Preiss, P., McKone, T. E., Horvath, A., and Jolliet, O. 2011. Intake Fraction for Particulate Matter: Recommendations for Life Cycle Impact Assessment, Enviro.Sci. & Tech., 45, 4808-4816, doi: 10.1021/es103563z

Hänninen O, Knol AB, Jantunen M, Lim TA, Conrad A, Rappolder M, Carrer P, Fanetti AC, Kim R, Buekers J, Torfs R, Iavarone I, Classen T, Hornberg C, Mekel OC, EBoDE Working Group. 2014. Environmental burden of disease in Europe: assessing nine risk factors in six countries. Environ Health Perspect 122, 439–446, doi:10.1289/ehp.1206154.

Hänninen, O., Sorjamaa, R., Lipponen, P., Cyrys, J., Lanki, T., and Pekkanen, J. 2013. Aerosol-based modelling of infiltration of ambient PM2.5 and evaluation against population-based measurements in homes in Helsinki, Finland. J. Aerosol Sci., 66, 111-122, doi:10.1016/j.jaerosci.2013.08.004.

Hänninen, O.O., Palonen, J., Tuomisto, J., Yli-Tuomi, T., Seppänen, O., and Jantunen, M.J. 2005. Reduction potential of urban PM2.5 mortality risk using modern ventilation systems in buildings. Indoor Air, 15, 4, 246-256.

Hänninen, O., Lebret, E., Ilacqua, V., Katsouyanni, K., Künzli, N., Sram, R., and Jantunen, M. 2004. Infiltration of ambient PM2.5 and levels of indoor generated non-ETS PM2.5 in residences of four European cities. Atmos. Environ., 38, 6411-6423, doi:10.1016/j.atmosenv.2004.07.015.

Ichoku, C. and Kaufman, Y.J., 2005. A method to derive smoke emission rates from MODIS fire radiative energy measurements. IEEE Transactions on Geoscience and Remote Sensing, 43, 11, 2636–2649

Im, U., Bianconi, R., Solazzo, E., Kioutsioukis, I., Badia, A., Balzarini, A., Baró, R., Bellasio, R., Brunner, D., Chemel, C., Curci, G., Denier van der Gon, H., Flemming, J., Forkel, R., Giordano, L., Jiménez-Guerrero, P., Hirtl, M., Hodzic, A., Honzak, L., Jorba, O., Knote, C., Makar, P. a., Manders-Groot, A., Neal, L., Pérez, J. L., Pirovano, G., Pouliot, G., San Jose, R., Savage, N., Schroder, W., Sokhi, R. S., Syrakov, D., Torian, A., Tuccella, P., Wang, K., Werhahn, J., Wolke, R., Zabkar, R., Zhang, Y., Zhang, J., Hogrefe, C. and Galmarini, S. 2014. Evaluation of operational online-coupled regional air quality models over Europe and North America in the context of AQMEII phase 2. Part II: Particulate matter. Atmos. Environ., 115, 404–420, doi:10.1016/j.atmosenv.2014.08.072.

INRO. 1994. EMME/2 User's manual. INRO Consultants Inc., Montreal, Canada.

Jalkanen, J.-P., Johansson, L., Kukkonen, J. Brink, A., Kalli, J., and Stipa, T. 2012. Extension of an assessment model of ship traffic exhaust emissions for particulate matter and carbon monoxide. Atmos. Chem. Phys., 12, 2641-2659, doi:10.5194/acp-12-2641-2012.

Jalkanen, J.-P., Brink, A., Kalli, J., Pettersson, H., Kukkonen, J., and Stipa, T. 2009. A modelling system for the exhaust emissions of marine traffic and its application in the Baltic Sea area. Atmos. Chem. Phys., 9, 9209–9223, doi:10.5194/acp-9-9209-200.

Janhäll, S., Andreae, M. O., and Pöschl, U. 2010. Biomass burning aerosol emissions from vegetation fires: particle number and mass emission factors and size distributions. Atmos. Chem. Phys., 10, 1427-1439, doi:10.5194/acp-10-1427-2010.

Justice, C., Giglio, L., Korontzi, L., Owens, J. Morisette, J. Roy, D. Descloitres, J. Alleaume, S. Petitcolin, F. Kaufman Y. 2002. The MODIS fire products. Remote. Sens. Environ., 83, 244–262.

Jylhä, K. 1991. Empirical scavenging coefficients of radioactive substances released from Chernobyl. Atmos. Environ. A., 25, 263–270, doi:10.1016/0960-1686(91)90297-K.

Kaiser, J.W., Heil, A., Andreae, M. O., Benedetti, A., Chubarova, N., Jones, L., Morcrette, J.-J., Razinger, M., Schultz, M. G., Suttie, M., and van der Werf, G. R. 2012. Biomass burning emissions estimated with a global fire assimilation system based on observed fire radiative power. Biogeosciences, 9, 1, 527–554, 9, 527-554, doi:10.5194/bg-9-527-2012.

Kaiser, J.W., Wooster, M.J. Roberts, G., Schultz, MG., Van Der Werf, G., and Benedetti, A. 2009. SEVIRI fire radiative power and the MACC atmospheric services. EUMETSAT Meteorological Satellite Conf., EUMETSAT, Darmstadt, Germany, 2005–2009 ISBN 978-92-9110-086-6, ISSN 1011-3932.

Karppinen, A., Kukkonen, J., Kauhaniemi, M., Härkönen, J., Nikmo, J., Sokhi, R.S., Luhana, L., Kousa, A., Alaviippola, B., Koskentalo, T. and Aarnio, P. 2005. Evaluation and application of a model for the urban and regional scale concentrations of PM2.5. Proceedings of the 5th International Conference on Urban Air Quality, Valencia, 29-31 March 2005. 4p. ISBN Number: 1-898543-92-5 (CD).

Karppinen, A. 2001. Meteorological pre-processing and atmospheric dispersion modelling of urban air quality and applications in the Helsinki Metropolitan Area. Finnish Meteorological Institute, Contributions No. 33, ISBN 951-697-552-6, University Press, Helsinki.

Karppinen, A., Kukkonen, J., Elolähde, T., Konttinen, M., Koskentalo, T., and Rantakrans, E. 2000a. A modelling system for predicting urban air pollution, Model description and applications in the Helsinki Metropolitan Area. Atmos. Environ., 34, 3723–3733, doi:10.1016/S1352-2310(00)00074-1.

Karppinen, A., Kukkonen, J., Elolähde, T., Konttinen, M., and Koskentalo, T. 200b. A modelling system for predicting urban air pollution,Comparison of model predictions with the data of an urban measurement network, Atmos. Environ., 34, 3735–3743, doi:10.1016/S1352-2310(00)00073-X

Karvosenoja N, Tanio, M., Kupiainen, K., Tuomisto, J. T., Kukkonen, J., and Johansson, M. 2008. Evaluation of the emissions and uncertainties of PM2.5 originated from vehicular traffic and domestic wood combustion in Finland. Boreal Environ. Res, 13, 465-474.

Kasischke, E.S. and Penner, J.E. 2004. Improving global estimates of atmospheric emissions from biomass burning. J. Geophy. Res. 109, doi: 10.1029/2004JD004972.

Kaufman, Y., Tanre, D., Boucher, O., 2002. A satellite view of aerosols in the climate system. Nature 419, 215-223, doi:10.1038/nature01091.

Kaufman, Y.J., Justice, C.O., Flynn, L.P., Kendall, J.D., Prins, E.M., Giglio, L., Ward, D.E., Menzel, W.P. and Setzer, A.W. 1998. Potential global fire monitoring from EOS-MODIS, J. Geophys. Res., 103, 32215–32238, doi:10.1029/98JD01644.

Kauhaniemi, M., Kukkonen, J. Härkönen J., Nikmo J., Kangas L., Omstedt G., Ketzel M., Kousa A., Haakana M., and Karppinen A. 2011. Evaluation of a road dust suspension model for predicting the

concentrations of PM10 in a street canyon, Atmos. Environ., 45, 3646-3654, doi:10.1016/j.atmosenv.2011.04.055.

Kauhaniemi, M., Karppinen, A., Härkönen, J., Kousa, A., Alaviippola, B., Koskentalo, T., Aarnio, P., Elolähde, T. and Kukkonen, J. 2008. Evaluation of a modelling system for predicting the concentrations of $PM_{2.5}$ in an urban area, Atmos. Environ., 42, 4517-4529, doi:10.1016/j.atmosenv.2008.01.071.

Kioumourtzoglou MA, Schwartz JD, Weisskopf MG, Melly SJ, Wang Y, Dominici F, Zanobetti A. 2016. Long-term PM2.5 exposure and neurological hospital admissions in the northeastern United States. Environ Health Perspect 124:23–29, http://dx.doi.org/10.1289/ehp.1408973.

Kjellström, E., Nikulin, G., Hansson, U., Strandberg, G., and Ullerstig, A. 2011. 21st century changes in the European climate: uncertainties derived from an ensemble of regional climate model simulations. Tellus Series A-Dynamic Meteorology and Oceanography, 63, 24–40, doi:10.1111/j.1600-0870.2010.00475.x.

Korhonen, H., Carslaw, K., and Romakkaniemi, S. 2010. Enhancement of marine cloud albedo via controlled sea spray injections: A global model study of the influence of emission rates, microphysics and transport, Atmos. Chem. Phys., 10, 4133–4143, doi:10.5194/acp-10-4133- 2010.

Kousa, A., Kukkonen, J., Karppinen, A., Aarnio, P., Koskentalo, T. 2002. A model for evaluating the population exposure to ambient air pollution in an urban area. Atmospheric Environment, 36, 2109-2119.

Kousa, A., Kukkonen, J., Karppinen, A., Aarnio, P., and Koskentalo, T. 200. Statistical and diagnostic evaluation of a new generation urban dispersion modelling system against an extensive dataset in the Helsinki Area, Atmos. Environ., 35, 4617-4628, doi:10.1016/S1352-2310(01)00163-7.

Kouznetsov, R., and Sofiev, M. 2012. A methodology for evaluation of vertical dispersion and dry deposition of atmospheric aerosols. J. Geophys. Res. 117, D01202.

Kukkonen, J., Härkönen, J., Walden, J., Karppinen, A., and Lusa, K. 2001. Evaluation of the dispersion model CAR-FMI against data from a measurement campaign near a major road. Int. J. Environ. Pollut., 35, 949–960.

Kulmala, M., Suni, T., Lehtinen, K. E. J., Dal Maso, M., Boy, M., Reissell, A., Rannik, Ü., Aalto, P., Keronen, P., Hakola, H., Bäck, J., Hoffmann, T., Vesala, T., and Hari, P. 2004. A new feedback mechanism linking forests, aerosols, and climate. Atmos. Chem. Phys., 4, 557–562.

Lamarque, J.-F., Bond, T. C., Eyring, V., Granier, C., Heil, A.,Klimont, Z., Lee, D., Liousse, C., Mieville, A., Owen, B., Schultz, M. G., Shindell, D., Smith, S. J., Stehfest, E., Aardenne, J. V., Cooper, O. R., Kainuma, M., Mahowald, N., Mc-Connell, J. R., Naik, V., Riahi, K., and van Vuuren, D. P.2010. Historical (1850–2000) gridded anthropogenic and biomass burning emissions of reactive

gases and aerosols: Methodology and application, Atmos. Chem. Phys., 10, 7017–7039, doi:10.5194/acp-10-7017-2010.

Lana, A., Bell, T. G., Simó, R., Vallina, S.M., Ballabrera-Poy, J., Kettle, A. J., Dachs, J., Bopp, L., Saltzman, E. S., Stefels, J., Johnson, J. E., and Liss, P. S. 2011. An updated climatology of surface dimethlysulfide concentrations and emission fluxes in the global ocean, Global Biogeochem. Cycles, 25, GB1004, doi:10.1029/2010GB003850.

Laurikko, J. 1998. On exhaust emissions from petrol-fuelled passenger cars at low ambient temperatures. VTT Publications 348, Technical Research Centre of Finland, Espoo, 21.

Laurikko, J., Kukkonen, J., Koistinen, K., and Koskentalo, T. 2003. Integrated modelling system for the evaluation of the impact of Transport-related measures to urban air quality. 2th symposium "Transport and Air Pollution", Avignon, France.

Levitin, J., Härkönen, J., Kukkonen, J., and Nikmo, J. 2005. Evaluation of the CALINE4 and CAR-FMI models against measurements near a major road, Atmos. Environ., 39, 4439–4452, doi:10.1016/j.atmosenv.2005.03.046.

Lewis, E. R., and Schwartz, S. E. 2006. Comment on "Size distribution of sea-salt emissions as a function of relative humidity". Atmos. Environ., 40, 588–590, doi:10.1016/j.atmosenv.2005.08.043.

Lewis, E. R., and Schwartz, S.E. 2004. Sea Salt Aerosol Production: Mechanisms, Methods, Measurements, and Models: A Critical Review, Geophys. Monogr. Ser., vol. 152, AGU, Washington, D. C.

Liora, N., Markakis, K., Poupkou, A., Giannaros, T.M., and Melas, D. 2015. The natural emissions model (NEMO): Description, application and model evaluation. Atmospheric Environment, 122, 493-504.

Liss, P. S. and Duce, R. A. (Eds.). 1997. The Sea Surface and Global Change, Cambridge University Press, Cambridge.

Loveland, T.R., Reed, B.C., Brown, J.F., Ohlen, D.O., Zhu, J., Yang, L., and Merchant, J.W. 2000. Development of a global land cover characteristics database and IGBP DISCover from 1-km AVHRR data. Int. J. Remote Sens., 21, 1,303–1,330

Lundgren, K., Vogel, B.,Vogel, H., and Kottmeier, C. 2013. Direct radiative effects of sea salt for the Mediterranean region under conditions of low to moderate wind speeds, J. Geophys. Res. Atmos., 118, 1906–1923, doi:10.1029/2012JD018629.

Makkonen, U., Virkkula, A., Mäntykenttä, J., Hakola, H., Keronen, P., Vakkari, V. and Aalto, P.P. 2012. Semi-continuous gas and inorganic aerosol measurements at a Finnish urban site: comparisons with filters, nitrogen in aerosol and gas phases, and aerosol acidity. Atmos. Chem. Phys., 12, 5617–5631.

Monahan, E. C., Spiel, D. E., and Davidson, K. L. 1986. A model of marine aerosol generation via whitecaps and wave disruption, in Oceanic Whitecaps. Edited by E. C. Monahan and G. MacNiochaill, 167–193, D. Reidel, Norwell, Mass.

Morton K. W. 1996. Numerical Solution of Convection-diffusion Problems. Applied Mathematics and Mathematical Computation 12, Chapman & Hall

Mårtensson, E. M., Nilsson, E. D., de Leeuw, G., Cohen, L. H., and Hansson, H.-C. 2003. Laboratory simulations and parameterisation of the primary marine aerosol production, J. Geophys. Res., 108, 4297, doi:10.1029/2002JD002263.

Nakićenović, N. 2000. Global greenhouse gas emissions scenarios: Integrated modeling approaches. Tech. Forecasting and Social Change, 63, 105–109.

Nilsson, E. D., Mårtensson, E. M., van Ekeren, J. S., de Leeuw, G., Moerman, M. M., and O'Dowd, C. D. 2007. Primary marine aerosol emissions: Size resolved eddy covariance measurements with estimates of the sea salt and organic carbon fractions, Atmos. Chem. Phys. Discuss., 7, 13,345–13,400, doi:10.5194/acpd-7-13345-2007, 2007.

Niemi J., Malkki M., Myllynen M., Lounasheimo J., Kousa A., Julkunen A., Koskentalo T. 2009. Air Quality in the Helsinki Metropolitan Area in 2008. YTV publications 15/2009. p. 60. 129 pp. (In Finnish).

O'Dowd, C. D., Smith, M. H. Consterdine, I. E., and Lowe, J. A. 1997. Marine aerosol, sea salt, and the marine sulphur cycle: A short review. Atmos. Environ., 31, 73–80, doi:10.1016/S1352-2310(96)00106-9.

Official Statistics of Finland (OSF): Time use survey [epublication], Helsinki: Statistics Finland, available at: http://www.stat.fi/til/akay/index_en.html, last access: January 25 2016.

Öttl, D., Kukkonen, J., Almbauer, R. A., Sturm, P. J., Pohjola, M., and Härkönen, J. H. 2001. Evaluation of a Gaussian and a Lagrangian model against a roadside dataset, with focus on low wind speed conditions, Atmos. Environ., 35, 2123–2132, doi:10.1016/S1352-2310(00)00492-1.

Pierce, J. R., and Adams, P. J. 2006. Global evaluation of CCN formation by direct emission of sea salt and growth of ultrafine sea salt. J. Geophys. Res., 111, D06203, doi:10.1029/2005JD006186.

Pohjola, M., Kousa, A., Kukkonen, J., Härkönen, J., Karppinen, A., Aarnio, P., Koskentalo, T. 2002. The Spatial and Temporal Variation of Measured Urban PM10 and PM2.5 concentrations in the Helsinki Metropolitan Area. International Journal on Water, Air and Soil Pollution: Focus, 2 (5-6), 189-201.

Pope, C.A., Thun, M. J., Namboodri, M.M., Dockery, D.W, Evans, J.S., Speizer, F.E., Heath, C.W.Jr. 1995. Particulate air pollution as a predictor of Mortality in a prospective study of U.S.adults. American Journal of Respiratory and Critical Care Medicine, 151, 669-674.

Prank, M. 2008. Evaluation of atmospheric composition simulations via comparison with remote-sensing and in-situ observations. Master's thesis, 74 , Dep. of Sci. and Technol., Univ. of Tartu, Tartu, Estonia.

Prank, M. Chapman, D.S. Bullock, J.M., Belmonte Soler, J. Berger, U., Dahl, A., Jäger, S., Kovtunenko, I., Magyar, D., Niemelä, S., Rantio-Lehtimäki, A., Rodinkova, V., Sauliene, I., Severova, E., Sikoparija, B., Sofiev, M. 2013. An operational model for forecasting ragweed pollen release and dispersion in Europe, Agriculture and forest meteorology, doi: 10.1016/j.agrformet.2013.08.003, 182-183, 43-53.

Prank, M., Sofiev, M., Tsyro, S., Hendriks, C., Semeena, V. S., Vazhappilly Francis, X., Butler, T., Denier van der Gon, H., Friedrich, R., Hendricks, J., Kong, X., Lawrence, M., Righi, M., Samaras, Z., Sausen, R., Kukkonen, J., and Sokhi, R. 2016. Evaluation of the performance of four chemical transport models in predicting the aerosol chemical composition in Europe in 2005, Atmos. Chem. Phys. Discuss., doi:10.5194/acp-2015-1028.

Poupkou, A., T. Giannaros, K. Markakis, I. Kioutsioukis, G. Curci, D. Melas, C. Zerefos. 2010. A model for European Biogenic Volatile Organic Compound emissions: Software development and first validation, Atm.Environ., 25, 1845-1856.

Putaud, J., Van Dingenen, R., Alastuey, A., Bauer, H., Birmili, W., Cyrys, J., Flentje, H., Fuzzi, S., Gehrig, R., Hansson, H., Harrison, R., Herrmann, H., Hitzenberger, R., Huglin, C., Jones, A., Kasper-Giebl, A., Kiss, G., Kousa, A., Kuhlbusch, T., Loschau, G., Maenhaut, W., Molnar, A., Moreno, T., Pekkanen, J., Perrino, C., Pitz, M., Puxbaum, H., Querol, X., Rodriguez, S., Salma, I., Schwarz, J., Smolik, J., Schneider, J., Spindler, G., ten Brink, H., Tursic, J., Viana, M., Wiedensohler, A., and Raes, F. 2010. A European aerosol phenomenology-3: Physical and chemical characteristics of particulate matter from 60 rural, urban, and kerbside sites across Europe, Atmos. Environ., 44, 1308–1320,doi:10.1016/j.atmosenv.2009.12.011.

Quinn, P. K., Coffman, D. J., Kaputin, V. N., Bates, T. S., and Covert, D. S. 1999. Surface submicron aerosol chemical composition: What fraction is not sulfate. J. Geophys. Res., 105, 6785–6805.

Remer, L., Kleidman, R., Levy, R., Kaufman, Y., Tanre, D., Mattoo, S., Martins, J.V., Ichoku, C.,Koren, I.,Yu, H., Holben, B.N. 2008. Global aerosol climatology from the MODIS satellite sensors. J. Geophys. Res.-Atmos., 113, D14S07, doi:10.1029/2007JD009661.

Roberts, G.J., and Wooster M.J. 2008. Fire detection and fire characterization over Africa using Meteosat SEVIRI, IEEE Trans. Geosci. Remote Sens., 46,1200–1218, doi:10.1109/TGRS.2008.915751

Roeckner, E., Brokopf, R., Esch, M., Giorgetta, M., Hagemann, S., Kornblueh, L., Manzini, E., Schlese, U., and Schulzweida, U. 2006. Sensitivity of simulated climate to horizontal and vertical resolution in the ECHAM5 atmosphere model. J. Clim., 19, 3771–3791, doi:10.1175/JCLI3824.1.

Rudich, Y., Donahue, N. M., and Mentel, T. F. 2007. Aging of organic aerosol: Bridging the gap between laboratory and field studies, Ann. Rev. Phys. Chem., 58, 321–352.

Russel, P.B. and Heintzenberg, J. 2001. An overview of the ACE-2 clear sky column closure experiment (CLEARCOLUMN). Tellus B, (s.l.], 52(2), ISSN 1600-0889, doi:10.3402/tellusb.v52i2.16173.

Saarikoski, S., Sillanpää, M., Sofiev, M., Timonen, H., Saarnio, K., Teinilä, K., Karppinen, A., Kukkonen, J., Hillamo, R. 2007. Chemical composition of aerosols during a major biomass burning episode over northern Europe in spring 2006: experimental and modelling assessments. Atmos. Environ., 41, 17, 3577–3589.

Schaap, M. F. S., Timmermans, R. M. A., Roemer, M., Velders, G., Beck, J., and Builtjes, P. J. H. 2008. The LOTOS-EUROS model:description, validation and latest developments, Int. J. Environ. Pollut., 32, 270–290.

Samuelsson, P., Jones, C.P., Willén, C. G., Ullerstig, U., Gollvik, A., Hansson, S., Jansson, U., Kjellström, C., Nikulin, E., and Wyser, K. 2011. The Rossby Centre Regional Climate model RCA3: Model description and performance. Tellus A, 63, 4–23, doi:10.111/j.1600-0870.2010.00478.x.

Scholes, M. and Andreae, M.O., 2000. Biogenic and pyrogenic emissions from Africa and their impact on the global atmosphere. Ambio, 29, 23–29.

Schultz, M.G., Heil, A., Hoelzemann, J.J., Spessa, A., Thonicke, K., et al. 2008. Global emissions from wildland fires from 1960 to 2000. Global Biogeochem. Cycles, 22, GB2002.

Schweizer, C., Edwards, R. D, Bayer-Oglesby, L., Gauderman, W. J., Ilacqua, V., Juhani, M., Lai, H. K., Nieuwenhuijsen, M., and Künzl, N. 2007. Indoor time-microenvironment-activity patterns in seven regions of Europe. J. Expo. Sci. Env. Epid., 17, 170–181, doi:10.1038/sj.jes.7500490.

Seinfield, J. H., and Pandis, S. N. 2006. Atmospheric Chemistry and Physics: From Air Pollution to Climate Change. 2nd ed., 1232, John Wiley, Hoboken, N. J.

Siljamo, P., Sofiev, M., Filatova, E., Grewling, L., Jäger, S., Khoreva, E., Linkosalo, T., Jimenez, S.O., Ranta, H., Rantio-Lehtimäki, A., Svetlov, A., Veriankaite, L., Yakovleva, E., Kukkonen, J. 2012. A numerical model of birch pollen emission and dispersion in the atmosphere. Model evaluation and sensitivity analysis. Int. J. Biometeorology, DOI 10.1007/s00484-012-0539-5, PMID 22434484.

Simó, R. 2001. Production of atmospheric sulfur by oceanic plankton: biogeochemical, ecological and evolutionary links, Trends Ecol. Evol.,16(6), 287–294.

Smith, F. B., and Clark, M. J. 1989. The transport and deposition of radioactive debris from the Chernobyl nuclear power plant accident with special emphasis on consequences to the United Kingdom. Meteorological Office Scientific Paper no. 42, HMSO London.

Singh, V., Sokhi, R., and Kukkonen, J. 2014. $PM_{2.5}$ concentrations in London for 2008 – A modeling analysis of contributions from road traffic, J. Air Waste Manage., 64, 509–518, doi:10.1080/10962247.2013.848244.

Sofiev, M. 2000. A model for the evaluation of long-term airborne pollution transport at regional and continental scales.Atmospheric Environment. 34, 15, 2481-2493.

Sofiev, M., Vira, J., Kouznetsov, R., Prank, M., Soares, J., and Genikhovich, E. 2015. Construction of the SILAM Eulerian atmospheric dispersion model based on the advection algorithm of Michael Galperin. Geosci. Model Dev., 8, 3497-3522, doi:10.5194/gmd-8-3497-2015.

Sofiev, M., Vira, J., Prank, M., Soares, J., Kouznetsov, R. 2014. An outlook of System for Integrated modeLling of Atmospheric coMposition SILAM v.5. Steyn, D. G., Builtjes, P. J. and Timmermans, R. M. (Eds.) Air Pollution Modeling and its Application XXII, Springer Netherlands, 2014, 397-400 doi:10.1007/978-94-007-5577-2_67.

Sofiev, M., Vankevich, R., Ermakova, T., and Hakkarainen, J. 2013. Global mapping of maximum emission heights and resulting vertical profiles of wildfire emissions. Atmospheric Chemistry and Physics, 13, 7039–7052.

Sofiev, M., Ermakova, T., and Vankevich, R., 2012a. Evaluation of the smoke-injection height from wild-land fires using remote-sensing data. Atmospheric Chemistry and Physics, 12, 1995–2006.

Sofiev, M., Siljamo, P., Ranta, H., Linkosalo, T., Jaeger,S., Rasmussen, A., Rantio-Lehtimaki, A., Severova, E., Kukkonen, J. 2012b. A numerical model of birch pollen emission and dispersion in the atmosphere. Description of the emission module. Int. J. Biometeorology, doi:10.1007/s00484-012-0532-z.

Sofiev, M., Genikhovich, E., Keronen, P. and Vesala, T. 2010. Diagnosing the Surface Layer Parameters for Dispersion Models within the Meteorological-to-Dispersion Modeling Interface. J. Appl. Meteor. Climatol., 49, 221–233, doi:10.1175/2009JAMC2210.1

Sofiev, M., Vankevich, R., Lotjonen, M., Prank, M., Petukhov, V., Ermakova, T., Koskinen, J., and Kukkonen, J. 2009. An operational system for the assimilation of the satellite information on wild-land fires for the needs of air quality modelling and forecasting. Atmos. Chem. Phys., 9, 6833–6847.

Sofiev, M., Galperin, M.V., and Genikhovich, E., 2008. Construction and evaluation of Eulerian dynamic core for the air quality and emergency modeling system SILAM. Borrego, C., Miranda, A.I. (Eds.), NATO Science for Peace and Security Series C: Environmental Security, Air Pollution Modelling and its Application, XIX. Springer-Verlag, Berlin, 699-701.

Sofiev, M., Siljamo, P., Valkama, I., Ilvonen, M., and Kukkonen, J. 2006. A dispersion modelling system SILAM and its evaluation against ETEX data. Atmos. Environ., 40, 674–685, 831, doi:10.1016/j.atmosenv.2005.09.069.

Sokhi, R., Mao, H., Srimath, S. T. G., Fan, S., Kitwiroon, N., Luhana, L., Kukkonen, K., Haakana, M., van den Hout, K. D., Boulter, P., McCrae, I. S., Larssen, S., Gjerstad, K. I., San Jose, R., Bartzis, J., Neofytou, P., van den Breemer, P., Neville, S., Kousa, A., Cortes, B. M., Karppinen, K., and Myrtveit,I. 2008. An integrated multi-model approach for air quality assessment: Development and evaluation of the OSCAR Air Quality Assessment System, Environ. Modell. Softw., 23, 268–281, doi:10.1016/j.envsoft.2007.03.006.

Solazzo, E., Bianconi, R., Pirovano, G., Matthias, V., Vautard, R., Moran, M. D., et al. 2012. Operational model evaluation for particulate matter in Europe and North America in the context of AQMEII. Atmospheric Environment, 53, 75-92.

Statistics Finland. 2012. Energy consumption in households [epublication], ISSN = 2323-329X, 2012, Appendix Figure 1, Energy consumption in households by energy source in 2012, Helsinki: http://www.stat.fi/til/asen/2012/asen_2012_2013-11-13_kuv_001_en.html

Stevens, G., Wilson, A., and Hammitt, J.K. 2005. A benefit-cost analysis of retrofitting diesel vehicles with particulate filters in the Mexico City metropolitan area. Risk Analysis, 25, 883–899.

Stohl, A., Klimont, Z., Eckhardt, S., Kupiainen, K., Shevchenko, V. P., Kopeikin, V. M., and Novigatsky, A. N. 2013. Black carbon in the Arctic: the underestimated role of gas flaring and residential combustion emissions. Atmos. Chem. Phys., 13, 8833-8855, doi:10.5194/acp-13-8833-2013.

Tainio, M., Sofiev, M., Hujo, M., Tuomisto, J. T., Loh, M., Jantunen, M. J., Karppinen, A., Kangas, L., Karvosenoja, N., Kupiainen, K., Porvari, P., Kukkonen, J. 2009. Evaluation of the European population intake fractions for European and Finnish anthropogenic primary fine particulate matter emissions. Atmos. Environ., 43, 3052−3059.

Textor, C., Schulz, M., Guibert, S., Kinne, S., Balkanski, Y., Bauer, S., Berntsen, T., Berglen, T., Boucher, O., Chin, M., Dentener, F., Diehl, T., Easter, R., Feichter, H., Fillmore, D., Ghan, S., Ginoux, P., Gong, S., Grini, A., Hendricks, J., Horowitz, L., Huang, P., Isaksen, I., Iversen, I., Kloster, S., Koch, D., Kirkevåg, A., Kristjansson, J. E., Krol, M., Lauer, A., Lamarque, J. F., Liu, X., Montanaro, V., Myhre, G., Penner, J., Pitari, G., Reddy, S., Seland, Ø., Stier, P., Takemura, T., and Tie, X. 2006. Analysis and quantification of the diversities of aerosol life cycles within AeroCom. Atmos. Chem. Phys., 6, 1777-1813, doi:10.5194/acp-6-1777-2006.

Tsyro, S., Aas, W., Soares, J., Sofiev, M., Berge, H., and Spindler, G. 2011. Modelling of sea salt pollution over Europe: key uncertainties and comparison with observations Atmos. Chem. Phys.,11, 10367-10388, doi:10.5194/acp-11-10367-2011.

Tørseth, K., Aas, W., Breivik, K., Fjæraa, A.M., Fiebig, M., Hjellbrekke, A.G., Lund M.C., Solberg, S., and Yttri, K.E. 2012. Introduction to the European Monitoring and Evaluation Programme (EMEP)

and observed atmospheric composition change during 1972–2009. Atmos. Chem. Physics, 12, 5447–5481, doi:10.5194/acp-12-5447-2012.

Vira, J. and Sofiev, M. 2012. On variational data assimilation for estimating the model initial conditions and emission fluxes for the short-term forecasting of SOx concentrations. Atmosph. Environ., 46, 318-328.

Virkkula, A., Levula, J., Pohja, T., Aalto, P. P., Keronen, P., Schobesberger, S., Clements, C. B., Pirjola, L., Kieloaho, A.-J., Kulmala, L., Aaltonen, H., Patokoski, J., Pumpanen, J., Rinne, J., Ruuskanen, T., Pihlatie, M., Manninen, H. E., Aaltonen, V., Junninen, H., Petäjä, T., Backman, J., Dal Maso, M., Nieminen, T., Olsson, T., Grönholm, T., Aalto, J., Virtanen, T.H., Kajos, M., Kerminen, V.-M., Schultz, D.M., Kukkonen, J., Sofiev, M., De Leeuw, G., Bäck, J., Hari, P., and Kulmala, M. 2014. Prescribed burning of logging slash in the boreal forest of Finland: emissions and effects on meteorological quantities and soil properties. Atmos. Chem. Phys., 14, 4473-4502, doi:10.5194/acp-14-4473-2014.

van der Werf, G. R., Randerson, J. T., Giglio, L., Collatz, G. J., Mu, M., Kasibhatla, P. S., Morton, D. C., DeFries, R. S., Jin, Y., and van Leeuwen, T. T. 2010. Global fire emissions and the contribution of deforestation, savanna, forest, agricultural, and peat fires (1997–2009), Atmos. Chem. Phys., 10, 11707-11735, doi:10.5194/acp-10-11707-2010.

Vogel, B., Vogel, H., Bäumer, D., Bangert, M., Lundgren, K., Rinke, R., and Stanelle, T. 2009. the comprehensive model system COSMO-ART-Radiative impact of aerosol on the state of the atmosphere on the regional scale. Atmos. Chem. Phys., 9, 8661-8680.

Wang, M., Ghan, S., Ovchinnikov, M., Liu, X., Easter, R., Kassianov, E., Qian, Y., and Morrison, H. 2011. Aerosol indirect effects in a multi-scale aerosol-climate model PNNL-MMF, Atmos. Chem. Phys., 11, 5431-5455, doi:10.5194/acp-11-5431-2011.

Warneck P. 1988. Chemistry of the natural atmosphere. International Geophysics Series. Wiley and Sons. Vol. 41. Academy Press, 757.

Witek, M.L., Diner, D.J., and Garay, M.J. 2016. Satellite assessment of sea spray aerosol productivity: Southern Ocean case study. J. Geophys. Res. Atmos., 121, doi:10.1002/2015JD023726.

WHO. 2006. Air quality guidelines. Global update 2005. Particulate matter, ozone, nitrogen dioxide and sulfur dioxide, WHO Regional Office for Europe, Copenhagen.

I

A regional-to-global model of emission and transport of sea salt particles in the atmosphere

Mikhail Sofiev,[1] Joana Soares,[1] Marje Prank,[1] Gerrit de Leeuw,[2,3] and Jaakko Kukkonen[1]

Received 6 July 2010; revised 9 August 2011; accepted 17 August 2011; published 2 November 2011.

[1] A parameterization for the emission of sea-salt aerosol (SSA) particles is presented and its application in the SILAM dispersion modeling system for regional and global SSA simulations is discussed. The SSA production term is based on the parameterization of Monahan et al. and on experimental data from Mårtensson et al., and Clarke et al. The observational data were used to extend the Monahan et al. SSA emission flux to particles as small as 10 nm (dry particle diameter D_P) and to account for water temperature and salinity. The result is an analytical formulation describing the SSA production fluxes for particles with D_p between 10 nm and 10 μm. This source function is implemented in the dispersion model SILAM and applied to compute the distribution of sea salt over the North Atlantic and Western Europe for the years 2000, 2003, 2007, 2009 and 2010, as well as globally for 2001 and 2008. The computed annual global production of SSA is between 6700 and 7400 Tg/year. Comparison of the SILAM near-surface SSA concentrations and its wet deposition with the in situ EMEP observations showed good agreement for summer periods while in winter time the model tends to under-estimate the wet deposition by a factor of ~3. The underestimation is attributed to the coarse fraction ($D_p > 10$ μm) and the spume production mechanism, which were excluded from the analysis, to the wet deposition parameterization in SILAM and to the under-estimated precipitation amount in the input meteodata. The predicted vertically integrated aerosol optical depth (AOD) showed a close match with satellite observations over SSA-dominated areas.

Citation: Sofiev, M., J. Soares, M. Prank, G. de Leeuw, and J. Kukkonen (2011), A regional-to-global model of emission and transport of sea salt particles in the atmosphere, *J. Geophys. Res.*, *116*, D21302, doi:10.1029/2010JD014713.

1. Introduction

[2] The sea salt aerosol (SSA), the major fraction of sea spray outside biologically active regions, is important for a wide variety of processes. Typically, the SSA particles contain ~55% of Cl, 30% of Na, 8% of sulphates, and other components in smaller fractions. SSA particles may also be enriched with organic material [*O'Dowd et al.*, 2004; *Cavalli et al.*, 2004; *Fuentes et al.*, 2010; *de Leeuw et al.*, 2011]. SSA affects the Earth radiation budget, atmospheric chemistry, cloud processes, and climate [*Intergovernmental Panel on Climate Change* (*IPCC*), 2007; *O'Dowd et al.*, 1997]. The mass concentration of SSA and its associated light scattering effects are not generally high in comparison with those of the anthropogenic aerosols in heavily polluted areas (with an exception of storm episodes where large amounts of coarse SSA are produced). However, the oceans cover 70% of the Earth whereas the highest concentrations of anthropogenic aerosols are confined to a relatively small part of the world. Therefore, the global annual impacts of anthropogenic and sea salt aerosols on the radiation budget are similar [*IPCC*, 2007; *Textor et al.*, 2006]. The effect of SSA is particularly important in the Southern Hemisphere where SSA is the major particulate compound. Two other major aerosol sources there are biomass burning and DMS oxidation, which, however, contribute only marginally to the global atmospheric aerosol mass [*Gong et al.*, 1997; *Chin et al.*, 2002; *Korhonen et al.*, 2008].

[3] Sea salt particles are hygroscopic and, in a humid environment, mainly exist as liquid droplets (but still referred to as "particles" throughout this paper). They are also readily activated to form cloud condensation nuclei [*Pruppacher and Klett*, 1997]. With increasing concentrations of cloud condensation nuclei, the cloud microphysical properties change, i.e., the available water vapor is re-distributed over more particles, on average resulting in smaller particle sizes, which in turn changes both cloud albedo and precipitation [*Latham and Smith*, 1990; *Lenton and Vaughan*, 2009; *Boyd*, 2008; *Korhonen et al.*, 2010]. The production of very coarse sea salt aerosols (dry particle diameter $D_P > 20$ μm) contributes to the transfer of heat and water vapor from the ocean to the atmosphere at very high wind speeds [*Andreas et al.*, 1995].

[4] With regard to the atmospheric transport, SSA particles are water-soluble with size, density, and light-scattering properties dependent on relative humidity [e.g., *Hess et al.*,

[1]Air Quality Research, Finnish Meteorological Institute, Helsinki, Finland.
[2]Climate Change, Finnish Meteorological Institute, Helsinki, Finland.
[3]Department of Physics, University of Helsinki, Helsinki, Finland.

0148-0227/11/2010JD014713

1998]. The primary SSA removal processes are scavenging by precipitation and dry deposition (including gravitational settling).

[5] To quantify the distribution and the effects of sea spray aerosol, accurate estimates of the SSA production, dispersion, and sinks are required. The corresponding models have to include descriptions of the main quantities governing the above processes. Over-simplified parameterizations may be insufficient because the changing climate will alter the surface winds, water temperature, salinity, etc., and thus change the conditions of sea spray emission and atmospheric dispersion [*Latham and Smith*, 1990].

[6] The SSA production at the sea surface is primarily dependent on wind speed but other parameters influencing this process have been identified as well, e.g., seawater temperature and salinity, atmospheric stability, wave height and steepness [*Monahan et al.*, 1986; *Mårtensson et al.*, 2003; *Gong et al.*, 1997; *Gong*, 2003; *Lewis and Schwartz*, 2004; *O'Dowd and de Leeuw*, 2007; *Witek et al.*, 2007a, 2007b; *O'Dowd and Smith*, 1993]. The wind stress at the water surface leads to formation of waves and, when the waves break, to formation of bubbles. The bubbles rise to the sea surface and, when they burst, seawater droplets are injected into the atmospheric layer adjacent to the water surface [*Monahan et al.*, 1986]. A substantial fraction of the initially emitted particles falls back into the sea while other particles are mixed upwards due to turbulence. This bubble-mediated SSA production mechanism is believed to be the main process responsible for sea salt production at moderate wind speeds [*Blanchard and Woodcock*, 1957; *Fitzgerald*, 1991; *Andreas et al.*, 1995; *Lewis and Schwartz*, 2004; *de Leeuw et al.*, 2011; *Woodcock*, 1953]. Bubbles bursting at the water surface produce two types of droplets: film drops ejected from the rim of the receding film cap when it breaks [*Spiel*, 1998] and jet drops formed from the break-up of the vertically rising water jet from the collapsing bubble cavity [e.g., *Blanchard and Woodcock*, 1957]. The film droplets are smaller in size (mainly sub-micron, up to hundreds per bubble), while the jet droplets (up to ten per bubble) are usually larger than 1 μm in radius [*Woodcock*, 1972].

[7] At strong winds, the direct production of spume droplets from breaking waves becomes important [*Andreas*, 1998]. Spume droplets generally have a dry particle diameter D_p larger than a few μm, i.e., their diameter at formation is larger than 10 μm resulting in an atmospheric life time which is so short that they have limited importance at regional and global scales.

[8] Multiple modeling studies have explored the main features of the SSA distribution over regions and the globe [e.g., *Gong et al.*, 1997; *Gong*, 2003; *Pierce and Adams*, 2006; *Witek et al.*, 2007a; *Jaeglé et al.*, 2011]. A major comparison of representation of aerosols in global models has been made by the AeroCom community (http://dataipsl.ipsl.jussieu.fr/AEROCOM) [*Schulz et al.*, 2009; *Textor et al.*, 2006, and references therein]. A critical analysis of the SSA modeling approaches can be also found in the major review of *Lewis and Schwartz* [2004], hereinafter referred to as LS04.

[9] The main goals of the current study are the development and evaluation of parameterization of the SSA emission, which would include the other key factors than wind speed controlling the bubble-mediated production, i.e., water surface temperature and salinity. The specific objectives are: (i) to develop a comprehensive and computationally efficient parameterization of the sea salt emission for particles with D_p ranging from 0.01 to 10 μm and for environmentally relevant ranges of water temperature and salinity, (ii) to implement the emission term in the dispersion model SILAM (System for Integrated modeling of Atmospheric coMposition), and (iii) to apply and evaluate the developed system at European and global scales. Therefore, the current paper is mainly limited to discussion of particles with $D_p < 10$ μm and on the bubble bursting process as the production term. The local effects of surf zones and very high wind speed conditions are out of the scope of the study.

2. Basic Terms and Equations

[10] The SSA emission is commonly parameterized in terms of a source function, which describes the upward flux of sea salt particles at or near the ocean surface as a function of atmospheric and oceanic parameters. For practical purposes the effective flux is often evaluated at an effective height of 10 m above the sea surface [*Monahan and O'Muircheartaigh*, 1980; *Monahan et al.*, 1986; *Lewis and Schwartz*, 2004]. In general form:

$$\frac{dF}{dD_p} = f(D_p, U_{10}, T_w, S_w, \ldots) \tag{1}$$

Here F is the effective particle number flux from a unit area of open water, so that $\frac{dF}{dD_p}$ is the flux density for an infinitely small range of the dry particle diameter D_p [μm], expressed in [# μm^{-1} m^{-2} s^{-1}], U_{10} is the wind speed at 10 m above the water surface [m s^{-1}], T_w is the water temperature [K], S_w is the water salinity [relative unit].

[11] In the general form (1), the emission depends on all parameters of the rhs of the equation and their effects can be inter-connected. However, in most parameterizations the processes are separated and, for instance, the dependence on particle size is considered only for some of them. This is somewhat artificial since there is neither strong experimental evidence that any of the forcing mechanisms affects production of particles of all sizes equally, nor strong evidence that these mechanisms can be considered independently from each other. For instance, some observations suggested that both bubble and aerosol spectra vary with wind [*Smith et al.*, 1993; *Smith and Harrison*, 1998; *Petelski and Piskozub*, 2006; *de Leeuw et al.*, 2003; *de Leeuw and Cohen*, 2001; LS04]. It was noted [*Wu et al.*, 1984; *de Leeuw*, 1988] that coarse particles can be suspended in the atmosphere longer at higher wind speed due to mechanical mixing compensating the gravitational fallout. In that case, a larger fraction of the coarse particles can reach the reference height of 10 m above the water surface and be counted as "emitted." Finally, the experiments of *Mårtensson et al.* [2003] demonstrated the dependence of the aerosol spectrum on water salinity and temperature.

[12] Considering these effects, the wind speed is the primary driver of the total aerosol production, whereas its impact on the particle spectrum is much smaller than that of water temperature and salinity. This impact is also smaller than the overall uncertainty of the existing SSA source functions. Therefore, in the current work the SSA production

is approximated as the product of a shape function (differential density of the SSA number flux – per unit whitecap area and unit D_p range), which depends only on particle size and not on any of the meteorological parameters, and several forcing terms:

$$\frac{dF}{dD_p} = W(U_{10})\ \frac{dF_0}{dD_p}(D_p)\ F_{TW}(D_p, T_w)\ F_{SW}(D_p, S_w), \quad (2)$$

where the forcing terms correspond to effects of wind speed (through the whitecap fraction), water-temperature, and salinity denoted as W, F_{TW} and F_{SW}, respectively.

[13] Throughout this paper, the particle size is characterized by its dry diameter D_p. To relate the particle sizes at different ambient humidity, *Fitzgerald* [1975] suggested descriptions of growth of different salt particles with increasing relative humidity, RH, but these require numerical solution of a transcendental equation. An accuracy within ~3% from SSA observations can be also obtained from empirical relations for relative humidity 98% > $RH > RH_{deliq}$, where RH_{deliq} = ~50% is a deliquescence relative humidity [*Gerber*, 1985; *Tang et al.*, 1997; *Lewis and Schwartz*, 2004, 2006; *K. M. Zhang et al.*, 2005]:

$$\frac{D_{0,S}}{D_{RH}} = 3.7\left(\frac{1.0 - RH}{2.0 - RH}\right)^{1/3}\left(\frac{0.035}{S}\right)^{1/3}\left(\frac{\rho_S}{\rho_{35}}\right)^{1/3} \quad (3)$$

Here $D_{0,S}$ is the diameter of a droplet formed from seawater with salinity S, D_{RH} is the equilibrium diameter of the particle at relative humidity RH [fraction]; and ρ_s and ρ_{35} are the densities of a droplet at salinity S and 35‰, respectively. Since ρ_s deviates from ρ_{35} by less than 1%, this term is usually omitted. For SSA, a simple relation $D_p = 0.5D_{80\%}$ is valid with < 5% error.

[14] Equation (3) is used hereinafter for conversion between the different humidity and salinity values reported by different authors, but with two amendments. First, it is applicable up to RH_{crit} ~0.98 whereas numerical schemes and parameterizations of atmospheric models allow $RH > 1$ in cloudy conditions. Therefore, for $RH > 0.98$, we replaced the formula (3) with its linear extrapolation starting from $RH = 0.98$. The values of $RH > 1.03$ are considered erroneous and replaced with $RH = 1.03$. Second, for $RH < RH_{deliq}$ the dry particle diameter is used.

[15] Most formulations for wind-forcing are expressed in terms of the fraction of the water area covered by white caps (whitecap fraction, W). *Monahan and O'Muircheartaigh* [1980] suggested an empirical power law fit for W as a function of the wind speed at 10 m above the surface U_{10}:

$$W(U_{10}) = 3.84 * 10^{-6} U_{10}^{3.41} \quad (4)$$

Other formulations for W have been published in the literature, which can diverge from equation (4) by up to an order of magnitude [*Anguelova and Webster*, 2006; *Smith et al.*, 1993; *Petelski et al.*, 2005; *Reid et al.*, 2001; LS04, and references therein] but equation (4) is the most widely used for modeling.

[16] Formulations for the shape function, dF_0/dD_p vary widely as well. One of the most used functions was suggested by *Monahan et al.* [1986], which, in terms of D_p, reads as:

$$\frac{dF_0}{dD_p} = 3.6*10^5 * \frac{1 + 0.057D_p^{1.05}}{D_p^3} *10^{1.19\exp\left(-\left(\frac{0.38-\lg D_p}{0.65}\right)^2\right)} \quad (5)$$

where D_p is in μm. This shape function was obtained from laboratory experiments for the production of SSA within the D_p size range from 0.8 μm to 8 μm.

[17] Numerous other schemes have been developed apart from equation (5) [*Andreas*, 1998; *O'Dowd and de Leeuw*, 2007; *Gong et al.*, 1997; *Vignati et al.*, 2001; *Gong*, 2003; *Grini et al.*, 2002; *de Leeuw et al.*, 2011; *Smith et al.*, 1993; LS04, and references therein]. Some of them utilize directly the Monahan function and extrapolate it to larger and/or smaller particles [e.g., *Gong et al.*, 1997; *Gong*, 2003; *Schulz et al.*, 2004; LS04], others attribute different mechanisms of SSA production to different parts of the spectrum, so that a resulting curve becomes a sum of two or more (lognormal) distributions [e.g., *O'Dowd et al.*, 1997; *Vignati et al.*, 2001]; several approaches use polynomial fits and their combinations with other functions [e.g., *Woolf et al.*, 1988; *Mårtensson et al.*, 2003; *Clarke et al.*, 2006], etc.

[18] Comparison of some of these source functions [*Schulz et al.*, 2004; *Textor et al.*, 2006; LS04; *de Leeuw et al.*, 2011] shows that, within the ranges for which the schemes were derived, their predictions are within one order of magnitude. It was noted however, that extrapolation significantly outside the original parameter ranges can lead to unpredictable results. Thus, according to *Mårtensson et al.* [2003], the extrapolated Monahan parameterization over-states the production of particles with $D_p < 0.1$ μm, but under-estimates the flux for 0.1 μm < D_p < 1 μm. It also underestimates the flux for very large particles (D_p > 10 μm), for which the formulations of *Andreas* [1998] can be used instead.

[19] A significant weakness of most of the currently used parameterizations is that they depend only on wind speed and do not include any effects of water temperature and salinity. However, as shown by *Mårtensson et al.* [2003], the variation of these parameters can change the production flux in certain size ranges by more than an order of magnitude. Recent work of *Jaeglé et al.* [2011] has also demonstrated the importance of the sea surface temperature.

3. Modeling Tools and Input Data

3.1. The Modeling System SILAM

[20] The modeling tool used in this study for the evaluation of the new parameterization, as well as for the global and regional simulations is the System for Integrated modeling of Atmospheric coMposition SILAM [*Sofiev et al.*, 2006, 2008]. Its dynamic core currently includes both Eulerian and Lagrangian advection-diffusion formulations. The Eulerian core used in the current study is based on the transport scheme of *Galperin* [1999, 2000], which incorporates the horizontal diffusion term and is combined with the extended resistance analogy of *Sofiev* [2002] for vertical diffusion.

[21] The removal processes are described via dry and wet deposition. Depending on the particle size, mechanisms of

dry deposition vary from the primarily turbulent diffusion driven removal of fine aerosols to the primarily gravitational settling of coarse particles [*Slinn and Slinn*, 1980; *Zhang et al.*, 2001]. The SILAM wet deposition parameterization [*Sofiev et al.*, 2006; *Horn et al.*, 1987; *Smith and Clark*, 1989; *Jylhä*, 1991] is based on direct observations performed for moderately hydrophobic aerosols (not sea salt, however). It distinguishes between sub- and in-cloud scavenging by both rain and snow. The particle size dependence of the impaction scavenging is taken into account by increasing the scavenging rate for super-micron particles in relation to their settling velocity.

[22] The system includes a meteorological pre-processor for diagnosing the basic features of the boundary layer and the free troposphere from the meteorological fields provided by numerical weather prediction (NWP) models [*Sofiev et al.*, 2010]. Physical-chemical transformation modules of SILAM include several tropospheric chemistry schemes, basic aerosol dynamics, and radioactive decay processes. The system accepts flexible definition of the particle size spectrum, which can be defined for each specific run depending on the application.

[23] In the current study, SILAM was used only as a hosting system for the SSA source term. Therefore, all other emission sources and all transformation modules were disabled leaving only transport and deposition modules active.

[24] The simulations were performed for the region covering Europe and Northern Atlantic for May–October 2003, full years 2000, 2007, 2009 and 2010, and for the whole globe for the full years 2001 and 2008. The choice of the years was somewhat arbitrary but we emphasized the recent years because of better quality of the meteorological data and more abundant observational data. The overall time span starting from 2000 covered the 11-year the solar cycle, which might otherwise introduce a bias in a shorter-period study.

[25] The resolution of the regional runs was 30 km while the global simulations were made with 1 degree grid spacing. The vertical grid consists of 9 unevenly spaced layers, with the lowest layer being 50 m thick and the ninth one reaching up to about 9 km above the surface. As shown by *Sofiev* [2002], this vertical structure is sufficient for accurate representation of the relevant concentration profiles and vertical fluxes. All simulations were made with a 15 min internal time step while the model results are provided as 1-h averages. The computations were made with spin-up of one week for regional and one month for global scales. The regional simulations were run with zero boundary conditions but over a sufficiently large domain so that the observational sites were more than 200 km from the border.

[26] The actual water temperature used in the model runs for the global simulations was obtained from the ECMWF analyses whereas the European model runs were made with seasonally averaged data with spatial resolution of 1°. Salinities were fixed at 33‰ for the oceans, at 9‰ for the Baltic Sea and at 0‰ for the fresh-water basins.

[27] For the long-term simulations, we used four bins with the D_p ranges 0.01–0.1 μm, 0.1–1 μm, 1–2.5 μm, and 2.5–10 μm. Inside each range, the fluxes are integrated, and the volume-weighted mean diameter of the particles is taken. This representation corresponds to the routine in situ observations of $PM_{2.5}$ and PM_{10}, which simplifies the model-measurement comparison. The number of ranges, together with the volume-weighted averaging and uneven distribution over the size ranges, provides accuracy better than ~10% for both total mass and aerosol optical depth (AOD) [*Witek et al.*, 2011]. For the detailed spectrum evaluation, 8 months in 2009 and 2010 were computed with high spectral resolution (18 bins over 0.01–10 μm range).

[28] For comparison with Na^+ observations in $PM_{2.5}$ and PM_{10}, the Na^+ fraction in SSA mass was assumed to be 30% and the D_p size ranges 0.01–2.5 μm and 0.01–10 μm were summed-up, respectively.

[29] The computations of the AOD of the atmospheric vertical column are based on Mie theory [*Mie*, 1908], which implementation in SILAM is described by *Prank* [2008]. The refractive indices for the Mie computations are taken from the OPAC database [*Hess et al.*, 1998], whereas the size of the particles for the ambient relative humidity was computed using the equation (3).

[30] Meteorological information and necessary geophysical and land cover maps are taken from the FMI-HIRLAM and ECMWF meteorological models.

3.2. Initial Formulations and Input Data

[31] The SSA source function development is based on the parameterization of *Monahan et al.* [1986] (further referred to as M86), equations (4), (5) , the data of *Mårtensson et al.* [2003] (further referred to as M03), and the results of the SEAS campaign [*Clarke et al.*, 2006] (Figure 1a).

[32] The M86 formulation does not cover the size range $D_p < 0.8$ μm, which has long atmospheric lifetime and large contribution to the SSA surface area and thus to optical thickness (Figure 1b). This range therefore is the most important one for regional and global scales and for interactions with atmospheric chemistry and climate. The parameterization also does not include the particle flux dependence on water temperature and salinity. The actual water temperature during the experiment is not mentioned in the M86 paper but as the experiment was performed in the laboratory, a typical room temperature of about 20°C can be assumed.

[33] The M03 experiments were made in a small tank with artificial seawater with salinities of 0‰, 9‰ and 33‰ and water temperatures of −2°C, 5°C, 15°C, and 25°C. Bubbles were generated by an aerator and the SSA particles were produced when the bubbles burst at the surface. Particle size distributions in the size range from 20 nm to 3 μm were measured in the headspace, which was first freed from particles by flushing the tank with the filtered air.

[34] Based on these observations, Mårtensson *et al.* suggested a parameterization, which, however, we found to be very sensitive to details of the numerical implementation. The coefficients of the suggested 6th order polynomial fits vary by over 15 orders of magnitude resulting in extremely fast fluctuations of the fit. In particular, no changes appeared possible in the definition of the size bins used in that work: different spectrum definitions appeared to change the fluxes. Therefore, below we develop the new parameterization using only the M03 observations.

[35] The SEAS data set is the only one that has observations for particles smaller than 0.02 μm. However, it was a field experiment conducted near the surf zone and thus influenced by local processes, which are beyond the scope of the current study. Since these processes mainly influence the coarser

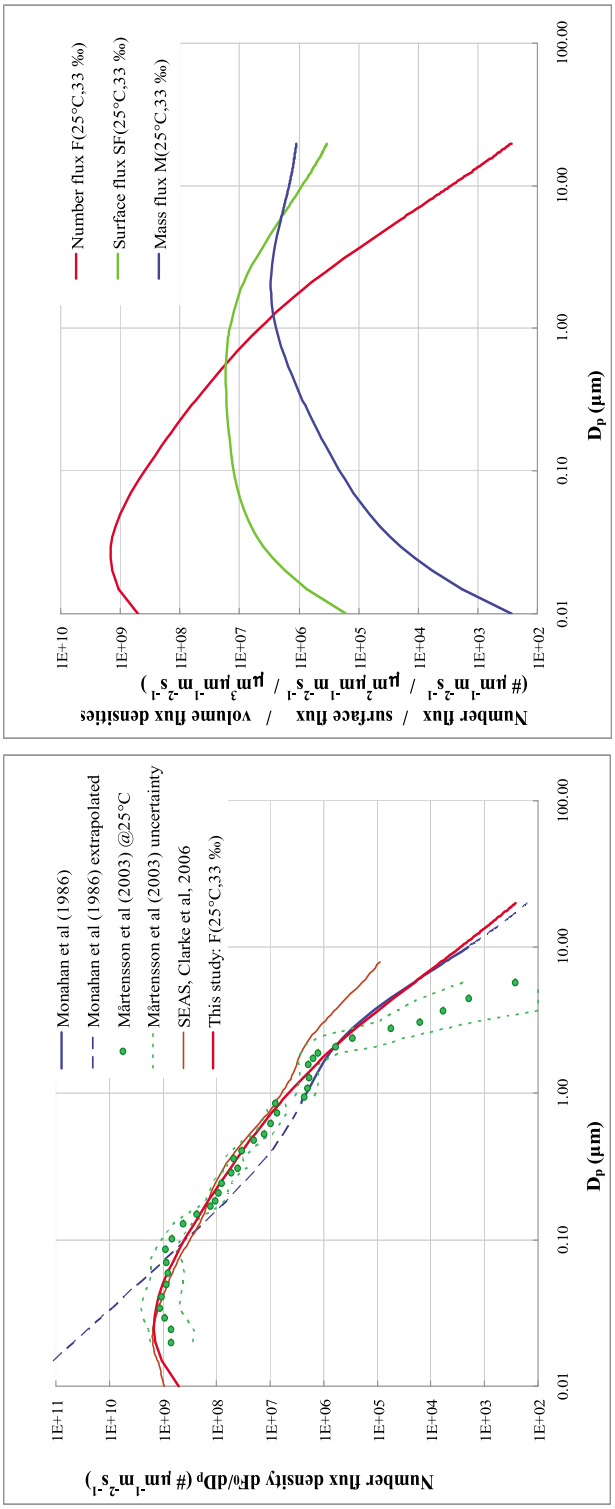

Figure 1. Shape functions of the SSA production term. (a) The number flux densities: this study equation (6) (red); the M86 equation (5) original (solid blue line) and extrapolated (dashed blue lines); the M03 shape (green dots) and its one-σ uncertainty (light-green dashed line) for $T_w = 25°C$, $S_w = 33‰$, the SEAS shape (narrow brown); (b) The particle number (red), surface (green) and volume (blue) flux densities, this study ($T_w = 25°C$, $S_w = 33‰$).

particles, we used the SEAS data only for particles smaller than 0.02 μm. The water temperature and salinity were not explicitly reported but *Clarke et al.* [2006] mentioned that they were similar to those of the M03 reference values (25°C and 33‰).

4. Suggested SSA Production Term

[36] In the current section, we provide a condensed description of the new SSA source term. More detailed discussion of the formulas, their connections to physical processes and relations to other models is given in section 6.

4.1. Adaptation of the M86 Formulations to the M03 Data

[37] The new shape function was obtained by modifying the M86 equation (5) in order to fit the observations extracted from the M03 paper for T_w = 25°C and S = 0.033 (33‰) and the SEAS data for D_p < 0.02 μm. The resulting curve was extrapolated from 8 to 10 μm to cover the whole target range 0.01–10 μm.

[38] The advantages of the M86 shape as a starting point are: (i) it was justified by M86 (though the reasoning was later criticized by LS04), (ii) it is a widely used function, which simplifies the comparison with other models, (iii) it is monotonous, smooth, and requires only modest adjustments to fit into the M03 and SEAS data. The only significant correction refers to sub-0.1 μm particles, for which an additional term has to be introduced to reduce the production.

[39] The resulting shape function for particles with D_p [μm] ranging from 0.01 to 10 μm reads as:

$$\left(\frac{dF_0}{dD_p}\right)_{33‰,25^\circ} = 1\cdot 10^6 \cdot \frac{\exp\left(\frac{-0.09}{D_p+3\cdot 10^{-3}}\right)}{2+\exp\left(-\frac{5}{D_p}\right)} \cdot \frac{1+0.05D_p^{1.05}}{D_p^3} \cdot 10^{1.05\exp\left(-\left(\frac{0.27-\lg D_p}{1.1}\right)^2\right)} \tag{6}$$

The function (6) is presented in Figure 1a together with the original and extrapolated M86 formulations (5), the M03 data and the SEAS shape function. Compared to the original M86 formula (5), the ratio of exponents in equation (6) reduces the production flux for particles smaller than ~0.1 μm while the adjusted coefficients in the other terms eliminate the underestimation of the flux in the 0.1–1 μm range and maintain the overall scale. The corresponding mass and particle surface fluxes are presented in Figure 1b.

4.2. Effects of Water Temperature and Salinity

[40] The shape function (6) describes the SSA number flux at the reference temperature of 25°C and at the reference salinity of 33 ‰. Below, we compute the correction factors F_{TW}, F_{SW} from equation (2) as functions of two variables – temperature/salinity and particle size.

4.2.1. Effect of Water Temperature

[41] For water temperatures other than 25°C, the correction functions F_{Tw} were derived by dividing the M03 observed fluxes at T_w = 15°C, 5°C and −2°C by the fluxes at 25°C. Figure 2a shows that the ratios of the M03 production fluxes at these three temperatures to the flux at T_w = 25°C are smooth and monotonically decreasing with increasing particle size. The apparent deviations from the otherwise good power law fit are around D_p ~ 0.1–0.2 μm and D_p ~ 2 μm where a few outliers appear in some correction functions (shown with lighter colors). These are related to non-monotonicity of the particle size distributions measured by M03 at different temperatures. M03 refer to maxima in the size spectra at these diameters as modes, but do not present any explanation for the occurrence of these modes. Therefore, at this stage it looks premature to build parameterizations taking them into account. In the following we disregard these outliers and approximate the data with the power law functions (Figure 2a):

$$\begin{aligned} F_{T_W=15^0C}(D_p) &= 0.48\cdot D_p^{-0.36} \\ F_{T_W=5^0C}(D_p) &= 0.15\cdot D_p^{-0.88} \\ F_{T_W=-2^0C}(D_p) &= 0.092\cdot D_p^{-0.96} \end{aligned} \tag{7}$$

where D_p is in [μm]. Due to monotonicity of the dependencies with regard to water temperature, the correction factors for other temperatures can be obtained by interpolation. Lacking information to justify more complicated interpolations, we suggest the use of linear functions.

[42] There are no data for extrapolation outside the M03 observed range for particles larger than 6–7 μm and smaller than 0.02 μm. However, for regional and large-scale applications, a sea-spray source function for dry diameters from 0.01 μm up to at least 10 μm is needed. Therefore, and by lack of any evidence of other extrapolations, the corrections (7) were used for the sea-spray particles with dry diameters up to 10 μm. However, the uncertainty in the extrapolated production flux is anticipated to be large.

4.2.2. Effect of Salinity

[43] The effect of salinity is evaluated following the same procedure as for the temperature correction. The salinity of 33‰ is taken as the reference and for other salinities the correction functions F_{Sw} are derived using the ratios of the M03 fluxes for 9.2‰ (e.g., Baltic Sea) and 0‰ ("fresh" water) to that at 33‰ (oceanic conditions). Fitting of these ratios to power law functions (Figure 2b) results in:

$$\begin{aligned} F_{S_W=0.0092} &= 0.12\cdot D_p^{-0.71} \\ F_{S_W=0} &= 5.85\cdot 10^{-5}\cdot D_p^{-1.7} \end{aligned} \tag{8}$$

where D_p is in [μm]. There is no observational data for intermediate salinities but the trend is clear and monotonic: lower salinity leads to lower SSA production. Therefore we again suggest linear interpolation between these two functions.

[44] The functions (8) apply only to the size range for which the M03 measurements are available but we used them for D_p up to 10 μm. Similar to the temperature correction, the uncertainty of the extrapolation is anticipated to be large but its impact is limited because the contribution of coarse particles to the flux from low-saline and fresh water is small (Figure 2b).

[45] Similar to F_{Tw}, the fresh-water ratio shows inhomogeneity at D_p ~ 0.1 μm. However, since it again has no clear explanation, we still use the single fit (8) over the whole D_p range.

[46] For the applications, one has to keep in mind an ambiguity connected with the SSA production from fresh water. In the M03 experiment, the "fresh" water was distilled water, which has much lower concentrations of dissolved

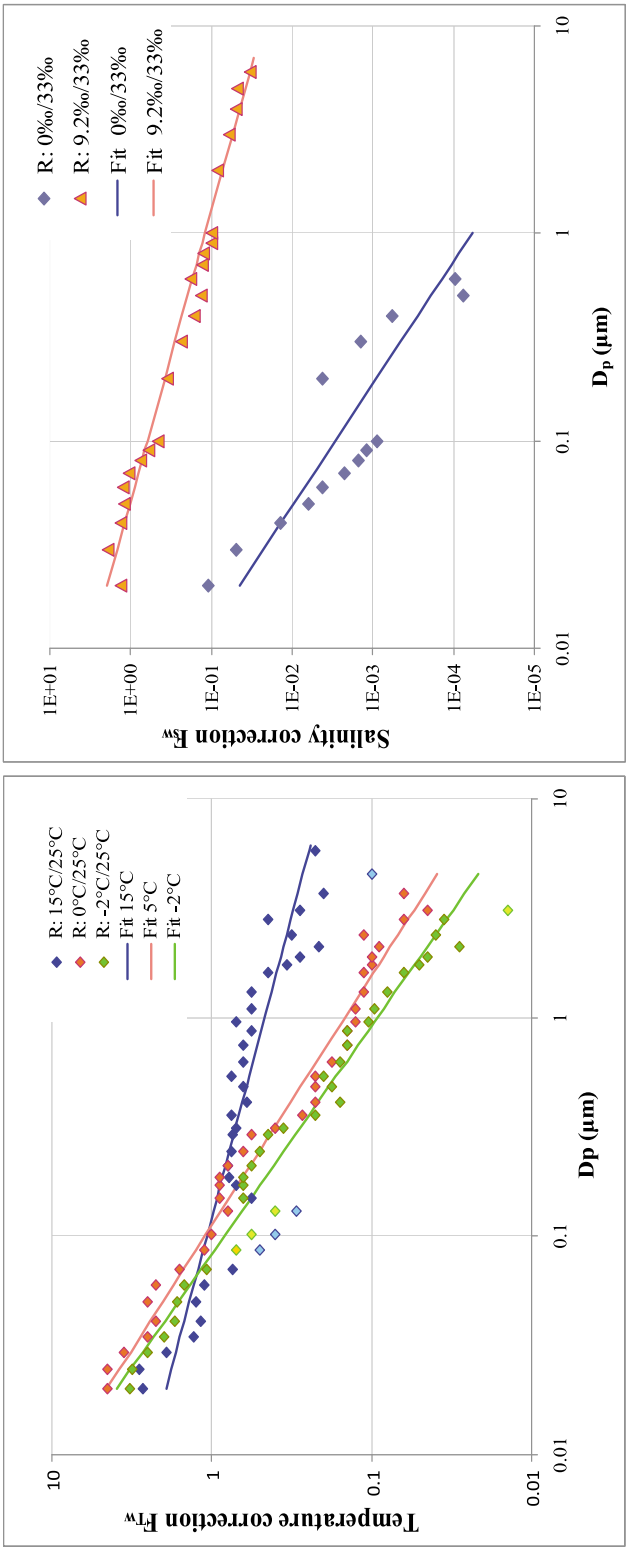

Figure 2. Temperature and salinity correction functions in equation (2). (a) Temperature corrections defined as ratios R of the SSA production flux at T_w of 15°C, 5°C, and −2°C to the flux at the reference T_w = 25°C – and fits for F_{TW}, equation (7). (b) Salinity corrections defined as ratios R of SSA production flux at S_w of 0‰ and 9.2‰ to the flux at S_w = 33‰ – and fits for F_{SW}, equation (8).

matter, such as various salts and organic matter, than natural fresh water. Therefore, in the M03 experiment, a large fraction of "fresh" water particles would evaporate completely before reaching the particle sampler while in natural water bodies the residual particles would remain. However, since there is no other information available, we used the M03 data to obtain equation (8) but would expect the flux from actual fresh-water bodies to be somewhat larger than the one suggested by the parameterization.

5. Evaluation of the SSA Emission Module Via SILAM CTM Calculations

[47] The new SSA production parameterization closely follows the M86 shape function and M03 data over most of their ranges of applicability (Figure 1a). For the finest particles, the SEAS shape is approached. The difference between the curves is smaller than the uncertainty of the functions themselves (e.g., three standard deviations of the M03 data, p = 0.001), except for $D_p > 1$ μm, where the parameterizations differ by more than an order of magnitude and where the new parameterization follows the M86 shape. Therefore the outcome of the existing evaluations of the original schemes (M86, M03 and SEAS) is applicable to the current one within the relevant particle size ranges and environmental conditions. In particular, M03 was evaluated against direct flux measurements by *Nilsson et al.* [2007] and *Mårtensson* [2007]. The M86 scheme was used in numerous studies, which included comparison of dispersion model results with observed concentrations [e.g., *Gong et al.*, 1997; LS04, chap. 4.1; *Witek et al.*, 2007a; *Jaeglé et al.*, 2011]. The effect of water temperature on the emission flux has been confirmed by eddy covariance measurements at Mace Head by *Nilsson et al.* [2007] and *Mårtensson* [2007]. Finally, *Pierce and Adams* [2006] used GCM GISS for comparison of the M86, M03 and SEAS schemes and evaluation of their fluxes and particle size spectra. They showed that the SEAS scheme is closer to the observed spectra for sub-0.1 μm than other schemes but shows much too high contribution of coarse particles ($D_p > 1$ μm). The M03 parameterization was somewhat better in 0.1–1 μm range. As seen from Figure 1a, the current parameterization approaches the corresponding schemes at each of these ranges. Since this comparison was made using different transport and meteo model than those of the current study, it was repeated following the same procedure as that of *Pierce and Adams* [2006].

[48] Below, we concentrate on comparison of the SILAM model predictions obtained using the SSA parameterizations (6)–(8) with observations.

[49] Observations of sea salt were obtained from five sources: (i) a few independent campaigns that provided aerosol size distributions in the marine boundary layer [*O'Dowd et al.*, 1997; *Clarke et al.*, 2006; *Vana et al.*, 2008]; (ii) several sites of the EMEP network (Co-operative Programme for monitoring and evaluation of the long-range transmission of air pollutants in Europe, http://www.emep.int) that perform regular analysis of Na^+ concentration in total PM; (iii) several EMEP stations that perform ion analysis of precipitation including Na^+; (iv) the satellite observations of aerosol optical depth, which can be considered representative for sea salt in remote regions (excluding areas with high influence of other aerosols); (v) the near-surface concentrations for global SILAM evaluation were taken from the paper of *Pierce and Adams* [2006] and references therein. These data sets are complementary. Indeed, the comparison with size distributions shows the system's ability to treat particles of different sizes but, e.g., the absolute concentration may not be representative due to the small amount of data obtained from a limited area. The mass concentrations of Na^+ in aerosol are measured near the surface and mainly reflect the amount of coarse-fraction SSA particles (the main SSA mass flux is within the size range 0.5–5 μm – Figure 1b). The scavenging with precipitation washes out the whole atmospheric column. Therefore, the Na^+ concentration in precipitation provides an insight into the column-integrated mass of SSA, which in turn is directly linked to the mass production and removal terms. Finally, AOD is proportional to the total particle area, for which the production peaks at the submicron size range (Figure 1b).

[50] The model-predicted sea salt concentrations are affected by a large number of processes including SSA production, transport, and removal from the atmosphere. Inaccuracies of the transport model or precipitation pattern can thus be misinterpreted as errors in the production term or the errors can compensate each other. However, the above mentioned independent and mutually complementary types of measurements with substantially different features and observed quantities might reduce the chance of such flukes.

5.1. Evaluation of the Sea-Salt Size Distribution

[51] The SSA number size distributions produced by the SILAM run for 2009–2010 with high spectral resolution is compared with the data from a cruise at the North-East Atlantic (NEAT) published by *O'Dowd et al.* [1997] - Figure 3. The set of measurements represents a typical Northeast Atlantic SSA number size distribution for end-1980s. The SILAM spectrum-resolving computations were made for November 2009 and, for comparison, July 2010, thus meeting the NEAT season (late autumn) but not the year. In the current parameterization the spectrum depends on water surface temperature and salinity but not on wind speed or any other dynamic meteorological parameter. The selection of different years then allows for explicit verification of this assumption. Indeed, averaging over the same season ensures that the water temperature and salinity are similar, whereas the different years eliminate any apparent connection to the short-term weather phenomena. Comparison of absolute levels of the concentrations indicates the stability of the frequency distribution of wind speed from year to year.

[52] As seen from Figure 3, the key features of the NEAT size distribution are reproduced by the model: the absolute peak of number concentrations at 20–30 nm (if the nucleation-produced aerosol with $D_p < \sim 0.01$ μm is excluded – see section 6), decreasing contribution of coarser particles, and similar absolute concentrations over the part of accumulation mode 0.1–1 μm. The only missing component refers to strong contribution of the local production of coarse aerosols ($D_p > \sim 2$ μm), which are under-estimated. Slight under-estimation of the fine-particle concentrations may indicate too strong removal of sub-micron particles in the model or the impact of aerosol processes. The shape of the fine-particle range of the spectrum has to be clarified further with aerosol dynamic processes taken into account – nucleation

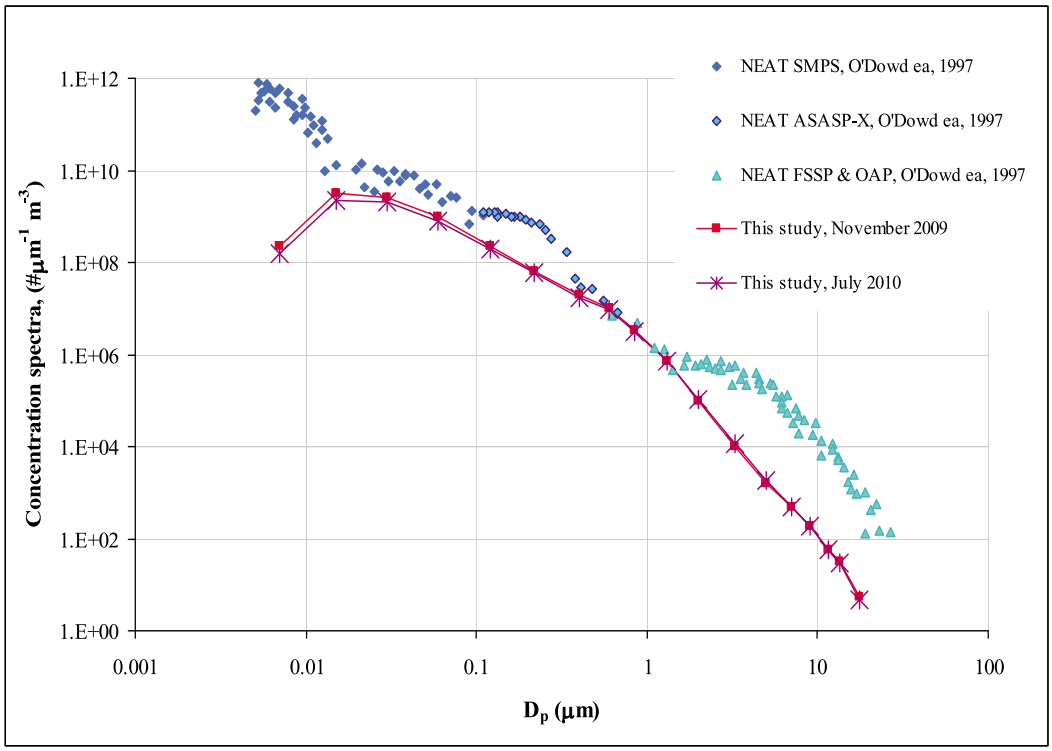

Figure 3. Observed (blue-color dots, mean over NEAT campaign [*O'Dowd et al.*, 1997]) and predicted by SILAM (lines, monthly averages) SSA concentration spectra in the Northeast Atlantic. Unit: [# μm^{-1} m^{-3}], dry size D_p.

in the clean marine atmosphere and coagulation sink for both newly nucleated particles and small sea salt aerosols.

[53] The slight difference between the spectra for November and July shows the impact of seasonal change. Stronger winds in November resulted in higher production of all particles (as well as their deposition), whereas colder temperatures suppressed production of coarse aerosols. As a result, the fine-particle concentration is higher in winter by a few tens of %, whereas the load of the coarse ones stayed the same.

[54] Comparison for the spectra over different parts of the globe is shown in Figure 4. There, four SILAM ranges are presented via their volume-weighted mean D_p. The SSA spectra observed from the cruises in open sea (panels in the upper two rows of the Figure 4) are reproduced well, whereas the coarse fraction is somewhat under-estimated near the coast (lower two rows). The effect is particularly strong in Cape Grim, which spectrum is very heavily dominated by coarse fraction – much more than in other data sets. These are probably originated from local surf-zone.

5.2. Evaluation of the Bulk SSA Mass Concentrations Near the Surface

[55] The bulk SSA mass concentrations computed with SILAM for 2000 and 2007 were compared with in situ data measured at EMEP stations for the same years. Computed and measured annual mean Na^+ concentrations at all available EMEP stations (7 for 2000 and 22 for 2007) are presented as a scatterplot in Figure 5a. A similar scatterplot for the wet deposition is shown in Figure 5b. For the comparison the mass fraction of Na in SSA dry mass was assumed to be 30%. The spatial distributions of several key statistical characteristics can be found in the auxiliary material, for the same two years.[1]

[56] The scatterplots in Figure 5 and the maps of the scores in the auxiliary material show that the predicted annual-mean SSA near-surface concentrations are reproduced very well, while the mean wet deposition is underestimated by about a factor of 3. The sites with wet deposition > 1 mg Na m^{-2} day^{-1} are reproduced poorly whereas the agreement for lower annual deposition is within a factor of ~2. The correlations between the modeled and measured daily concentrations vary widely with the correlation coefficients exceeding 0.5 for several sites (Table 1 and auxiliary material). Note that such correlation coefficient is already approaching the maximum reachable value (about 0.7) between the daily time series [see *Galperin and Sofiev*, 1994].

[57] The comparison of wet deposition time series is complicated due to very high variability of this variable and its dependence on quality of the input precipitation fields. In particular, the uncertainty of its statistics is always larger than a factor of two. As a result the model scores vary strongly between the stations and regions (see auxiliary material).

[1]Auxiliary materials are available in the HTML. doi:10.1029/2011JD014713.

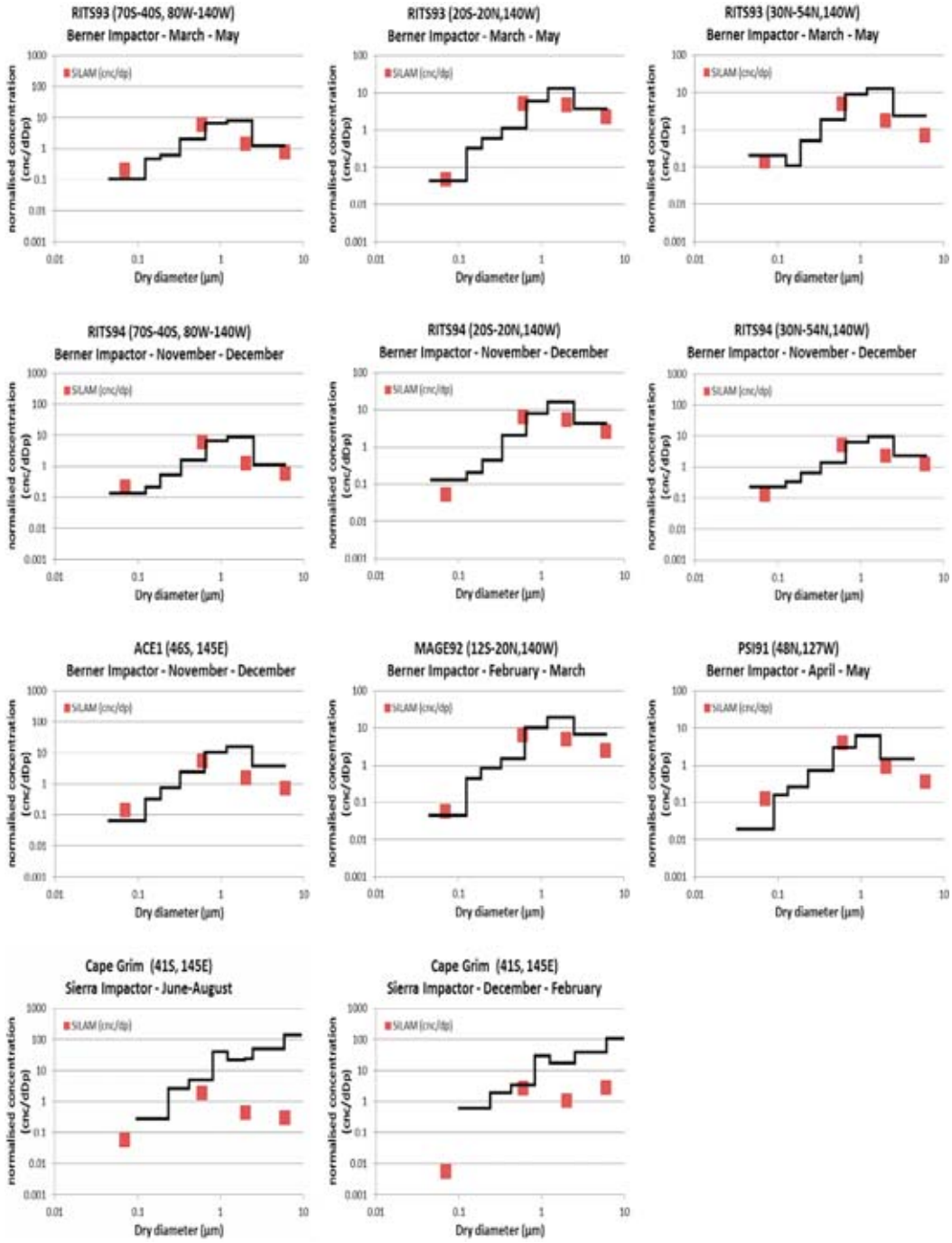

Figure 4. Observed (black lines, extracted from work by *Pierce and Adams* [2006]) and SILAM predicted (red squares) SSA mass concentration over the globe. Modeled values are reported at mass-weighted mean diameters of the four computational bins; see section 3.1. Unit: [μg SSA m^{-3} μm^{-1}], dry size D_p.

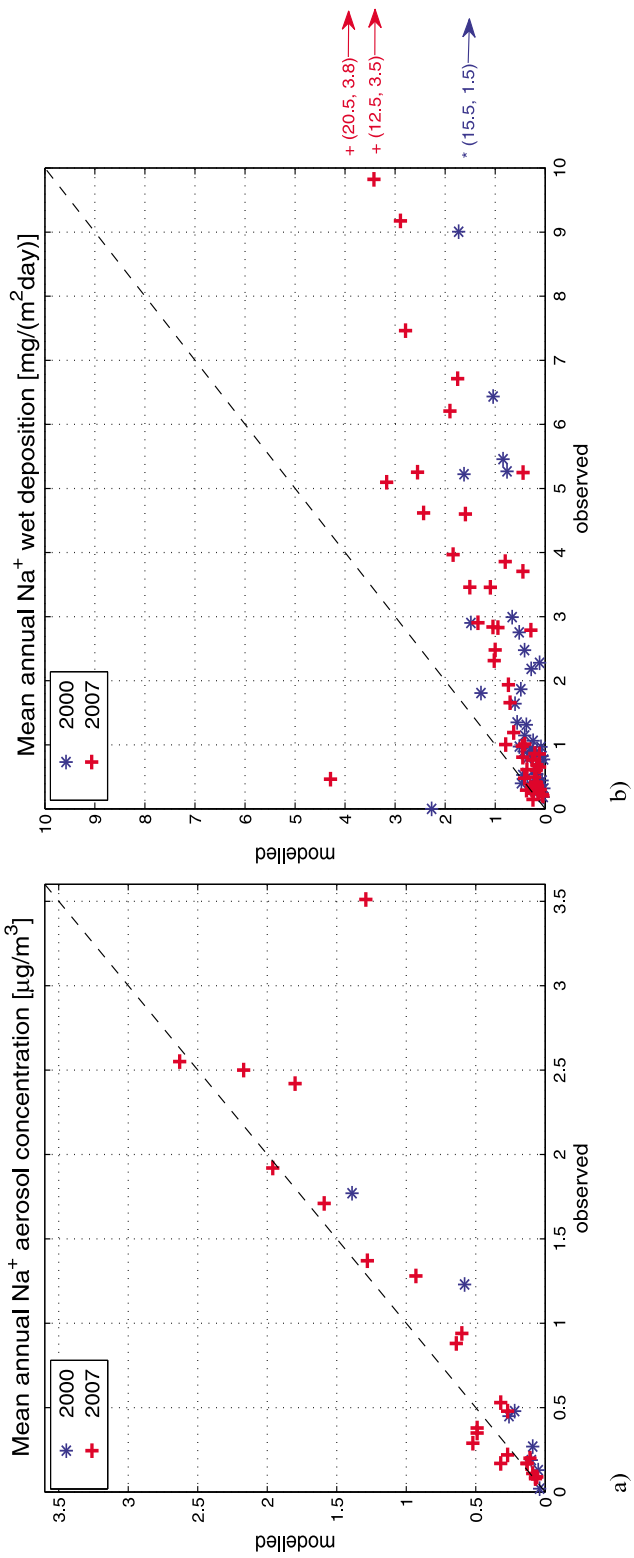

Figure 5. Evaluation of Na^+ concentration and wet deposition versus observations of the EMEP network. (a) Na^+ concentration in aerosol (total PM), mean 2000 and 2007, [μg Na m^{-3}]; (b) Na^+ wet deposition, mean 2000 and 2007, [mg Na m^{-2} day^{-1}]. Dots that fell outside the axes scales are marked by arrows with actual values shown in brackets.

Table 1. Comparison of SILAM Prediction of Na Concentrations in $PM_{2.5}$ and PM_{10} With Observations at the Coastal and Terrestrial Sites in Finland

Site	Substance	Number of Points	Mean Observation	Mean Model	Correlation	RMS
Hyytiala (land)	Na^+ in $PM_{2.5}$	27	0.01	0.04	0.2	0.05
Hyytiala (land)	Na^+ in PM_{10}	27	0.03	0.05	0.51	0.06
Helsinki (coast)	Na^+ in $PM_{2.5}$	107	0.039	0.056	0.1	0.09
Helsinki (coast)	Na^+ in PM_{10}	181	0.080	0.060	0.41	0.12

However, the tendency toward underestimation is visible for practically all stations for both years (but stronger for 2000). The underestimation largely originates from only partly reproduced deposition peaks reported by the observations (see example in Figure 6 for Southern Norway in 2000), which results in too small short-term dynamic range of predicted wet deposition (up to 0.1 g Na^+ m^{-2} day^{-1} instead of observed maximum of almost 1 g Na^+ m^{-2} day^{-1}). The underestimation of the peaks can have several reasons: (i) omission of the surf zone SSA emission and the spume-drop production mechanism, (ii) missing wind gustiness, (iii) SILAM scavenging parameterization may be too conservative for highly hygroscopic aerosols, (iv) under-estimated precipitation amount by the HIRLAM model in 2000 (Figure 6c and auxiliary material Figure A3).

[58] Importantly, the appearance of the precipitation events is well reproduced by the NWP models (Figure 6), i.e., the input information on occurrence of wet deposition episodes is available. The absolute amount of precipitation, however, has little effect on the wet deposition evaluation because even quite small rain removes the bulk of the SSA mass from the column (as these particles are the highly soluble and coarse). Indeed, the improvement in the precipitation data from 2000 (under-estimated, auxiliary material Figure A3) to 2007 (mostly unbiased, auxiliary material Figure A6) somewhat reduced the wet deposition under-estimation but did not eliminate it completely (Figure 5b, auxiliary material Figures A2 and A5).

[59] To evaluate the impact of possibly too conservative SILAM scavenging parameterization, a sensitivity model run over 2007 was arranged with the scavenging rate increased 100-fold. The resulting increase of total monthly wet deposition was from 10 to 15% in winter up to 20% in summer.

[60] Therefore, the limitations of the precipitation information and conservative SILAM scavenging parameterization are contributing but clearly not the main limiting factors, leaving the omitted contribution of the spume-drop production, wind gustiness and the surf zone emission as the primary reasons for the under-estimation.

[61] Considering the seasonal variations, the model showed a close match of both concentrations and wet deposition during summer but a pronounced underestimation during winter time (Figure 6). The latter is expected because the particles with $D_p > 10$ μm are not considered in this study – but they are still generated and can be suspended in air during winter storms, thus contributing to the total mass (also inland). The generation of such large particles occurs not only via the bubble-mediated mechanism considered here but also by direct tearing off the spume droplets from the wave tops at the wind speeds exceeding ~9 ms^{-1} [*Monahan et al.*, 1986; *Andreas*, 1998; LS04]. Also, during the wintertime, the gustiness over the sea surface increases [*Cvitan*, 2003] resulting in enhanced SSA production. Neglecting these processes in the present simulations can lead to significant underestimation of the SSA mass in winter, especially at the near-coast observation sites.

[62] Evaluation of the near-surface concentrations in different parts of the globe was based on the data extracted from the paper of *Pierce and Adams* [2006] - Figure 7. The observational plots were taken "as-is," whereas the SILAM results were summed up to $D_a < 10$ μm. This range probably deviates from the observations [*Guelle et al.*, 2001], which typically cover particles with <10 μm ambient-humidity size, i.e., $D_p < \sim 6$ μm. As follows from Figure 1b, such extension adds about 10–20% to the SSA mass production, which is within the uncertainty of the estimates. Increase of the concentrations is even lower due to high deposition rates of particles with actual diameter exceeding 10 μm.

[63] As seen from Figure 7, the model is capable of reproducing the range of concentrations from ~1μg SSA m^{-3} at Alert and Palmer sites, up to 20–30 SSA μg m^{-3} at Barbados and Bermuda, with intermediate levels shown at e.g., Cheju and Miami. A systematic underestimation is shown for Cape Grim, which has large fraction of coarse aerosols of presumably local origin. However, if compared with the Cape Grim observational results presented by *Gong et al.* [1997], the agreement is substantially better (Figure 7, first row, third panel). The dissimilarity between the measurements can be due to the different years, instruments, and actual positioning of the inlets used for the measurement campaigns, Both sources mention PM_{10} as the analyzed quantity.

[64] The seasonality is mostly dependent on the input wind speed, which seem to be reproduced at most of the sites. Large problems are seen only at Mace Head and Helmaey, i.e., in the Northern Atlantic, where winter maxima are not captured – similar to the above EMEP-based comparison.

[65] In comparison with results of *Pierce and Adams* [2006] for individual schemes (M86, M03, SEAS), the current model is in much better agreement at the tropical sites and shows similar performance in other parts of the globe. As shown in the sensitivity tests in section 6, the eliminated underestimation of SSA in tropics is largely attributed to actual SST included in the new parameterization.

5.3. Evaluation of SSA-Induced AOD

[66] The global distribution of the SSA contribution to the AOD was computed with SILAM for 2001 and 2008 and compared with AOD provided by the MODIS instruments onboard the NASA satellites Aqua and Terra (Collection 5: for level-2 data http://modis.gsfc.nasa.gov, for averaged values http://disc.sci.gsfc.nasa.gov/giovanni) (Figure 8). The comparison required pre-processing of both MODIS data and SILAM output. First, the cloud contamination of the MODIS level-2 data [*J. Zhang et al.*, 2005; *Remer et al.*, 2008] was reduced by removing pixels with AOD > 1 (see *Levy et al.* [2009] for more sophisticated approach). Then the frames

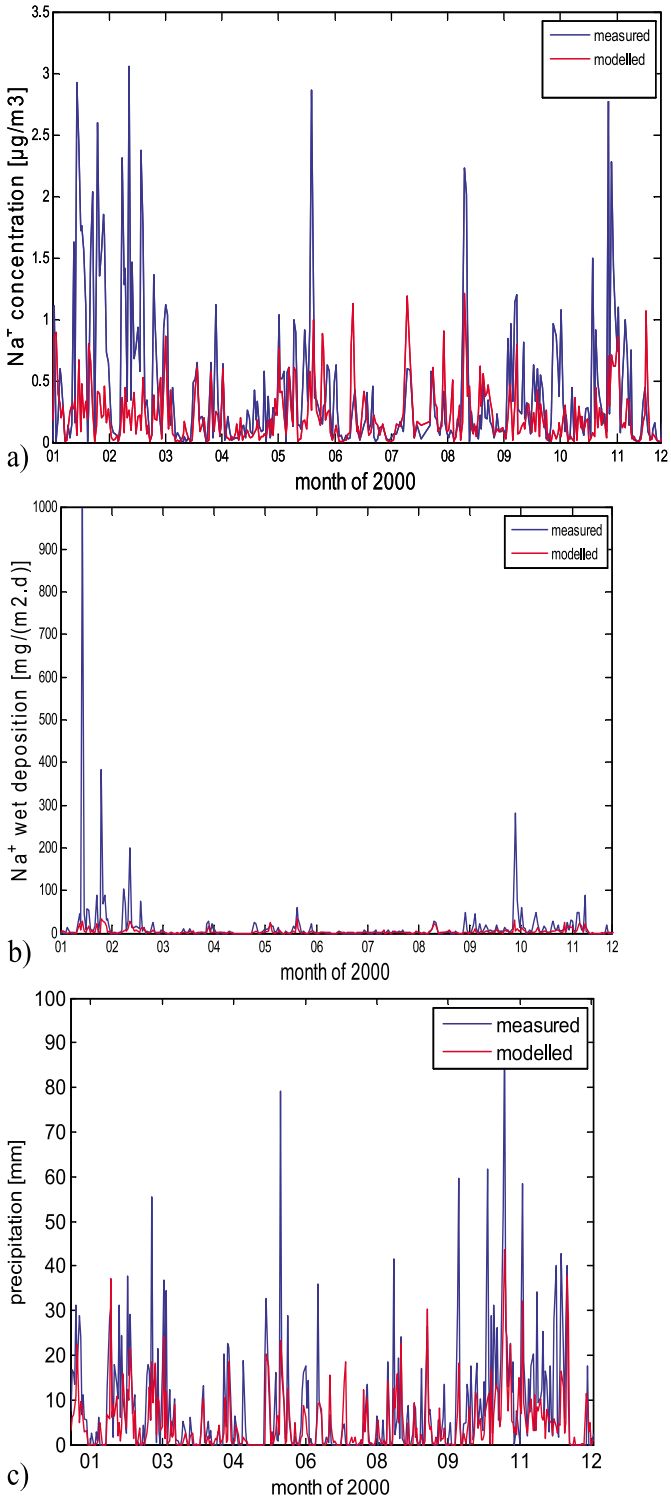

Figure 6. Examples of comparison of SILAM simulations for 2000 with EMEP measurement station NO0008r (Skreådalen, Southern Norway, ~60 km from the coast line). (a) Na^+ concentration in aerosol (total PM) [μg Na m^{-3}], (b) Na^+ wet deposition [mg Na m^{-2} day $^{-1}$], and (c) daily precipitation amount [mm day^{-1}] observed at the site and obtained from the HIRLAM NWP model.

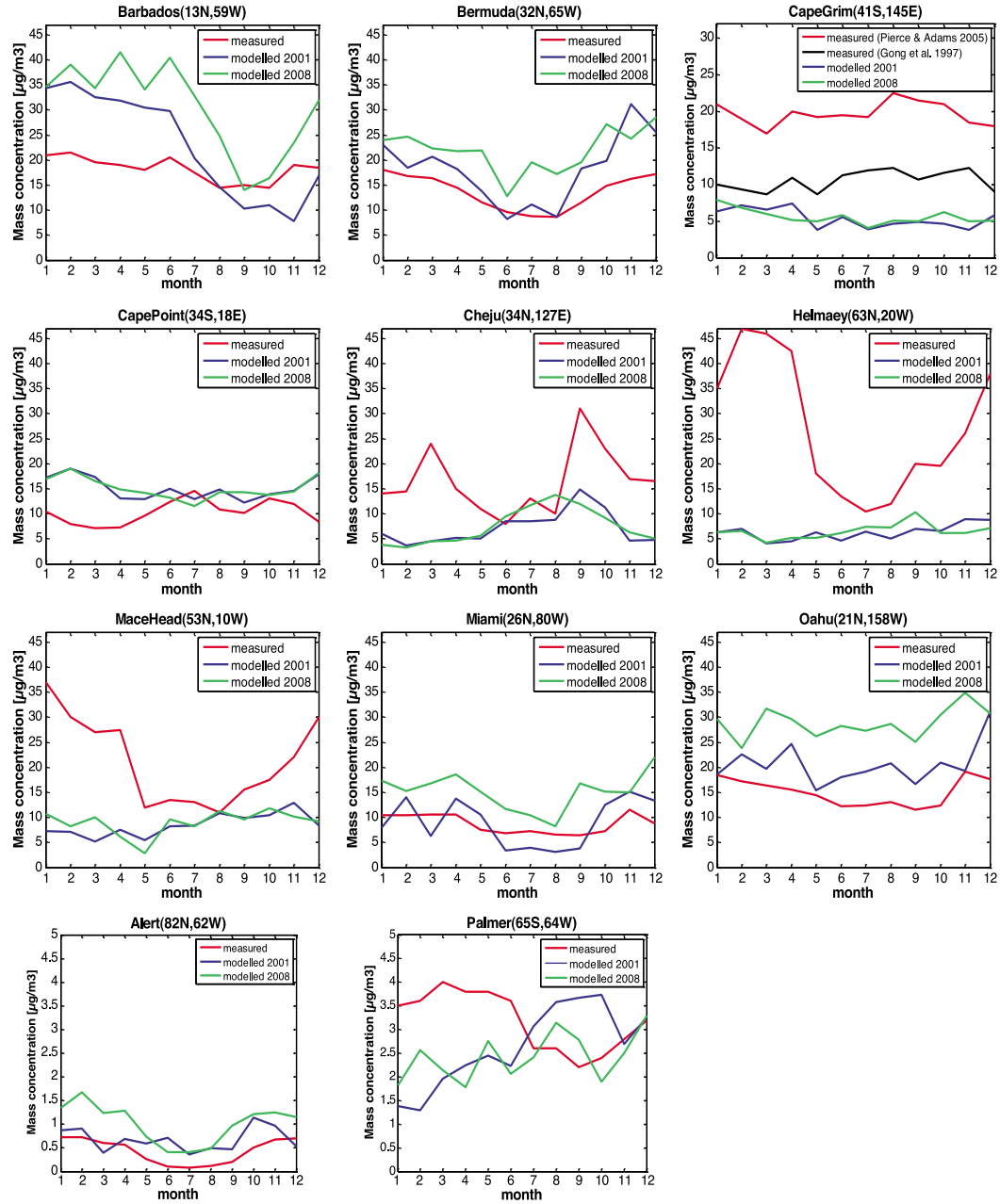

Figure 7. Observed (red lines extracted from work by *Pierce and Adams* [2006], black from work by *Gong et al.* [1997]) and SILAM-predicted (blue lines for 2001, green for 2008, $D_p < 10$ μm) SSA mean monthly mass concentration at several sites over the globe. Locations are shown in each panel, data are averaged for each month over the whole period of the observations at each site. Unit: [μg SSA m^{-3}].

were projected to the SILAM grid, aggregated for each hour, and the AOD observations falling into the same SILAM grid cells were averaged. Second, for each hour the SILAM output has been picked only for the grid cells where the MODIS information is available. These two steps ensured the maximum possible co-location of the observations and model results both in space and in time.

[67] Co-locating the data sets, however, is not enough: the MODIS AOD includes the contribution of aerosols of all types and origin, while the SILAM computations include only SSA. Hence the comparison was restricted to the areas where the SSA load is dominant, i.e., where the AOD is least influenced by non-sea-salt aerosols. These are the oceanic regions at the midlatitudes in the Southern Hemisphere, the

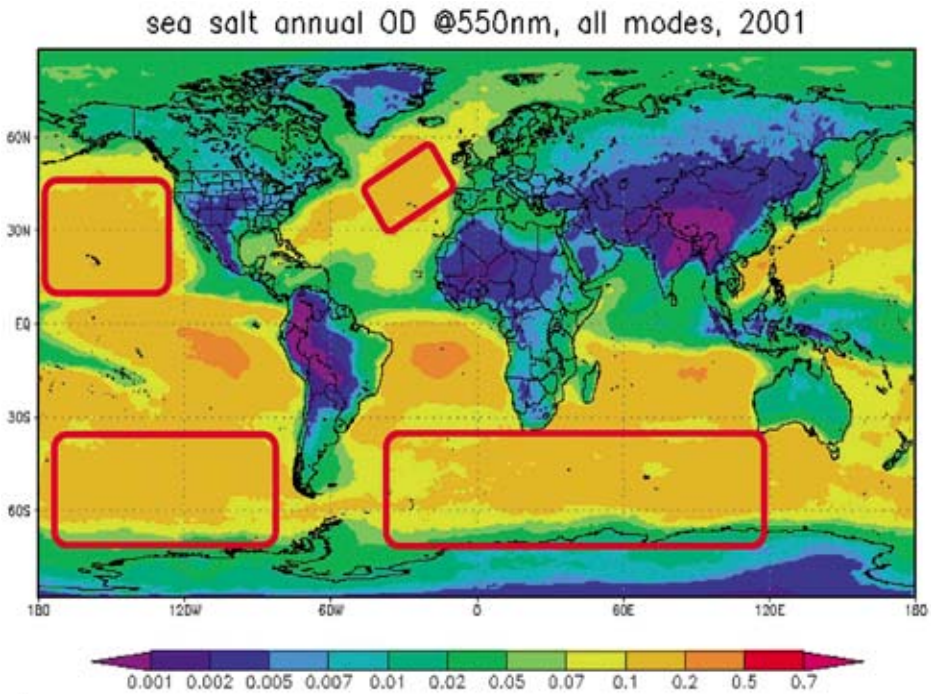

a)

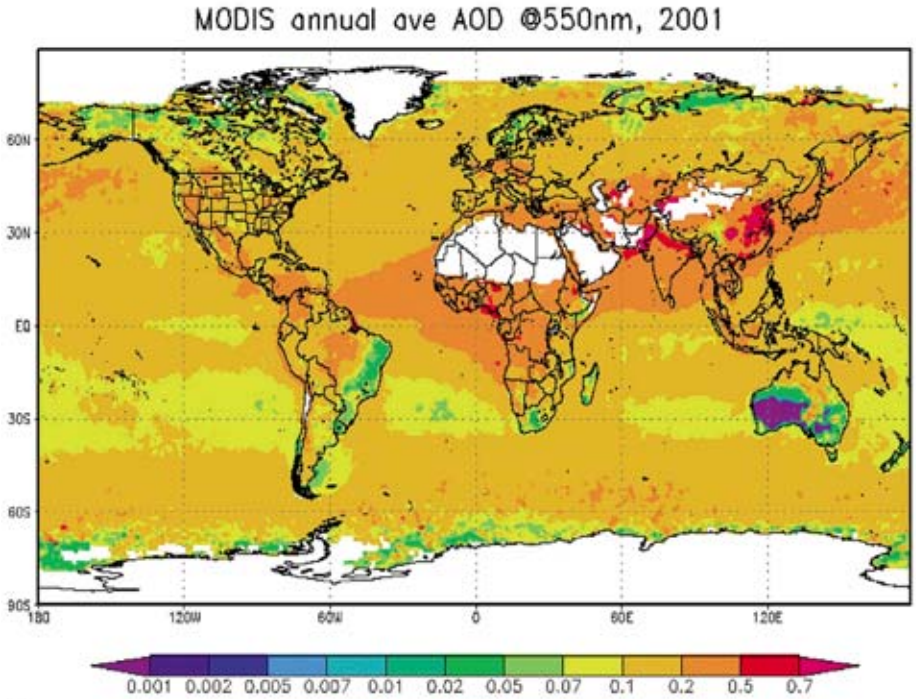

b)

Figure 8. Mean AOD for 2001: (a) SILAM predicted AOD due to SSA only, co-located with MODIS data; (b) AOD due to all aerosol types observed by MODIS (http://disc.sci.gsfc.nasa.gov/giovanni). Red rectangles show the SSA-dominated areas where AOD from MODIS can be compared with SSA-only SILAM AOD.

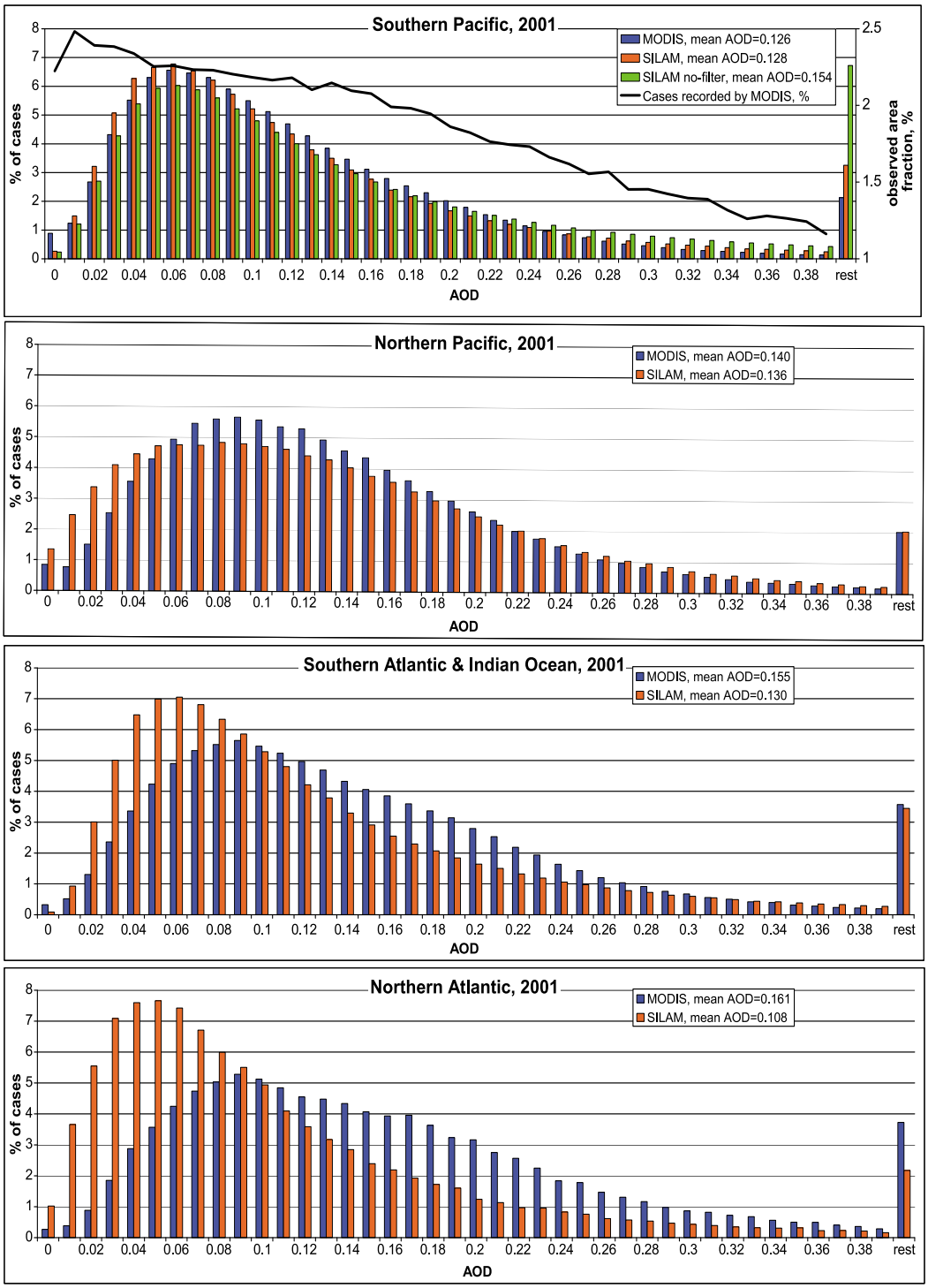

Figure 9. AOD normalized histograms for selected regions. (first panel) Co-located SILAM (red bars) and MODIS (blue bars) data; green bars: unfiltered SILAM AOD with all model data for the region regardless of MODIS availability; black line (right-hand axis): a fraction of SILAM cells observed by MODIS for each AOD range. (second through fourth panels) Co-located SILAM (red) and MODIS (blue) sets. All cases with AOD > 0.4 are summed-up in the "rest" range at the right-hand-side of the x-axes.

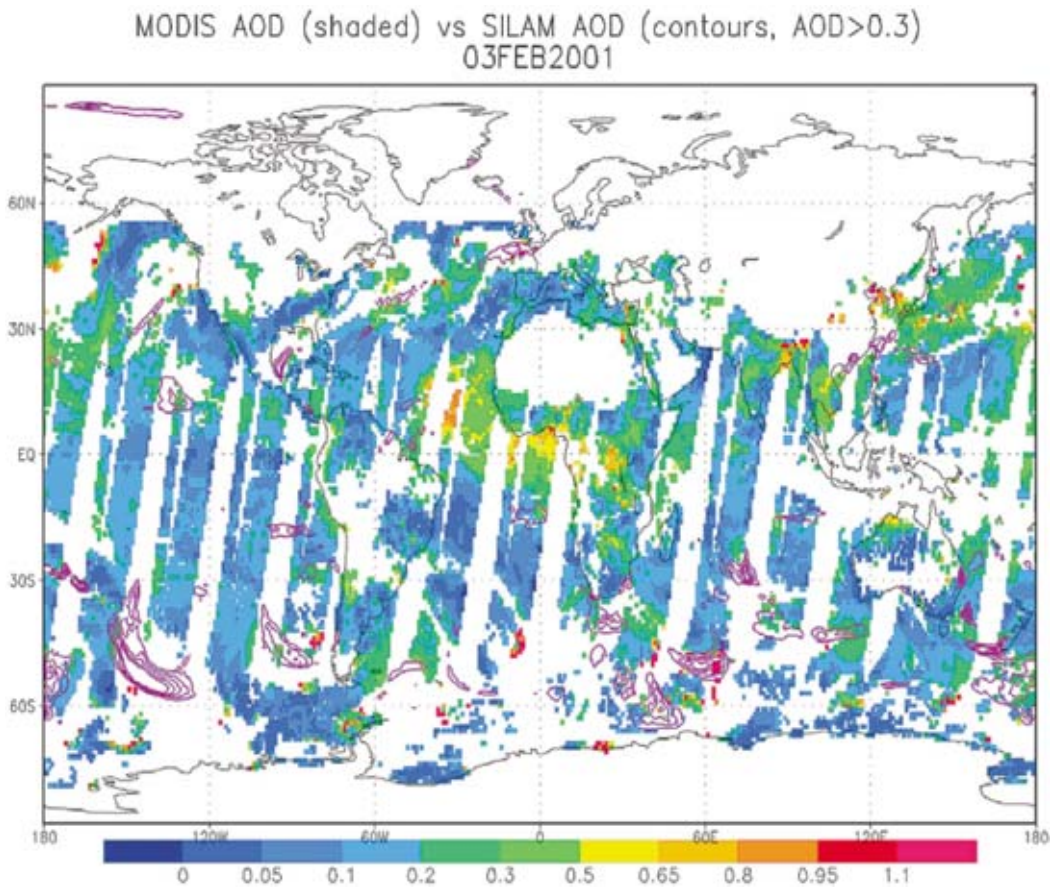

Figure 10. Missing AOD observations over high-SSA regions due to clouds. Color shades: daily mean MODIS AOD. Contours: SILAM-predicted AOD > = 0.3 (distance between the contour lines $\Delta_{AOD} = 0.05$).

central part of the North Atlantic and the North-Eastern part of the Pacific Ocean. These areas are encircled in Figure 8a.

[68] The comparison of the annual-mean co-located SILAM and MODIS AOD patterns shows that in the indicated SSA-dominated regions their difference from each other is within 20–40% of the observed values (example in Figure 8 for 2001). In particular, a high-SSA pattern in the Southern Hemisphere (latitude belt of 40S-60S) is well captured: high AOD is predicted at the same latitudes, and its mean level inside the belt is within 20–30% of the observed values. The observed MODIS AOD reaches up to 0.2, with a weak and very wide peak around 60S. Likewise, SILAM predicts AOD close to 0.2 over the same region.

[69] Consideration of the AOD maps in Figure 8 and histograms in Figure 9 shows that the regions least affected by the contribution from terrestrial aerosol sources are the Southern and Northern Pacific Ocean. There, the MODIS and SILAM AOD histograms are very similar and the mean-AOD difference is less than 2%. The difference between the two considered years does not exceed 10–15% in any specific histogram range (not shown). The impact of non-SS aerosol on the AOD over the Northern Atlantic and parts of the Southern Atlantic and the Indian Oceans is noticeable from the shift of the predicted SSA-only histograms to the lower AOD values as compared to MODIS.

[70] A specific source of uncertainty of the visible-range optical instruments is that they cannot retrieve AOD through dense clouds and tend to over-estimate the AOD at the edge of cloudy areas [*J. Zhang et al.*, 2005; *Remer et al.*, 2008]. The latter can be reduced but missing areas had to be excluded from the comparison. It is illustrated in Figure 10 where the areas of high SSA concentrations predicted by SILAM correlate strongly with the missing-data parts of the MODIS frames. The reason is the correlation of the SSA emission with storms and cyclones accompanied with dense clouds. To quantify the effect, we compared the SILAM AOD histograms with and without MODIS-based screening (Figure 9, first panel). As one can see, the mean regional AOD without MODIS-based screening is higher by almost 20% than the value obtained from the co-located data. Also, the fraction of cases of each specific AOD range recorded by MODIS is not uniform over the histogram but rather demonstrates a strong anti-correlation with AOD: it falls from about 2% for low-AOD cases to about 1% for AOD ~ 0.3.

[71] Despite the difficulty with high-AOD regions, the comparison of predicted and observed AOD in the cloud-free areas (i.e., largely outside the high-SSA zones) still provides sufficient amount of information for the model evaluation. But for studies solely based on the satellite AOD data, especially averaged over long time periods, the missing high-SSA data may lead to significant bias toward smaller AOD.

[72] Apart from the histogram and annual maps analyses, a time-resolving comparison of AODs was performed for all four regions marked in Figure 8 to highlight the model ability to reproduce the temporal dynamics of the SSA load (driven by wind rather than slowly varying water temperature). In agreement with the histograms in Figure 9, both SILAM and MODIS data were centered around the AOD ~0.07–0.1. For the Southern Pacific over 90% of the predictions are within the factor of 2 from the observations. The other regions show both somewhat worse correlation of the observed and predicted episodes and, where the non-SSA impact is significant, systematic low bias (Atlantic and part of Indian Ocean). The strongest impact of non-SS aerosols is in Northern Atlantic where the under-estimation reaches ~40% (also seen in Figure 8).

6. Discussion

6.1. Small Particles Over Sea

[73] The current SSA source function is derived for the SSA particles with D_p between 0.01 and 10 μm and its shape function (6) for the number flux peaks at D_p about 0.03 μm. However, the suggested shape function falls toward 0.01 μm somewhat faster than that of SEAS (Figure 1a). There are no direct observations of SSA below 0.01 μm but recent high-resolution general-aerosol measurements in the marine boundary layer suggest that the main origin of smaller particles is nucleation [*Vana et al.*, 2008]. The suggested shape function (6) takes it into account by reducing the production flux toward 0.01 μm but the uncertainty is evidently large. For the temperature and salinity correction factors, the M03 data set seems to suggest some leveling of the trends or at least an increase of uncertainty for 0.02–0.03 μm particles (Figure 2), whereas the limited number of observations around 0.02 μm is not sufficient for quantitative analysis. Therefore, the extrapolation of the temperature and salinity corrections to $D_p < 0.02$ μm involves large uncertainties.

[74] A source of small non-SSA particles, which can affect the AOD observations, is the DMS emission followed by oxidation and generation of sulphate aerosol in the free troposphere (FT) [*Charlson et al.*, 1987; *Korhonen et al.*, 2008]. This contribution is substantial over biologically active areas but has strong seasonality: it is practically negligible in winter while in summer up to 50% of cloud condensation nuclei can originate from DMS. At annual averaging, the DMS contribution to aerosols over open-ocean areas is likely to stay within 10–30% of the total number concentrations. Since the DMS-originating particles are formed by nucleation and grow up to CCN size (D_p~0.1 μm), they will contribute to the corresponding spectrum ranges (however, the details of the spectrum modification are very uncertain). This addition to the SILAM-predicted fields may result in some over-estimation of AOD over the Southern Pacific but it also partly explains the under-estimation over other regions (Figure 9).

6.2. Influence of Sea Surface Temperature

[75] The production term strongly depends on the sea surface temperature T_w. As seen from the correction functions (7) and Figure 2a, the effect of T_w differs for different particle sizes, which can originate from the differences between the production mechanisms [*Woodcock*, 1972; *Monahan et al.*, 1986; *Fitzgerald*, 1991; *O'Dowd et al.*, 1997]. The fine particles are mainly produced from the film droplets whereas the coarse ones are mainly produced from the jet droplets. The M03 observations suggest that these processes have different temperature dependence: with decreasing water temperatures the film-droplet production increases while the jet-droplet production decreases. Both trends seem to be persistent: the 15°C production is an intermediate between the ones at 25°C and near zero (Figure 2a). Qualitatively, these observations can be connected with the smooth and monotonic decrease of water viscosity with increasing temperature (the surface tension varies by < 10% for the environmentally relevant temperatures and thus cannot explain the strong dependence): the kinematic viscosity falls from $1.8 \cdot 10^{-6}$ m^2 sec^{-1} at 0°C down to $0.9 \cdot 10^{-6}$ m^{2}sec^{-1} at 25°C [*Mostafa et al.*, 2010]. Based on the above observations, one can argue that the jet-droplets production is reduced in more viscous water while the film-droplets production is enhanced.

[76] To illustrate the impact of T_w on the SILAM simulations, the global model run over 2001 was repeated with the fixed T_w = 15°C. The comparison of this sensitivity run with the basic simulations with the actual T_w is shown in Figure 11a (basic run with the actual T_w, panel b: for T_w = 15°C).

[77] The base run showed the highest SSA concentrations at tropical and middle latitudes (0–50 degrees north and south). In the "roaring 40s," particularly over the Southern Hemisphere, the wind speeds are higher than in other regions and thus the enhanced SSA concentrations are due to wind speed induced production. In tropical regions, however, it is the warm water that leads to enhanced SSA production. Indeed, the results of the sensitivity run (Figure 11b) show that the SSA concentration in tropical regions is much higher if the actual water surface temperature is used. In the polar areas the effect is opposite: the concentrations are lower in the actual-temperature run. Finally, the overall sea salt mass production over the globe is about 1.5 times larger if the actual T_w is considered, with the bulk of the mass emitted in the warm regions.

[78] The simulations also show that AOD is somewhat less sensitive to T_w than the surface concentrations due to the larger contribution from sub-micron particles, for which the water temperature effect is less strong than for coarser particles mainly contributing to the SSA mass. Still, disregarding the actual T_w jeopardizes the agreement with MODIS observations. Comparing the AOD histograms for the sensitivity run in Figure 12 (fixed T_w) with the base run results in Figure 9 (actual T_w), one can see that the sensitivity simulations agree much worse with the observed AOD. Thus, near the tropics (Northern Pacific region, the actual T_w is higher than 15°C) the region-mean AOD of the sensitivity run is lower than the observations by nearly a factor of 2, while near the Antarctic (the real T_w is colder than 15°C) it is higher by 10–20%.

6.3. Influence of Water Salinity

[79] The physical ground of the water salinity impact on the SSA spectrum and production flux is quite straightforward:

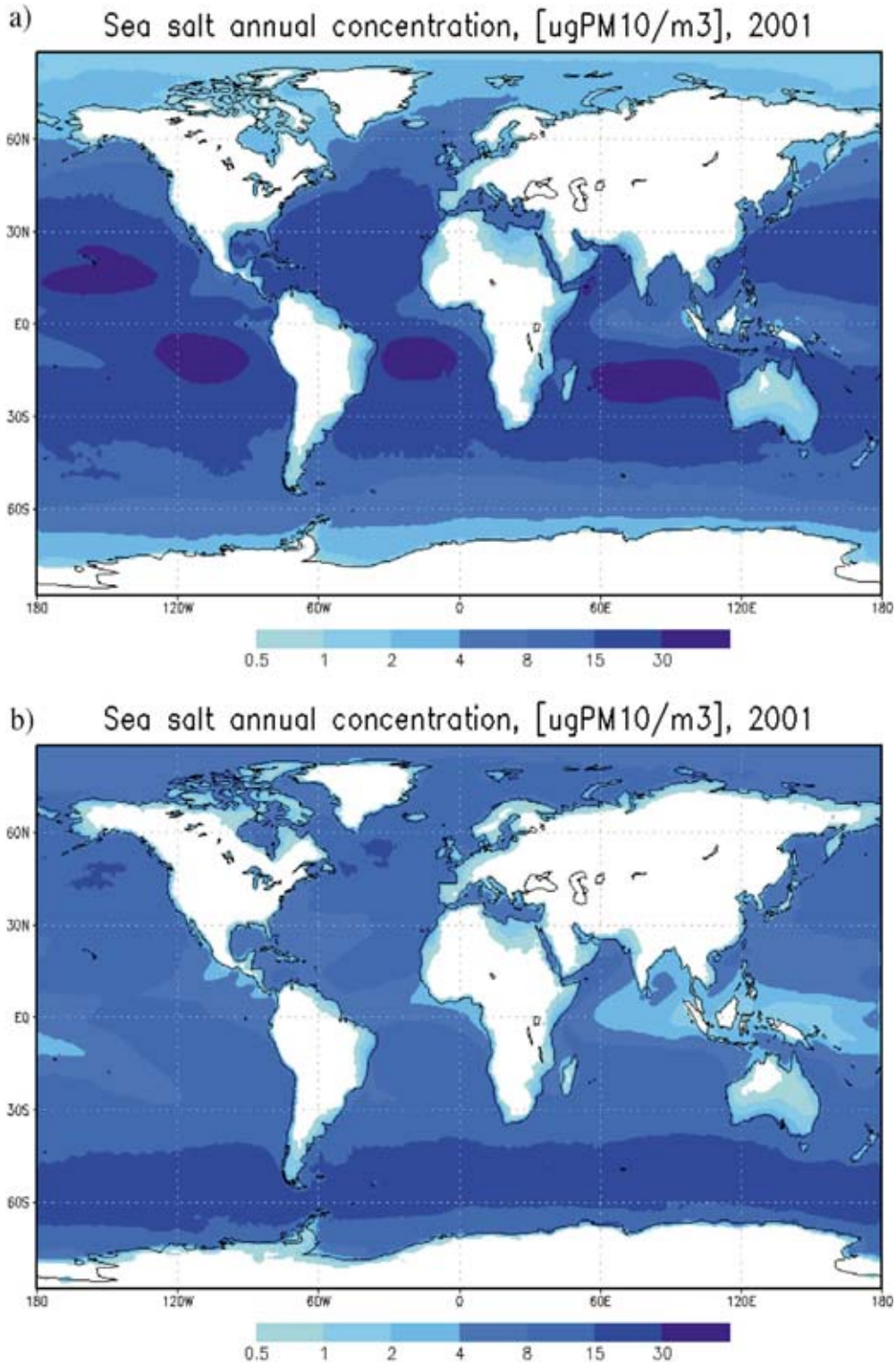

Figure 11. SSA near-surface concentrations ($D_p < 10\ \mu$m) for (a) simulations with the actual sea surface temperature T_w and (b) the run with fixed $T_w = 15$°C. Mean over 2001. Unit: [μg SSA m^{-3}].

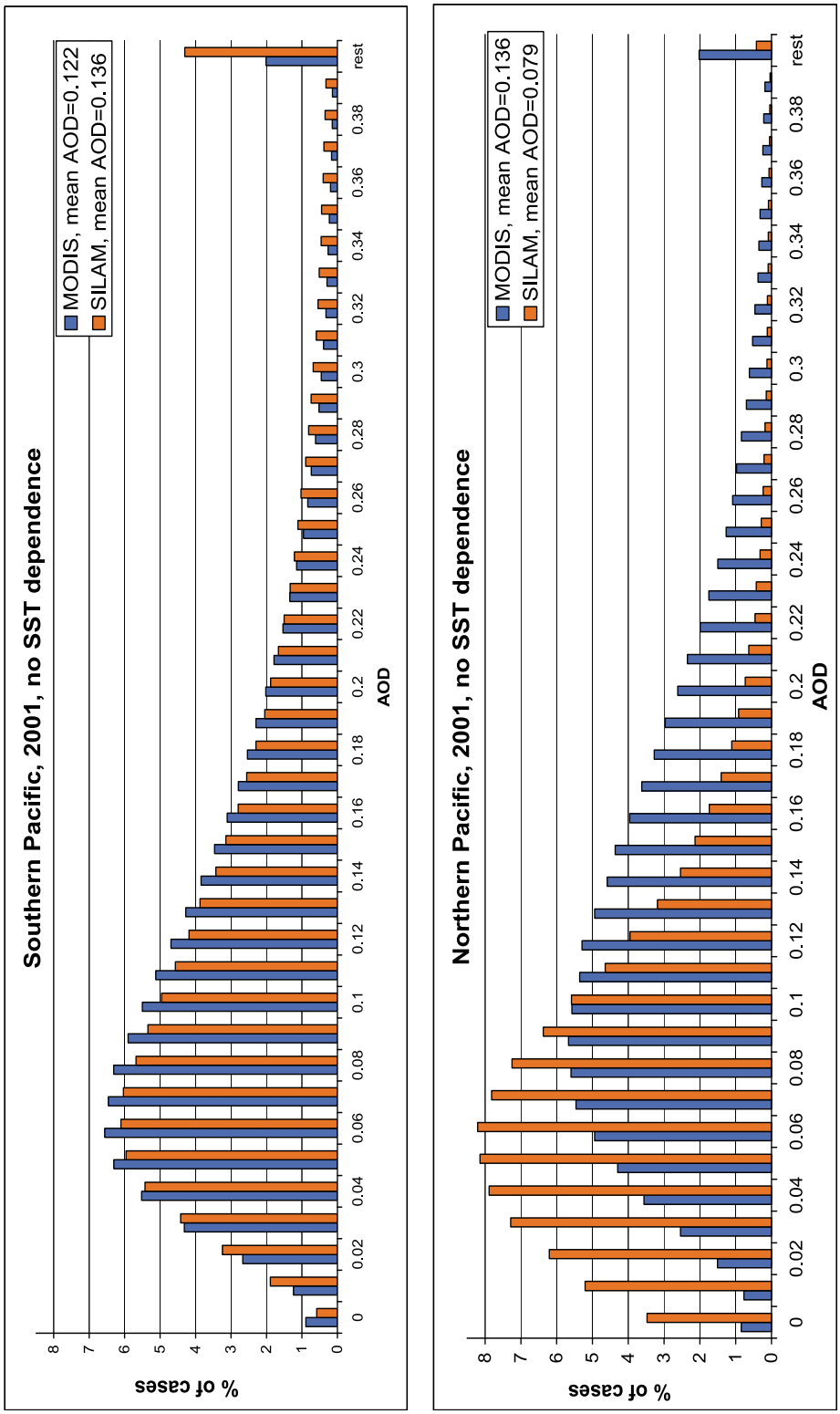

Figure 12. Normalized AOD histograms for SSA-dominated regions for the 2001 simulations, co-located SILAM and MODIS sets, fixed $T_w = 15°C$. (top) Southern Pacific. (bottom) Northern Pacific.

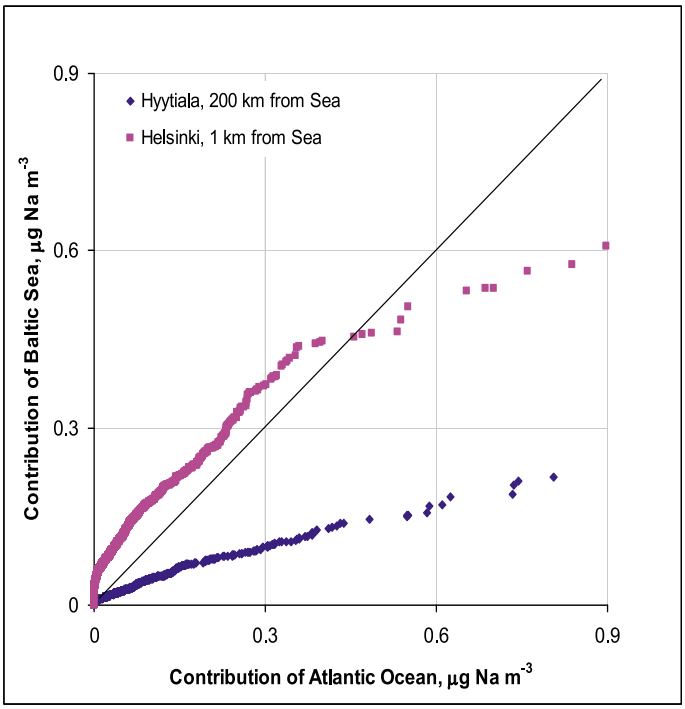

Figure 13. Predicted impact of Atlantic Ocean and Baltic Sea on Fennoscandia: quantile chart for the Na^+ concentrations originated from Baltic Sea versus those originated from Atlantic Ocean. Plots for Helsinki (southern coast of Finland) and Hyytiälä (~150 km inland). Unit: μg Na^+ m^{-3}.

lower salinity results in smaller size of the particles after water evaporates from droplets. Since coarser particles are produced in fewer numbers, the overall production decreases. However, this effect is very difficult to verify due to the small salinity variations across the World's oceans, except for local seas, such as Baltic Sea. On the other hand, its importance for the corresponding regions is evidently very large. The salinity correction functions (8) and Figure 2b indicate that, for the same wind speed and water temperature, the aerosol emission at the Baltic Sea would produce approximately ten times less SSA mass per unit area than at the open ocean. As an illustration, in the SILAM simulations for 2009 and 2010 the SSA production from the Baltic Sea area was separated from that of the Atlantic Ocean. As seen from Figure 13, the contribution of the Baltic Sea emission to the SSA concentration even at the sea coast is about the same as that of the Atlantic Ocean. Further inland, the Atlantic Ocean SSA fraction is clearly over 50%. Without the salinity correction, the resulting SSA concentration at the Baltic coast would be 5–10 times higher in the SILAM runs.

[80] The credibility of the above model-based conclusions can be verified only indirectly – via model-measurement comparison for the region. A series of campaigns in Hyytiälä (~150 km east of the Bothnian Bay, ~200 km north of the Gulf of Finland) and Helsinki (southern coast of Finland) provided 9 months of observations of Na^+ in aerosol during 2009 and 2010. The main parameter for comparison was Na^+ concentration in PM_{10} with limited data for Na in $PM_{2.5}$. We assumed that sodium is entirely from sea salt and summed-up the corresponding model size bins to obtain the predictions. The comparison (Table 1) showed that: (i) the model captured well the concentration of Na^+ in aerosol, especially for the coarse fraction – the scores are similar to those for the European measurements shown in section 5.2 (those sites are practically not affected by Baltic Sea); (ii) there is a tendency of over-estimation of the fine fraction; (iii) correlation of daily time series for Na^+ in PM_{10} is quite good.

[81] The comparison also showed that the 10-fold reduced contribution of the Baltic Sea to SSA concentrations due to its low salinity is a step in the right direction. Otherwise the model over-estimation at Hyytiälä would be very large and strongly differing from the model scores at the European sites (section 5.2). There can be, of course, other model parameters affecting the comparison – e.g., the scavenging parameterization or the vertical profile accuracy. However, they affect the model comparison at all sites and thus cannot cover this 10-fold jump. The only place-specific factor refers to the missing surf zone emission in the Helsinki archipelago, which probably caused the under-estimation of the concentrations and low correlation at that coastal site (Helsinki is the only coastal site in the data set).

6.4. The SSA Budget Predicted by the SILAM Simulations

[82] The global budget of SSA includes three terms: production flux, dry deposition, and wet deposition. Their relations strongly depend on particle size and vary from region to region, depending on meteorological conditions. They also depend on implementation of the source term – especially dry deposition is sensitive to the vertical injection profile.

Table 2. Main Parameters of the SILAM-Predicted SSA Budget for 2001[a]

Bin, μm	Mass in Air (%)	Dry Deposition (%)	Wet Deposition (%)	Lifetime (days)
0.01–0.1	1.04	41	57	3.8
0.1–1	1.57	25	73	5.7
1–2.5	0.83	57	42	3.0
2.5–10	0.36	76	23	1.3

[a]The relative values are normalized with the annual SSA emission in the corresponding size ranges.

[83] The suggested parameterization uses the observations made at different heights above the water surface and assumes that the corresponding parameterizations (M86, M03, SEAS) are representative for the effective emission flux at 10 m height. However, formal application of the above source term in the model leads to mixing of the SSA over the first layer (for regional and global models, often 50–100 m thick) within one model time step. For the current simulations, the first model layer was 50 m thick and the model time step was 15 min. As shown in section 2.9 of LS04, this mixing does not lead to excessive errors for particles with $D_p < 20$ μm.

[84] Being released from a near-surface wide-area source, a substantial fraction of the SSA mass is removed from the air shortly after the release before it gets mixed throughout the boundary layer – the process formally attributed to dry deposition (see discussion in chapter 2 of LS04). Consequently, the comparison of the SILAM-predicted dry and wet deposition shows that the dry deposition flux, together with sedimentation, contributes more than 50% to the removal, being especially large for coarse particles. Wet deposition becomes dominant in all size classes only outside the source areas. This conclusion is in line with estimates of the atmospheric life time with regard to these processes summarized in Chapter 2, Table 8 of LS04.

[85] Comparison of the SILAM-computed SSA concentrations with those computed by, e.g., *Gong et al.* [1997] and *Grini et al.* [2002] shows that the spatial distributions are similar. In terms of the total production and loss budget, SILAM predicted a global SSA emission of 6700 Tg yr^{-1} in 2001 and 7400 Tg yr^{-1} in 2008, which is within the range of other global sea salt flux estimates: *Petrenchuck* [1980] estimated it as 1000 Tg yr^{-1}, *Gong et al.* [1997] 11700 Tg yr^{-1}, *Tegen et al.* [1997] 5900 Tg yr^{-1}, *Takemura et al.* [2000] 3300 Tg yr^{-1}, and *Grini et al.* [2002] 6500 Tg yr^{-1}. More estimates can be found in the review of *Textor et al.* [2006], who showed a range from less than 2000 Tg yr^{-1} up to more than 20000 Tg yr^{-1}.

[86] The bulk features of the SSA budget (Table 2) qualitatively agree with the values reported by *Pierce and Adams* [2006] from the computations of the GCM GISS, which was tried with all emission schemes used in the current study: M86, M03, and SEAS. The wet deposition is somewhat weaker in SILAM computations: its ratio to dry deposition varies from 3 for sub-micron particles to 0.3 for the coarse ones. Pierce and Adams's computations showed the max value up to 10 or even more for some parameterizations. The life time of the particles was somewhat shorter in those simulations: less than a day for coarse particles and less than 3 days for fine particles. However, the budget details, especially the SSA life time, should be considered only as very crude estimates where an agreement within a factor of 2 has to be compared with an order-of-magnitude uncertainty in the emission fluxes if the meteorological model is changed [*Pierce and Adams*, 2006]. Large uncertainties of these details are also stressed by LS04 (their section 2.7).

[87] Corrections to the SILAM budget could originate from several sources. The current simulations do not include the contribution of the spume particles. Their size is large and atmospheric life time is short, which makes them not very important for large-scale dispersion, but they still contribute to the mass budget. A mild increase can also be expected if the wind gustiness is taken into account. Therefore, the above budget is likely to increase if these additional sources are taken into account.

[88] The simulations for the North Atlantic show that the main contribution to the sea salt mass in the atmosphere comes from particles in the 1 μm–10 μm size ranges with coarse particles dominating the mass in the lower troposphere: stronger mass emission flux (Figure 1b) outweighs their shorter atmospheric lifetime. However, the sub-micron particles dominate the number concentration – both due to the stronger production (Figure 1b) and the longer atmospheric life time. This is in agreement with other modeling studies [e.g., *Gong et al.*, 1997; *Gong*, 2003] and reflects the generally accepted estimates that super-micron particles contribute about 95% of aerosol mass, but only 5–10% of number concentrations in the marine boundary layer [*Fitzgerald*, 1991; *Seinfeld and Pandis*, 2006; LS04].

[89] The comparison of near-surface mass concentrations and AOD maps reveals both similarities and differences in their spatial patterns. The mass concentration decreases with growing distance from the sea and becomes negligible at a few hundreds of kilometers inland from the coast (Figure 11a). A qualitatively similar pattern is observed in the AOD (Figure 8a) but the gradient is smaller: whereas the near-surface concentrations (Figure 11a) drop by a factor of 10–100, the AOD decreases by less than a factor of 10. This model-predicted effect can also be seen from the AOD observations: e.g., at the eastern coast of South America the background AOD over land at ~500 km inland is only 6–10 times lower than that over the adjacent areas of South Atlantic at ~500 km offshore. This is to be expected since: (i) the sub-micron particles can be transported far inland with minor removal, (ii) the aerosol surface emission flux is the largest in the sub-micron range (Figure 1b) and the AOD is proportional to the particle surface area, (iii) the particles that have reached the free troposphere also can be brought inland thus contributing to AOD but not to surface concentrations, (iv) once the air parcel is away from the surface source of SSA (i.e., over land), the dry deposition quickly depletes the SSA mass in the lowest layer but not the upper ones, which would take longer time to deposit.

7. Conclusions

[90] The presented sea salt emission parameterization combines several independent approaches and data sets. It takes into account the effects of wind speed, water salinity, and water temperature. The source function is applicable to SSA particles with dry diameters between 0.01 and 10 μm,

low-to-moderate wind speeds, water salinity ranging from 0‰ to 33‰ and water temperature ranging from −2°C to 25°C.

[91] The parameterization has been implemented in the modeling system SILAM and the system was used to simulate the sea salt concentrations for Europe and adjacent seas for the years 2000, 2003, 2007, 2009, and 2010, and for the whole globe for 2001 and 2008.

[92] Model evaluation against several campaigns, long-term in situ (for 2000, 2007, part of 2009 and 2010) and remote-sensing data (2001 and 2008) showed that: (i) predicted AOD is very close to the MODIS-observed AOD for the areas where it is dominated by SSA, (ii) mass concentrations and wet deposition flux are well reproduced during the summer whereas they are under-estimated during winter in the Northern Atlantic, whereas in the other parts of the globe the seasonality is captured better, (iii) over the globe, the SSA spectrum is reproduced well, except for the coarse part, which is somewhat under-estimated. The under-estimation can be mainly attributed to the omission of the spume production mechanism from the current study. For wet deposition, the conservative scavenging parameterization in SILAM system and inaccuracies of the input precipitation information also played a role. Additional uncertainty was introduced by extrapolation of the water surface temperature and salinity corrections toward the particles larger than 6 μm.

[93] The global emission of SSA in 2001 and 2008 was estimated as 6700 and 7400 Tg yr^{-1}, respectively, which is in the range of estimates provided by other models (1000–20000 Tg yr^{-1}).

[94] Further efforts for the scheme refinement should address the coarse particle size ranges and the spume production mechanism.

[95] **Acknowledgments.** The study has been performed within the EU-GEMS project. The support of the Maj and Tor Nessling Foundation, Estonian Science Foundation (project SF180038s08), Academy of Finland (IS4FIRES project), and COST-ES0602 are kindly acknowledged. Help of J. Hakkarainen, J. Vira, and R. Kouznetsov with the data processing is appreciated. We also would like to thank anonymous reviewers for the extensive comments, which led to substantial improvement of the manuscript.

References

Andreas, E. L. (1998), A new sea spray generation function for wind speeds up to 32 m s^{-1}, *J. Phys. Oceanogr.*, *28*, 2175–2184, doi:10.1175/1520-0485(1998)028<2175:ANSSGF>2.0.CO;2.

Andreas, E. L., J. B. Edson, E. C. Monahan, M. P. Rouault, and S. D. Smith (1995), The spray contribution to net evaporation from the sea: A review of recent progress, *Boundary Layer Meteorol.*, *72*(1–2), 3–52, doi:10.1007/BF00712389.

Anguelova, M. D., and F. Webster (2006), Whitecap coverage from satellite measurements: A first step toward modeling the variability of oceanic whitecaps, *J. Geophys. Res.*, *111*, C03017, doi:10.1029/2005JC003158.

Blanchard, D. C., and A. H. Woodcock (1957), Bubble formation and modification in the sea and its meteorological significance, *Tellus*, *9*, 145–158, doi:10.1111/j.2153-3490.1957.tb01867.x.

Boyd, P. W. (2008), Ranking geo-engineering schemes, *Nat. Geosci.*, *1*, 722–724, doi:10.1038/ngeo348.

Cavalli, F., et al. (2004), Advances in characterization of size-resolved organic matter in marine aerosol over the North Atlantic, *J. Geophys. Res.*, *109*, D24215, doi:10.1029/2004JD005137.

Charlson, R. J., J. E. Lovelock, M. O. Andreae, and S. G. Warren (1987), Oceanic phytoplankton, atmospheric sulfur, cloud albedo and climate, *Nature*, *326*, 655–661, doi:10.1038/326655a0.

Chin, M., P. Ginoux, S. Kinne, O. Torres, B. N. Holben, B. N. Duncan, R. V. Martin, J. A. Logan, A. Higurashi, and T. Nakajama (2002), Tropospheric aerosol optical thickness from the GOCART model and comparison with satellite and Sun photometer measurements, *J. Atmos. Sci.*, *59*, 461–483, doi:10.1175/1520-0469(2002)059<0461:TAOTFT>2.0.CO;2.

Clarke, A. D., S. R. Qwens, and J. Zhou (2006), An ultrafine sea-salt flux from breaking waves: Implications for cloud condensation nuclei in the remote marine atmosphere, *J. Geophys. Res.*, *111*, D06202, doi:10.1029/2005JD006565.

Cvitan, L. (2003), Determining wind gusts using mean hourly wind speed, *Geofizika*, *20*, 63–73.

de Leeuw, G. (1988), The occurrence of large salt-water droplets at low-elevations over the open ocean, in *The Climate and Health Implications of Bubble-Mediated Air-Sea Exchange*, edited by E. C. Monahan and M. A. Van Patten, pp. 65–82, Conn. Sea Grant College Program, Groton.

de Leeuw, G., and L. H. Cohen (2001), Bubble size distributions on the North Atlantic and the North Sea, in *Gas Transfer and Water Surfaces*, *Geophys. Monogr. Ser.*, vol. 127, edited by M. A. Donelan et al., pp. 271–277, AGU, Washington, D. C.

de Leeuw, G., M. M. Moerman, L. H. Cohen, B. Brooks, M. H. Smith, and E. Vignati (2003), Aerosols, bubbles and sea spray production studies during the RED experiments, paper presented at AMS Conference, Am. Meteorol. Soc., Long Beach, Calif.

de Leeuw, G., E. L. Andreas, M. D. Anguelova, C. W. Fairall, E. R. Lewis, C. D. O'Dowd, M. Schulz, and S. E. Schwartz (2011), Production flux of sea-spray aerosol, *Rev. Geophys.*, *49*, RG2001, doi:10.1029/2010RG000349.

Fitzgerald, J. W. (1975), Approximation formulas for the equilibrium size of an aerosol particle as a function of its dry size and composition and the ambient relative humidity, *J. Appl. Meteorol.*, *14*, 1044–1049, doi:10.1175/1520-0450(1975)014<1044:AFFTES>2.0.CO;2.

Fitzgerald, J. W. (1991), Marine aerosols: A review, *Atmos. Environ., Part A*, *25*, 533–546.

Fuentes, E., H. Coe, D. Green, G. de Leeuw, and G. McFiggans (2010), On the impacts of phytoplankton-derived organic matter on the properties of primary marine aerosol- Part 1: Source fluxes, *Atmos. Chem. Phys.*, *10*, 9295–9317, www.atmos-chem-phys.net/10/9295/2010/doi:10.5194/acp-10-9295-2010, doi:10.5194/acp-10-9295-2010.

Galperin, M. V. (1999), Approaches for improving the numerical solution of the advection equation, in *Large-Scale Computations in Air Pollution Modelling*, edited by Z. Zlatev et al., pp. 161–172, Kluwer Acad., Dordrecht, Netherlands.

Galperin, M. V. (2000), The approaches to correct computation of airborne pollution advection, in *Problems of Ecological Monitoring and Ecosystem Modelling* (in Russian), vol. XVII, pp. 54–68, Gidrometeoizdat, St. Petersburg, Russia.

Galperin, M., and M. Sofiev (1994), Errors in the validation of models for long-range transport and critical loads stipulated by stochastic properties of pollution fields, in *EMEP Workshop on the Accuracy of Measurements*, edited by T. Berg and J. Schaug, pp. 162–179, EMEP, Kjeller, Norway.

Gerber, H. E. (1985), Relative-humidity parameterisation of the Navy Aerosol Model (NAM), *NTIS ADA1632090*, Naval Res. Lab., Washington, D. C.

Gong, S. L. (2003), A parameterization of sea-salt aerosol source function for sub- and super-micron particles, *Global Biogeochem. Cycles*, *17*(4), 1097, doi:10.1029/2003GB002079.

Gong, S. L., L. A. Barrie, J. M. Prospero, D. L. Savoie, G. P. Ayers, J.-P. Blanchet, and L. Spacek (1997), Modelling sea-salt aerosols in the atmosphere: 2. Atmospheric concentrations and fluxes, *J. Geophys. Res.*, *102*(D3), 3819–3830, doi:10.1029/96JD03401.

Grini, A., G. Myhre, J. K. Sundet, and I. S. A. Isaksen (2002), Modelling the annual cycle of sea salt in the global 3D model Oslo CTM2: Concentrations, fluxes, and radiative impact, *J. Clim.*, *15*, 1717–1730.

Guelle, W., M. Schulz, and Y. Balkanski (2001), Influence of the source formulation on modeling the atmospheric global distribution of sea salt aerosol, *J. Geophys. Res.*, *106*, 27,509–27,524, doi:10.1029/2001JD900249.

Hess, M., P. Koepke, and I. Schulz (1998), Optical properties of aerosols and clouds: The software package OPAC, *Bull. Am. Meteorol. Soc.*, *79*, 831–844, doi:10.1175/1520-0477(1998)079<0831:OPOAAC>2.0.CO;2.

Horn, H.-G., H. Bonka, and M. Maqua (1987), Measured particle bound activity size-distribution, deposition velocity, and activity concentration in rainwater after the Chernobyl accident, *J. Aerosol Sci.*, *18*, 681–684, doi:10.1016/0021-8502(87)90096-6.

Intergovernmental Panel on Climate Change (IPCC) (2007), *Climate Change 2007: The Scientific Basis. The Fourth Assessment Report*, edited by S. Solomon et al., 996 pp., Cambridge Univ. Press, Cambridge, U. K.

Jaeglé, L., P. K. Quinn, T. S. Bates, B. Alexander, and J.-T. Lin (2011), Global distribution of sea salt aerosols: New constraints from in situ and remote sensing observations, *Atmos. Chem. Phys.*, *11*, 3137–3157, doi:10.5194/acp-11-3137-2011.

Jylhä, K. (1991), Empirical scavenging coefficients of radioactive substances released from Chernobyl, *Atmos. Environ., Part A*, *25*(2), 263–270.

Korhonen, H., K. S. Carslaw, D. V. Spracklen, G. W. Mann, and M. T. Woodhouse (2008), Influence of oceanic dimethyl sulfide emissions on cloud condensation nuclei concentrations and seasonality over the remote Southern Hemisphere oceans: A global model study, *J. Geophys. Res.*, *113*, D15204, doi:10.1029/2007JD009718.

Korhonen, H., K. S. Carslaw, and S. Romakkaniemi (2010), Enhancement of marine cloud albedo via controlled sea spray injections: A global model study of the influence of emission rates, microphysics and transport, *Atmos. Chem. Phys.*, *10*, 4133–4143, doi:10.5194/acp-10-4133-2010.

Latham, J., and M. H. Smith (1990), Effect on global warming of wind-dependent aerosol generation at the ocean surface, *Nature*, *347*, 372–373, doi:10.1038/347372a0.

Lenton, T. M., and N. E. Vaughan (2009), The radiative forcing potential of different climate geoengineering options, *Atmos. Chem. Phys.*, *9*, 5539–5561, doi:10.5194/acp-9-5539-2009.

Levy, R. C., G. G. Leptoukh, R. Kahn, V. Zubko, A. Gopalan, and L. A. Remer (2009), A critical look at deriving monthly aerosol optical depth from satellite data, *IEEE Trans. Geosci. Remote Sens.*, *47*, 2942–2956, doi:10.1109/TGRS.2009.2013842.

Lewis, E. R., and S. E. Schwartz (2004), *Sea Salt Aerosol Production: Mechanisms, Methods, Measurements, and Models: A Critical Review*, *Geophys. Monogr. Ser.*, vol. 152, AGU, Washington, D. C.

Lewis, E. R., and S. E. Schwartz (2006), Comment on "Size distribution of sea-salt emissions as a function of relative humidity," *Atmos. Environ.*, *40*, 588–590, doi:10.1016/j.atmosenv.2005.08.043.

Mårtensson, M. (2007), Submicrometre aerosol emissions from sea spray and road traffic, Ph.D. thesis, Univ. of Stockholm, Stockholm.

Mårtensson, E. M., E. D. Nilsson, G. de Leeuw, L. H. Cohen, and H.-C. Hansson (2003), Laboratory simulations and parameterization of the primary marine aerosol production, *J. Geophys. Res.*, *108*(D9), 4297, doi:10.1029/2002JD002263.

Mie, G. (1908), Beiträge zur Optik trüber Medien, speziell kolloidaler Metallösungen [Contribution to the optics of turbid media, particularly of colloquial metal solutions Royal Aircraft Establishment], *Ann. Phys.* *25*(3), 377–445.

Monahan, E. C., and I. O'Muircheartaigh (1980), Optimal power-law description of oceanic whitecap coverage dependence on wind speed, *J. Phys. Oceanogr.*, *10*, 2094–2099, doi:10.1175/1520-0485(1980)010<2094:OPLDOO>2.0.CO;2.

Monahan, E. C., D. E. Spiel, and K. L. Davidson (1986), A model of marine aerosol generation via whitecaps and wave disruption, in *Oceanic Whitecaps*, edited by E. C. Monahan and G. MacNiochaill, pp. 167–193, D. Reidel, Norwell, Mass.

Mostafa, H. S., J. H. Lienhard V, and S. M. Zybair (2010), Thermophysical properties of seawater: A review of existing correlations and data, *Desalin. Water Treat.*, *16*, 354–380.

Nilsson, E. D., E. M. Mårtensson, J. S. Van Ekeren, G. de Leeuw, M. M. Moerman, and C. D. O'Dowd (2007), Primary marine aerosol emissions: Size resolved eddy covariance measurements with estimates of the sea salt and organic carbon fractions, *Atmos. Chem. Phys. Discuss.*, *7*, 13,345–13,400, doi:10.5194/acpd-7-13345-2007.

O'Dowd, C., and G. de Leeuw (2007), Marine aerosol production: A review of the current knowledge, *Philos. Trans. R. Soc. A*, *365*, 1753–1774, doi:10.1098/rsta.2007.2043.

O'Dowd, C. D., and M. H. Smith (1993), Physico-chemical properties of aerosol over the North East Atlantic: Evidence for wind speed related sub-micron sea-salt aerosol production, *J. Geophys. Res.*, *98*, 1137–l149, doi:10.1029/92JD02302.

O'Dowd, C. D., M. H. Smith, I. E. Consterdine, and J. A. Lowe (1997), Marine aerosol, sea salt, and the marine sulphur cycle: A short review, *Atmos. Environ.*, *31*, 73–80, doi:10.1016/S1352-2310(96)00106-9.

O'Dowd, C. D., M. C. Facchini, F. Cavalli, D. Ceburnis, M. Mircea, S. Decesari, S. Fuzzi, Y. J. Yoon, and J. P. Putaud (2004), Biogenically driven organic contribution to marine aerosol, *Nature*, *431*, 676–680, doi:10.1038/nature02959.

Petelski, T., and J. Piskozub (2006), Vertical coarse aerosol fluxes in the atmospheric surface layer over the North Polar waters of the Atlantic, *J. Geophys. Res.*, *111*, C06039, doi:10.1029/2005JC003295.

Petelski, T., J. Piskozub, and B. Paplinska-Swerpel (2005), Sea spray emission from the surface of the open Baltic Sea, *J. Geophys. Res.*, *110*, C10023, doi:10.1029/2004JC002800.

Petrenchuk, O. P. (1980), On the budget of sea salts and sulphur in the atmosphere, *J. Geophys. Res.*, *85*, 7437–7444, doi:10.1029/JC085iC12p07439.

Pierce, J. R., and P. J. Adams (2006), Global evaluation of CCN formation by direct emission of sea salt and growth of ultrafine sea salt, *J. Geophys. Res.*, *111*, D06203, doi:10.1029/2005JD006186.

Prank, M. (2008), Evaluation of atmospheric composition simulations via comparison with remote-sensing and in-situ observations, Master's thesis, 74 pp., Dep. of Sci. and Technol., Univ. of Tartu, Tartu, Estonia.

Pruppacher, H. R., and J. D. Klett (1997), *Microphysics of Clouds and Precipitation*, 2nd ed., 954 pp., Kluwer Acad., Dordrecht, Netherlands.

Reid, J. S., H. H. Jonsson, M. H. Smith, and A. Smirnov (2001), Evolution of the vertical profile and flux of large sea-salt particles in a coastal zone, *J. Geophys. Res.*, *106*(D11), 12,039–12,053, doi:10.1029/2000JD900848.

Remer, L. A., et al. (2008), Global aerosol climatology from the MODIS satellite sensors, *J. Geophys. Res.*, *113*, D14S07, doi:10.1029/2007JD009661.

Schulz, M., G. de Leeuw, and Y. Balkanski (2004), Sea-salt aerosol source functions and emissions, in *Emission of Atmospheric Trace Compounds*, pp. 333–359, Kluwer Acad., Dordrecht, Netherlands.

Schulz, M., M. Chin, and S. Kinne (2009), The Aerosol Model Comparison Project, AeroCom, Phase II: Clearing up diversity, *IGAC Newsl.*, *41*, 24 pp.

Seinfield, J. H., and S. N. Pandis (2006), *Atmospheric Chemistry and Physics: From Air Pollution to Climate Change*, 2nd ed., 1232 pp., John Wiley, Hoboken, N. J.

Slinn, S., and W. Slinn (1980), Predictions for particle deposition on natural waters, *Atmos. Environ.*, *14*(9), 1013–1016, doi:10.1016/0004-6981(80)90032-3.

Smith, F. B., and M. J. Clark (1989), The transport and deposition of radioactive debris from the Chernobyl nuclear power plant accident with special emphasis on consequences to the United Kingdom, *Meterorol. Off. Sci. Pap. N42*, HMSO, London.

Smith, M. H., and N. M. Harrison (1998), The sea spray generation function, *J. Aerosol Sci.*, *29*, S189–S190, doi:10.1016/S0021-8502(98)00280-8.

Smith, M. H., P. M. Park, and I. E. Consterdine (1993), Marine aerosol concentrations and estimated fluxes over the sea, *Q. J. R. Meteorol. Soc.*, *119*(512), 809–824.

Sofiev, M. (2002), Extended resistance analogy for construction of the vertical diffusion scheme for dispersion models, *J. Geophys. Res.*, *107*(D12), 4159, doi:10.1029/2001JD001233.

Sofiev, M., P. Siljamo, I. Valkama, M. Ilvonen, and J. Kukkonen (2006), A dispersion modelling system SILAM and its evaluation against ETEX data, *Atmos. Environ.*, *40*, 674–685, doi:10.1016/j.atmosenv.2005.09.069.

Sofiev, M., M. Galperin, and E. Genikhovich (2008), Construction and evaluation of Eulerian dynamic core for the air quality and emergency modelling system SILAM, in *Air Pollution Modelling and Its Application XIX*, *NATO Sci. Peace Security Ser. C: Environ. Security*, edited by C. Borrego and A. I. Miranda, pp. 699–701, Springer, New York.

Sofiev, M., E. Genikhovich, P. Keronen, and T. Vesala (2010), Diagnosing the surface layer parameters for dispersion models within the meteorological-to-dispersion modelling interface, *J. Appl. Meteorol. Climatol.*, *49*, 221–233, doi:10.1175/2009JAMC2210.1.

Spiel, D. E. (1998), On the birth of film drops from bubbles bursting on seawater surfaces, *J. Geophys. Res.*, *103*, 24,907–24,918, doi:10.1029/98JC02233.

Takemura, T., H. Okamoto, Y. Maruyama, A. Numaguti, A. Higurashi, and T. Nakajima (2000), Global three-dimensional simulation of aerosol optical thickness distribution of various origins, *J. Geophys. Res.*, *105*, 17,853–17,873, doi:10.1029/2000JD900265.

Tang, I. N., A. C. Tridico, and K. H. Fung (1997), Thermodynamic and optical properties of sea salt aerosols, *J. Geophys. Res.*, *102*(D19), 23,269–23,275, doi:10.1029/97JD01806.

Tegen, I., P. Hollrig, M. Chin, I. Fung, D. Jacob, and J. Penner (1997), Contribution of different aerosol species to the global aerosol extinction optical thickness: Estimates from model results, *J. Geophys. Res.*, *102*(D20), 23,895–23,915, doi:10.1029/97JD01864.

Textor, C., et al. (2006), Analysis and quantification of the diversities of aerosol life cycles within AeroCom, *Atmos. Chem. Phys.*, *6*, 1777–1813, doi:10.5194/acp-6-1777-2006.

Vana, M., M. Ehn, T. Petäjä, H. Vuollekoski, P. Aalto, G. de Leeuw, D. Ceburnis, C. D. O'Dowd, and M. Kulmala (2008), Characteristic features of air ions at Mace Head on the west coast of Ireland, *Atmos. Res.*, *90*, 278–286, doi:10.1016/j.atmosres.2008.04.007.

Vignati, E., G. de Leeuw, and R. Berkowicz (2001), Modelling coastal aerosol transport and effects of surf-produced aerosols on processes in

the marine atmospheric boundary layer, *J. Geophys. Res.*, *106*(D17), 20,225–20,238, doi:10.1029/2000JD000025.

Witek, M. L., P. J. Flatau, P. K. Quinn, and D. L. Westphal (2007a), Global sea-salt modeling: Results and validation against multicampaign shipboard measurements, *J. Geophys. Res.*, *112*, D08215, doi:10.1029/2006JD007779.

Witek, M. L., P. J. Flatau, J. Teixeira, and D. L. Westphal (2007b), Coupling an ocean wave model with a global aerosol transport model: A sea salt aerosol parameterisation perspective, *Geophys. Res. Lett.*, *34*, L14806, doi:10.1029/2007GL030106.

Witek, M. L., P. J. Flatau, J. Teixeira, and K. M. Markowicz (2011), Numerical investigation of sea salt aerosol size bin partitioning in global transport models: Implications for mass budget and optical depth, *Aerosol Sci. Technol.*, *45*, 401–414, doi:10.1080/02786826.2010.541957.

Woodcock, A. H. (1953), Salt nuclei in marine air as a function of altitude and wind force, *J. Meteorol.*, *10*, 362–371, doi:10.1175/1520-0469(1953)010<0366:SNIMAA>2.0.CO;2.

Woodcock, A. H. (1972), Smaller salt particles in oceanic air and bubble behavior in the sea, *J. Geophys. Res.*, *77*, 5316–5321, doi:10.1029/JC077i027p05316.

Woolf, D. K., E. C. Monahan, and D. E. Spiel (1988), Quantification of the marine aerosol produced by whitecaps, paper presented at Seventh Congress on Ocean-Atmosphere Interaction, Am. Meteorol. Soc., Anaheim, Calif.

Wu, J., J. J. Murray, and R. J. Lai (1984), Production and distributions of sea spray, *J. Geophys. Res.*, *89*, 8163–8169, doi:10.1029/JC089iC05p08163.

Zhang, J., J. S. Reid, and B. N. Holben (2005), An analysis of potential cloud artifacts in MODIS over ocean aerosol optical thickness products, *Geophys. Res. Lett.*, *32*, L15803, doi:10.1029/2005GL023254.

Zhang, K. M., E. M. Knipping, A. S. Wexler, P. V. Bhave, and G. S. Tonnesen (2005), Size distribution of sea-salt emissions as a function of relative humidity, *Atmos. Environ.*, *39*, 3373–3379, doi:10.1016/j.atmosenv.2005.02.032.

Zhang, L., S. Gong, J. Padro, and L. Barrie (2001), A size-segregated particle dry deposition scheme for an atmospheric aerosol module, *Atmos. Environ.*, *35*(3), 549–560, doi:10.1016/S1352-2310(00)00326-5.

G. de Leeuw, Climate Change, Finnish Meteorological Institute, PO Box 503, Helsinki 00101, Finland.

J. Kukkonen, M. Prank, J. Soares, and M. Sofiev, Air Quality Research, Finnish Meteorological Institute, PO Box 503, Helsinki 00101, Finland. (mikhail.sofiev@fmi.fi)

II

Atmos. Chem. Phys. Discuss., doi:10.5194/acp-2015-1056, 2016
Manuscript under review for journal Atmos. Chem. Phys.
Published: 16 February 2016

Atmospheric Chemistry and Physics Discussions
Open Access

Impact of climate change on the production and transport of sea salt aerosol on European seas

J. Soares[1], M. Sofiev[1], C.Geels[2], J.H.Christensen[2], C.Andersson[3], S. Tsyro[4], J.Langner[3]

[1] Finnish Meteorological Institute, Helsinki, Finland

[2] Department of Environmental Science, Aarhus University, Roskilde, Denmark

[3] Swedish Meteorological and Hydrological Institute, Norrköping, Sweden

[4] EMEP MSC-W, Norwegian Meteorological Institute, Oslo, Norway

Correspondence to: J. Soares (joana.soares@fmil.fi)

Abstract

The impact of climate change on sea salt aerosol production, dispersion, and fate over the Europe is studied using four offline regional chemistry transport models driven by the climate scenario SRES A1B over two periods: 1990-2009 and 2040-2059. The study is focused mainly on European seas: Baltic, Black, North and Mediterranean. The differences and similarities between predictions of the individual models on the impact on sea salt emission, concentration and deposition due to changes in wind gusts and seawater temperature are analysed. The results show that the major driver for the sea-salt flux changes will be the seawater temperature, as wind speed is projected to stay nearly the same. There are, however, substantial differences between the model predictions and their sensitivity to changing seawater temperature, which demonstrates substantial lack of current understanding of the sea-salt flux predictions. Although seawater salinity changes are not evaluated in this study, sensitivity of sea-salt aerosol production to salinity is similarly analysed, showing once more the differences between the different models. An assessment on the impact of SSA to the radiative balance is presented.

Atmos. Chem. Phys. Discuss., doi:10.5194/acp-2015-1056, 2016
Manuscript under review for journal Atmos. Chem. Phys.
Published: 16 February 2016

Atmospheric Chemistry and Physics Discussions

1 Introduction

The sea salt aerosol (SSA) affects the Earth radiation budget, atmospheric chemistry, cloud processes, and climate (O'Dowd et al., 1997; IPCC, 2013). Anthropogenic and natural aerosols have similar annual impacts on the global radiative balance, though being predominant in different locations (Textor et al., 2006). SSA dominates the particulate mass and it is the major contributor to aerosol optical depth (AOD) over the ocean (Quinn et al, 1998).

SSA originates from sea spray droplets resulting from waves breaking on the seawater surface, forming whitecaps that cause the entrainment of air into the water. The two main mechanisms responsible for sea spray formation are air bubble bursting during whitecap formation and decay, and direct tearing of droplets from the top of breaking waves. Therefore, the formation of primary SSA is mainly dependent on wind speed: the emission of SSA is generally considered to be proportional to surface winds cubed (Monahan et al., 1986), suggesting that small changes in surface winds can have a substantial impact on the emission of this natural aerosol. Further on, studies on the marine aerosol size distribution (e.g. Covert et al., 1998; Russell and Heintzenberg, 2000; Bates et al., 2002; Huebert et al., 2003) suggest that for high wind speeds the production of very coarse SSA (with particle diameter (Dp) > 20 mm) increases, contributing to a higher transfer of heat and water vapour from the ocean to the atmosphere (Andreas et al., 1995). These processes have a strong impact on the climate forcing. Other parameters influencing the formation of primary SSA have been identified, e.g., seawater temperature and salinity, atmospheric stability, and wave height and steepness (O'Dowd and Smith, 1993; Gong et al., 1997; Gong, 2003; Mårtensson et al., 2003; Lewis and Schwartz, 2004; O'Dowd and de Leeuw, 2007; Witek et al., 2007a, 2007b; Ovadnevaite et al., 2014). Laboratory studies by Mårtensson et al. (2003) and in situ measurements by Nilsson et al. (2007) show that for nano-sized particles, the aerosol number emission decrease with increasing seawater temperature, and for particles with Dp > 100 nm, the number SSA increase with increasing seawater temperature; reflecting different sea spray formation processes. Seawater salinity also affects the droplet formation, where formation of particles with Dp < 0.2 μm are not affected by salinity, but for larger Dp's, salinity impact is substantial: higher salinity contributes to higher production (Mårtensson et al., 2003). The SSA removal processes are scavenging by precipitation and dry deposition (including gravitational settling). SSA has an effect on secondary aerosols formed by gas-to-particulate conversion process such as condensation and nucleation (binary homogeneous and heterogeneous) (Twomey, 1997). SSA serves as a sink for condensable gases and smaller aerosol particles, and serves also as a medium for aqueous-phase reaction of

Atmos. Chem. Phys. Discuss., doi:10.5194/acp-2015-1056, 2016
Manuscript under review for journal Atmos. Chem. Phys.
Published: 16 February 2016

Atmospheric Chemistry and Physics Discussions

reactive gases, e.g. H_2SO_4. This can lead to nucleation suppression for other components of the marine aerosol and consequently change their size distribution, creating a feedback on climate. Furthermore, SSA formation results in a size spectrum ranging from 0.01 to 100 μm, which can lead to cloud formation. With increasing concentrations of cloud condensation nuclei, the cloud microphysical properties change, i.e., the available water vapour is re-distributed over more particles, on average resulting in smaller particle sizes, which in turn changes both cloud albedo and precipitation (Latham et al., 2008, Lenton and Vaughan, 2009; Boyd, 2008; Korhonen et al., 2010, Wang et al., 2011). With dry diameter lower than 1 μm, SSA can easily be transported for long distances in the atmosphere, serving as a cloud seed outside of heavily clouded regions. The cloud drop number concentration can be spatially different, depending on the wind speed, atmospheric transport and particle loss via dry and wet deposition (Korhonen et al., 2010).

Changes in atmospheric transport pathways, precipitation patterns, and sea ice cover influence transport, removal and distribution of SSA. The main features of the regional and global SSA distribution and the climate impact on SSA production due to these physical drivers have been discussed in studies such as Liao et al. (2006), Pierce and Adams (2006), Manders et al. (2010), Sofiev et al. (2011), Struthers et al. (2011), and Tsyro et al. (2011). The understanding of sea spray emissions has increased substantially but process-based estimates of the total mass and size distribution of emitted sea spray particles continue to have large uncertainties (de Leeuw et al., 2011). Chemical transport models (CTM) and general circulation models (GCM) estimates of sea salt burden may vary over 2 orders of magnitude (Textor et al., 2006) and climate models disagree about the balance of effects, ranging from little (Mahowald et al., 2006a) to a considerable sensitivity to climate change (Bellouin et al., 2011). The difference between the available estimations might be due to the wind speed predicted by the climate models, with little understanding of how wind speed may change over the ocean in a warmer climate (IPCC, 2013).

The main goals of the current study are to assess the sensitivity of the production, surface concentrations and removal of SSA to climate change. A multi-model approach using four state-of-the-art offline CTMs was taken to assess the uncertainty/robustness of model predictions over Europe. The sensitivity of simulated emission, concentration, and deposition of SSA to changes in climate was evaluated by comparing a past (1990-2009) and a future (2040-2049) period. This study is a follow-up to the climates studies of Langner et al. (2012) focusing on surface ozone and Simpson et al. (2014) focusing on nitrogen deposition.

Atmos. Chem. Phys. Discuss., doi:10.5194/acp-2015-1056, 2016
Manuscript under review for journal Atmos. Chem. Phys.
Published: 16 February 2016

Atmospheric Chemistry and Physics Discussions

2 Methods

This study uses the same modelling structure as in Langner et al. (2012) for ozone and in Simpson et al (2014) for nitrogen. We focus on the comparison of SSA simulations from three offline European-scale CTMs - EMEP MSC-W, MATCH and SILAM - and one offline hemispheric CTM, DEHM. The models were run through a past (1990-2009) and a future (2040-2059) climate scenarios and the results for the European seas (Baltic, North, Mediterranean, and Black Seas) were compared. The climate meteorology data from a GCM were used in a regional climate model (RCM) and the hemispheric model DEHM. The regional models where driven by the downscaled meteorology from the RCM and the boundary conditions from DEHM. The horizontal grid for DEHM is 150x150 km^2 and for the regional CTMs identical to the RCM (ca. 50×50 km^2).

Throughout the paper, the SSA mass refers to the total mass of dry particles. Since the observations measure sodium (Na^+) concentrations rather than total SSA mass, it is assumed that Na^+ mass fraction is ~30% (Seinfeld and Pandis, 2006). Particle sizes are also provided for dry conditions and, unless otherwise stated, the dry diameter D_p ranges up to 10 μm.

2.1 Climate meteorology

Results of the global ECHAM5/MPIOM GCM (Roeckner et al., 2006), driven by emissions from the SRES A1B scenario (Nakicenovic, 2000), were downscaled over Europe with the Rossby Centre Regional Climate model, version 3 (RCA3) (Samuelsson et al., 2011; Kjellstrom et al., 2011). The global ECHAM5/MPIOM model is defined in spectral grid T63, which at mid-latitudes corresponds to a horizontal resolution of ca. 140×210 km^2. The horizontal resolution of RCA3 was 0.44°×0.44° on a rotated latitude-longitude grid, and data were provided with 6-hourly resolution. The climate, as downscaled by RCA3, reflects the broad features simulated by the parent GCM, but from earlier studies with the current setup it is clear that the global ECHAM5/MPIOM model projects a slightly warmer and wetter climate over Europe than the regional model RCA3 (Langner et al., 2012; Simpson et al., 2014).

The wind speed is higher over the ocean and can be up to two times slower, in average, over the inner seas (Fig. 1, first panel on the left). Wind patterns are different between the Seas, with some areas over individual seas being more affected by wind gusts than others: e.g. in the Mediterranean, the wind speed is higher over the Levantine Sea than over other areas. For the wind speed, RCA3 predicts an stronger increase at the Norwegian Sea, Black Sea, Gulf of Bothnia (Baltic Sea) and Aegean Sea (Mediterranean Sea) and a stronger decrease between Italy and Tunisia and Libya

Atmos. Chem. Phys. Discuss., doi:10.5194/acp-2015-1056, 2016
Manuscript under review for journal Atmos. Chem. Phys.
Published: 16 February 2016

Atmospheric Chemistry and Physics Discussions

(Mediterranean Sea) in the future period (Fig. 1, first panel on the right). Nevertheless, the absolute change is no more than 0.4 m/s. Trend analysis considering only marine grid cells for each sea (Fig. S1 in supplementary material) shows that there is no significant trend between past and future periods.

Typically, the surface water temperature is higher at southern latitudes. For the same latitude, the Black and Mediterranean Seas have, in general, higher temperature than the Atlantic Ocean and the Baltic Sea (Fig. 1, second panel on the left). RCA3 predicts a general increase of the water surface temperature between the past and the future periods (Fig. 1, second panel on the left). The most substantial changes are for the northern part of the Atlantic Ocean and for the Baltic Sea (maximum 1.17 ºC). Trend analysis for the monthly mean temperature is significant for all the European inner-seas (Fig. S2 in supplementary material). The temperature is rising for all the seas with the highest rise over the Black Sea and the lowest over the North Sea.

The precipitation tends to be higher over the ocean and lower over the inner seas. The lowest precipitation amount is seen over the Mediterranean Sea; on an annual level the difference from the ocean can be up-to two orders of magnitude (Fig. 1, third panel on the left). The climate model predicts that the precipitation will strongly decrease over the Mediterranean and increase over the Baltic and North Seas, whereas over different parts of Atlantic Ocean the opposite trends can coexist (Fig. 1, third panel on the right). Trend analysis shows that none of the trends is significant (Fig. S3 in supplementary material).

2.2 SSA boundary conditions

Sea salt concentrations (as fine and coarse modes, see the description of DEHM below) provided by the hemispheric DEHM model, were used as lateral and top boundaries for the regional models. The boundary values taken from DEHM were updated every 6 h and interpolated from the DEHM grid to the respective geometry of each regional CTM. The DEHM model was driven by the global ECHAM5-r3 meteorology, without the RCA-3 downscaling.

2.3 Chemical transport models

The models used in this study have been introduced in the previous studies: Langner et al. (2012) and Simpson et al. (2014). Below, we focus on their handling of the production and removal of SSA. All the SSA source functions in the current study are based on white-cap-area based parameterizations of Monahan et al. (1986), for formation of super-micron particles and follow

Atmos. Chem. Phys. Discuss., doi:10.5194/acp-2015-1056, 2016
Manuscript under review for journal Atmos. Chem. Phys.
Published: 16 February 2016

Atmospheric Chemistry and Physics Discussions

Mårtensson et al. (2003) for the sub-micron aerosols. The difference between the various source functions is the dependence on temperature and salinity for the SSA generation (**Table 1**).

2.3.1 DEHM

In DEHM the production of SSA at the ocean surface is based on two parameterization schemes describing the bubble-mediated sea spray production of smaller and larger aerosols. In each time step the production is calculated for seven size bins and thereafter summed up to give an aggregated production of fine (with dry diameters <1.3 μm) and coarse (with dry diameters ranging 1.3-6 μm) aerosols. For the fraction with dry diameters less than 1.25 μm a source function based on Mårtensson et al. (2003) is used, while for sizes larger than that the Monahan et al. (1986) source function is applied. They both include an $U_{10}^{3.41}$ dependency on wind speed and the production of the smaller aerosols is also a function of the sea surface temperature. An ambient relative humidity of 80% is assumed in the calculations and the size of the produced SSA is assumed to depend on the salinity at the actual location. Here a monthly climatology of current day salinity on a 0.25°x0.25° grid (Boyer et al., 2005) is applied for both time periods in focus in the current paper. Within the atmosphere, the fine and coarse fraction of SSA is treated separately in terms of transport and removal. Wet deposition includes in-cloud and below-cloud scavenging, while dry deposition velocities are based on typical resistance methods for various land surface types (see Simpson et al., 2003; Emberson et al., 2000). The fine and coarse fractions in the DEHM model are in the current paper assigned the dry diameters of 1 μm and 6 μm.

DEHM is continuously validated against available measurements from e.g. the EMEP network and an evaluation of an earlier version of the sea salt routine in DEHM showed that the model gives satisfactory results for sea salt over Europe (Brandt et al. 2012).

2.3.2 EMEP MSC-W

The standard Unified EMEP model runs include sea salt particles with ambient diameters up to about 10 µm, which mainly originate from the bubble mediated sea spray (Tsyro et al, 2011). The parameterisation scheme for calculating sea salt generation in the EMEP model makes use of two source functions for bubble-mediated sea spray production. The first one is a source function for sea spray droplets at 80% relative humidity from Monahan et al. (1986) and the second one is a source function for sea salt particles from the work of Mårtensson et al. (2003), which is formulated for a salinity of 33‰. In the EMEP model, the SSA fluxes can be calculated for particle dry Dp ranging from 0.02 to 12 µm, whereas operationally and for this work SSA with Dp up to 6 µm are included.

Atmos. Chem. Phys. Discuss., doi:10.5194/acp-2015-1056, 2016
Manuscript under review for journal Atmos. Chem. Phys.
Published: 16 February 2016

Atmospheric Chemistry and Physics Discussions

Mårtensson et al. (2003) parameterisation is applied for smaller size bins, while Monahan et al. (1986) parameterisation is used for the coarser ones. From the fluxes of sea spray, the sea salt mass is calculated assuming sea salt density of 2200 kg/m3. The total production rates of fine and coarse sea salt are calculated by integrating the size resolved fluxes (7 in the fine and 3 in the coarse fractions) over respective size intervals. In the model, generated SSA is assumed to be instantaneously mixed within the model lowest layer at each time step. The transport and removal of sea salt is described individually for the fine and coarse fractions in the EMEP model. Dry deposition parameterisation for aerosols is calculated using a mass-conservative equation from Venkatram and Pleim (1999). The dry deposition due to gravitational settling is size-dependent and diameters of 0.33 and 4.8 µm are assumed for the fine and coarse SSA. . Wet scavenging is treated with simple scavenging ratios, accounting for in-cloud and sub-cloud processes. The scavenging ratios are assigned to crudely reflect the solubility of different aerosol components, and the size differentiated collection efficiencies are used in sub-cloud aerosol washout.

The present sea salt parameterisation was shown to give the best overall results as compared to a number of other source functions within the EMEP model (Tsyro et al., 2011). The model SSA calculations are extensively evaluated against long-term observations (Tsyro et al., 2011; EMEP Reports http://www.emep.int).

2.3.3 MATCH

The treatment of SSA production in MATCH is based on the parameterization of Mårtensson et al. (2003) for dry particle sizes of up to 0.4 μm aerodynamic radius, and on Monahan et al. (1986) for larger particle sizes. The temperature correction following Sofiev et al. (2011) is applied to the estimates from the Monahan scheme. The number of bins is flexible, but in this study four size bins were used with Dp ranges 0.02–0.1 μm, 0.1–1 μm, 1–2.5 μm, 2.5–10 μm. The production of sea salt droplets is calculated assuming an ambient relative humidity of 80% and a particle density of 1150 kg/m3 and is integrated over each size bin while dry removal rates are calculated using the geometric mean size in each bin. Dry deposition over land is following Zhang et al. (2001) while a separate parameterization accounting for bubble burst activity is used over sea (Pryor and Barthelmie, 2000). Sea salt is assumed to 100% activated or scavenged by hydrometeors in-cloud while below-cloud scavenging is handled following Dana and Hales (1976). The distribution of salinity in sea water is taken from NOAA (2013). Further details and evaluation of MATCH sea salt simulations using observed meteorology can be found in Foltescu et al. (2005) and Andersson et al. (2014).

Atmos. Chem. Phys. Discuss., doi:10.5194/acp-2015-1056, 2016
Manuscript under review for journal Atmos. Chem. Phys.
Published: 16 February 2016

Atmospheric Chemistry and Physics Discussions
Open Access

2.3.4 SILAM

The SSA production via bubble-mediated mechanism takes into account the effects of wind speed, salinity, and water temperature and covers sea salt particles with dry diameter from 20 nm to 10 µm. The observations from the Mårtensson et al. (2003) study for seawater surface temperature 298 K and sea water salinity 33 ‰ were used to extrapolate the scheme from Monahan et al. (1986) to particle sizes down to 20 nm. To calculate SSA production for other water temperatures and salinities, correction factors are applied which were derived based on the experimental data of Mårtensson et al. (2003). The full description of the parameterisation in the SILAM model can be found in Sofiev et al. (2011). The description of the temperature correction in Sofiev et al. (2011) was changed. Currently, the water temperature reference for the unified shape function is 20 ºC, instead of 25 ºC as referred in Sofiev et al. (2011). The shape function has been updated accordingly and the new shape function (dF_0/dD_p) for particles with Dp ranging from 0.01 to 10 μm is described below:

$$\frac{dF_0}{dD_p} = (1 + 0.05 * D_p) * \frac{\exp\left(\frac{-0.11}{D_p}\right)}{0.4 + \exp\left(\frac{-0.2}{D_p}\right)} * \frac{6 * 10^5}{\left(1 * 10^{-4} * D_p^2 + D_p\right)^3} * 10^{1.19 * \exp\left(-\left(\frac{0.35 - \lg D_p}{0.8}\right)^2\right)} \quad (1)$$

For the current study the spume droplet formation based on Andreas (1998) was included, with spume being supressed for 10m wind speed lower than 6 m/s. The production of sea salt droplets is calculated assuming a dry particle density of 2200 kg/m^3. The size distribution is described by flexible bins. Production is integrated over each size bin while dry and wet removal rates are calculated using mass-weighted mean diameter in each bin. Depending on particle size, mechanisms of dry deposition vary from primarily turbulent diffusion driven removal of fine aerosols to primarily gravitational settling of coarse particles (Kouznetsov and Sofiev, 2012). Wet deposition distinguishes between sub- and in-cloud scavenging by both rain and snow (Sofiev et al., 2006; Horn et al., 1987; Smith and Clark, 1989; Jylhä, 1991). Gravitational settling, dry deposition and optical properties take into account the particle hygroscopic growth. For the simulations, five bins with the Dp ranges of 0.01–0.1 μm, 0.1–1.5 μm, 1.5–6 μm, 6–15 μm; and 15-30 μm were used. The distribution of salinity in sea water is taken from NOAA (2013).

SILAM model has been evaluated against a wide range of observations and models utilizing the above described parameterization (Sofiev et al., 2011; Tsyro et al., 2011).

Atmos. Chem. Phys. Discuss., doi:10.5194/acp-2015-1056, 2016
Manuscript under review for journal Atmos. Chem. Phys.
Published: 16 February 2016

Atmospheric Chemistry and Physics Discussions

2.4 Model evaluation

Sea water is the predominant source of Na^+ in the atmosphere, which can be used as its tracer in most regions of Europe. Evaluation of the model predictions was performed via comparison with observations available from the EMEP network (Co-operative Programme for monitoring and evaluation of the long-range transmission of air pollutants in Europe, http://www.emep.int, Tørseth et al. 2012) that perform regular measurements across Europe. The observations include Na^+ concentration in aerosol and ion analysis of precipitation including Na^+. Concentration measurements are sampled daily by a filter pack sampler (cut-off at D_p = ~10 μm), at 2 m height; the concentration in precipitation is mainly sampled by a "wet-only" sampler and, in a few places, with bulk collectors. The wet deposition of Na^+ is obtained by multiplying the weighted mean concentration by the total amount of precipitation in a daily basis. For more details about the sampling the reader is referred to e.g., Hjellbrekke and Fjæra (2009). These sampling methods do not distinguish if the sodium is originated from natural (e.g. mineral dust) or anthropogenic sources. In some regions there might be certain amounts coming from combustion processes and industry, but overall the contribution of anthropogenic sources to the sodium budget is low (van Loon et al., 2005).

The measurement data were averaged to monthly level with the minimum completeness requirement of 75% temporal coverage per month and per year, between 1990 and 2009. The CTMs predictions for the measurement sites satisfying the temporal criterion were averaged on a monthly basis over the 20 years. Since the model computations were driven by climate model fields, no temporal collocation was done. Therefore, the primary parameter considered was the monthly Na^+ concentrations averaged over the past period. Modelled values were obtained from the model's lowest layer mid-point, which is defined somewhat differently for each model (**Table 1**). No near-surface concentration profiling was made, with the exception of EMEP where concentrations are corrected to 3 m height, largely due to unreliable stability estimates based on climate-model fields.

The model performance was evaluated by the following statistical measures: bias, spatial Pearson correlation coefficient (R), root mean square error (RMSE), bias and standard deviation (SD) ratio ($SD_{model}/SD_{observations}$). The evaluation included Na^+ concentration in aerosols at 29 measurement sites and ion analysis of Na^+ wet deposition at 133 measurement sites, which we consider sufficient for computing the basic statistical scores and plotting scatter plots. The location of the measurement sites are shown in Fig. S4 in the supplementary material.

Atmos. Chem. Phys. Discuss., doi:10.5194/acp-2015-1056, 2016
Manuscript under review for journal Atmos. Chem. Phys.
Published: 16 February 2016

Atmospheric Chemistry and Physics Discussions

2.5 Radiative transfer modelling

The radiative transfer modelling was completed offline with the libRadtran software package for radiative transfer calculations (Mayer and Kylling, 2005). This tool calculates radiances, irradiances and actinic fluxes for the given optical properties. The Earth radiative balance results from the difference between the incoming (direct and diffusive-downwards) and outgoing (diffusive upwards) radiation. The impact of SSA is assessed by the difference between an atmosphere with SSA and without SSA, for the past and future periods. The calculations were defined at the top of the atmosphere (TOA), with wavelength ranging from 0.2 to ~4 μm, in order to compute the integrated shortwave irradiance. All the runs considered wet and icy clouds, with the cloud cover taken from the climate model RCA3 and optical properties taken from MODIS observations (Pincus et al. 2011). Monthly-basis observations from AQUA and TERRA obtained from 2002 to 2014 were averaged in order to have climatological cloud optical fields. These fields were the same for both past and future period calculations. Earth albedo information is included in the calculations and is obtained from the NASA model, GLDAS Noah Land Surface Model L4 (Rodell et al., 2004), on a monthly basis for the period between 1990 and 2012. This dataset was averaged to obtain climatological surface albedo fields, remaining the same for both past and future periods. The calculations for an atmosphere with SSA included the AOD computed by SILAM: the AOD at 550 nm was computed for the full size-spectrum of the SSA described in Table 1. SILAM's optical thickness predictions are based on size distribution and spectral refractive index of SSA (Prank, 2008). The AOD data was monthly-averaged for every hour in a day, for the past and future periods. This allowed taking into consideration the length of the day, since solar zenith angle is computed for every hour. The description of the runs and assumptions are provided in Table 2. This setting was chosen in order to reflect an atmospheric state closer to reality, since there were no other aerosols available for this study. Keeping the atmospheric and cloud conditions constant between the past and the future, will allow pinpointing the impact of the SSA on the radiative balance.

3 Results

3.1 Comparison with observations

Figure 2 and Figure 3 show the performance of the CTMs estimating Na^+ surface concentrations and wet deposition, respectively, during the past period; Table 3 and Table 4 complete the statistical evaluation of the models for the surface concentrations and wet deposition, respectively. The

Atmos. Chem. Phys. Discuss., doi:10.5194/acp-2015-1056, 2016
Manuscript under review for journal Atmos. Chem. Phys.
Published: 16 February 2016

Atmospheric Chemistry and Physics Discussions

models showed similar performance with quite high correlation coefficients varying from 0.71 up to 0.85 for the concentrations but substantially lower for wet deposition (from 0.24 up to 0.41). The difference between the model performances is quite small and varying for the different scores. The highest correlation with the concentration observations was shown by DEHM (0.85), which also demonstrated the highest RMSE and bias originating from a stronger overestimation over the regions with observed low concentrations. EMEP showed the lowest RMSE and bias, as well as one of the best correlation factors. SILAM tends to overestimate the lowest observed values (positive bias) whereas MATCH has a stronger underestimation of the highest values (negative bias). Comparing the winter (December, January and February) and the summer (June, July and August) seasons, one can notice that the models perform better in summer, with higher correlation and lower bias. The observed winter time levels are likely harder to be reproduced due to stronger winds and faster changing weather, which might not be captured by the climatological runs.

Comparison of Na^+ wet deposition with measurements shows low correlation and substantial under-prediction. This is particularly true for the high-deposition observations, which resulted in a strong negative bias for all the models. The evaluation of modelled precipitation was presented in Simpson et al. (2014), Table 4, and shows an overestimation of precipitation in the RCA3 model (reginal CTMs) and underestimation in the precipitation used in DEHM. The overestimation leads to an overestimation of the deposition of SSA close to the sources. Consequently, less SSA reaches the shore and the measurement sites. The second major reason for discrepancy is that the observed wet deposition does not cut-off the size of the particles, i.e. SSA coarser than 10 μm is accounted for, including the SSA produced in the surf zone. This mostly explains the large negative bias of the models, which reported PM_{10} only, and, to some extent, the low correlation. This is demonstrated when comparing SILAM scores taking into account the full size range available (Dp = [0.01-30] μm): accounting for the coarser aerosols strongly reduced the bias, correlation strongly improved, and RMSE became slightly smaller. In summer, the scores are slightly better than in winter, but the absolute values and importance of this removal process is smaller in summer time.

In Simpson et al. (2014), it was shown that CTMs driven by RCM meteorology are likely to perform worse than they would with data from numerical weather prediction models. Nevertheless, the current comparison showed that CTMs can predict mean concentrations and depositions within ~30% uncertainty (for depositions, prediction of full size range is a pre-requisite), whereas the spatial distribution patterns are reproduced with correlation higher than 0.7 also when driven by climate model meteorology.

Atmos. Chem. Phys. Discuss., doi:10.5194/acp-2015-1056, 2016
Manuscript under review for journal Atmos. Chem. Phys.
Published: 16 February 2016

Atmospheric Chemistry and Physics Discussions

3.2 Current and future climate SSA emissions

The annual SSA emission in the reference period predicted by DEHM, MATCH and SILAM is shown in Figure 4 (left panel). EMEP did not have this variable as an output. As expected, all models predict the highest emissions over the Atlantic Ocean, with the Mediterranean Sea being the second highest source. MATCH predicted, in average, 25% higher emissions over the Mediterranean than SILAM. The emissions are mainly driven by the wind and typically expressed by the white-cap produced by the surface-winds via the Monahan and O'Muircheartaigh (1980) parameterisation. This empirical power-law is taken by all models participating in this study and suggests emission (E) to be proportional to the 10m-wind speed (U_{10}) to the power of 3.41: $E \approx U_{10}^{3.41}$, the so-called wind-forcing. Consequently, the SSA emissions (Fig. 4, left panel) clearly correlate with the wind-forcing (Figure 5, left panel), in particular over the open ocean. However, the use of the same functional dependence and input meteorology does not guarantee identical emission, as it will be discussed further on. MATCH and SILAM seem more sensitive to the wind-forcing over the Mediterranean than DEHM, possibly due to the horizontal resolution difference between the hemispheric and regional CTMs (e.g. the Mediterranean is not properly resolved by the global climate model, the driver for DEHM). Apart from the wind forcing, laboratory studies have shown the relation between the emissions of SSA and seawater surface temperature and salinity: SSA mass will be higher at sea areas with higher surface water temperatures and salinity (Mårtensson et al, 2003). The temperature and salinity dependencies are included in the parameterizations, therefore, the models predict for the same wind forcing, higher emissions for higher water temperatures: the Mediterranean and Black Seas (Fig. 1 and Fig. 4, left panel). The effect of salinity is best seen in the Baltic Sea (salinity ~ 9 ‰), which has comparable wind forcing to some areas of the Mediterranean and the Atlantic (salinity ~33 ‰) but lower emission. SILAM and MATCH show the highest difference between the inner-seas with at least 3 times lower emissions over the Baltic Sea.

In absolute terms, the climate impact on SSA emissions (Fig. 4, right panel) is mainly positive according to the regional models whereas DEHM shows a general decrease. The exception goes for the Atlantic Ocean, in the west side of the domain, where all the models agree in a decrease of emissions. The difference between the past and future periods is only due to the wind forcing and temperature changes, since salinity was kept constant. Thus, this change (Fig. 4, right panel) highly correlates with the changes for wind-forcing (Fig. 5, right panel), adjusted by the changes in water temperature (Fig. 1, right panel). For example, the pronounced decrease of emission over western

Atmos. Chem. Phys. Discuss., doi:10.5194/acp-2015-1056, 2016
Manuscript under review for journal Atmos. Chem. Phys.
Published: 16 February 2016

Atlantic is mainly driven by the reduction of wind speed but the decrease is limited by the rising temperature in the north and east: higher temperature leads to production of more SSA even for somewhat slower wind speed.

The models demonstrated different sensitivity to seawater temperature: it seems to be less important for DEHM than for other models, whereas SILAM is the most sensitive. For instance, MATCH and SILAM showed an increase of emissions over the east of Iceland where temperature is predicted to rise by almost 2 K. The increase of seawater temperature, supported by higher wind speed, over the Black and Aegean Seas (Fig. 1, right panel), will lead to higher emissions. DEHM might not be so sensitive to the local storms due to the coarse horizontal resolution. The absolute difference between future and past is the smallest for the Baltic Sea, but in relative terms all the models show an increase up to 20% in Gulf of Bothnia, which is actually higher than, e.g. 5-15% of increase predicted for North Sea (minimum for DEHM and maximum for MATCH).

Trend analysis for the Baltic, Black, Mediterranean and North Seas (only sea cells are taken into consideration) is available as supplementary material: Fig. S5 for the Baltic, Fig. S6 for the Black, Fig. S7 for the Mediterranean, and Fig. S8 for the North Seas. The trend is only statistically significant ($p < 0.001$) for all the models for the Black Sea, with all models agreeing on an increase of concentration in the future.

Figure 6 (left panel) shows the SSA emission difference between the winter and summer for the past period. The difference between seasons in terms of SSA production can be substantial: SSA emission is up to 3 times higher in winter time. Seasonally, there are differences between the driving processes for SSA production: the winter period has a larger SSA production, due to more frequent and stronger storms; but the summer time shows pronounced maxima over specific areas mostly influenced by the seawater temperature. The latter is mostly true for MATCH and SILAM, since their temperature sensitivity is higher. SSA emission in winter will be accentuated in the future for MATCH (more emphasized) and SILAM: Figure 6 (right panel) shows pronounced maxima around Iceland and the British Isles; distinct differences in the SSA emission are also seen in the Mediterranean. DEHM does not show much difference between the periods.

3.3 Current and future climate SSA concentrations

Concentration is a function of emission and transport of the SSA, that is dependent on ventilation of an area over inner seas (wind speed), and on removal processes largely controlled by precipitation and relative humidity (via settling). Generally, the pattern of SSA concentration follows the

emission areas with stronger winds and frequent storms. Concentrations are, therefore, higher at the Atlantic Ocean and lower at the European inner-seas. All the models show lower concentrations for the Baltic Sea, reaching up to 10 times difference from the ocean (Fig. 7, left panel). The Mediterranean Sea is the inner sea with the highest concentrations. For the Baltic Sea, DEHM and MATCH show the highest and the lowest concentrations, respectively, with a difference of a factor of ~1.3 between each other. For the Black Sea, DEHM and EMEP show the highest concentrations and a similar spatial distribution pattern, and SILAM the lowest; nonetheless the difference is not so substantial. For the Mediterranean Sea, EMEP shows the lowest concentrations, MATCH being the highest: with 30% difference. All models show pronounced maximums at the Balearic Sea and the Levantine Sea. Transport over land is quite similar among the models, especially for the regional CTMs. The biggest difference lies over the western-central Europe with MATCH showing lower concentration over land. Transport of SSA inland is visible hundreds of km's inland; near the coast line it can contribute up to 6 $\mu g/m^3$ to PM_{10}.

The models predict relatively similar pattern for the SSA spatial distribution for the past period but, they seem to have different responses to the future climate, with MATCH and SILAM clearly being the most sensitive and EMEP the least. Figure 7 (right panel) shows the difference between the past and future periods for the different models. DEHM and EMEP foresee almost no change or a decrease of SSA concentrations over the open sea, whereas MATCH and SILAM predict an increase. These results were expected due to the predicted emissions (Sect. 3.2). All models agree in an increase in SSA surface concentration over the north of Iceland, the Black Sea, and over land in southern latitudes. The models agree somehow on an increase of the Mediterranean and Black Seas SSA concentration but it is MATCH and SILAM that show the highest positive change in concentrations. The impact over land is slightly positive for all the models in the Southern part of the domain, while at more Northern latitudes DEHM and EMEP from one side, and MATCH and SILAM models from another, disagree on the trend signal: a reduction of the SSA load over land is predicted by the first two models and an increase by the latter pair.

Overall, EMEP is the least sensitive and MATCH the most sensitive model to a changing climate. SILAM is the most sensitive over the Norwegian Sea. The difference between the past and future period concentrations is more substantial than that of emissions: the factors seemingly having exacerbated this difference are the decrease of ventilation over the west-Mediterranean, changes in mixing patterns, etc.

Atmos. Chem. Phys. Discuss., doi:10.5194/acp-2015-1056, 2016
Manuscript under review for journal Atmos. Chem. Phys.
Published: 16 February 2016

Atmospheric Chemistry and Physics Discussions

Trend analysis (supplementary material: Fig. S9 for the Baltic, Fig. S10 for the Black, Fig. S11 for the Mediterranean, and Fig. S12 for the North Seas) suggest that trends are only significant ($p < 0.001$) for MATCH and SILAM for both Mediterranean and Black seas, all with a positive signal.

Seasonally, the concentrations follow the same pattern as the emissions: higher in winter time. When analysing the changes between winter and summer, the models can again be grouped into DEHM-EMEP and MATCH-SILAM. In winter (Fig. 8, left panel), the first pair presents a larger amount of SSA mass generally over sea and land surfaces. Conversely, MATCH and SILAM predict a decrease of SSA surface concentration around the British Isles, Mediterranean and Black Seas, though the coast lines have sharper peaks of SSA mass during winter. The difference between the future and past periods (Fig. 8, right panel) is relatively similar for all the models over the open sea: predictions show an increase of concentration around the British Isles and a decrease over the Norwegian Sea, in the future. MATCH and SILAM show sharper increase or decrease along the Mediterranean Sea. The changes predicted can be 3 times higher than the changes predicted for the emissions (Figure 6, right panel). The changes can also have different signal, e.g. the Eastern-basin of the Mediterranean where it is predicted an increase of emissions but a decrease of concentrations, implicating that the ventilation over this area was quite effective.

3.4 Current and future climate SSA deposition

The deposition (wet+dry) patterns for SSA are depicted in Fig. 9 (left panel). Typically the deposition is higher over the sources areas and close to the coastal areas. Over land, SILAM shows less deposition and DEHM and EMEP predict the highest levels. There are different patterns over the Atlantic, mostly attributable to the boundary conditions treatment by each model. DEHM predicts quite high values over all the seas. Over the Black Sea, the deposition is more accentuated in the predictions by EMEP and less by SILAM. MATCH also shows higher values for deposition over the Mediterranean, and SILAM the lowest. Deposition is not substantial over the Baltic Sea, with exception of DEHM, owing to low SSA mass released from its surface.

The impact of future climate conditions (Fig. 9, right panel) on deposition, in absolute levels, is small and mostly noticeable over the Atlantic Ocean. For all models, the most significant positive change in the deposition is seen around Iceland. This is expected according to the changes seen in precipitation between future and past periods (Fig. 1, third panel on the right). All regional CTMs show a strong signal on the west side of the domain, an artefact due to the boundary conditions. In

Atmos. Chem. Phys. Discuss., doi:10.5194/acp-2015-1056, 2016
Manuscript under review for journal Atmos. Chem. Phys.
Published: 16 February 2016

relative terms, Scandinavia, east of UK, central-western Europe and Mediterranean are the most affected with 5-20% more deposition predicted by MATCH and SILAM.

Trend analysis (supplementary material: Fig. S13 for the Baltic, Fig. S14 for the Black, Fig. S15 for the Mediterranean, and Fig. S16 for the North Seas) suggests that none of models show a significant trend.

Seasonally, SSA deposition is higher in winter than in summer, due to the higher emissions and frequent precipitation in winter months. This difference is mainly accentuated over the source areas: MATCH and SILAM have the lowest difference over the Baltic and Black Seas, due to the lower production; DEHM shows the highest at Mediterranean Sea. The difference of deposition between winter and summer will also change in the future period (Fig. 10, right panel) with all models showing a slight increase of the deposition in summer over the Mediterranean and along the coast of Norway. An increase of deposition in winter was suggested around Iceland and British Isles, North Sea and coastal areas of Mediterranean Sea.

4 Impact of meteorology and seawater properties on the emission and fate of SSA

The multi-model comparison presented in Sect. 3 shows that there are significant difference between the models in terms of emission and fate of the SSA. The latter is particularly true for the inner seas. The differences between the models lead to a more uncertain answer about the impact of the future climate on the production and transport of SSA and its possible feedback to climate. The SSA emission in the models is driven by three parameters: wind speed, water temperature, and water salinity. All models use the same $U_{10}^{3.41}$ dependence on wind speed; hence the differences in emission have to be attributed to parameterization of temperature and salinity dependencies. Formally, all models used the Monahan et al. (1986) and Mårtensson et al. (2003) parameterizations or, at least, the available data for deriving the emission flux parametrizations (SILAM). Specifics of the implementation, however, appeared significant. To understand the latter, box-model calculations of the SSA mass flux as a function of temperature were made for seawater salinity 10 and 35 ‰, representing Baltic Sea and Atlantic Ocean, respectively, and with wind-speed fixed at 15 m/s (Fig. 11, left-hand panel).

In general, all the models show an increase of mass flux of SSA with temperature and salinity, except EMEP that does not apply any correction for salinity. Both DEHM and EMEP mass flux show little difference between low and high temperatures; SILAM and MATCH show a substantial

dependency of the mass flux on temperature throughout the size ranges. This difference is explained by the way dependency on seawater temperature is implemented: only for the fine mode in DEHM and EMEP, based on the Mårtensson et al. (2003) source function, and for both fine and coarse modes in SILAM and MATCH. In MATCH, the implementation of seawater temperature correction is done by combining the temperature correction included in the Mårtensson et al. (2003) for size-range below Dp = 0.4 μm and the use of the temperature corrections from Sofiev et al. (2011) for the coarser sizes. In SILAM the source function is scaled with Sofiev et al. (2011) size-dependent temperature correction function. This explains why the results in Sect. 3 could be paired between the models. EMEP is the model that shows the highest amount of SSA produced, with the exception for seawater temperature higher than 15 ºC and high salinity, with MATCH and SILAM predicting the highest amount of SSA. For the lowest salinity, SILAM is the model that produces less SSA, with DEHM being surpassed by MATCH around 17 ºC. For the highest salinity, both MATCH and SILAM start to predict higher SSA flux than DEHM around 9 ºC. This is due to the temperature correction factor described in Sofiev et al. (2011) that assumes that for low seawater temperature, the production of coarse SSA, where the mass is significant, is very low. This analysis clarifies why MATCH and SILAM tend to have higher emissions than DEHM where waters are warmer and lower when colder (e.g. Baltic Sea), and why MATCH shows the highest values for the SSA mass flux. Also explains the smaller difference between winter and summer predicted by DEHM, since the changes in SSA mass flux depending on seawater temperature is very low.

Figure 11 (right panel) shows how the different models distribute the mass between the fine and coarse modes, for the same wind and salinity conditions described above. Both DEHM and EMEP assume that the contribution of the coarser mode is reduced with temperature, since more SSA is produced with higher temperatures, for size ranges below 2.5 μm. EMEP has the highest contribution for the coarse mode, independent of the temperature. For MATCH and SILAM, the contribution to the coarser mode increases with temperature, though MATCH has a lower coarse mode contribution than SILAM. The only agreement between the DEHM, MATCH and SILAM is that for higher salinities, the coarse mode contribution is higher. The ratio between fine and coarse mode is very relevant for the deposition processes, and it could explain why deposition is higher for DEHM and EMEP (Fig. 9), though in this case, it is hard to evaluate the real impact due to different deposition schemes implemented in the models.

It is pertinent to discuss the difference between DEHM, EMEP and MATCH, since these models apply the same parameterization for SSA number flux, though having different salinity fields and

salinity correction function. Mårtensson et al. (2003) defines very strict size ranges for the computation of the 6th order polynomial for particles between 0.02 to 2.8 μm in dry diameter. In case the models define size ranges outside of the tabulated in that study, it can result in very different results. The linkage between the two parameterizations can also result in different outcomes: DEHM links the two parameterizations at dry diameter of 1.25 μm, EMEP at 1.5 μm and MATCH at 0.4 μm. In the case of MATCH, an extrapolation of the Monahan et al. (1996) function is needed, in order to bring it to Mårtensson et al. (2003) range.

5 SSA and climate change: production, fate and radiative impact

The regional-scale impact of SSA production and fate caused by a changing climate has been shown in Sect. 3. We show that the change in SSA emission between the past and future periods is not so large, arguably due to the small change in wind speed between the two time periods. Climates studies such as Gregow et al. (2011) projected higher wind speed changes in periods closer to the years 2100, in Scandinavia. Nevertheless, the available climate estimations of wind can differ substantially given the little understanding of how wind speed may change over the ocean in a warmer climate (IPCC, 2013). Studies such as Salisbury et al. (2013) suggest that other variables, in addition to wind forcing, influence the whitecap fraction, such as the seawater temperature or the sea state. New parameterization for whitecap fraction, based on satellite observations, claims that the whitecap-area based parameterization used by all the models in this study is misrepresenting the absolute values. Albert et al. (2015) suggests that for higher latitudes the values are overestimated, and underestimated for lower latitudes. If following that parameterization, the emission over the Mediterranean is underestimated. This could mean that the changes in seawater temperature would impact the SSA emission flux more substantially than suggested by this study.

The aerosol direct radiative effect (DRE) is defined as the difference between net radiative fluxes at TOA in the presence and absence of SSA. The radiative forcing depends on the AOD of the aerosol species in the atmosphere, the surface albedo and the vertical position of clouds. In this study, all-sky conditions were considered, i.e. clouds are included. Over the seawater surfaces, SSA directly scatters solar radiation back to space, resulting in a cooling effect on the climate by decreasing the amount of radiation absorbed by the water surface. Over land, there can be both cooling over the low-reflectance surfaces, and warming over high-albedo surfaces (e.g., Haywood and Boucher, 2000). Adding only a low absorbing aerosol, such as SSA, and assuming the same atmospheric and

cloud conditions for the all the runs (with and without SSA), the upward scattering by SSA will be the only radiation impact in this study.

Figure 12 shows the DRE due to SSA in the past (left panel) and the change in DRE due to the changing climate (right panel). These calculations are based on the AOD predicted by SILAM for the past and future. As expected, the past computations predict the highest cooling effect due to SSA over the areas where concentrations (Fig. 7, left-lower panel) are the highest and where the surface albedo is the lowest (seawater surfaces). The strongest effect is seen over the Mediterranean Sea due to the lowest cloud cover and the largest number of hours of sunlight per year. Studies such as Ma et al. (2008) and Lundgren et al. (2013), state that the impact of clouds can be substantial, reducing the direct radiative impact of SSA. The lowest cooling effect is predicted over land where the albedo is higher and SSA amount is the lowest. Conversely, warming is predicted where the albedo is high and the AOD is low, e.g. over the mountain tops in Norway and Italy. The current study estimates the upward scattering by SSA, at TOA, to be up to 0.5 W m^{-2} over seawater surfaces. This value is within the estimates on upward scattering of radiation by SSA: ranging between 0.08 and 6 W m^{-2}, at wavelengths in the range of 0.3-4 μm (Lewis and Schwartz, 2004).

Figure2, right panel, depicts the change in the DRE due to SSA between future and past. The results suggest overall cooling (negative change) in the future: North of Iceland, Norwegian and North Seas are the areas where the cooling is more accentuated. The Mediterranean area seems to be again the most sensitive area in our study: it is predicted an overall warming for this area, both over sea and over land, but also cooling, in particular in the east of the eastern basin. DRE pattern for the whole year is highly influenced by the summer period due to largest number of daylight hours. This can be seen in Fig. 13, right panel, which shows the change between future and past but considering only the summer months (JJA). This study predicts a substantial seasonal variation for the DRE in the sea surface waters. This is expected due to the variation shown in Sect. 3.2 and 3.3. The upward scattering in the summer time can be up to 1.7 times higher than in winter, due to lower cloudiness and lengthier daylight.

Figure 13 shows the change in winter (left panel) and summer (right) between the future and the past. The strongest impact in winter is seen over the Mediterranean area: negative over the sea surface and positive over land. In summer, the highest impact is over the seawater surfaces, predicting a cooling effect in the future, with exception over the western basin of the Mediterranean and the western side of the British Isles and France.

The results presented in this study for the present period are in accordance with the regional simulations for a summer month presented by Lundgren et al (2013) and the global simulations presented by, e.g. Grini et al. (2002) and Ma et al. (2008). The results are shown in Table 5.

The radiative forcing calculation is also sensitive to the SSA single scattering albedo. Thus, setting the SSA's single scattering albedo as low as 0.95 (Russel et al, 2002), leads to a wide areas over land where warming is substantial: essentially, over all surfaces with albedos exceeding 0.5 and low (<0.03) aerosol load (not shown). We have chosen to show results for a more realistic SSA single scattering albedo of 0.99 (Lundgren et al., 2013).

6 Conclusion

This study has compared predictions of SSA emissions, surface concentration and deposition from four CTMs for both current condition and future scenarios, focusing on the European Seas: Baltic, North, Mediterranean, and Black Seas. The three European-scale CTMs (EMEP, MATCH and SILAM) were driven by the regional climate model (RCA3) meteorology and by the hemispheric model (DEHM) boundary conditions. The hemispheric model was driven by the ECHMA5 meteorology. The impact of climate change on SSA production and fate, due to changes in wind speed and seawater temperature, was analysed. Additionally, consideration about the impact of seawater salinity on emissions was given.

The impact of climate change on SSA production and fate has different response from the models, with the similar results between DEHM and EMEP, and between MATCH and SILAM. DEHM-EMEP show almost no difference between future and past periods, and MATCH-SILAM shows a general increase of the emissions and surface concentrations with levels reaching 30% in change. The emissions increase is substantial in the Black Sea, Gulf of Bothnia (Baltic) and Levantine Sea (Mediterranean), correlating well with the wind-forcing ($\approx U_{10}^{3.41}$) computed with the changes predicted between the same periods. Nevertheless, the major driver of the changes of the sea-salt fluxes from the sea surface will be the changing seawater temperature, since near-surface wind speed is projected to stay nearly the same in the climate scenario used, in absolute levels the wind will change less than a meter per second, in average, between the two periods. The concentrations are predominantly increasing in Black and Mediterranean Sea. The impact of climate change on SSA on deposition is not really relevant; though an increase is projected around Iceland by all the models. Boundary conditions impact on the predictions is substantial.

The discrepancies between the models raised additional question about the implementation of the SSA production formulations, since three of the models are based on the same parameterizations. This study shows that the way a given parameterizations is implemented in the models and the temperature and salinity correction functions play an important role for the final scaling of the SSA flux: size range prescription may play a substantial role on the SSA flux calculation.

Simple calculations with the libRadTran allowed understanding the impact of SSA on the direct radiative forcing. According to this study the upward scattering by SSA, at TOA, can to be up to 0.5 W m^{-2} over the seawater surfaces in the present period, predicting an overall cooling in the future. The most affected areas by cooling will be North of Iceland, Norwegian and North Seas, and the eastern basin of the Mediterranean; warming is predicted manly in Mediterranean Sea, including over land.

Acknowledgements

This study was supported by the Nordic Council of Ministers, EnsCLIM and CarboNord projects. The authors also thank Antti Arola for his guidance in the radiative forcing calculations and interpretation of the results.

References

Albert, M. F. M. A., Anguelova, M. D., Manders, A. M. M., Schaap, M., and de Leeuw, G.: Parameterization of oceanic whitecap fraction based on satellite observations, Atmos. Chem. Phys. Discuss., 15, 21219-21269, doi:10.5194/acpd-15-21219-2015, 2015.

Andersson, C., Bergström, R., Bennet, C., Robertson, L., Thomas, M., Korhonen, H., Lehtinen, K. E. J., and Kokkola, H.: MATCH-SALSA – Multi-scale Atmospheric Transport and CHemistry model coupled to the SALSA aerosol microphysics model – Part 1: Model description and evaluation, Geosci. Model Dev., 8, 171-189, doi:10.5194/gmd-8-171-2015, 2015.

Andreas, E. L.: A new sea spray generation function for wind speeds up to 32 m s−1, J. Phys. Oceanogr., 28, 2175–2184, doi:10.1175/1520-0485(1998)028<2175:ANSSGF>2.0.CO;2., 1998

Andreas, E. L., Edson, J. B., Monahan, E. C., Rouault, M. P., and Smith, S. D.: The spray contribution to net evaporation from the sea: A review of recent progress, Boundary Layer Meteorol., 72(1–2), 3–52, doi:10.1007/BF00712389, 1995.

Bates, T. S., Coffman, D. J., Covert, D. S., and Quinn, P. K.: Regional marine boundary layer aerosol size distributions in the Indian, Atlantic, and Pacific Oceans: A comparison of INDOEX measurements with ACE-1, ACE-2, and Aerosols99, J. Geophys. Res., 107(D18), 8026, doi:10.1029/2001JD001174, 2002.

Bellouin, N., Rae, J., Jones, A., Johnson, C., Haywood, J., and Boucher, O.: Aerosol forcing in the Climate Model Intercomparison Project (CMIP5) simulations by HadGEM2-ES and the role of ammonium nitrate, J. Geophys. Res., 116, D20206, doi:10.1029/2011JD016074, 2011.

Boyer, T. P., Levitus S., Garcia, H. E., Locarnini, R. A., Stephens, C., Antonov, J. I.; Objective analyses of annual, seasonal, and monthly temperature and salinity for the world ocean on a 0.25 degrees grid. Int. J. Climatol. 25 (7), 931-945, 2005.

Boyd, P. W.: Ranking geo-engineering schemes, Nat. Geosci., 1, 722–724, doi:10.1038/ngeo348, 2008.

Brandt J, Brandt, J., Silver, J., Frohn, L. M., Geels, C., Gross, A., Hansen, A. B., Hansen, K. M., Hedegaard, G. B., Skjøth, C. A., Villadsen, H., Zare, A., and Christensen, J. H.: An integrated model study for Europe and North America using the Danish Eulerian Hemispheric Model with focus on intercontinental transport of air pollution. Atmos.Environ. 53:156-176, 2012.

Covert, D. S., Gras, J. L, Wiedensohler, A., and Stratmann, F.: Comparison of directly measured CCN with CCN modeled from the number-size distribution in the marine boundary layer during ACE I at Cape Grim, Tasmania, J. Geophys. Res., 103, 16,597-16,608, 1998.

de Leeuw, G., Andreas, E. L, Anguelova, M. D., Fairall, C. W., Lewis, E. R., O'Dowd, C., Schulz, M. and Schwartz, S. E.: Production flux of sea spray aerosol, Rev. Geophys., 49, RG2001, doi:10.1029/2010RG000349, 2011.

Dana, M. T., and Hales, J. M.; Statistical aspects of the washout of polydisperse aerosols. Atmos. Environ. 10, 45-50, 1976.

Emberson, L. D., Ashmore, M. R., Cambridge, H. M., Simpson, D., and Tuovinen, J. P.: Modelling stomatal ozone flux across Europe, Environ. Pollut., 109, 403–413, 2000.

Foltescu, V. L., Pryor, S. C. and Bennet, C.: Sea salt generation, dispersionand removal on the regional scale. Atmospheric Environment 39, 2123-2133, 2005.

Gregow, H., Ruosteenoja, K., Pimenoff, N., and Jylhä, K.: Changes in the mean and extreme geostrophic wind speeds in Northern Europe until 2100 based on nine global climate models. Int. J. Climatol., 32, 1834–1846, 2011.

Grini, A., Myhre, G., Sundet, J. K., and Isaksen, I. S. A.: Modeling the annual cycle of sea salt in the global 3D model OsloCTM2: Concentrations, fluxes, and radiative impact, J. Climate, 15, 1717–1730, 2002.

Gong, S. L.: A parameterization of sea-salt aerosol source function for sub- and super-micron particles, Global Biogeochem. Cycles, 17(4), 1097, doi:10.1029/2003GB002079, 2003.

Gong, S. L., Barrie, L. A., Prospero, J. M., Savoie, D. L., Ayers, G. P., Blanchet, J.-P., and Spacek, L.: Modelling sea-salt aerosols in the atmosphere: 2. Atmospheric concentrations and fluxes, J. Geophys. Res., 102(D3), 3819–3830, doi:10.1029/96JD03401, 1997.

Haywood, J., and Boucher, O.: Estimates of the direct and indirect radiative forcing due to tropospheric aerosols: A review, Rev. Geophys., 38(4), 513–543, doi:10.1029/1999RG000078, 2000.

Haywood, J., Ramaswamy, V., and Soden, B.: Tropospheric aerosol climate forcing in clear-sky satellite observations over the oceans, Science, 283, 1299– 1303, 1999.

Hjellbrekke, A.-G. & Fjæra, A. M.: Data Report: Acidifying and eutrophying compounds and particulate matter. EMEP/CCC-Report 1/2011, 2009.

Horn, H., Bonka, H., and Maqua, M.: Measured particle bound activity size-distribution, deposition velocity, 700 and activity concentration in rainwater after the Chernobyl accident, J. of Aerosol Science, 18, 681–684, 10.1016/0021-8502(87)90096-6, 1987.

Huebert, B. J., Bates, T., Russell, P. B., Shi, G., Kim, Y. J., Kawamura, K., Carmichael, G., and Nakajima, T.: An overview of ACE-Asia: Strategies for quantifying the relationships between Asian aerosols and their climatic impacts, J. Geophys. Res., 108(D23), 8633, doi:10.1029/2003JD003550, 2003.

IPCC: Climate Change 2013: The Physical Science Basis. Contribution of Working Group I to the Fifth Assessment Report of the Intergovernmental Panel on Climate Change [Stocker, T.F., D. Qin, G.-K. Plattner, M. Tignor, S.K. Allen, J. Boschung, A. Nauels, Y. Xia, V. Bex and P.M. Midgley (eds.)]. Cambridge University Press, Cambridge, United Kingdom and New York, NY, USA, 1535 pp, doi:10.1017/CBO9781107415324, 2013

Jylhä, K.: Empirical scavenging coefficients of radioactive substances released from Chernobyl, Atmos. Environ. A., 25, 263–270, 10.1016/0960-1686(91)90297-K, 1991.

Kjellström, E., Nikulin, G., Hansson, U., Strandberg, G., and Ullerstig, A.: 21st century changes in the European climate: uncertainties derived from an ensemble of regional climate model simulations, Tellus Series A-Dynamic Meteorology and Oceanography, 63, 24–40, 10.1111/j.1600-0870.2010.00475.x, 2011.

Kaskaoutis, D. G., Kambezidis, H. D., Hatzianastassiou, N., Kosmopoulos, P. G., and Badarinath, K. V. S.: Aerosol climatology: dependence of the Angstrom exponent on wavelength over four AERONET sites, Atmos. Chem. Phys. Discuss., 7, 7347-7397, doi:10.5194/acpd-7-7347-2007, 2007.

Kusmierczyk-Michulec J. and van Eijk, A.M.J.: Atmospheric Optics: Models, Measurements, and Target-in-the-Loop Propagation III, 74630G; Stephen M. Hammel; Alexander M. J. van Eijk; Mikhail A. Vorontsov, Editor(s) doi: 10.1117/12.828394, 2009.

Korhonen, H., K. Carslaw, S., and Romakkaniemi, S.: Enhancement of marine cloud albedo via controlled sea spray injections: A global model study of the influence of emission rates, microphysics and transport, Atmos. Chem. Phys., 10, 4133–4143, doi:10.5194/acp-10-4133-2010, 2010.

Kouznetsov, R. and Sofiev, M.: A methodology for evaluation of vertical dispersion and dry deposition of atmospheric aerosols, J. Geophys. Res., 117, 10.1029/2011JD016366, 2012.

Langner, J., Engardt, M., and Andersson, C.: European summer surface ozone 1990–2100, Atmos. Chem. Phys., 12, 10097-10105, doi:10.5194/acp-12-10097-2012, 2012.

Latham, J., and Smith, M. H.: Effect on global warming of wind dependent aerosol generation at the ocean surface, Nature, 347, 372–373, doi:10.1038/347372a0, 1990.

Lenton, T. M., and Vaughan, N. E.: The radiative forcing potential of different climate geoengineering options, Atmos. Chem. Phys., 9, 5539–5561, doi:10.5194/acp-9-5539-2009, 2009.

Lewis, E. R., and Schwartz, S. E.: Comment on "Size distribution of sea-salt emissions as a function of relative humidity," Atmos. Environ., 40, 588–590, doi:10.1016/j.atmosenv.2005.08.043, 2006.

Liao, H., Chen, W. T., and Seinfeld, J. H.: Role of climate change in global predictions of future tropospheric ozone and aerosols. J. Geophys. Res., 111, D12304, 2006.

Lundgren, K., Vogel, B.,Vogel, H., and Kottmeier, C.: Direct radiative effects of sea salt for the Mediterranean region under conditions of low to moderate wind speeds, J. Geophys. Res. Atmos., 118, 1906–1923, doi:10.1029/2012JD018629, 2013.

Ma, X., von Salzen, K., and Li, J.: Modelling sea salt aerosol and its direct and indirect effects on climate, Atmos. Chem. Phys., 8, 1311-1327, doi:10.5194/acp-8-1311-2008, 2008.

Mahowald, N. M., Lamarque, J.-F., Tie, X. X., and Wolff, E.: Sea-salt aerosol response to climate change: Last Glacial Maximum, preindustrial, and doubled carbon dioxide climates, J. Geophys. Res., 111, D05303, doi:10.1029/2005JD006459, 2006.

Manders, A. M. M., Schap, M., Querol, X., Albert, M. F., Vercauteren, J., Kuhlbusch, T. A. J., and Hoogerbrugge, R.: Sea salt concentrations across the European continent, Atmos. Environ., 44, 2434–2442, doi:10.1016/j.atmosenv.2010.03.028, 2010.

Mayer, B. and Kylling, A.: Technical note: The libRadtran software package for radiative transfer calculations - description and examples of use, Atmos. Chem. Phys., 5, 1855-1877, doi:10.5194/acp-5-1855-2005, 2005.

Mie, G.: Beiträge zur Optik trüber Medien, speziell kolloidaler Metallösungen [Contribution to the optics of turbid media, particularly of colloquial metal solutions Royal Aircraft Establishment], Ann. Phys.25(3), 377–445, 1908.

Monahan, E. C., Spiel, D. E., and Davidson, K. L.: A model of marine aerosol generation via whitecaps and wave disruption, in Oceanic Whitecaps, edited by E. C. Monahan and G. MacNiochaill, 167–193, D. Reidel, Norwell, Mass, 1986.

Mårtensson, E. M., Nilsson, E. D., de Leeuw, G., Cohen, L. H., and Hansson, H.-C.: Laboratory simulations and parameterization of the primary marine aerosol production, J. Geophys. Res., 108(D9), 4297, doi:10.1029/2002JD002263, 2003

Nakićenović, N.: Global greenhouse gas emissions scenarios: Integrated modeling approaches, Tech. Forecasting & Social Change, 63, 105–109, 2000.

Nilsson, E. D., Mårtensson, E. M., van Ekeren, J. S., de Leeuw, G., Moerman, M. M., and O'Dowd, C. D.: Primary marine aerosol emissions: Size resolved eddy covariance measurements with

estimates of the sea salt and organic carbon fractions, Atmos. Chem. Phys. Discuss., 7, 13,345–13,400, doi:10.5194/acpd-7-13345-2007, 2007.

NOAA: World Ocean Atlas 2013. http://www.nodc.noaa.gov/OC5/woa13/, 2013

O'Dowd, C., and de Leeuw, G.: Marine aerosol production: A review of the current knowledge, Philos. Trans. R. Soc. A, 365, 1753–1774, doi:10.1098/rsta.2007.2043, 2007.

O'Dowd, C. D., and Smith, M. H.: Physico-chemical properties of aerosol over the North East Atlantic: Evidence for wind speed related sub-micron sea-salt aerosol production, J. Geophys. Res., 98, 1137–l149, doi:10.1029/92JD02302, 1993.

O'Dowd, C., Lowe, J., Smith, M., and Kaye, A.: The relative importance of non-seasalt sulphate and sea-salt aerosol to the marine cloud condensation nuclei population: An improved multi-component aerosolcloud droplet parameterization, Q. J. R. Meteorol. Soc., 125, 1295–1313, 1999.

O'Dowd, C. D., Smith, M. H. Consterdine, I. E., and Lowe, J. A.: Marine aerosol, sea salt, and the marine sulphur cycle: A short review, Atmos. Environ., 31, 73–80, doi:10.1016/S1352-2310(96)00106-9, 1997

Ovadnevaite, J., Manders, A., de Leeuw, G., Ceburnis, D., Monahan, C., Partanen, A.-I., Korhonen, H., and O'Dowd, C. D.: A sea spray aerosol flux parameterization encapsulating wave state, Atmos. Chem. Phys., 14, 1837-1852, doi:10.5194/acp-14-1837-2014, 2014.

Pierce, J. R., and Adams, P. J.: Global evaluation of CCN formation by direct emission of sea salt and growth of ultrafine sea salt, J. Geophys. Res., 111, D06203, doi:10.1029/2005JD006186, 2006.

Pincus, R., Platnick, S., Ackerman, S. A., Hemler, R. S., and Hofmann, R. J. P.: Reconciling simulated and observed views of clouds: MODIS, ISCCP, and the limits of instrument simulators, Journal of Climate, 2011.

Pryor, S. C., and Barthelmie, R. J.: Particle dry deposition to water surfaces: processes and consequences. Marine Pollution Bulletin 41, 220-231, 2000.

Prank, M.: Evaluation of atmospheric composition simulations via comparison with remote-sensing and in-situ observations, Master's thesis, 74 pp., Dep. of Sci. and Technol., Univ. of Tartu, Tartu, Estonia, 2008.

Quinn, P. K., Coffman, D. J., Kapustin, V. N., Bates, T. S., Covert, D. S.: Aerosol optical properties in the marine boundary layer during the First Aerosol Characterization Experiment (ACE 1) and the underlying chemical and physical aerosol properties, J. Geophys. Res., 103, D13, 547-16,563, 1998

Roeckner, E., Brokopf, R., Esch, M., Giorgetta, M., Hagemann, S., Kornblueh, L., Manzini, E., Schlese, U., and Schulzweida, U.: Sensitivity of simulated climate to horizontal and vertical resolution in the ECHAM5 atmosphere model, J. Clim., 19, 3771–3791, 10.1175/JCLI3824.1, 2006.

Rodell, M., Houser, P.R., Jambor, U., Gottschalck, J., Mitchell, K., Meng, C.-J., Arsenault, K. Cosgrove, B., Radakovich, J., Bosilovich, M., Entin, J.K., Walker, J.P., Lohmann, D., and Toll, D.: The Global Land Data Assimilation System, Bull. Amer. Meteor. Soc., 85(3), 381-394, 2004

Russel, P.B., and Heintzenberg, J.: An overview of the ACE-2 clear sky column closure experiment (CLEARCOLUMN). Tellus B, [S.l.], 52(2), ISSN 1600-0889, doi:http://dx.doi.org/10.3402/tellusb.v52i2.16173, 2011.

Russell, P. B., Redemann, J., Schmid, B., Bergstrom., R. W., Livingston, J. M., McIntosh, D. M., Ramirez, S. A., Hartley, S., Hobbs, P. V., Quinn, P. K., Carrico, C. M., Rood, M. J., Öström, E., Noone, K. J., von Hoyningen-Huene, W., and Remer, L.: Comparison of Aerosol Single Scattering Albedos Derived by Diverse Techniques in Two North Atlantic Experiments. J. Atmos. Sci., 59, 609–619, doi: http://dx.doi.org/10.1175/1520-0469(2002)059<0609:COASSA>2.0.CO;2, 2002

Salisbury, D. J., Anguelova, M. D., and Brooks, I. M.: On the variability of whitecap fraction using satellite-based observations, J. Geophys. Res.-Oceans, 118, 6201–6222, 2013.

Samuelsson, Jones, P., Willén, C. G., Ullerstig, U., Gollvik, A., Hansson, S., Jansson, U., Kjellström, C., Nikulin, E., and Wyser, K.: The Rossby Centre Regional Climate model RCA3: Model description and performance, Tellus A, 63, 4–23, doi:10.111/j.1600-0870.2010.00478.x, 2011.

Seinfield, J. H., and Pandis, S. N.: Atmospheric Chemistry and Physics: From Air Pollution to Climate Change, 2nd ed., 1232, John Wiley, Hoboken, N. J., 2006.

Simpson, D., Andersson, C., Christensen, J.H., Engardt, M., Geels, C., Nyiri, A., Posch, M., Soares, J., Sofiev, M., Wind, P., and Langner, J.: Impacts of climate and emission changes on nitrogen

deposition in Europe: a multi-model study, Atmos. Chem. Phys., 14, 6995-7017, doi:10.5194/acp-14-6995-2014, 2014.

Simpson, D., Fagerli, H., Jonson, J. E., Tsyro, S., Wind, P., and Tuovinen, J.-P: Transboundary Acidification, Eutrophication and Ground Level Ozone in Europe, PART I, Unified EMEP Model Description, 1-104, 2003.

Smith, F. B., and Clark, M. J.: The transport and deposition of radioactive debris from the Chernobyl nuclear power plant accident with special emphasis on consequences to the United Kingdom, Meteorological Office Scientific Paper no. 42, HMSO London, 1989.

Sofiev, M., Siljamo, P., Valkama, I., Ilvonen, M., and Kukkonen, J.: A dispersion modelling system SILAM and its evaluation against ETEX data, Atmos. Environ., 40, 674–685, 10.1016/j.atmosenv.2005.09.069, 2006.

Sofiev, M., Soares, J., Prank, M., de Leeuw, G., and Kukkonen, J.: A regional-to-global model of emission and transport of sea salt particles in the atmosphere, J. Geophys. Res., 116, D21302, doi:10.1029/2010JD014713, 2011.

Struthers, H., Ekman, A. M. L., Glantz, P., Iversen, T., Kirkevåg, A., Mårtensson, E. M., Seland, Ø., and Nilsson, E. D.: The effect of sea ice loss on sea salt aerosol concentrations and the radiative balance in the Arctic, Atmos. Chem. Phys., 11, 3459-3477, doi:10.5194/acp-11-3459-2011, 2011.

Tsyro, S., Aas, W., Soares, J., Sofiev, M., Berge, H., and Spindler, G.: Modelling of sea salt pollution over Europe: key uncertainties and comparison with observations Atmos. Chem. Phys., 11, 10367-10388, doi:10.5194/acp-11-10367-2011, 2011.

Textor, C., Schulz, M., Guibert, S., Kinne, S., Balkanski, Y., Bauer, S., Berntsen, T., Berglen, T., Boucher, O., Chin, M., Dentener, F., Diehl, T., Easter, R., Feichter, H., Fillmore, D., Ghan, S., Ginoux, P., Gong, S., Grini, A., Hendricks, J., Horowitz, L., Huang, P., Isaksen, I., Iversen, I., Kloster, S., Koch, D., Kirkevåg, A., Kristjansson, J. E., Krol, M., Lauer, A., Lamarque, J. F., Liu, X., Montanaro, V., Myhre, G., Penner, J., Pitari, G., Reddy, S., Seland, Ø., Stier, P., Takemura, T., and Tie, X.: Analysis and quantification of the diversities of aerosol life cycles within AeroCom, Atmos. Chem. Phys., 6, 1777-1813, doi:10.5194/acp-6-1777-2006, 2006.

Twomey S.: Atmospheric Aerosol, Elviser, Amesterdam, 1977.

Tørseth, K., Aas, W., Breivik, K., Fjæraa, A. M., Fiebig, M., Hjellbrekke, A. G., Lund Myhre, C., Solberg, S., and Yttri, K. E.: Introduction to the European Monitoring and Evaluation Programme (EMEP) and observed atmospheric composition change during 1972–2009, Atmos. Chem. Physics, 12, 5447–5481, 10.5194/acp-12-5447-2012, http://www.atmos-chem-phys.net/12/5447/2012/, 2012.

Wang, M., Ghan, S., Ovchinnikov, M., Liu, X., Easter, R., Kassianov, E., Qian, Y., and Morrison, H.: Aerosol indirect effects in a multi-scale aerosol-climate model PNNL-MMF, Atmos. Chem. Phys., 11, 5431-5455, doi:10.5194/acp-11-5431-2011, 2011.

Witek, M. L., P. J. Flatau, J. Teixeira, and K. M. Markowicz: Numerical investigation of sea salt aerosol size bin partitioning in global transport models: Implications for mass budget and optical depth, Aerosol Sci. Technol., 45, 401–414, doi:10.1080/02786826.2010.541957, 2011.

Witek, M. L., Flatau, P. J., Quinn, P. K., and Westphal, D. L.: Global sea-salt modeling: Results and validation against multicampaign shipboard measurements, J. Geophys. Res., 112, D08215, doi:10.1029/2006JD007779, 2007a.

Witek, M. L., Flatau, P. J., Teixeira, K., and Westphal, D. L: Coupling an ocean wave model with a global aerosol transport model: A sea salt aerosol parameterization perspective, Geophys. Res. Lett., 34, L14806, doi:10.1029/2007GL030106, 2007b.

van Loon, M., Tarrasón, L., and Posch, M.: Modelling Base Cations in Europe, Technical Report MSC-W, Norwegian Meteorological Institute, ISSN 0804-2446, 2005

Zhang, L., Gong, S., Padro, J., and Barrie, L.: A size-segregated particle dry deposition scheme for an atmospheric aerosol module. Atmospheric Environment 35, 549-560., 2001.

Atmos. Chem. Phys. Discuss., doi:10.5194/acp-2015-1056, 2016
Manuscript under review for journal Atmos. Chem. Phys.
Published: 16 February 2016

Table 1 Model characteristics for SSA computations.

model	**mode**	**Dp [μm]**	**source function**	**dependency**	**humidity**	**Lowest model layer thickness (m)**
DEHM	fine	<1.3	MA02	T S	static (80%)	60
	coarse	[1.3-10]	MO86	S		
EMEP	fine	<2.5	MA02	T	static (80%)	90
	coarse	[2.5-10]	MO86	-		
MATCH	fine	[0.02–0.1] [0.1–1] [1–2.5]	MA02	T S	dynamic	60
	coarse	[2.5–10]	MO86	T (SO11) S		
SILAM	fine	[0.01–0.1] [0.1–1.5]	SO11	T S	dynamic	25
	coarse	[1.5–6]				
		[6–15]	SO11	T S		
		[15-30]				

T: temperature, **S**: salinity, **MO86**: Monahan et al. (1986); **MA03**: Mårtensson et al. (2003), **SO11**: Sofiev et al. (2011). In bold, the modes not used for the PM_{10} analysis.

Atmos. Chem. Phys. Discuss., doi:10.5194/acp-2015-1056, 2016
Manuscript under review for journal Atmos. Chem. Phys.
Published: 16 February 2016

Atmospheric Chemistry and Physics Discussions
Open Access

Table 2 Assumption for the radiative transfer modelling libRadTran2.0 for present and future.

Clouds (icy and wet)	cloud cover	monthly averaged RCA3 fields (1990-2009); same for both periods
	AOD	monthly averaged MODIS data (2002-2014) (Pincus et al. 2011); same for both periods
	vertical profiles	wc.dat*; wc.dat*
Atmospheric properties	vertical profiles	subarctic winter, latitude over 60°: afglsw.dat* subarctic summer, latitude over 60°: afglss.dat* mid-latitude winter, latitude below 60°: afglmw.dat* mid-latitude summer, latitude below 60°: afglms.dat*
	altitude, pressure and temperature	monthly averaged RCA3 fields (1990-2009); same for both periods
Aerosol properties	vertical profile	aerosol_default*
	AOD	dynamic: SILAM AOD calculations
	asymmetry factor	0.8 (Ma et al. 2008)
	single scattering albedo	0.99 (Lundgren et al, 2013)
	angstrom coefficient	0.2 (Kaskaoutis et al, 2007; Kusmierczyk-Michulec & van Eijk, 2009)
solar zenith angle		dynamic: computed with libRadTran sza tool
surface albedo		monthly averaged NOAA data (1990-2012) (Rodell et al., 2004); same for both periods
RTE solver		DISORT
integrated shortwave calculation scheme		KATO2 (wavelength ~[0.2, 4] μm)

*standard file in libRadTran

Atmos. Chem. Phys. Discuss., doi:10.5194/acp-2015-1056, 2016
Manuscript under review for journal Atmos. Chem. Phys.
Published: 16 February 2016

Atmospheric Chemistry and Physics Discussions
Open Access
EGU

Table 3 Statistical evaluation of model results for surface SSA concentration ($Na^{+}\mu g\ m^{-3}$), considering the whole year (annual), winter (December, January and February) and summer periods (June, July and August), for 33 EMEP measuring sites, between 1990 and 2009.

	annual	**winter**	**summer**	**annual**	**winter**	**summer**
Obs	0.72	0.94	0.55			
DEHM	1.08	1.39	0.74			
EMEP	0.64	0.75	0.49			
MATCH	0.45	0.42	0.42			
SILAM	0.86	0.78	0.94			
		correlation			StdRatio	
DEHM	0.85	0.87	0.81	1.72	1.57	1.79
EMEP	0.82	0.84	0.80	0.69	0.54	0.85
MATCH	0.75	0.82	0.77	0.48	0.33	0.66
SILAM	0.71	0.77	0.75	1.05	0.75	1.59
		RMSE			Bias	
DEHM	0.97	1.11	0.70	0.36	0.45	0.18
EMEP	0.53	0.75	0.36	-0.08	-0.18	-0.06
MATCH	0.69	1.03	0.41	-0.27	-0.52	-0.14
SILAM	0.71	0.76	0.74	0.14	-0.16	0.38

Atmos. Chem. Phys. Discuss., doi:10.5194/acp-2015-1056, 2016
Manuscript under review for journal Atmos. Chem. Phys.
Published: 16 February 2016

Atmospheric Chemistry and Physics Discussions
Open Access

Table 4 Statistical evaluation of model results for SSA wet deposition (Na^{+}mg m^{-2}), considering the whole year (annual), winter (December, January and February) and summer periods (June, July and August) for 133 EMEP measurement sites, between 1990 and 2009. SILAM5m is the evaluation if considering the whole possible size range for SSA Dp = [0.01-30] μm.

	annual	**winter**	**summer**	**annual**	**winter**	**summer**
obs	1.59E+06	6.88E+05	1.36E+05			
DEHM	1.41E+06	5.59E+05	1.40E+05			
EMEP	1.64E+06	6.44E+05	1.65E+05			
MATCH	6.08E+05	1.77E+05	9.64E+04			
SILAM	8.42E+05	2.81E+05	1.25E+05			
SILAM5m	1.70E+06	6.70E+05	1.83E+05			
		correlation			StdRatio	
DEHM	0.55	0.53	0.41	0.36	0.31	0.55
EMEP	0.38	0.32	0.33	0.47	0.44	0.53
MATCH	0.49	0.50	0.34	0.13	0.11	0.26
SILAM	0.49	0.45	0.38	0.22	0.19	0.41
SILAM5m	0.62	0.63	0.37	0.86	0.84	0.93
		RMSE			Bias	
DEHM	3477	5513	866	-114	-327	10
EMEP	3778	6006	912	34	-112	74
MATCH	3879	6122	892	-634	-1304	-102
SILAM	3737	5945	871	-483	-1038	-29
SILAM5m	3335	5070	1032	73	-44	122

Atmos. Chem. Phys. Discuss., doi:10.5194/acp-2015-1056, 2016
Manuscript under review for journal Atmos. Chem. Phys.
Published: 16 February 2016

Atmospheric Chemistry and Physics Discussions
Open Access

Table 5 Predicted direct radiative effect (W m^{-2}) by SSA for the past period

	annual	**winter**	**summer**
sea	-0.25±0.22	-0.077±0.053	-0.21±0.012
land	-0.20±0.18	-0.073±0.0019	-0.083±0.0030

Atmos. Chem. Phys. Discuss., doi:10.5194/acp-2015-1056, 2016
Manuscript under review for journal Atmos. Chem. Phys.
Published: 16 February 2016

Atmospheric Chemistry and Physics Discussions
Open Access

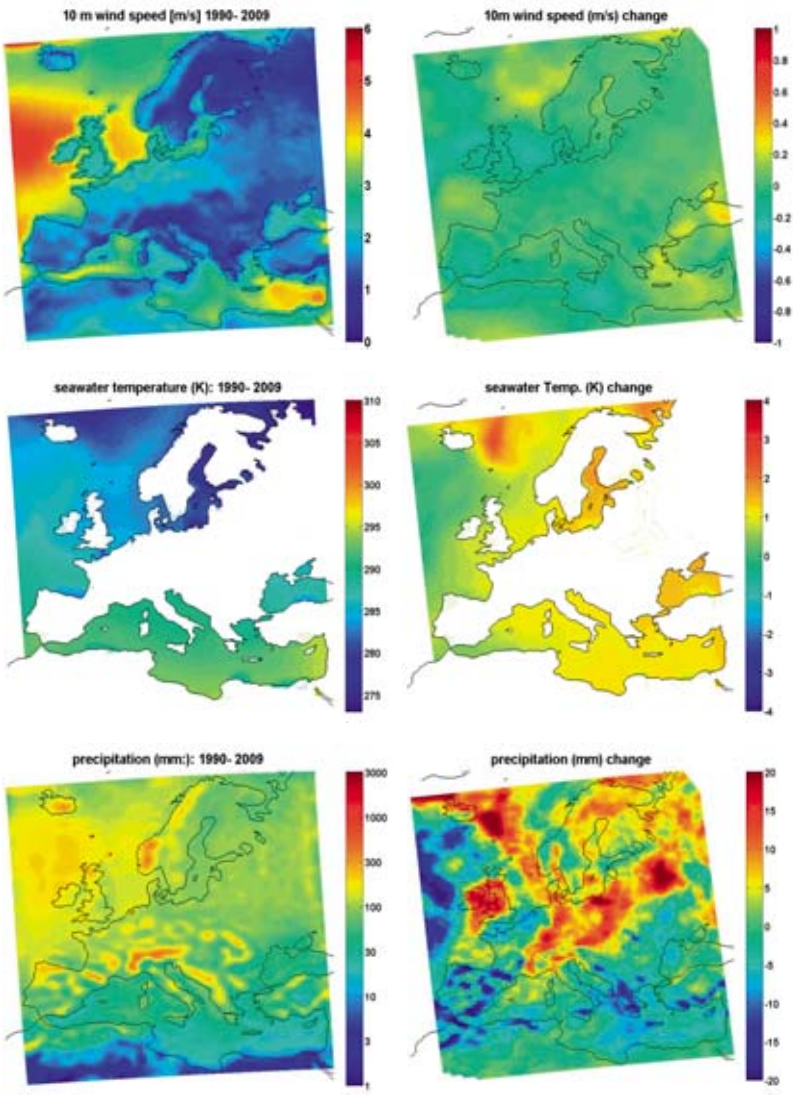

Figure 1. Top: Sea surface temperature (K), middle: wind speed (m s^{-1}), bottom: precipitation (mm). Left panel: mean value for the past period (1990-2009); right panel: absolute difference between the future (2040-2059) and past periods.

Atmos. Chem. Phys. Discuss., doi:10.5194/acp-2015-1056, 2016
Manuscript under review for journal Atmos. Chem. Phys.
Published: 16 February 2016

Atmospheric Chemistry and Physics Discussions
Open Access

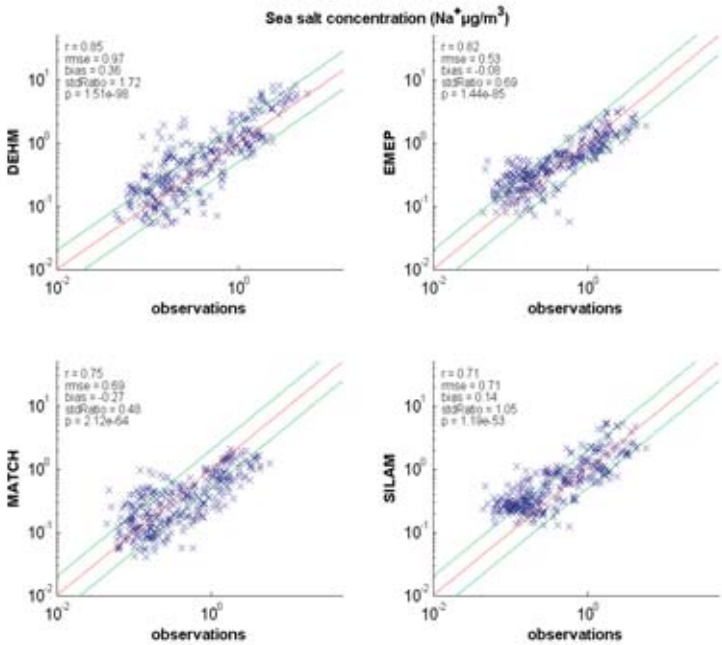

Figure 2. Model-measurement comparison for Na^+ monthly mean concentration ($\mu g\ m^{-3}$) for 29 EMEP measuring sites, between 1990 and 2009. The Person correlation (r), root mean square error (rmse), bias, standard deviation ration (stdRatio), p-value (p), 1:1 (red solid), 1:2 (green), and 2:1 (green) lines are shown for each CTM.

Atmos. Chem. Phys. Discuss., doi:10.5194/acp-2015-1056, 2016
Manuscript under review for journal Atmos. Chem. Phys.
Published: 16 February 2016

Atmospheric Chemistry and Physics
Discussions
Open Access

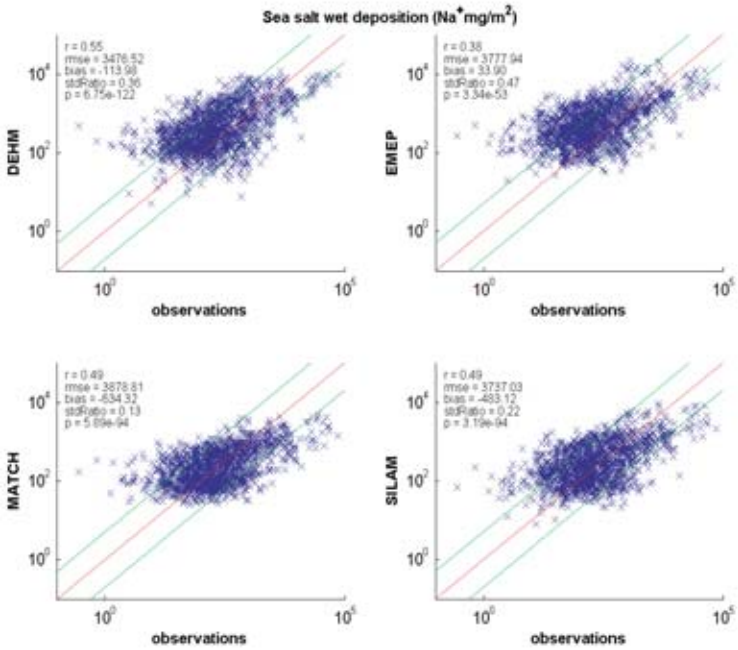

Figure 3. Model-measurement comparison for Na^+ monthly wet deposition (μg m^{-2}) for 133 EMEP measuring sites, between 1990 and 2009. The Person correlation (r), root mean square error (rmse), bias, standard deviation ration (stdRatio), p-value (p), 1:1 (red solid), 1:5 (green), and 5:1 (green) lines are shown for each CTM.

Atmos. Chem. Phys. Discuss., doi:10.5194/acp-2015-1056, 2016
Manuscript under review for journal Atmos. Chem. Phys.
Published: 16 February 2016

Atmospheric Chemistry and Physics Discussions
Open Access

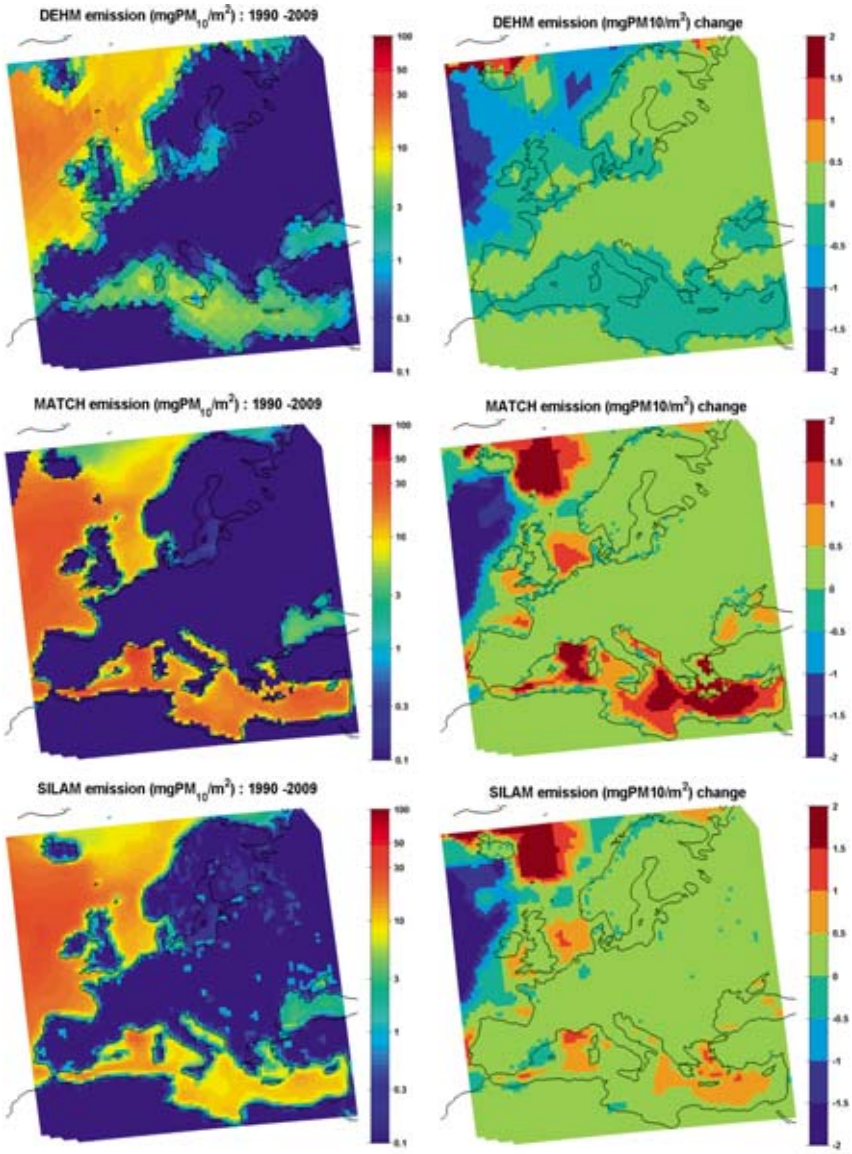

Figure 4. Annual sea salt emission ($mgPM_{10}\ m^{-2}$) for DEHM, MATCH and SILAM models. Left panel mean value for the past period (1990-2009); right panel: absolute difference between the future (2040-2059) and past periods.

Atmos. Chem. Phys. Discuss., doi:10.5194/acp-2015-1056, 2016
Manuscript under review for journal Atmos. Chem. Phys.
Published: 16 February 2016

Atmospheric Chemistry and Physics
Discussions
Open Access

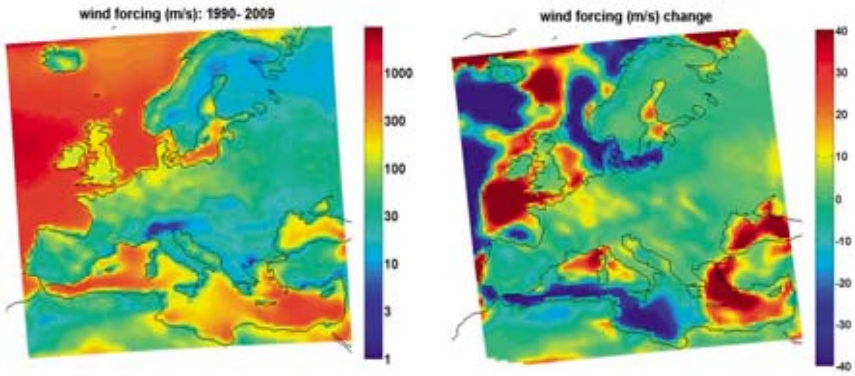

Figure 5. Wind forcing ($\approx U_{10}^{3.41}$). Left panel: past period (1990-2009); right panel: absolute difference between the future (2040-2059) and past periods.

Atmos. Chem. Phys. Discuss., doi:10.5194/acp-2015-1056, 2016
Manuscript under review for journal Atmos. Chem. Phys.
Published: 16 February 2016

Atmospheric Chemistry and Physics Discussions
Open Access

1

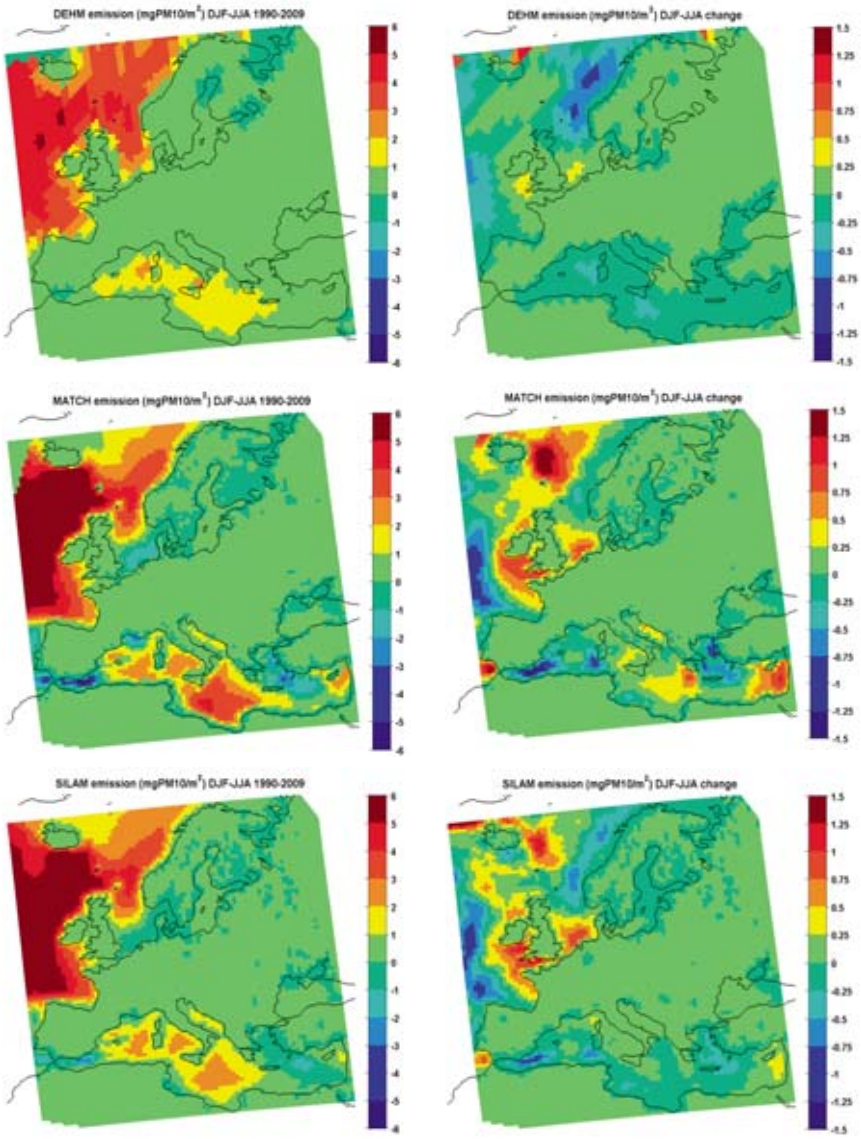

2 **Figure 6** Sea salt emission (mgPM_{10} m^{-2}) difference between winter (December, January and
3 February, DJF) and summer (June, July and August, JJA) for DEHM, MATCH and SILAM

Atmos. Chem. Phys. Discuss., doi:10.5194/acp-2015-1056, 2016
Manuscript under review for journal Atmos. Chem. Phys.
Published: 16 February 2016

models. Left panel: past period (1990-2009); right panel: absolute difference between the future (2040-2059) and past periods.

Atmos. Chem. Phys. Discuss., doi:10.5194/acp-2015-1056, 2016
Manuscript under review for journal Atmos. Chem. Phys.
Published: 16 February 2016

Atmospheric Chemistry and Physics Discussions
Open Access

1

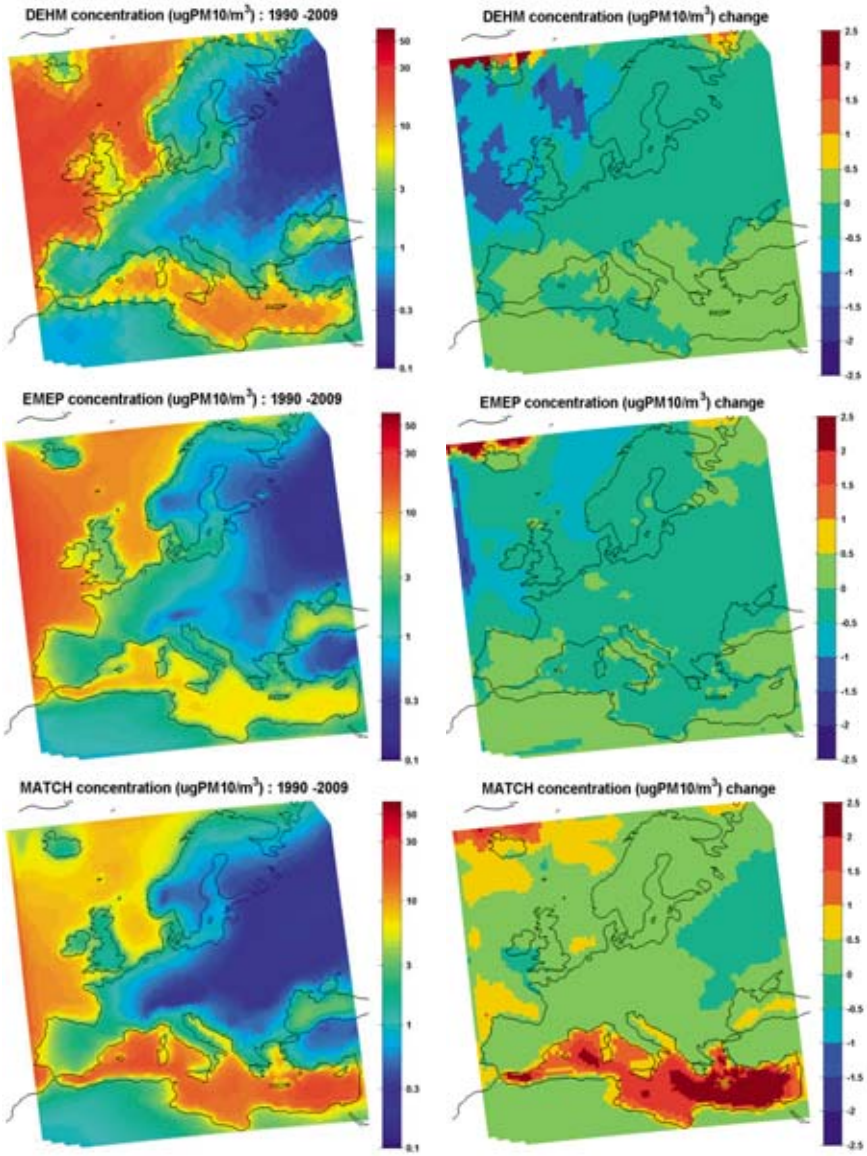

Atmos. Chem. Phys. Discuss., doi:10.5194/acp-2015-1056, 2016
Manuscript under review for journal Atmos. Chem. Phys.
Published: 16 February 2016

Atmospheric Chemistry and Physics Discussions
Open Access

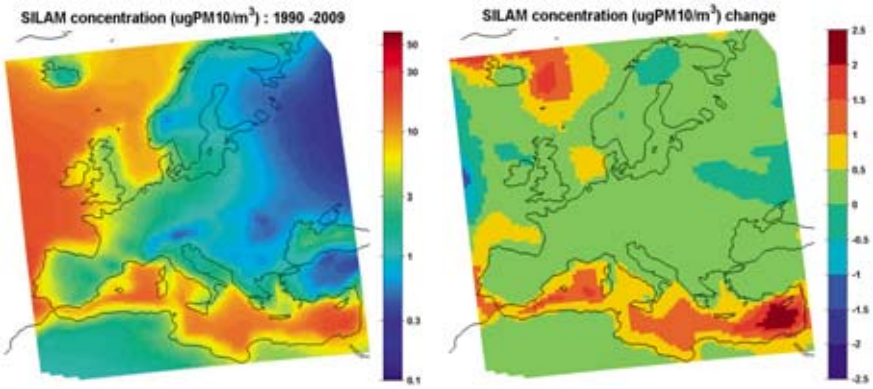

Figure 7. Sea salt surface concentration (μgPM_{10} m^{-3}) for DEHM, MATCH, EMEP and SILAM models. Left panel: mean value for the past period (1990-2009); right panel: absolute difference between the future (2040-2059) and past periods.

Atmos. Chem. Phys. Discuss., doi:10.5194/acp-2015-1056, 2016
Manuscript under review for journal Atmos. Chem. Phys.
Published: 16 February 2016

Atmospheric Chemistry and Physics Discussions
Open Access

1

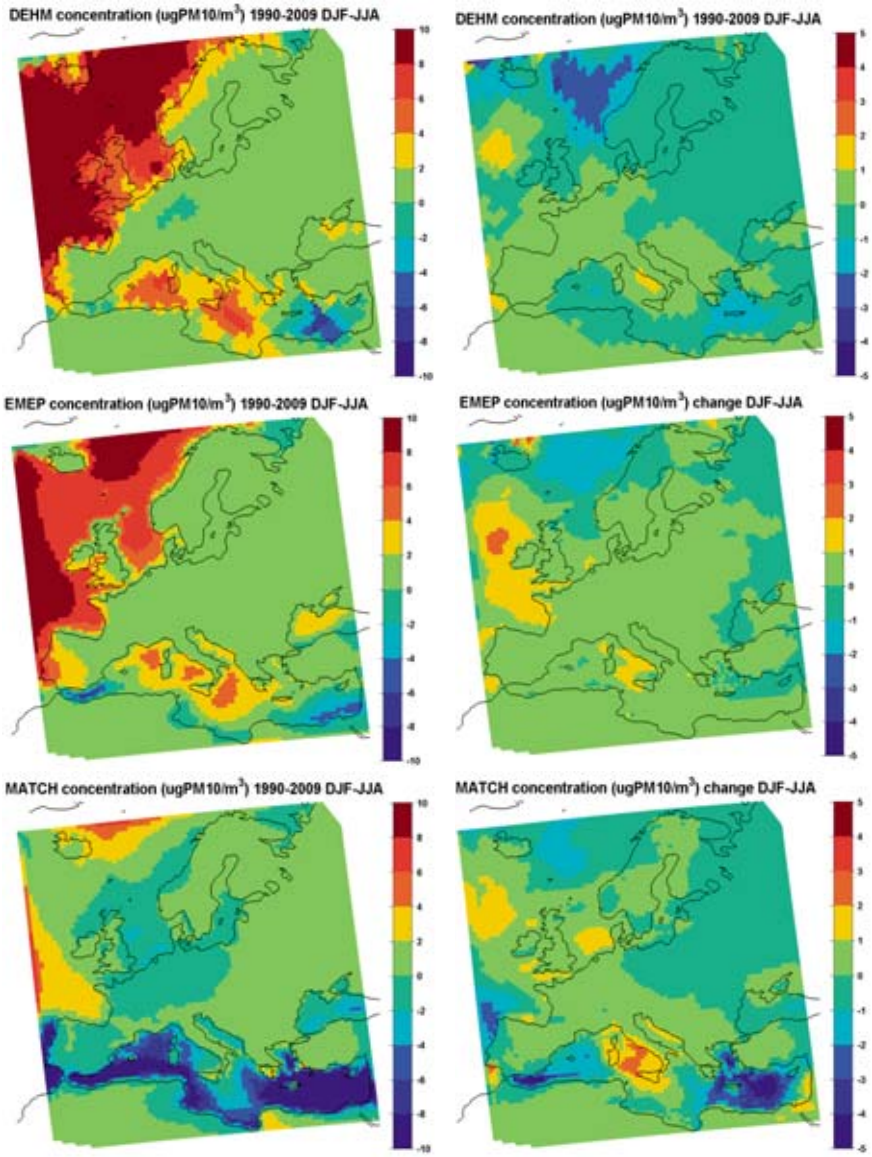

Atmos. Chem. Phys. Discuss., doi:10.5194/acp-2015-1056, 2016
Manuscript under review for journal Atmos. Chem. Phys.
Published: 16 February 2016

Atmospheric Chemistry and Physics Discussions
Open Access

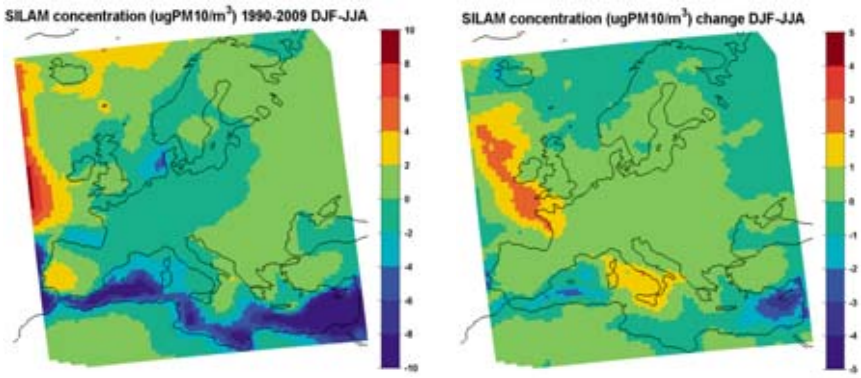

Figure 8 Sea salt concentration ($\mu gPM_{10}\ m^{-3}$) difference between winter (December, January and February, DJF) and summer (June, July and August, JJA) for DEHM, MATCH and SILAM models. Left panel: past period (1990-2009); right panel: absolute difference between the future (2040-2059) and past periods.

Atmos. Chem. Phys. Discuss., doi:10.5194/acp-2015-1056, 2016
Manuscript under review for journal Atmos. Chem. Phys.
Published: 16 February 2016

Atmospheric Chemistry and Physics Discussions
Open Access

1

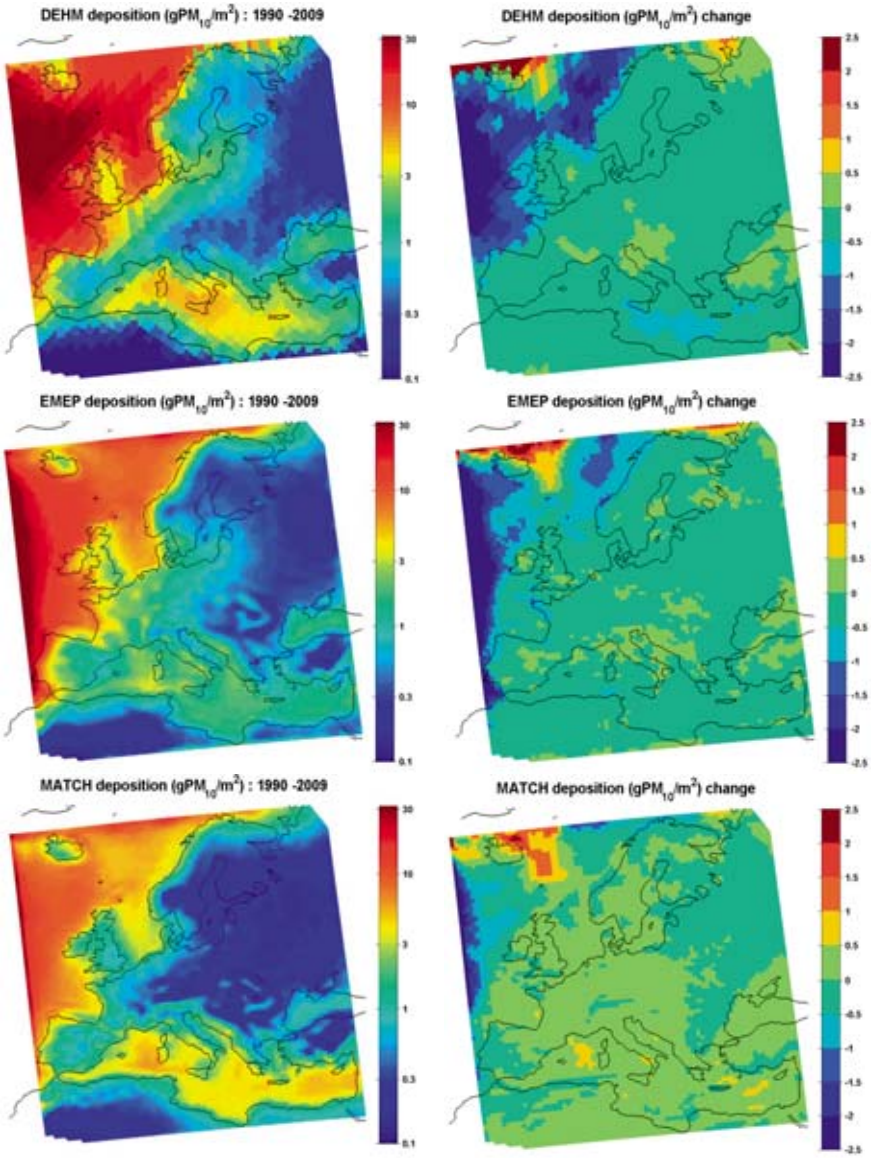

Atmos. Chem. Phys. Discuss., doi:10.5194/acp-2015-1056, 2016
Manuscript under review for journal Atmos. Chem. Phys.
Published: 16 February 2016

Atmospheric Chemistry and Physics Discussions
Open Access

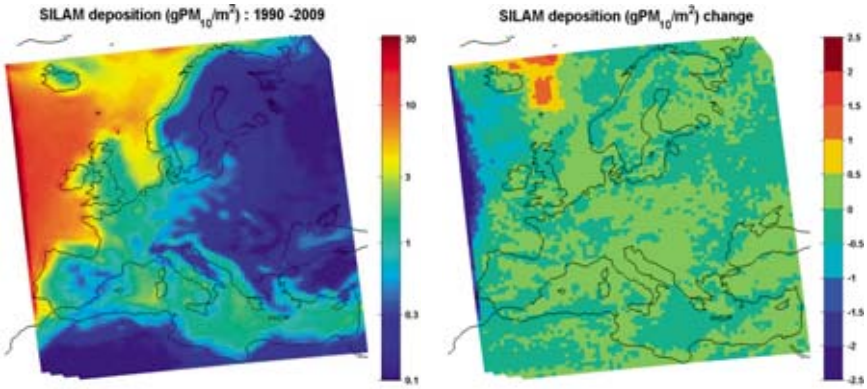

Figure 9 Sea salt deposition (wet+dry) ($mgPM_{10}$ m^{-2}) for DEHM, MATCH, EMEP and SILAM models. Left panel: mean value for the past period (1990-2009); right panel: absolute difference between the future (2040-2059) and past periods.

Atmos. Chem. Phys. Discuss., doi:10.5194/acp-2015-1056, 2016
Manuscript under review for journal Atmos. Chem. Phys.
Published: 16 February 2016

Atmospheric Chemistry and Physics Discussions
Open Access

1

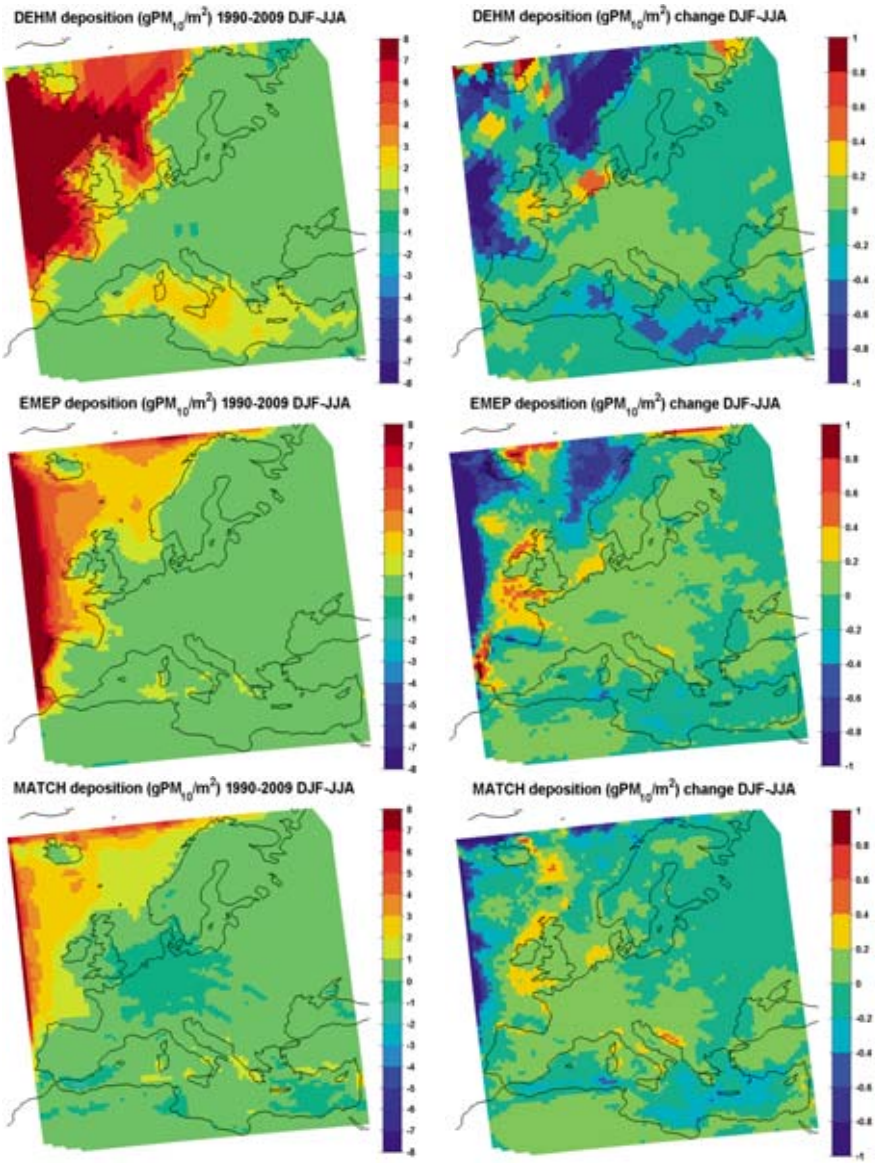

Atmos. Chem. Phys. Discuss., doi:10.5194/acp-2015-1056, 2016
Manuscript under review for journal Atmos. Chem. Phys.
Published: 16 February 2016

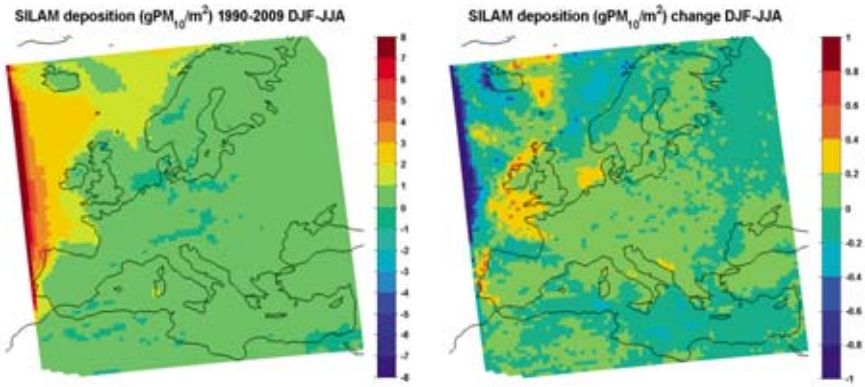

Figure 10 Sea salt annual deposition (gPM_{10} m^{-2}) difference between winter (December, January and February, DJF) and summer (June, July and August, JJA) for DEHM, MATCH and SILAM models. Left panel: past period (1990-2009); right panel: absolute difference between future (2040-2059) and past periods.

Atmos. Chem. Phys. Discuss., doi:10.5194/acp-2015-1056, 2016
Manuscript under review for journal Atmos. Chem. Phys.
Published: 16 February 2016

Atmospheric Chemistry and Physics Discussions
Open Access

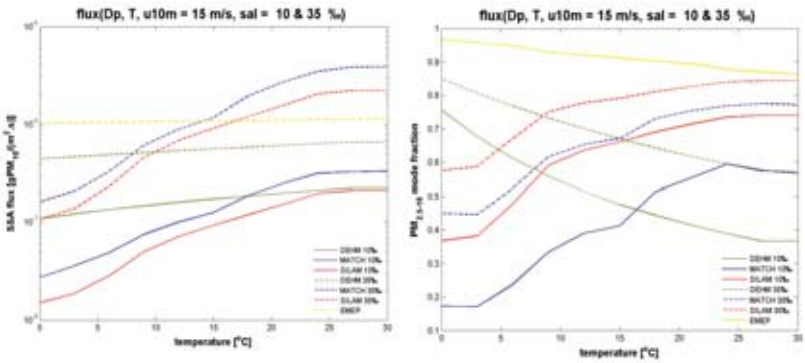

Figure 11. SSA mass flux [gPM_{10} m^{-2} s^{-1})] box calculations (left) and coarse mode fraction of the mass flux (right): as a function of radius (dry for DEHM and SILAM and RH = 80 % for MATCH) and temperature, for wind speed 15 m s^{-1} and salinities 10 ‰ and 35 ‰.

Atmos. Chem. Phys. Discuss., doi:10.5194/acp-2015-1056, 2016
Manuscript under review for journal Atmos. Chem. Phys.
Published: 16 February 2016

Atmospheric Chemistry and Physics Discussions
Open Access

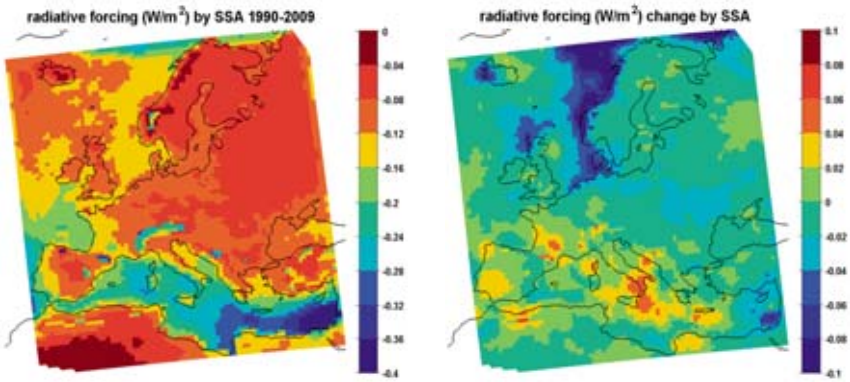

Figure 12. Radiative forcing by sea salt (W m^{-2}). Left panel: past period (1990-2009); right panel: absolute difference between future (2040-2059) and past periods.

Atmos. Chem. Phys. Discuss., doi:10.5194/acp-2015-1056, 2016
Manuscript under review for journal Atmos. Chem. Phys.
Published: 16 February 2016

Atmospheric Chemistry and Physics Discussions
Open Access

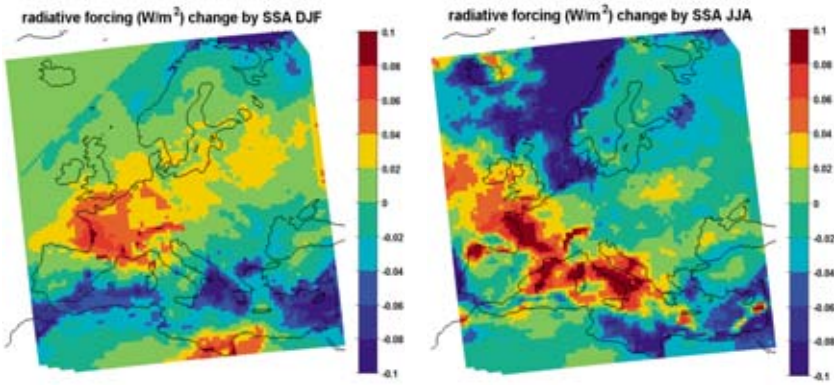

Figure 13. Radiative forcing by sea salt (W m^{-2}): difference between future (2040-2059) and past periods. Left panel: winter (December, January and February); right panel: summer (June, July and August)

Suplements

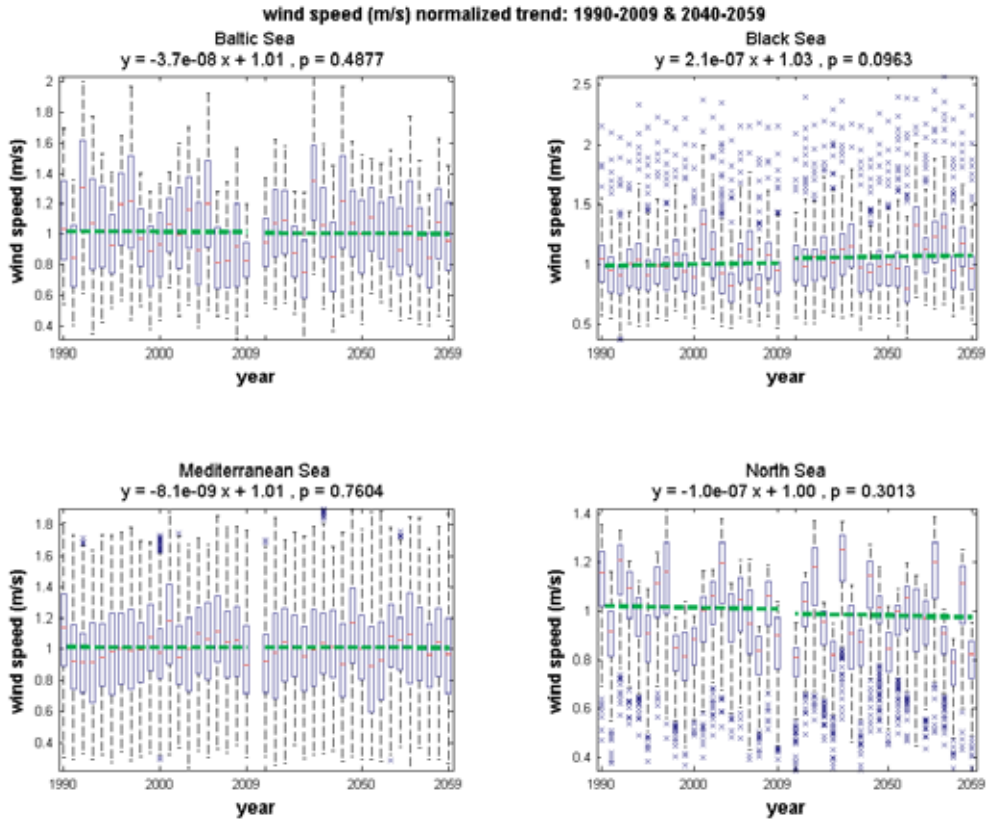

Figure S1 Annual mean win speed (m s^{-1}) normalized trend (y) over the past and future periods (x [year]), over the Baltic, Black, North and Mediterranean Seas. Only sea cells considered.

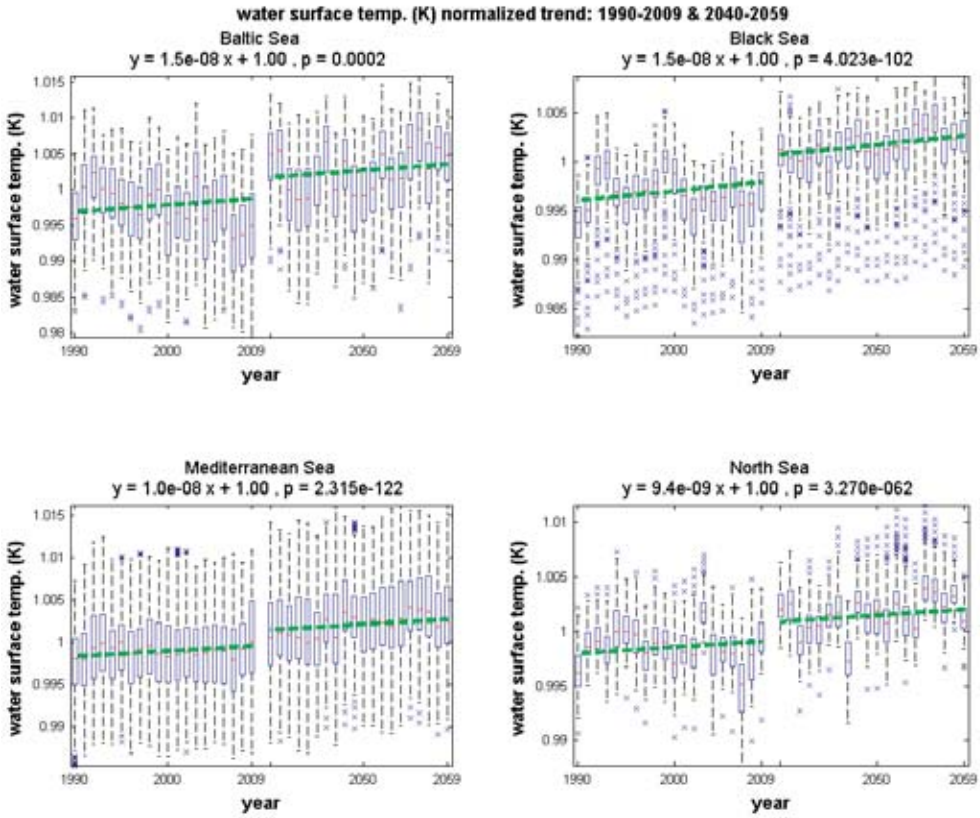

Figure S2 Annual mean water surface temperature (K) normalized trend (y) over the past and future periods (x [year]), over the Baltic, Black, North and Mediterranean Seas. Only sea cells considered.

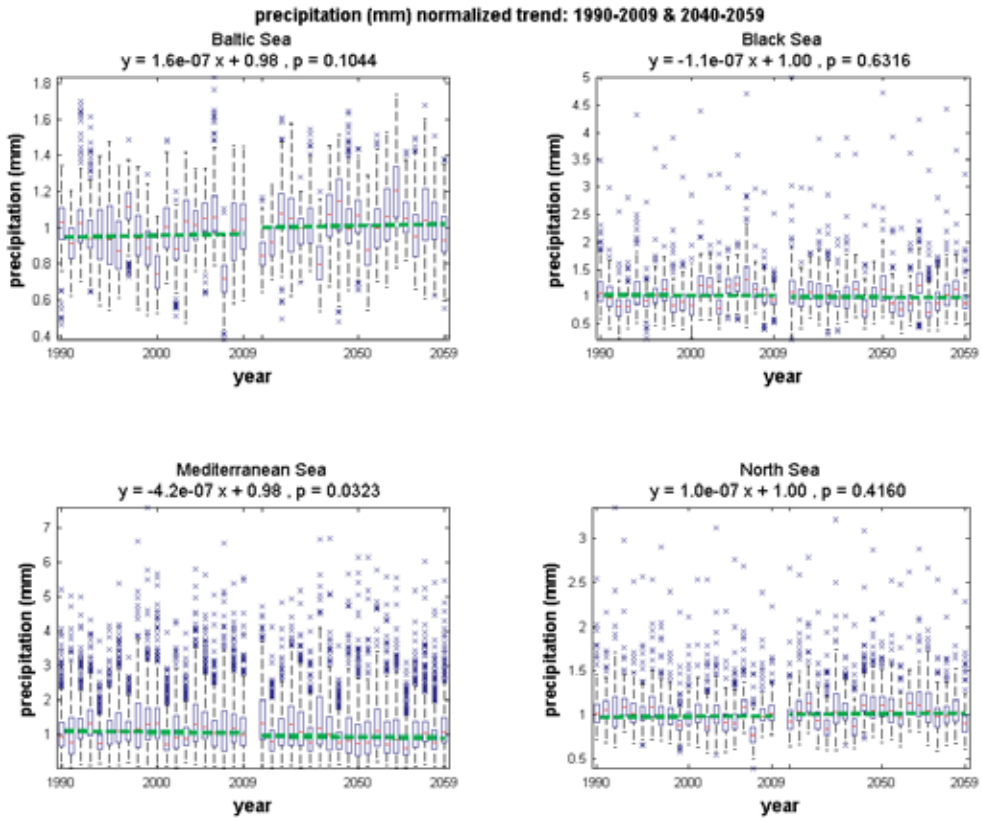

Figure S3 Annual precipitation (mm) normalized trend (y) over the past and future periods (x [year]), over the Baltic, Black, North and Mediterranean Seas. Only sea cells considered.

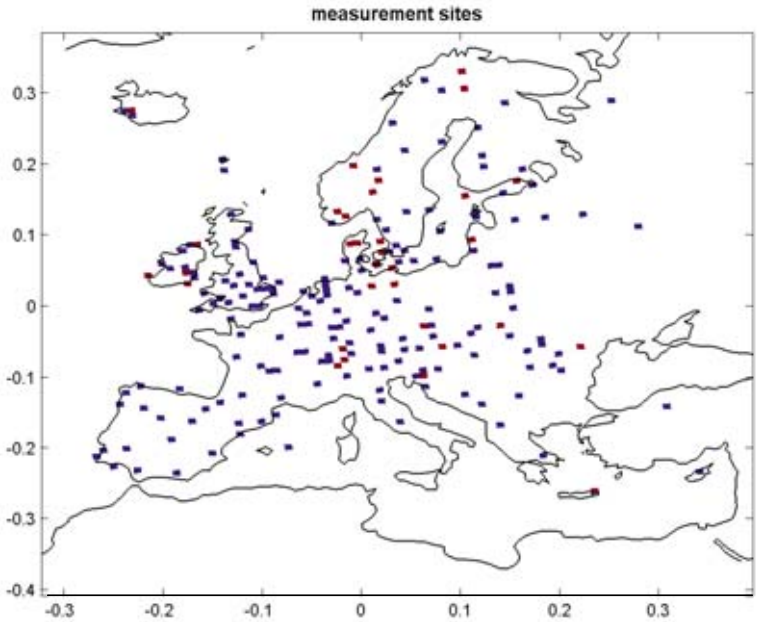

Figure S4 Location of the EMEP measurement sites measuring concentration and wet deposition of Na^+. The ones measuring both quantities are marked in red.

1

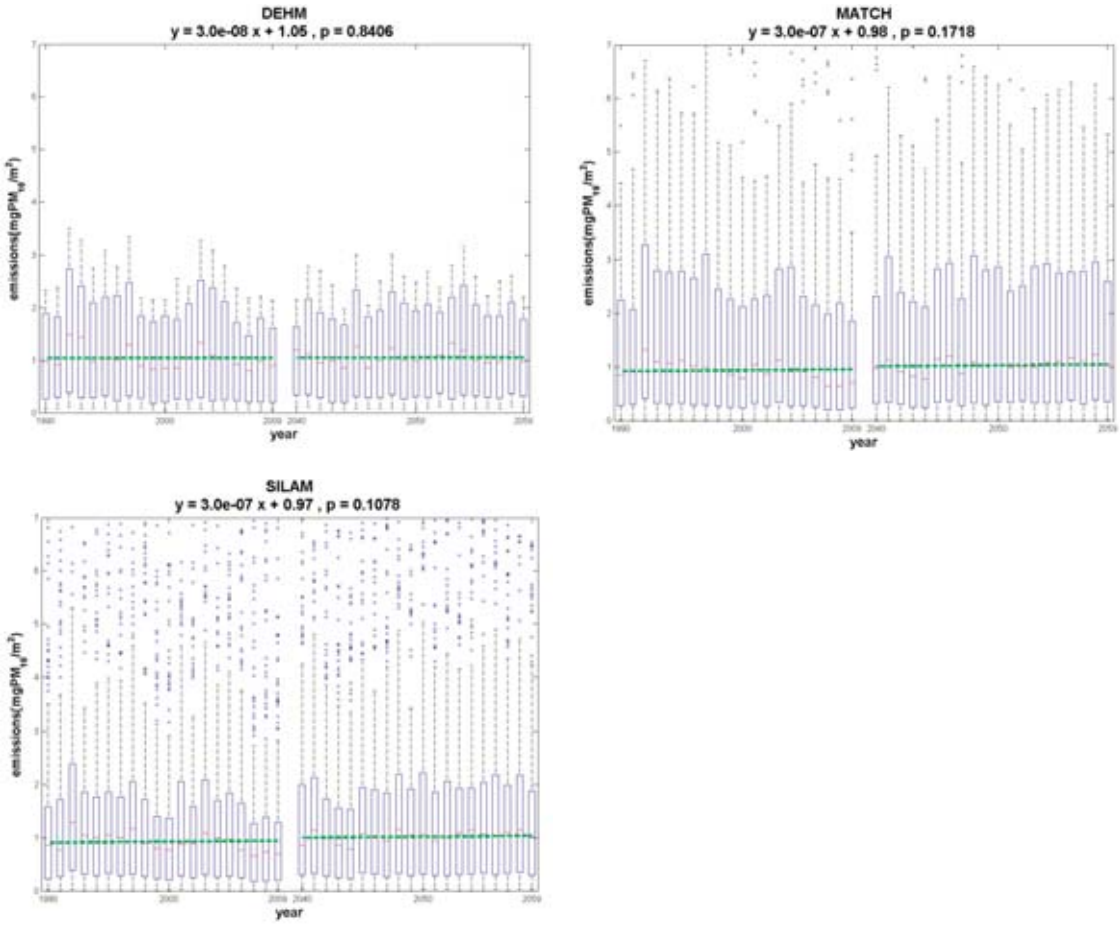

2 **Figure S5** Baltic Sea SSA annual emission ($mgPM_{10}$ m^{-2}) normalized trend (y) over the past
3 and future periods (x [year]).

4

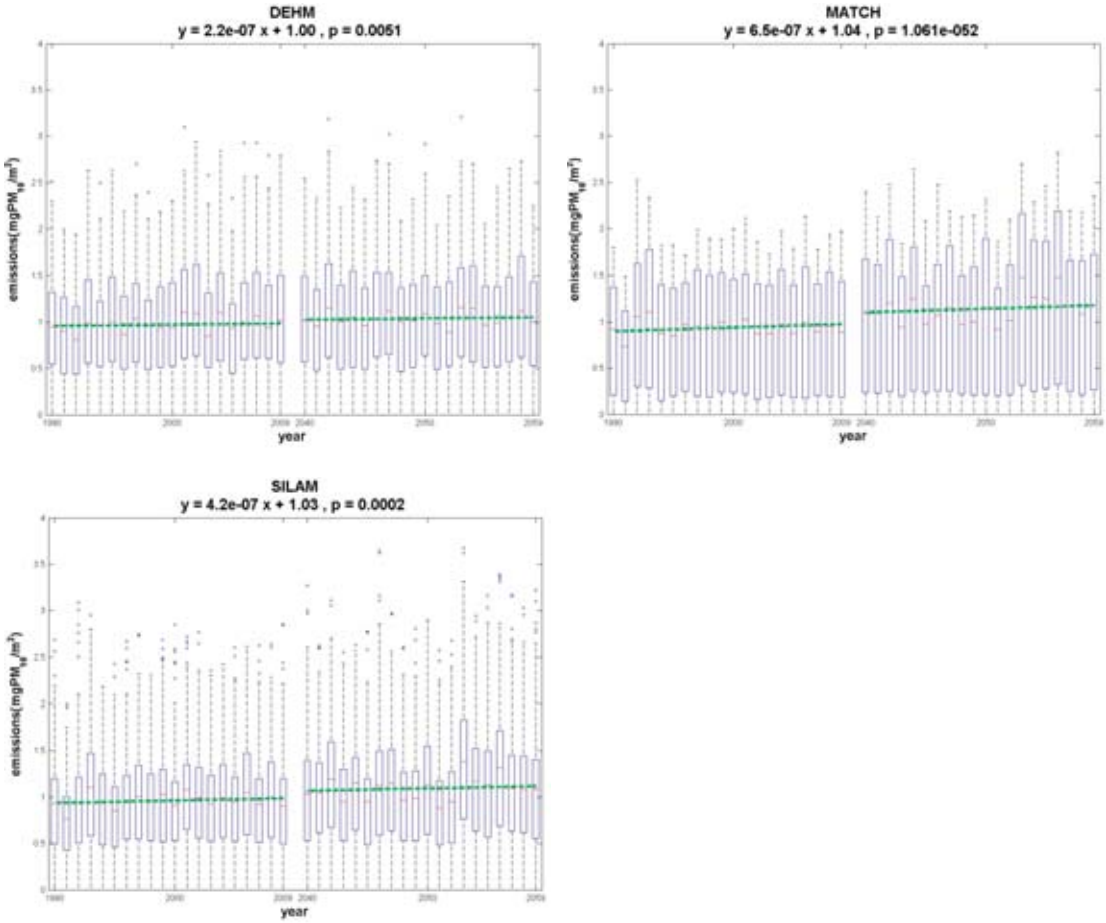

Figure S6 Black Sea SSA annual emission ($mgPM_{10}$ m^{-2}) normalized trend (y) over the past and future periods (x [year]).

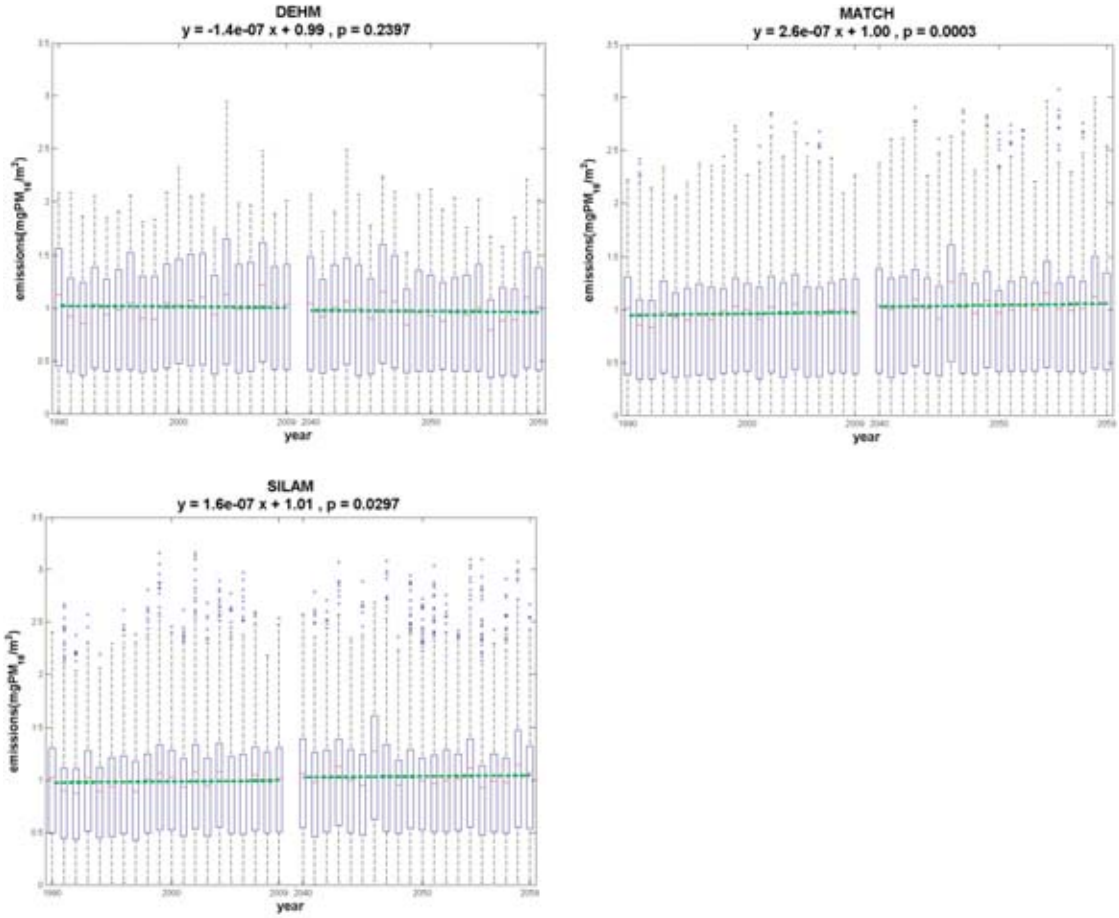

Figure S7 Mediterranean Sea SSA annual emission ($mgPM_{10}$ m^{-2}) normalized trend (y) over the past and future periods (x [year]).

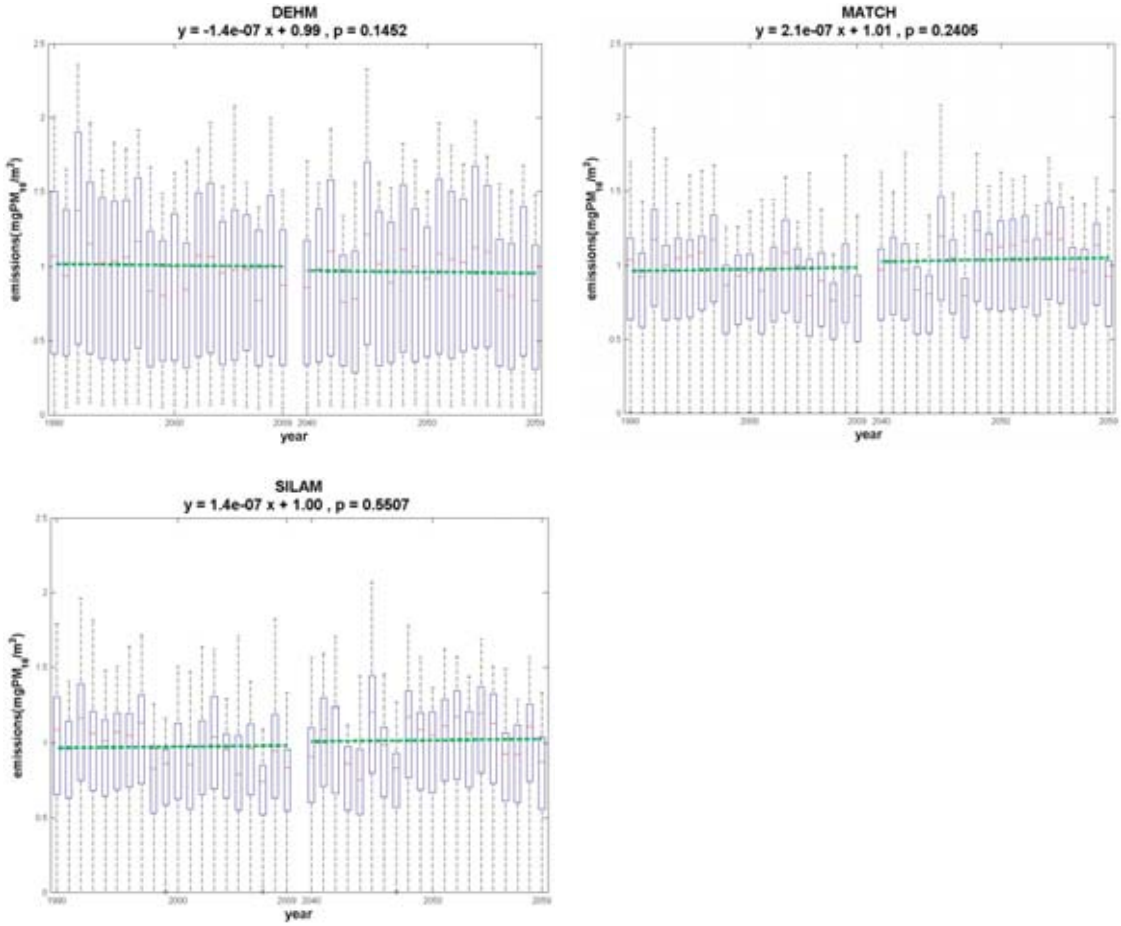

Figure S8 North Sea SSA annual emission ($mgPM_{10}$ m^{-2}) normalized trend (y) over the past and future periods (x [year]).

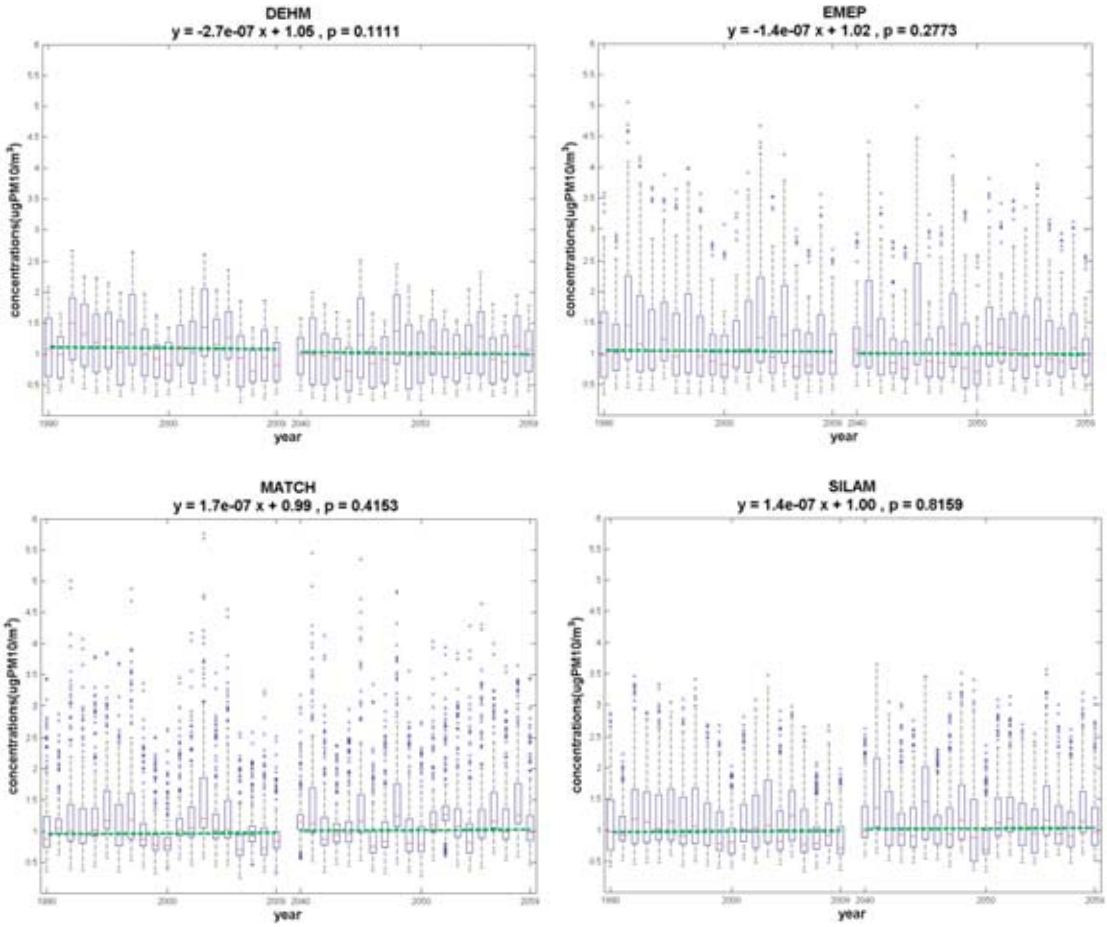

Figure S9 Baltic Sea SSA mean concentration ($\mu gPM_{10}\ m^{-3}$) normalized trend (y) over the past and future periods (x [year]).

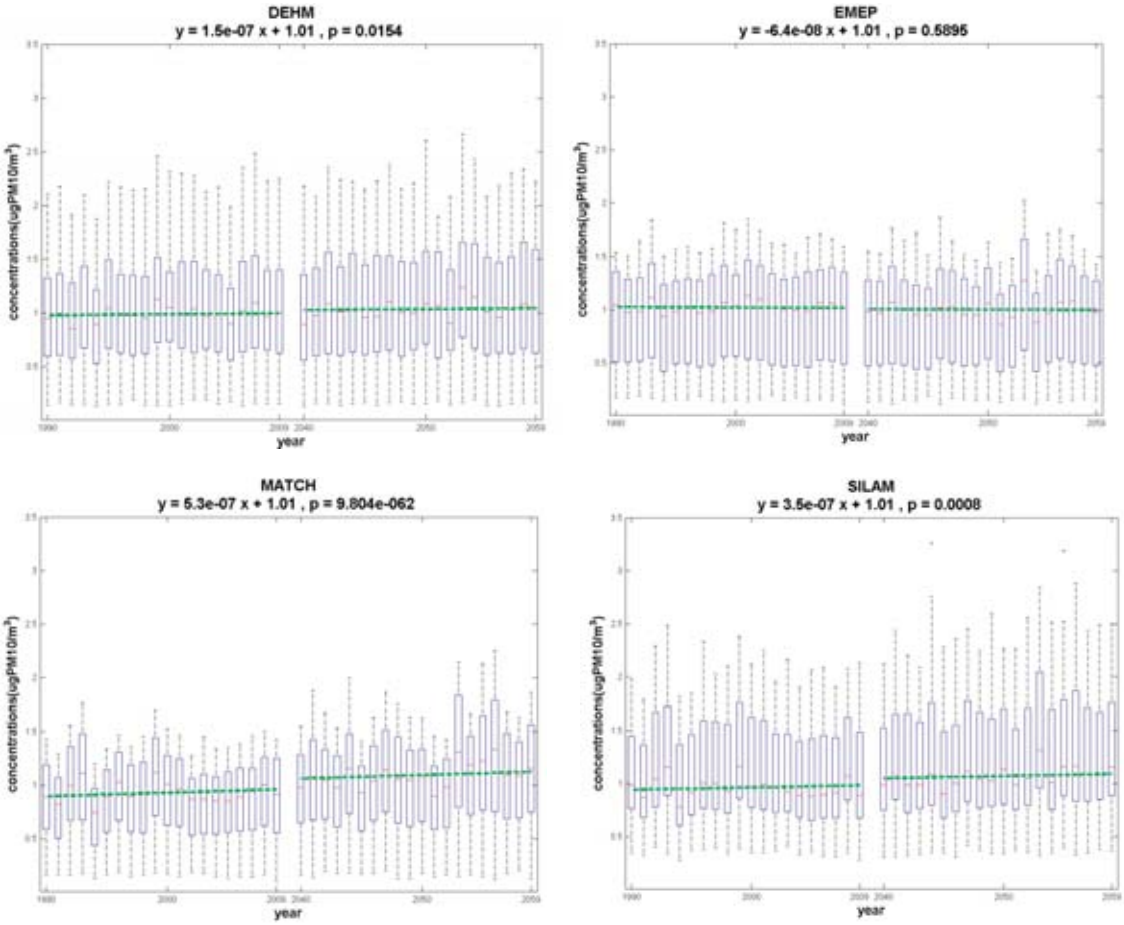

Figure S10 Black Sea SSA mean concentration ($\mu gPM_{10}\ m^{-3}$) normalized trend (y) over the past and future periods (x [year]).

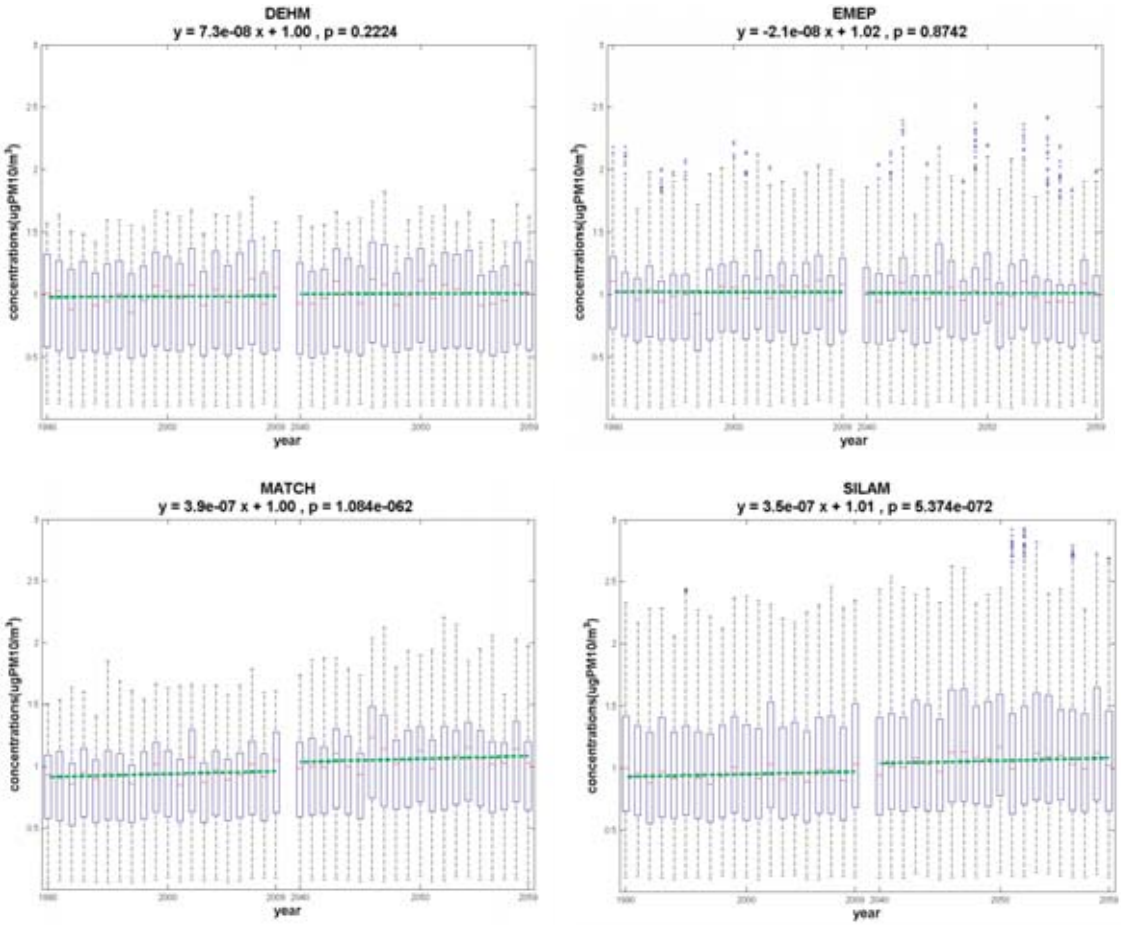

1

2 **Figure S11** Mediterranean Sea SSA mean concentration ($\mu gPM_{10}/m^3$) normalized trend (y)
3 over the past and future periods (x [year]).

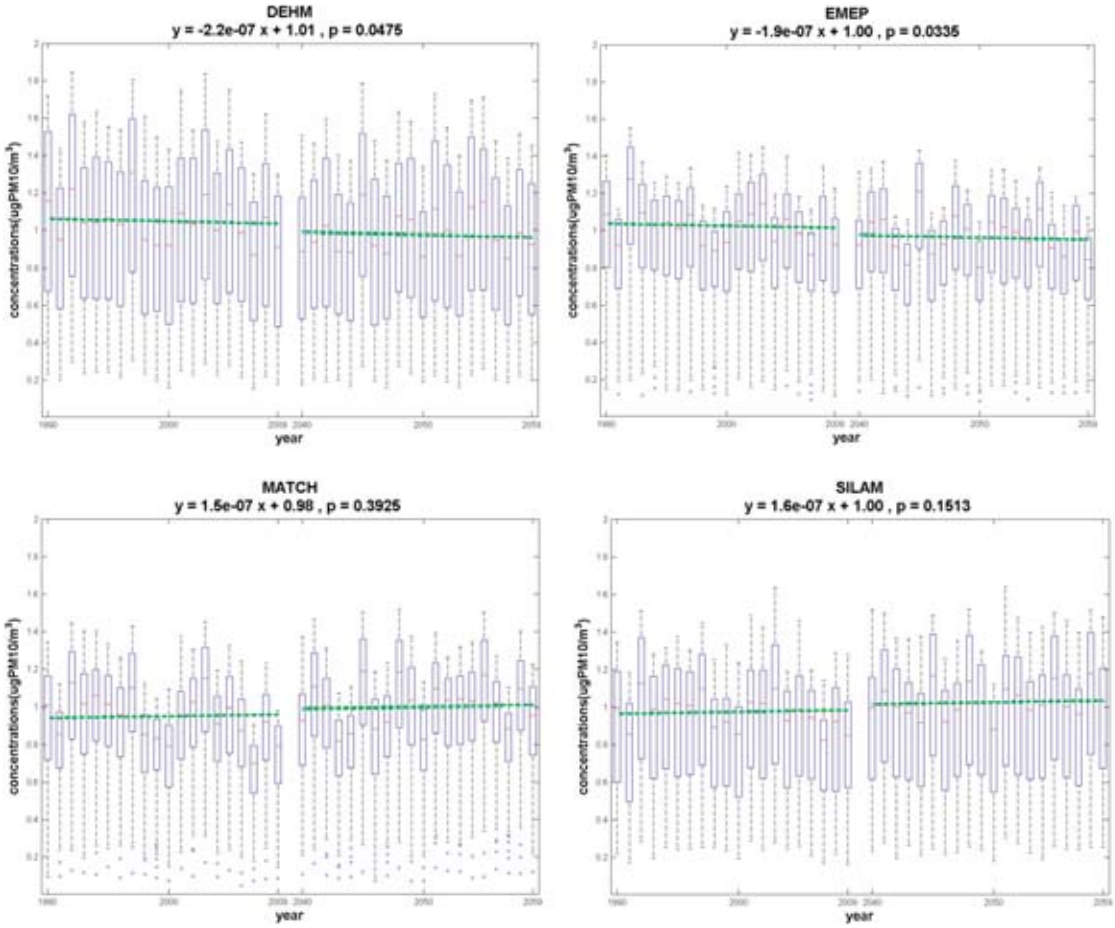

Figure S12 North Sea SSA mean concentration ($\mu gPM_{10}\ m^{-3}$) normalized trend (y) over the past and future periods (x [year]).

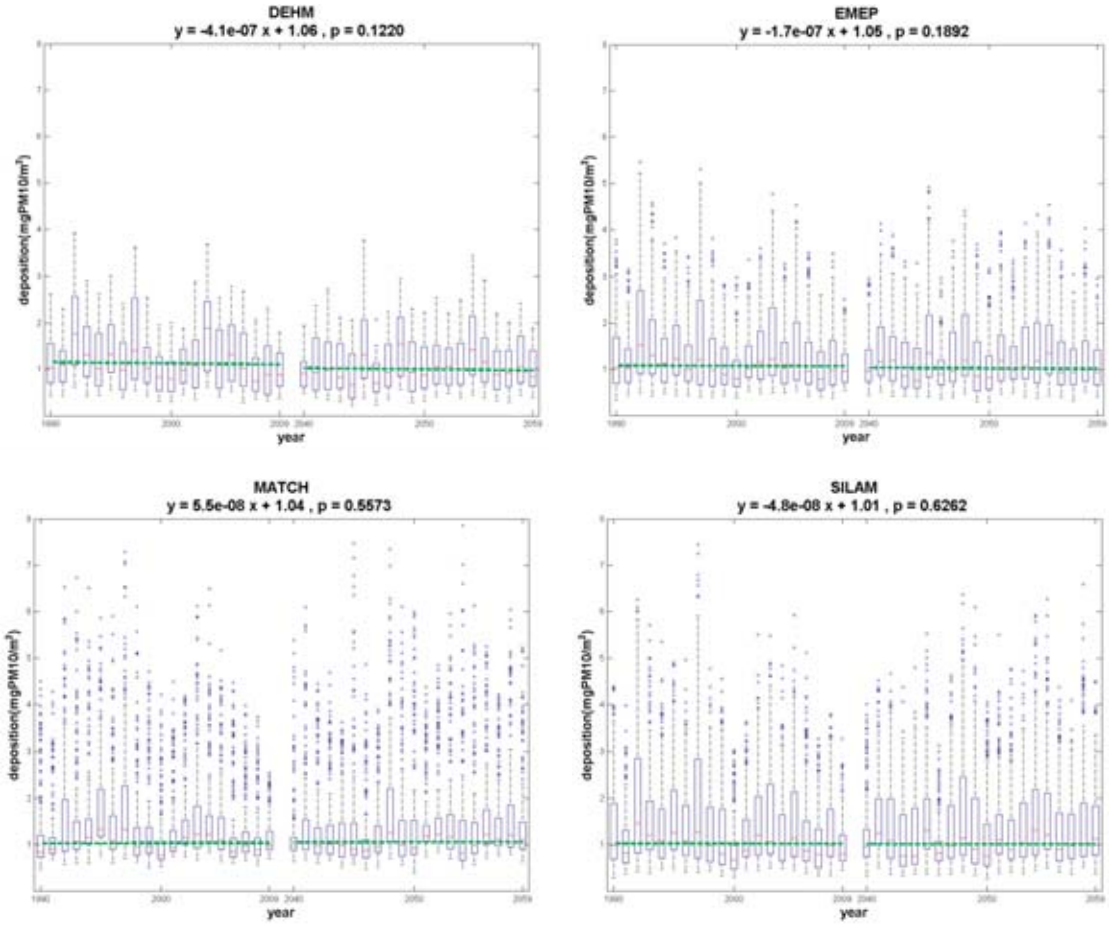

Figure S13 Baltic Sea SSA annual deposition ($mgPM_{10}$ m^{-2}) normalized trend (y) over the past and future periods (x [year]).

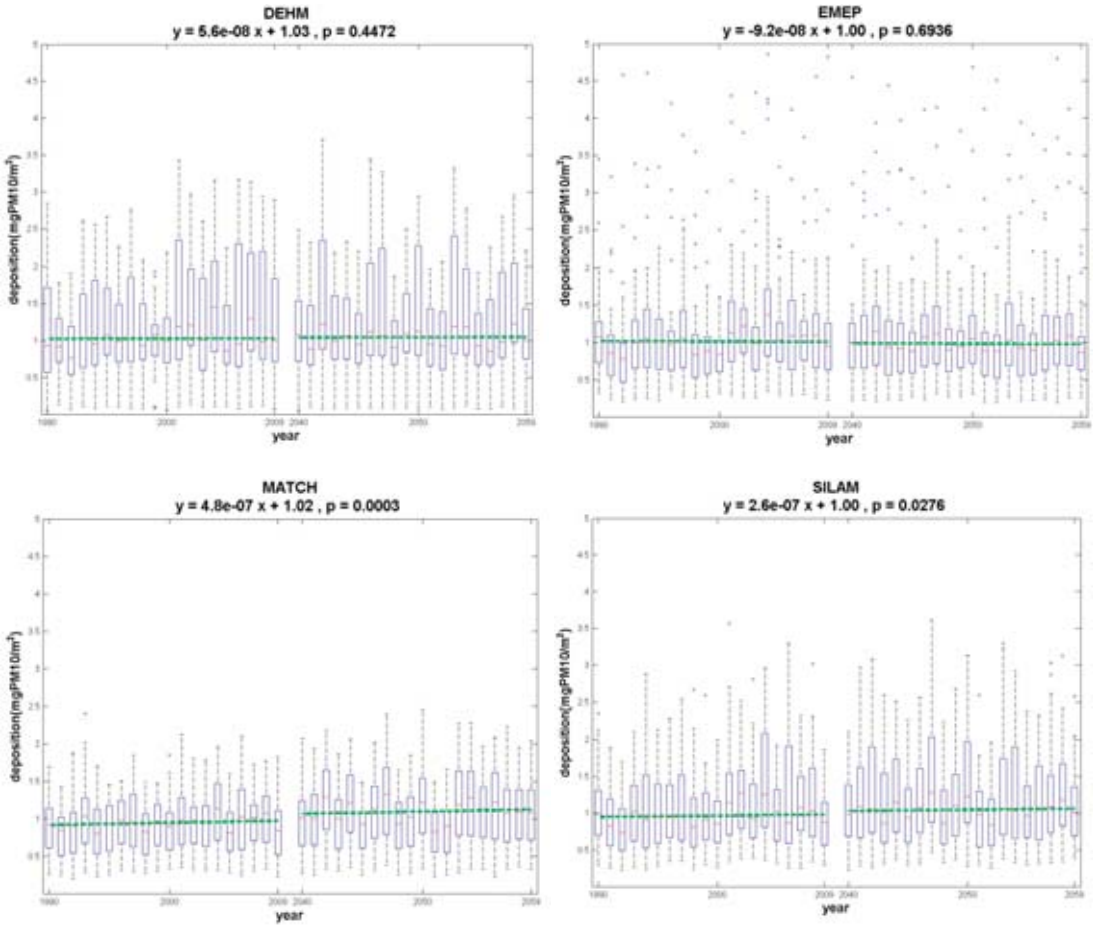

Figure S14 Black Sea SSA annual deposition ($mgPM_{10}$ m^{-2}) normalized trend (y) over the past and future periods (x [year]).

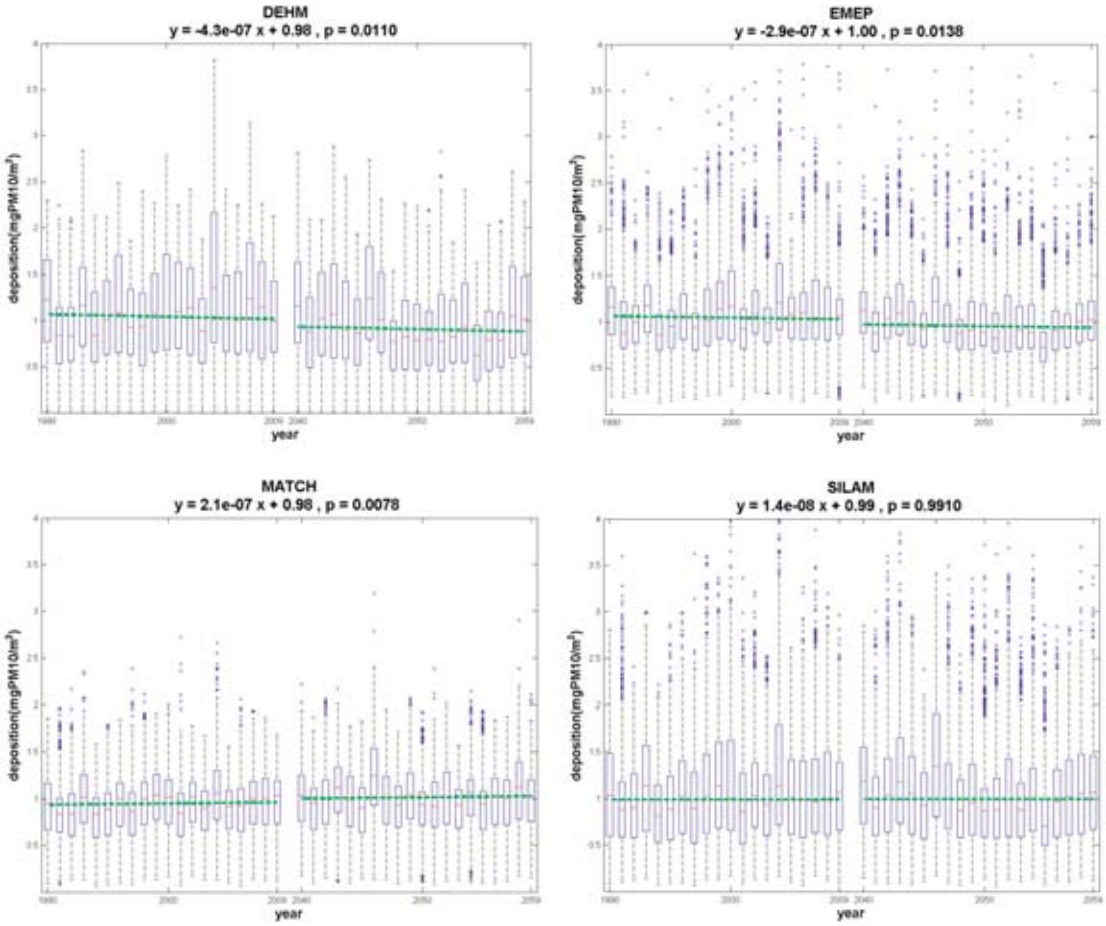

Figure S15 Mediterranean Sea SSA annual deposition ($mgPM_{10}$ m^{-2}) normalized trend (y) over the past and future periods (x [year]).

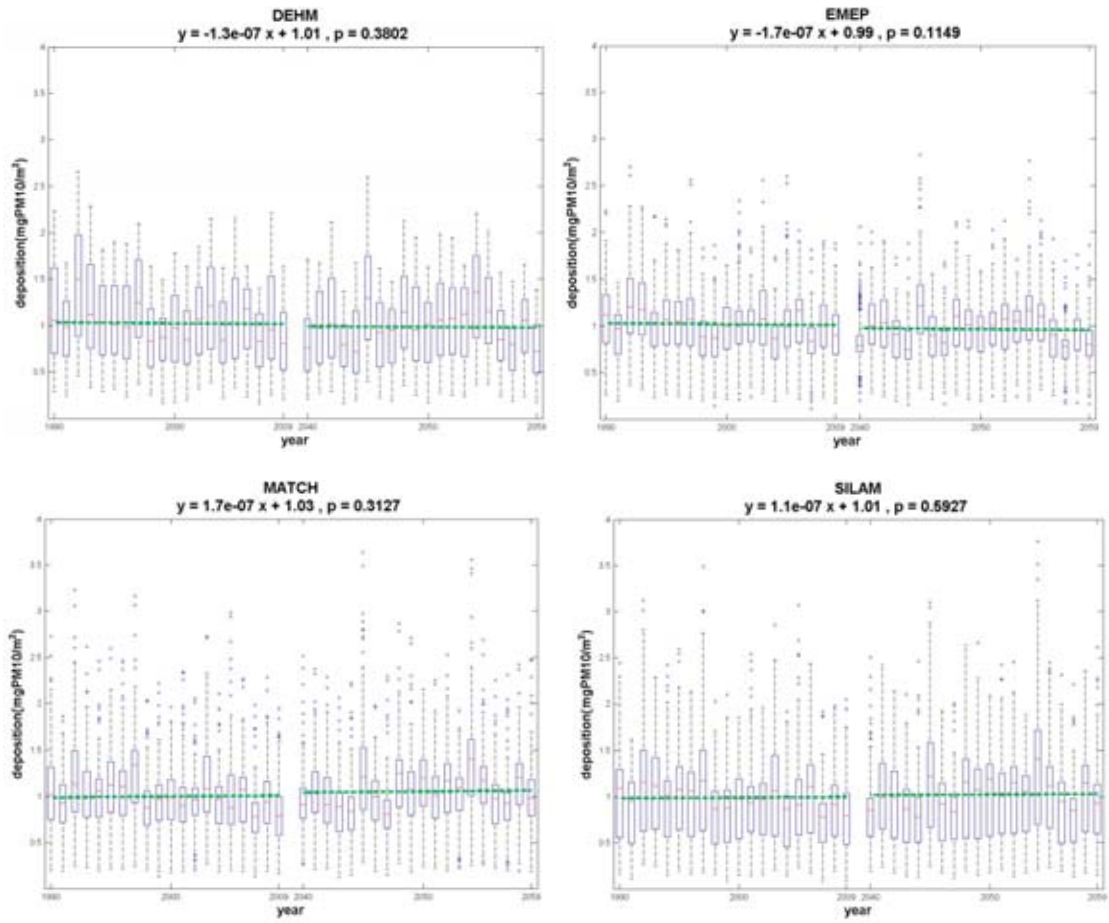

Figure S16 North Sea SSA annual deposition ($mgPM_{10}$ m^{-2}) normalized trend (y) over the past and future periods (x [year]).

III

Atmospheric Environment 115 (2015) 361–370

Contents lists available at ScienceDirect

Atmospheric Environment

journal homepage: www.elsevier.com/locate/atmosenv

Uncertainties of wild-land fires emission in AQMEII phase 2 case study

J. Soares*, M. Sofiev, J. Hakkarainen

Finnish Meteorological Institute, Atmospheric Dispersion Modelling Group, P.O. BOX 503, FI-00101 Helsinki, Finland

HIGHLIGHTS

- Main uncertainties of wild-land fire emission estimates is discussed.
- Total emission can be over-estimated up to 50% with individual-fire emission accuracy.
- IS4FIRESv1 emissions in Europe are over-estimated in-average by 20–30%.
- Impact on total emissions probably comes from under-stated injection height.
- High-energy sources mis-interpreted by MODIS as fires bring about a few tens of %.

ARTICLE INFO

Article history:
Received 3 June 2014
Received in revised form
26 January 2015
Accepted 29 January 2015
Available online 30 January 2015

Keywords:
Fire emission uncertainty
IS4FIRES
Fire radiative power
Fire modelling

ABSTRACT

The paper discusses the main uncertainties of wild-land fire emission estimates used in the AQMEII-II case study. The wild-land fire emission of particulate matter for the summer fire season of 2010 in Eurasia was generated by the Integrated System for wild-land Fires (IS4FIRES). The emission calculation procedure included two steps: bottom-up emission compilation from radiative energy of individual fires observed by MODIS instrument on-board of Terra and Aqua satellites; and top-down calibration of emission factors based on the comparison between observations and modelled results. The approach inherits various uncertainties originating from imperfect information on fires, inaccuracies of the inverse problem solution, and simplifications in the fire description. These are analysed in regard to the Eurasian fires in 2010. It is concluded that the total emission is likely to be over-estimated by up to 50% with individual-fire emission accuracy likely to vary in a wide range. The first results of the new IS4FIRESv2 products and fire-resolving modelling are discussed in application to the 2010 events. It is shown that the new emission estimates have similar patterns but are lower than the IS4FIRESv1 values.

1. Introduction

Wild-land fires were recognised among the most-powerful sources of atmospheric tracers, such as CO_2, CO, particulate matter (PM), and precursors for secondary pollutants, several decades ago (Eagan et al., 1974; Crutzen et al., 1979; Seiler and Crutzen, 1980). However, the estimates of fire emissions are arguably known within a factor of a few times, even if large-scale and long-term averages are considered. Estimates of the globally consumed biomass usually range between 5 and 10 Gt annually (Scholes and Andreae, 2000; Chin et al., 2002) with prescribed fires accounting for 3.5–3.9 Gt (Lauk and Erb, 2009). Estimates of released CO_2 also differ within a factor of 2 between different studies, ranging from 1.4 up to 2.8 Mt of carbon per year (Schultz et al., 2008b).

In the most-classic form, the amount of emitted tracer E_i is assumed to be proportional to the area affected by the fires (burnt area) and empirical coefficients characterising the combustion process (Crutzen et al., 1979):

$$E_i = EF_i*BA*BD*CF \quad (1)$$

Here EF is the emission factor for the emitted species i [g/kg dry matter burned], BA is the size of the burned area [km^2], BD is the biomass density [$g/kg/km^2$], and CF is the combustion completeness factor reflecting combustion efficiency of the fires [dimensionless].

Direct measurements of EFs and combustion efficiency are possible in field and laboratory studies (e.g. Miranda et al., 2005; Campbell et al., 2007; French et al., 2011; Turetsky et al., 2011). The EFs obtained from these experiments are typically used in bottom-up inventories, i.e. extrapolated from the laboratory experiments or field campaign(s) to large-scale applications. Apart from

* Corresponding author.
E-mail address: joana.soares@fmi.fi (J. Soares).

http://dx.doi.org/10.1016/j.atmosenv.2015.01.068
1352-2310/

extrapolation errors, variables in Eq. (1) also inherit uncertainties: i) the spatial extent and duration of the fires; ii) amount and distribution of available biomass or fuels; iii) fraction of biomass or fuel consumed from the different carbon reservoirs (French et al., 2004).

What seems to be consistent, is that bottom-up burnt-area based approaches tend to underestimate PM emissions but demonstrate better skills for other major tracers (Kaiser et al., 2012a; Sofiev et al., 2009; Van der Werf et al., 2006, 2010). Parallel to burnt-area based algorithms, approaches using active-fire remote-sensing observations have been developed. Historically, the active-fire products started from simple hot-spot counts. Arguably the main problem of the data was the scarcity of the observations. Contrary to burnt-area, the active-fire observations are time-critical: the satellite must register the fire while it burns. The data can be obtained only in cloud-free situation and suffer from infrequent satellite overpasses. For instance, evaluation of ATSR hot-spot product shows correct location of the fires but manifested general under-estimation of their number ((Arino and Plummer, 2001), as reported by Flemming (2005)). Finally, the simple counts were unable to provide information on the fire intensity, which further complicated their quantitative application.

Based on Kaufman et al. (1998a,b) and Ichoku and Kaufman (2005) it is possible to relate the energy of the fire with the rate of biomass consumption and derive a relationship similar to Eq. (1), by relating the physical quantities of the biomass burned (BA*BD*CF) with radiant component of the energy release of the fire. This energy release is the so-called fire radiative power (FRP).

$$E_i = C_{ia}*FRP \quad (2)$$

Here C_{ia} is the emission coefficient [kg MJ^{-1}].

This approach has been used for several emission inventories (Wooster et al., 2005; Kaiser et al., 2012a; Sofiev et al., 2009; Giglio et al., 2006). Its main challenge is the critical dependence of the estimates on completeness and quality of the fire observations (Schultz et al., 2008). It also requires the algorithm for integrating the observed instant FRP into time-integrated FRE, which is then converted into emission.

The goal of the current paper is to critically review and quantify the uncertainties of the fire PM emission estimations by Integrates System for wild-land Fires (IS4FIRES) v1, which product was used in the second phase of the AQMEII (Air Quality Model Evaluation International Initiative; http://aqmeii.jrc.ec.europa.eu) model intercomparison exercise. The study concerned the summer fire season of 2010 in Eurasia, where severe wildfires occurred due to anomalously high temperatures, in particular over Russia and Portugal.

The next section outlines the methodology of the analysis: models involved and input data. Section 3 quantifies the key contributors to the overall emission uncertainty and presents examples of the new IS4FIRES calibration. The Discussion section analyses the impact of the key uncertainties and presents the outcome of the sensitivity studies.

2. Models and input data

2.1. Remote sensing data

2.1.1. Fire radiative power

The FRP data are obtained from the active-fire observations by Moderate Resolution Imaging Spectro-radiometer (MODIS) instruments on-board Aqua and Terra satellites (http://modis.gsfc.nasa.gov, Justice et al., 2002; Kaufman et al., 1998a,b). This dataset is the only existing collection that covers the whole globe over more than a decade and provides FRP and other characteristics of active fires. We used level-2 data from Collection 5 from both instruments, starting from their first day till November 2012. The raw data – a series of granules, each corresponding to 5 min of the satellite retrievals – are averaged daily to 0.1° spatial resolution. The procedure is described in Sofiev et al. (2009).

FRP products are also available from the Infrared Imager SEVIRI onboard the Meteosat MSG satellite (Kaiser et al., 2009; Roberts and Wooster, 2008). Its pixels are quite large – more than 10×10 km^2 – and often cover many individual fires. Secondly, SEVIRI has limited domain: a circle with radius of about 60°, which covers Africa, Europe except northern Europe, limited areas in Asia and South America. However, high temporal resolution (15 min) makes SEVIRI a valuable source of information about temporal evolution of the fire intensity. Calculations were made using SEVIRI data for three vegetation classes: forest, grass and mixed (Sofiev et al., 2013).

2.1.2. Aerosol optical thickness

The global distribution of the aerosol optical depth (AOD) is provided by the MODIS instruments. We used level-2 data from Collection 5 (before 2009) and 5.1. (Kaufman et al., 2002; Remer et al., 2008). The data were projected to a global $1° \times 1°$ grid: the AOD observations falling into the same grid cell were averaged, for each hour. At least 25 pixels per grid-cell were required to avoid biased AOD values. These two steps ensured the maximum possible co-location of the observations and model results both in space and in time.

2.2. Dispersion model SILAM v.5.3

The model used for calibration and evaluation of IS4FIRES is the System for Integrated modeLling of Atmospheric composition, SILAM (Sofiev et al., 2008). The physical-chemical modules of SILAM cover gas-phase inorganic and organic chemistry, formation of secondary inorganic aerosols, and transformation and removal of size-resolved primary particles of various types (Kouznetsov and Sofiev, 2012; Sofiev, 2000; Sofiev et al., 2006). The system also includes a meteorological pre-processor for evaluation of basic features of the boundary layer and the free troposphere using meteorological fields provided by numerical models (Sofiev et al., 2010). To facilitate the comparison with remote-sensing instruments, AOD at 550 nm was computed for all aerosol components with specific size-spectrum. The optical properties are calculated on the basis of the microphysical data: size distribution and spectral refractive index (Prank, 2008). The fire-induced aerosols were split to two bins – $PM_{2.5}$ for particles from 0.01 μm to 2.5 μm in diameter and $PM_{2.5-10}$ for 2.5 μm–10 μm – assuming homogeneous distribution inside each bin. Other species had their own sectional representation. The extinction coefficients are calculated for the given wave length (550 nm for MODIS AOD) via integrating over the size ranges of the corresponding bins. For the current study, SILAM simulations included anthropogenic (Granier et al., 2011), fire-induced (described in Section 2.3), wind-blown dust and sea salt (Sofiev et al., 2011) emissions. The results shown in this study are based on global runs for time period between 2003 and 2012 with a horizontal resolution of 1*1° and the vertical profile represented by 9 uneven layers reaching up to the tropopause, with the lowest layer being 25 m thick. The model was driven by ERA-Interim meteorological data (Dee et al., 2011). All simulations had the output averaged over 1 h.

2.3. Wild-land fires emissions: IS4FIRES

IS4FIRES is based on the active-fire observation products of MODIS. It compiles the fire emission bottom-up from individual-

fire FRPs registered by MODIS. The emissions coefficients are obtained from the top-down calibration step, which is performed only once at the system setup and involves solution of inverse dispersion problem for the fire smoke plumes. During the calibration step, the SILAM model is used to calculate the atmospheric dispersion of the emitted masses, thus producing both the near-surface PM concentrations and AOD. The obtained plumes are attributed the vegetation type prevailing at the fire place, built on the basis of GLCC land-use inventory (Loveland et al., 2000).

The emission factor for each land-use type is obtained via fitting the modelled PM concentrations and AOD into the observed ones. Upon obtaining the EFs, the bottom-up calculation of emission from each observed fire is performed, finally ending up with daily biomass-burning emission maps. The last stage needs only MODIS-FRP products and the vegetation classification.

2.3.1. IS4FIRESv1

In IS4FIRESv1 the linear relationship between the FRP and emission of PM (Eq. (2)) is based on Ichoku and Kaufman (2005). The calibration step is performed over a limited period in Europe for well-observed fire plumes (28.04–05.05.2006, 15.08–25.08.2006 and August 2008), by combining FRP from MODIS (MODIS-FRP) with ground-based observations of aerosol concentrations and AOD from MODIS (MODIS-AOD). The fire plumes are classified according to three vegetation classes: forest, grass and mixed (Sofiev et al., 2009).

The recommended plume injection height is described as a homogeneous profile from the surface up to 1 km altitude, which is based on a mean top of the fire plumes measured by MISR instrument over several years (<1300 m). The diurnal cycle suggested is based on a conservative diurnal variation (Saarikoski et al., 2007), where day-time emission is 50% higher and night-time is 50% lower than the daily-mean value.

2.3.2. IS4FIRESv2

IS4FIRESv2 distinguishes between seven vegetation classes: boreal, temperate and tropical forests, residual crop, grass, shrub and peat. The linear relationship between FRP and PM is based on the IS4FIRESv1 EFs but proportionally scaled to the vegetation classes types based on the biomass burning emission factors for different vegetation classes described in Akagi et al. (2011a,b). The calibration step is based on a long-term comparison (2002–2013) of remote sensing measurements (MODIS) and SILAM results. Hourly values of AOD from MODIS (MODIS-AOD) and modelled AOD (SILAM-AOD) were spatially and temporally collocated and sequentially averaged to daily and monthly values. The calibration used only the fire-dominated cells as predicted by SILAM: daily-mean fire-induced AOD was requested to be bigger than combined AOD from all non-fire sources (sea-salt, wind-blown dust, primary anthropogenic and secondary inorganic aerosol). In other words, only AOD values with over 50% of the predicted fire contribution were used. The observed AOD is then corrected by subtracting the non-fire SILAM-AOD components. This correction is made under the assumption that the fire-induced AOD over the fire-dominated pixels is the most-uncertain part of the total AOD. The final step of the optimisation fit was to run an unconstrained minimisation of the root mean square error (RMSE) between the SILAM and MODIS AOD by adjusting the EFs for the vegetation classes. The optimisation is run independently for each year maintaining the initial scaling factors as a starting point for the optimisation. A single scaling factor for each vegetation class is attained by averaging the values obtained from each optimisation run.

In IS4FIRESv2, the plume injection height is derived for individual fires. The semi-empirical formula for fire-plume top height was obtained from MISR fire plume observations by Sofiev et al. (2012). The diurnal variation is based on FRP data obtained from the geostationary-orbit MSG SEVIRI (SEVIRI-FRP) instrument. From that dataset, the diurnal cycle of fires was parameterised for the above vegetation classes (Sofiev et al., 2013).

Elvidge et al. (2013) indicated that some sources, such as gas flares and large industrial installations, could be misinterpreted by MODIS as fires. An effort to mask-out these sources has been undertaken in IS4FIRESv2 by calculating the frequency of fires occurring in each 3 × 3 km pixel over the globe, based on the MODIS-FRP. Grid cells with more than 50 fire days in a year have been flagged as suspicious. Over the 12-year period 2002–2013, 402 cells were flagged 4 times or more. After considering the location of these cells and their possible FRP sources, it was decided to permanently remove all FRP values recorded over these locations from IS4FIRESv2.

3. Quantification of fire emission uncertainty

Within the current section, we shall quantify the main uncertainties of IS4FIRESv1 products for AQMEII and compare them with the burnt-area based emission inventories and the most-recent fire emission database obtained from IS4FIRESv2. We shall concentrate on the total-emission bias as the most-important parameter for large-scale assessment of the fire impact.

3.1. Emission fluxes estimation: comparison between burnt-area and active-fire products

In this sub-section, we compare the GFED, GFAS and IS4FIRES emission inventories. The GFED estimates for fire emissions are based on a biogeochemical model and satellite-derived estimates of area burned, fire activity, and plant productivity (Van der Werf et al., 2010), whereas GFAS and IS4FIRES use FRP. Conversion of FRP to emission flux is based on empirical EFs, which differ between GFAS and IS4FIRES. GFAS uses scaling from FRP to biomass combustion rate distinguishing between eight land use classes. The values were derived from regression analysis against the Global Fire Emission Database GFED3.1 (Kaiser et al., 2012). From the consumed biomass, the emission of specific pollutants is calculated using the EFs from Andreae and Merlet (2001). As noted by (Kaiser et al., 2012), GFAS-PM emission is too low, so that an enhancement factor of 3.4 is to be applied as a 1st order correction.

From Fig. 1, it is evident that fire activity estimates and smoke emission, derived from burnt-area and FRP satellite products, generally agree on spatial patterns but have large differences in the absolute levels of atmospheric emissions. Active-fire based inventories tend to show larger areas of the fire emission and also report higher totals. GFAS showed the values in-between the outcome of burnt-area and FRP-based approaches: its actual fires and their relative emission fluxes are obtained from the MODIS-FRP, whereas the overall total is scaled to the GFED values. The total PM emissions obtained by IS4FIRESv1 for August 2010 are 70% and 40% higher than GFED and GFAS (if scaled with 3.4 factor, as recommended by Kaiser et al. (2012)), respectively.

3.2. Constraining emissions

The top-down calibration used in IS4FIRES to determine the EFs constrains the final emission estimates using the comparison of modelled fire smoke concentrations with measurements. Fig. 2 illustrates that IS4FIRES method captures the mean emission factor for “typical” fires but leaves substantial scatter. The IS4FIRESv1 calibration was based on European in-situ observations, which led to quite accurate mean AOD for Europe but left substantial scatter and a tendency to over-predict AOD (Fig. 2a). For Africa, this

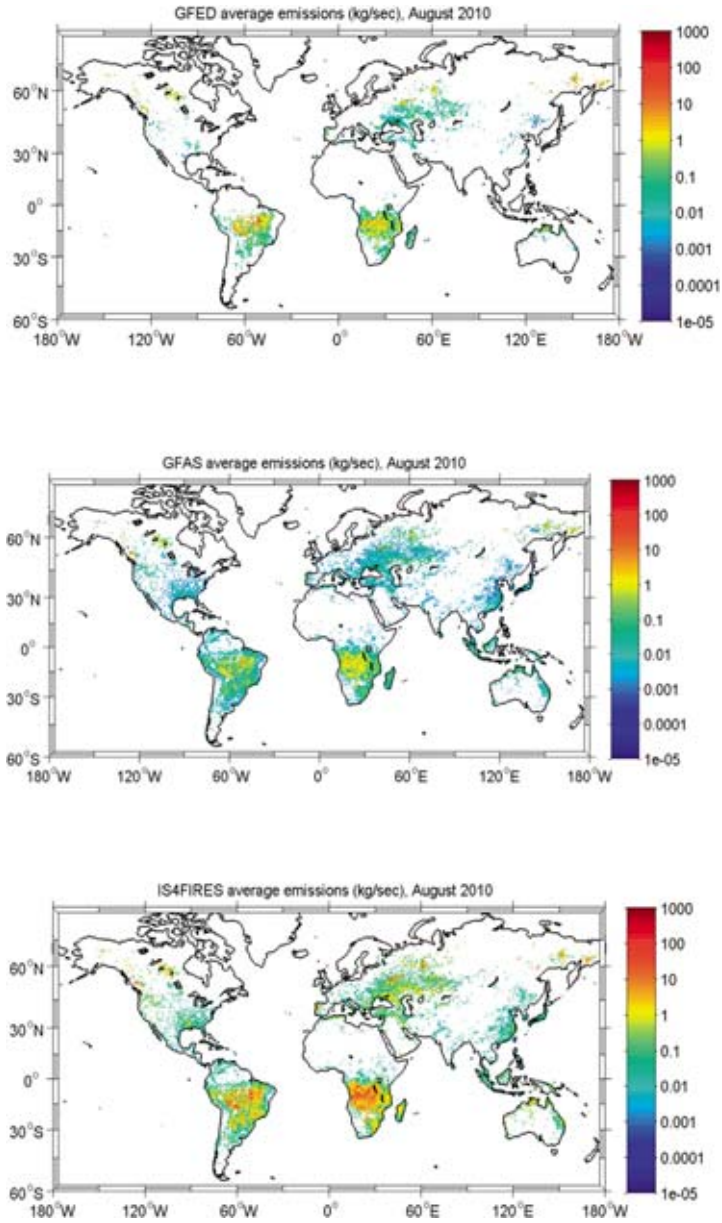

Fig. 1. Wildland fire total PM emissions fluxes [kg/s] for August 2010: a) GFED3; b) GFAS v1 (no 3.4 multiplier); c) IS4FIRESv1 Source: GEIA ECCAD portal, http://eccad.sedoo.fr/.

calibration is inappropriate (Fig. 2b, also seen from Fig. 1): the resulting median AOD is about twice the MODIS level.

Increasing the number of land-use types from three (IS4FIRESv1) to seven (IS4FIRESv2) improves the prediction scores by reducing the overestimation of the system, and improving mean values and RMS (Fig. 2 and Table 1). The difference is expectedly not particularly substantial in Eurasia but strong for Africa. The RMSE is reduced by half if the number of land-use types is increased.

Lumping of vegetation classes brings less description of the global vegetation but is a necessary feature when modelling at a global scale. Misattribution of some specific GLCC land-uses to the selected three or seven classes also introduce errors to the emissions. When analysing the results per region the difference is not significant but for specific episodes and locations, the correction of land-use attribution can lead to about 10% reduction of AOD (not shown).

Fig. 4 shows the outcome of masking out the highly energetic sources from MODIS-FRP database. There are clear cases of persistence of grid-cells that are reported as fires, in particular as areas such as Arabian Peninsula (Fig. 4a). The impact of non-fire high-temperature sources in August of 2010 has been simulated with SILAM with and without these sources (the fractional difference is shown in Fig. 4b). According to these results, the AQMEII outcome can change substantially but over limited areas. Thus, when the oil extraction/production plants in Russia are masked-out from the fire emission database, AOD can be reduced by ~80% in the

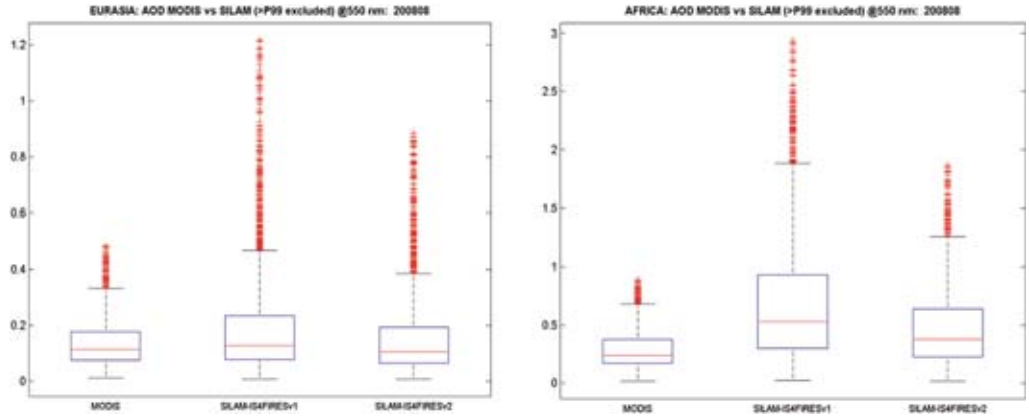

Fig. 2. Boxplots for fire dominating cells (daily averages) for Eurasia (a) and Africa (b) in August, 2008: AOD predicted (MODIS) and computed with fire emissions estimated by IS4FIRESv1 (SILAM-IS4FIRESv1) and IS4FIRESv2 (SILAM-IS4FIRESv2).

immediate vicinity of these sources but the effect quickly falls out when distance from the sources grow. In case of the Portuguese fires, according to our calculations, there is no impact from the highly energetic sources. The most-significant difference (in relative terms) was shown in equatorial regions and part of Sahel, but the absolute AOD values in August are low over these areas.

3.3. Impact of vertical profile and diurnal cycle

The vertical emission injection profile suggested for AQMEII is homogeneous from the surface up to 1 km height. A recent study for typical plume height by (Sofiev et al., 2013) suggests that the plume top height of 2 km is a more realistic long-term mean estimate for both Portuguese and Russian fires. The 1-km profile evidently leads to: (i) about-twice increase of the near-surface concentrations; (ii) sharp reduction of the concentrations above 1 km and their strong dependence on the boundary layer depth and turbulent exchange; (iii), lower concentrations away from fire sources, due to over-estimated surface uptake near the fires.

The diurnal cycle suggested to AQMEII is based on a conservative diurnal variation: daily-mean ± 50%. Studies, such as Beck and Trevvit (1989) and Beck et al. (2001), show that this variation depends on land-use and meteorology and can vary strongly. The typical shape of such variation was estimated from FRP observations by geostationary MSG-SEVIRI instrument. Nevertheless, extrapolation outside the observed areas can follow the land-use classification but will still inherit the uncertainties due to variability of the vegetation characteristics inside each class.

Fig. 5 shows the daily variation of the fire intensity based on SEVIRI-FRP, considering the three land-use classes and the hourly profile used in the AQMEII computations. It is clear that the daily variation used in AQMEII is not as sharp as what is observed by SEVIRI. The differences between night and day-time emissions should be more accentuated and the peak of emissions is shifted for a couple of hours. However, specific features of the 2010 Eurasian fire events indicate that climatological diurnal cycles from SEVIRI may be inappropriate (see discussion Section 4.2).

4. Discussion

4.1. Key contributors to fire emission uncertainty and means of constraining them

The emission estimation methodology based on FRP observations has both strong and weak points. In comparison with the burnt-area approaches, it avoids using the extremely uncertain parameters, such as the fuel load and combustion efficiency, as well as the guess-work on the fire intensity, its temporal evolution, injection height, etc. The utilisation of the direct fire power observations, especially if they are made several times a day, provides more information.

The main weak points originate essentially from the instant character of the FRP observations, which lead to strong undersampling of the dataset. Indeed, the single FRP number quantifies only the intensity of the fire at the moment of the observation. It says nothing about the history of the fire, neither on its further development. Moreover, Kasischke et al. (2003) highlights problems, such as cloud obscuration of the fires, which are particularly common across the boreal region.

There are difficulties in observing small fires, fires (partly) overshadowed by trees, as well as low-temperature but strongly emitting smouldering fires, all leading to underestimation of the emissions (Wooster et al., 2005). According to FREEVAL project (Schultz et al., 2008), the minimum-FRP detection threshold for MODIS is about 7–10 W m^{-2}. This is in agreement with a predicted sensitivity limit of 10–20 W m^{-2} (Kaufman et al. 1998a,b). For very strong fires, the sensor saturation at about 450 K (4 μm channel, (Kaufman et al., 1998a,b)) leads to the FRP cut-off at ~700 W m^{-2}.

Difficulties in detection of small fires and related losses due to insufficient MODIS sensitivity cause the main concern: BIRD-HSRS data suggests that fire with FRP lower than 10 MW are the most frequent (64%) but often missed by MODIS data (Zuhkov et al., 2006). Thus, Schroeder et al. (2008) suggested about 75% of small fires missed by MODIS at a single-pass (collections 3 and 4). Since IS4FIRES operates with daily time step and sums-up the information of collection 5.1 from two MODIS instruments, its daily fire map is usually a sum of at least 4 images. But the fires with FRP below the above detection-limit will still be missed. A very rough estimate of the fire emission lost due to these limits can be made if the distribution of Fig. 6 is extrapolated towards small FRP values. Noteworthy, the frequency distribution is levelling-off at ~15 W m^{-2} and already goes down at the detection limit of 10 W m^{-2}. As a rough assumption, one can take the frequency at 10 W m^{-2} (3.8e4 fires detected within the bin 9.98 W m^{-2} – 10.03 W m^{-2}). Integrating this flat tail with FRP $\leq$10 M m^{-2} evidently leads to 7.6e6 fires constituting 3.8e7 W m^{-2} of FRP that will be missed. Out of totally 1.8e7 fires, the undetected fraction is ~42% – but only 2.9% of the total FRP because the missed fires are small. This undetected fraction is close to the fraction obtained by Wooster et al. (2003) who found that the less intense fires are being

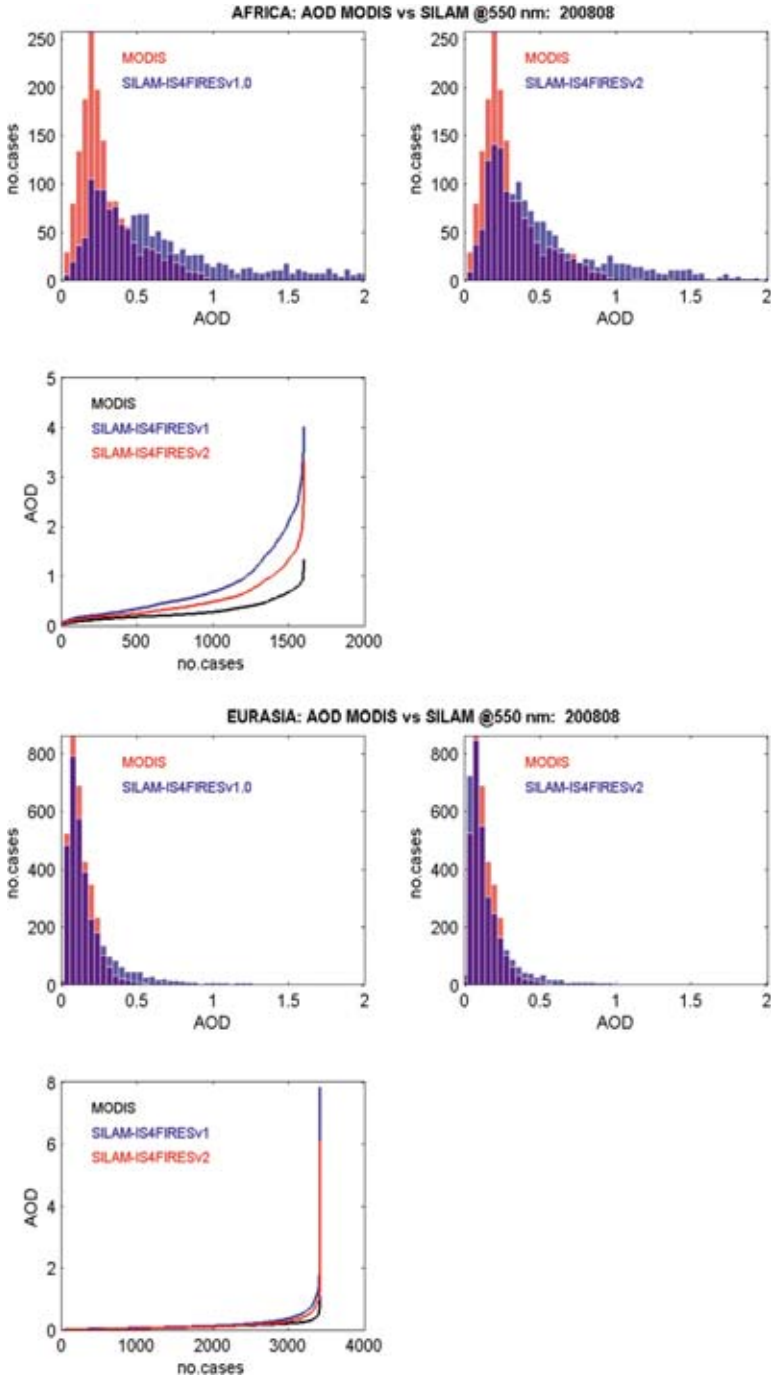

Fig. 3. Histograms and cumulative distribution for fire dominating cells (daily averages) for Eurasia and Africa in August, 2008: AOD predicted (MODIS) and computed with fire emissions estimated by IS4FIRESv1 (SILAM-IS4FIRESv1) and IS4FIRESv2 (SILAM-IS4FIRESv2).

underestimated in 46% by MODIS in comparison to BIRD-HSRS. Since the burning conditions for small fires are probably worse than in average, one can argue for higher emission factors for the missed cases. This is rather an upper-limit estimate but, for instance, if the scaling of peat fires is applied, the potentially missing emission mounts up to 17% (Akagi et al., 2011a,b).

The second major contributor to the overall uncertainty of the emission coefficients is the high sensitivity of PM emission to burning characteristics. They are mainly related to the type of vegetation and the type of burning. For instance, well-developed

Table 1
Statistics for the measured (MODIS) and predicted AOD (SILAM with IS4FIRESv1 (SILAM-IS4FIRESv1), and IS4FIRESv2 (SILAM-IS4FIRESv2), for fire dominated cells (daily averages) for Eurasia and Africa in August, 2008: median, median, root mean square (RMS), root mean square error (RMSE) and correlation coefficient (R).

		MODIS	SILAM IS4FIRESv1	SILAM IS4FIRESv2
Eurasia	Median	0.11	0.13	0.11
	Mean	0.14	0.21	0.17
	RMS	0.17	0.35	0.27
	RMSE	–	0.27	0.19
	R	–	0.38	0.40
Africa	Median	0.24	0.54	0.38
	Mean	0.30	0.76	0.52
	RMS	0.36	1.01	0.67
	RMSE	–	0.69	0.37
	R	–	0.79	0.75

flames of crown fires in forests result in much better combustion efficiency than largely smouldering low-vegetation fires. By resolving a limited number of vegetation classes and taking a single emission factor for one class, all this variability is linked to the type of burning vegetation.

The above main uncertainties, if left unconstrained, result in substantial and poorly determined biases in the total emission estimation. The only possibility to constrain them is the calibration step: the dispersion calculations integrate the fire emission and mix-up the plumes from many fires. The subsequent comparison with observations and adjustment of the coefficients then incorporates all errors into the optimised EFs. The same is true for seasonal variation of the fire types, which can be driven by, e.g. varying fuel moisture content: year-long optimisation window averages it out leaving only the mean value. One can argue that this is barely better than compensating one error with another, which helps to lower the bias but may be less efficient for correlation. However, for large-scale studies reduction of total bias is the first priority.

The efficiency of the calibration step depends on accuracy of MODIS-AOD and SILAM-AOD. MODIS-AOD has been evaluated in several studies. Its standard deviation is $\Delta\tau = \pm 0.05 \pm 0.15\tau$ over land and $\Delta\tau = \pm 0.03 \pm 0.05\tau$ over water surface (Remer et al., 2005, 2008) including, in particular, mis-attribution of aerosol origin and optical properties. These uncertainties constitute less than 10% of the characteristic AOD values used for the IS4FIRES calibration (Fig. 3).

The accuracy of SILAM-AOD relies on a number of simplifications, e.g. aerosol size distribution, chemical composition and hygroscopy, that can lead to underestimation. In addition, secondary organic aerosol is not currently available in SILAM. By selecting fire dominated cells, the uncertainty of underestimating non-fire aerosol is reduced, though missing or underestimating AOD components could still cause errors.

The calibration step also could add inaccuracies. To avoid highly biased averaged AOD values, the minimum number of MODIS pixels was set to 25. The constraint could have been higher but it would have resulted in absence of data in the most northern part of the

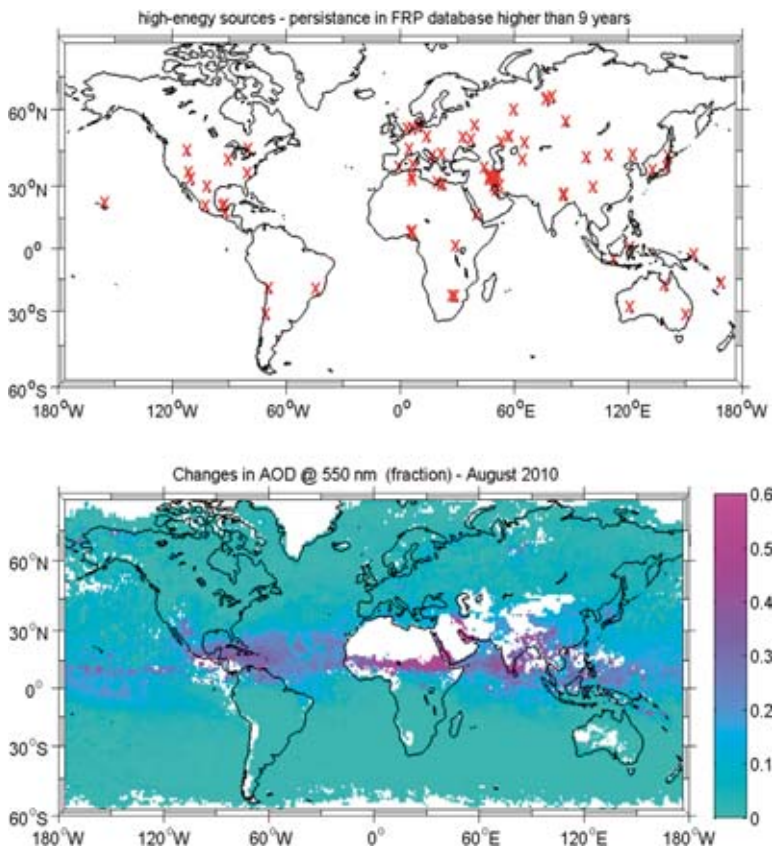

Fig. 4. Upper panel: a map of non-fire pixels excluded from the MODIS database (red crosses); lower panel: relative AOD reduction due to masking out these pixels.

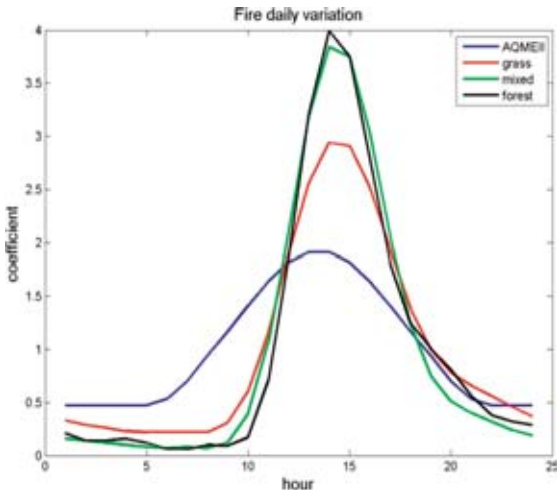

Fig. 5. Diurnal variation of fire intensity used in AQMEII and derived from SEVIRI observations for grass, mixed and forest land-use types.

Northern Hemisphere. The colocation is also constrained by MODIS values available for the collocation. This that can lead to missing the fire all together or resulted in high bias since MODIS is likelier to miss the high concentration pixels.

Differences in the fire characteristics lead to different speciation of the released smoke and, consequently, PM emission rates, even if the total FRP over the MODIS pixel may be similar. In-essence, it means that the assumption of linear relation between FRP and emission holds for the total emission (roughly 90% of which is CO_2 and other 9% attributed to CO (Andreae and Merlet, 2001) but not necessarily to the individual species. A good indicator of such variability might be the Modified Combustion Efficiency (MCE), which is the ratio of CO_2 and $CO + CO_2$ emission rates. For flames, MCE approaches unity (~0.98), whereas for smouldering fires is can be 0.9 or lower (Freeborn et al., 2008). One can expect that stronger fires are associated with better burning conditions and higher MCE, thus resulting in lower fraction of PM and other non-CO_2

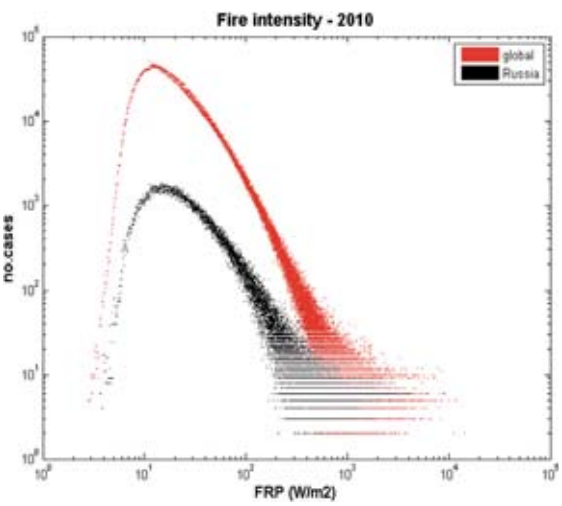

Fig. 6. Frequency distribution for FRP for the fires detected globally and in Russia, in 2010.

components in the emission fluxes. Unfortunately, we are not aware about any established way to derive MCE from satellite observations.

The non-linearity between FRP and emissions for individual species has been approached during IS4FIRESv2 calibration but proved to be extremely difficult: scatter between the predicted and observed AOD due to fire plumes is too large to suggest statistically justifiable shapes of such dependences.

Increasing the number of land-use classes one can improve the representation of fires that occur in different ecosystems. The results show that expanding the number of vegetation classes improves the overall performance of the IS4FIRES, in particular for areas outside of Eurasia.

4.2. AQMEII phase 2 case study: Eurasian fires

Some of the above issues may be of particularly high or low importance for the AQMEII case. The summer season of 2010 (especially in Russia) was record-breaking in several senses: anomalously high temperature and low precipitation created a possibility for record-strong fires that have not been observed before in the region. In this connection, one can question the applicability of any of existing fire emission databases: they all contain empirical coefficients obtained under conditions not representative for the episode. In this section, we consider some of the additional uncertainties or apparent error compensations.

Due to hot windy weather and very large flames, the combustion efficiency was probably better than usual. The fires used for the IS4FIRESv1 calibration were less powerful. If we assume that stronger flames lead to higher MCE, the CO_2 fraction in the smoke would be larger, whereas the PM part would reduce. Also, the cloud obscuration could be less critical for summers, such as the one in 2010, with low precipitation and cloud cover (Boles and Verbyla, 2000). This would lead to higher-than-average fraction of fires noticed by MODIS. As a result, the IS4FIRESv1 PM emission estimates should be biased high.

Strong fires and hot weather contributed to another bias: the smoke injection was bound to be higher than both the MISR-based mean value suggested for AQMEII runs and the more recent 2 km estimate of (Sofiev et al., 2013). One can expect the plumes to be injected at 2.5–3 km or, during strong pyro-convection events, higher. This bias has limited relation to the total fire emission but evidently leads to proportional growth of near-surface concentrations predicted by the dispersion models even if the grand emission total is accurate.

As concerns the temporal evolution of fire intensity, the specifics of 2010 season in Siberia was that the day- and night-time FRP values were much closer to each other than usually (Kaiser et al., 2012). As a result, the conservative AQMEII variation (Fig. 5) appeared to be a good approximation of the reality, at least during the main part of the episode. Utilisation of SEVIRI-based variations would result in too strong day–night difference in emission fluxes.

5. Summary

Present state of knowledge of the wild-land fire emission to the atmosphere is far from being complete. Even the most-sophisticated analyses so far failed to agree on the amount of particulate matter released into the atmosphere. The difference between fire emission inventories can be as large as a few times even for bulk estimates. Individual episodes can be completely missing in some inventories and over-estimated in others.

The AQMEII-II fire emission dataset is based on IS4FIRESv1 calculations using the FRP data and a combination of top-down and bottom-up approaches. Recent improvements of the methodology

in IS4FIRESv2, as well as richer set of available information, showed that IS4FIRESv1 emissions in Europe are over-estimated in-average by 20–30%. In specific episodes of AQMEII-II, higher-than-usual combustion efficiency probably reduced the PM mass fraction in smoke, thus raising the over-estimation to about 50% as a rough estimate.

Strong impact on total emissions has probably come from under-stated injection height. In the vicinity of the sources, it can lead to 2–3 times of additional over-estimation of the near-surface concentrations, with simultaneous reduction of elevated plumes.

Oil and gas flares and large industrial installations, misinterpreted by MODIS as fires, can bring about a few tens of % in the regions with high concentration of such sources.

The conservative diurnal variation used in AQMEII, being different from the typical profiles, are presumably representative for the Russian fires, which have quite similar night- and day-time fire intensity.

Acknowledgement

We gratefully acknowledge the input data of TNO (anthropogenic emissions); ECMWF/MACC project & Météo-France/CNRM-GAME (chemical boundary conditions). The development of IS4FIRES was performed within Academy of Finland IS4FIRES project; support of FP7-PEGASOS and Academy of Finland ASTREX projects are kindly acknowledged.

References

Akagi, S.K., Yokelson, R.J., Wiedinmyer, C., Alvarado, M.J., Reid, J.S., Karl, T., Wennberg, P.O., 2011a. Emission factors for open and domestic biomass burning for use in atmospheric models. Atmos. Chem. Phys. 11 (9), 4039–4072. http://dx.doi.org/10.5194/acp-11-4039-2011.

Akagi, S.K., et al., 2011b. Emission factors for open and domestic biomass burning for use in atmospheric models. Atmos. Chem. Phys. 11 (9), 4039–4072. Available at: http://www.atmos-chem-phys.net/11/4039/2011/ (accessed 24.05.14.).

Andreae, M.O., Merlet, P., 2001. Emission of trace gases and aerosols from biomass burning. Global Biogeochem. Cycles 15 (4), 955–966.

Arino, O., Plummer, S., 2001. The Along-track Scanning Radiometer World Fire Atlas Detection of Night-time Fire Activity. Validation report, IGBP-DIS Working Pap. 23, Stockholm.

Beck, J.A., Alexander, M.E., Harvey, S.D., Beaver, A.K., 2001. Forecasting diurnal variation in fire intensity for use in wildland fire management applications. Proc.. of Forth Symposium on Fire and Forest Meteorology. Am. Met. Soc. http://ams.confex.com/ams/4FIRE/techprogram/meeting4FIRE.htm.

Beck, J.A., Trevitt, A.C.F., 1989. Forecasting diurnal variations in meteorological parameters for predicting fire behaviour. Can. J. For. Res. 19, 791–797.

Boles, S.H., Verbyla, D.B., 2000. Comparison of three AVHRR-based fire detection algorithms for interior Alaska. Remote Sens. Environ. 72, 1–16.

Campbell, J., Donato, D., Azuma, D., Law, B., 2007. Pyrogenic carbon emission from a large wildfire in Oregon, United States. J. Geophys. Res. 112, G04014. http://dx.doi.org/10.1029/2007JG000451.

Chin, M., et al., 2002. Tropospheric aerosol optical thickness from the GOCART model and comparison with satellite and sun photometer measurements. J. Atmos. Sci. 59, 461–483.

Crutzen, P.J., et al., 1979. Biomass burning as a source of atmospheric gases CO, H_2, N_2O, NO, CH_3Cl, and COS. Nature 282, 253–256.

Dee, D.P., et al., 2011. The ERA-interim reanalysis: configuration and performance of the data assimilation system. Q. J. R. Meteorol. Soc. 137 (656), 553–597.

Eagan, R.C., Hobbs, P.V., Radke, L.F., 1974. Measurements of cloud condensation nuclei and cloud droplet size distributions in the vicinity of forest fires. J. Appl. Meteorol. 13, 553–557.

Elvidge, C., et al., 2013. VIIRS nightfire: satellite pyrometry at night. Remote Sens. 5 (9), 4423–4449. Available at: http://www.mdpi.com/2072-4292/5/9/4423/ (accessed 30.05.14.).

Flemming, J., 2005. Emissions for GEMS (Biomass Burning), HALO Discussion Paper. Available at: http://www.ecmwf.int/research/EU_projects/HALO/pdf/paper_HALO_GEMS_emissions.pdf.

French, N.H.F., et al., 2011. Model comparisons for estimating carbon emissions from North American wildlandfire. J. Geophys. Res. 116, G00K05. http://dx.doi.org/10.1029/2010JG001469.

French, N., Goovaerts, P., Kasischke, E., 2004. Uncertainty in estimating carbon emissions from boreal forest fires. J. Geophys. Res. 109, D14S08. http://dx.doi.org/10.1029/2003JD003635.

Freeborn, P.H., et al., 2008. Relationships between energy release, fuel mass loss, and trace gas and aerosol emissions during laboratory biomass fires. J. Geophys. Res. 113 (D1), 1–17. Available at: http://www.agu.org/pubs/crossref/2008/2007JD008679.shtml (accessed 11.08.11.).

Giglio, L., Csiszar, I., Justice, C.O., 2006. Global distribution and seasonality of active fires as observed with the Terra and Aqua Moderate Resolution Imaging Spectroradiometer (MODIS) sensors. J. Geophys. Res. 111 (G2), G02016. Available at: http://doi.wiley.com/10.1029/2005JG000142 (accessed 30.05.14.).

Granier, C., Bessagnet, B., Bond, T., D'Angiola, A., van der Gon, H.D., Frost, G.J., Heil, A., Kaiser, J.W., Kinne, S., Klimont, Z., Kloster, S., Lamarque, J., Liousse, C., Masui, T., Meleux, F., Mieville, A., Ohara, T., Raut, J., Riahi, K., Schultz, M.G., Smith, S.J., Thompson, A., van Aardenne, J., van der Werf, G.R., van Vuuren, D.P., 2011. Evolution of anthropogenic and biomass burning emissions of air pollutants at global and regional scales during the 1980–2010 period. Climate Change 109 (1–2), 163–190.

Ichoku, C., Kaufman, Y.J., 2005. A method to derive smoke emission rates from MODIS fire radiative energy measurements. IEEE Trans. Geosci. Remote Sens. 43 (11), 2636–2649. Available at: http://ieeexplore.ieee.org/lpdocs/epic03/wrapper.htm?arnumber=1522624.

Justice, C., Giglio, L., Korontzi, S., Owens, J., Morisette, J., Roy, D., Descloitres, J., Alleaume, S., Petitcolin, F., Kaufman, Y., 2002. The MODIS fire products. Remote. Sens. Environ. 83, 244–262.

Kaiser, J.W., et al., 2012a. Biomass burning emissions estimated with a global fire assimilation system based on observed fire radiative power. Biogeosciences 9 (1), 527–554.

Kaiser, J.W., et al., 2012b. Biomass burning emissions estimated with a global fire assimilation system based on observed fire radiative power. Biogeosciences 9 (1), 527–554. Available at: http://www.biogeosciences.net/9/527/2012/ (accessed 16.11.12.).

Kaiser, J.W., Wooster, M.J., Roberts, G., Schultz, M.G., Van Der Werf, G., Benedetti, A., 2009. SEVIRI fire radiative power and the MACC atmospheric services. In: EUMETSAT Meteorological Satellite Conf. EUMETSAT, Darmstadt, Germany, pp. 2005–2009. ISBN 978-92-9110-086-6, ISSN 1011-3932.

Kasischke, E.S., Hewson, J.H., Stocks, B., van der Werf, G., Randerson, J., 2003. The use of ATSR active fire counts for estimating relative patterns of biomass burning – a study from the boreal forest region. J. Geophys. Res. 30 (18), 1969,. http://dx.doi.org/10.1029/2003GL017859.

Kaufman, Y., Tanre, D., Boucher, O., 2002. A satellite view of aerosols in the climate system. Nature 419, 215–223. http://dx.doi.org/10.1038/nature01091.

Kaufman, Y.J., et al., 1998a. Potential global fire monitoring from EOS-MODIS. J. Geophys. Res. Atmos. 103 (D24), 32215–32238.

Kaufman, Y.J., et al., 1998b. Potential global fire monitoring from EOS-MODIS. J. Geophys. Res. 103 (D24), 32215–32238. Available at: http://www.cstars.ucdavis.edu/papers/html/kaufmaneta1998a/index.html.

Kouznetsov, R., Sofiev, M., 2012. A methodology for evaluation of vertical dispersion and dry deposition of atmospheric aerosols. J. Geophys. Res. 117, D01202.

Loveland, T.R., Reed, B.C., Brown, J.F., Ohlen, D.O., Zhu, J., Yang, L., Merchant, J.W., 2000. Development of a global land cover characteristics database and IGBP DISCover from 1-km AVHRR data. Int. J. Remote Sens. 21 (6/7), 1,303–1,330.

Lauk, C., Erb, K., 2009. Biomass consumed in anthropogenic vegetation fires: global patterns and processes. Ecol. Econ. 69 (2), 328–334.

Miranda, A., Ferreira, J., Valente, J., Santos, P., Amorim, J.H., Borrego, C., 2005. Smoke measurements during Gestosa-2002 experimental field fires. Int. J. Wildland Fire 14, 107–116. http://dx.doi.org/10.1071/WF04069.

Prank, M., 2008. Evaluation of Atmospheric Composition Simulations via Comparison with Remote-sensing and In-situ Observations. University of Tyartu.

Remer, L. a, et al., 2008. Global aerosol climatology from the MODIS satellite sensors. J. Geophys. Res. 113 (D14), D14S07. Available at: http://doi.wiley.com/10.1029/2007JD009661 (accessed 13.11.14.).

Remer, L.A., et al., 2005. The MODIS aerosol algorithm, products, and validation. J. Atmos. Sci. 62, 947–973.

Roberts, G.J., Wooster, M.J., 2008. Fire detection and fire characterization over Africa using Meteosat SEVIRI. IEEE Trans. Geosci. Remote Sens. 46, 1200–1218. http://dx.doi.org/10.1109/TGRS.2008.915751.

Saarikoski, S., et al., 2007. Chemical composition of aerosols during a major biomass burning episode over northern Europe in spring 2006: experimental and modelling assessments. Atmos. Environ. 41 (17), 3577–3589.

Scholes, M., Andreae, M.O., 2000. Biogenic and pyrogenic emissions from Africa and their impact on the global atmosphere. Ambio 29, 23–29.

Schroeder, W., et al., 2008. Validation of GOES and MODIS active fire detection products using ASTER and ETM+ data. Remote Sens. Environ. 112, 2711–2726.

Schultz, M.G., et al., 2008a. FREEVAL Final Report.

Schultz, M.G., et al., 2008b. Global emissions from wildland fires from 1960 to 2000. Global Biogeochem. Cycles 22, GB2002.

Seiler, W., Crutzen, P.J., 1980. Estimates of gross and net fluxes of carbon between the biosphere and the atmosphere from biomass burning. Clim. Change 2, 207–247.

Sofiev, M., Soares, J., Prank, M., de Leeuw, G., Kukkonen, J., 2011. A regional-to-global model of emission and transport of sea salt particles in the atmosphere. J. Geophys. Res. 116, D21302. http://dx.doi.org/10.1029/2010JD014713.

Sofiev, M., et al., 2006. A dispersion modelling system SILAM and its evaluation against ETEX data. Atmos. Environ. 40 (4), 674–685.

Sofiev, M., 2000. A model for the evaluation of long-term airborne pollution transport at regional and continental scales. Atmos. Environ. 34 (15), 2481–2493.

Sofiev, M., et al., 2009. An operational system for the assimilation of the satellite information on wild-land fires for the needs of air quality modelling and

forecasting. Atmos. Chem. Phys. 9 (18), 6833–6847.
Sofiev, M., et al., 2010. Diagnosing the surface layer parameters for dispersion models within the meteorological-to-dispersion modeling Interface. J. Appl. Meteorol. Climatol. 49 (2), 221–233.
Sofiev, M., et al., 2013. Global mapping of maximum emission heights and resulting vertical profiles of wildfire emissions. Atmos. Chem. Phys. 13 (14), 7039–7052. Available at: http://www.atmos-chem-phys.net/13/7039/2013/ (accessed 05.05.14.).
Sofiev, M., Ermakova, T., Vankevich, R., 2012. Evaluation of the smoke-injection height from wild-land fires using remote-sensing data. Atmos. Chem. Phys. 12 (4), 1995–2006.
Sofiev, M., Galperin, M.V., Genikhovich, E., 2008. Construction and evaluation of Eulerian dynamic core for the air quality and emergency modeling system SILAM. In: Borrego, C., Miranda, A.I. (Eds.), NATO Science for Piece and Security Series C: Environmental Security, Air Pollution Modelling and its Application, XIX. Springer-Verlag, Berlin, pp. 699–701.
Turetsky, M., et al., 2011. Recent acceleration of biomass burning and carbon losses in Alaskan forests and peatlands. Nature Geosci. http://dx.doi.org/10.1038/NGEO1027.
Van der Werf, G.R., et al., 2010. Global fire emissions and the contribution of deforestation, savanna, forest, agricultural, and peat fires (1997–2009). Atmos. Chem. Phys. 10 (23), 11707–11735. Available at: http://www.atmos-chem-phys.net/10/11707/2010/ (accessed 16.10.12.).
Van der Werf, G.R., et al., 2006. Interannual variability in global biomass burning emissions from 1997 to 2004. Atmos. Chem. Phys. 6, 3423–3441.
Wooster, M.J., et al., 2005. Retrieval of biomass combustion rates and totals from fire radiative power observations: FRP derivation and calibration relationships between biomass consumption and fire radiative energy release. J. Geophys. Res. 110, D24311.
Wooster, M.J., Zhukov, B., Oertel, D., 2003. Fire radiative energy for quantitative study of biomass burning: derivation from the BIRD experimental satellite and comparison to MODIS fire products. Remote Sens. Environ. 86, 83–107.
Zuhkov, B., Lorenz, E., Oertel, D., Wooster, M., Roberts, G., 2006. Spaceborne detection and characterization of fires during the bi-spectral infrared detection (BIRD) experimental small satellite mission (2001-2004). Remote Sens. Environ. 100, 29–51.

IV

Geosci. Model Dev., 7, 1855–1872, 2014
www.geosci-model-dev.net/7/1855/2014/
doi:10.5194/gmd-7-1855-2014

Geoscientific Model Development
Open Access

Refinement of a model for evaluating the population exposure in an urban area

J. Soares[1], A. Kousa[2], J. Kukkonen[1], L. Matilainen[2], L. Kangas[1], M. Kauhaniemi[1], K. Riikonen[1], J.-P. Jalkanen[1], T. Rasila[1], O. Hänninen[3], T. Koskentalo[2], M. Aarnio[1], C. Hendriks[4], and A. Karppinen[1]

[1]Finnish Meteorological Institute, Erik Palménin aukio 1, P.O. Box 503, 00101 Helsinki, Finland
[2]Helsinki Region Environmental Services Authority P.O. Box 521, 00521 Helsinki, Finland
[3]National Institute for Health and Welfare, P.O. Box 95, 70701 Kuopio, Finland
[4]TNO, department of Climate, Air and Sustainability, Utrecht, The Netherlands

Correspondence to: J. Soares (joana.soares@fmi.fi)

Received: 16 February 2014 – Published in Geosci. Model Dev. Discuss.: 10 April 2014
Revised: 15 July 2014 – Accepted: 25 July 2014 – Published: 2 September 2014

Abstract. A mathematical model is presented for the determination of human exposure to ambient air pollution in an urban area; the model is a refined version of a previously developed mathematical model EXPAND (EXposure model for Particulate matter And Nitrogen oxiDes). The model combines predicted concentrations, information on people's activities and location of the population to evaluate the spatial and temporal variation of average exposure of the urban population to ambient air pollution in different microenvironments. The revisions of the modelling system containing the EXPAND model include improvements of the associated urban emission and dispersion modelling system, an improved treatment of the time use of population, and better treatment for the infiltration coefficients from outdoor to indoor air. The revised model version can also be used for estimating intake fractions for various pollutants, source categories and population subgroups. We present numerical results on annual spatial concentration, time activity and population exposures to $PM_{2.5}$ in the Helsinki Metropolitan Area and Helsinki for 2008 and 2009, respectively. Approximately 60 % of the total exposure occurred at home, 17 % at work, 4 % in traffic and 19 % in other microenvironments in the Helsinki Metropolitan Area. The population exposure originating from the long-range transported background concentrations was responsible for a major fraction, 86 %, of the total exposure in Helsinki. The largest local contributors were vehicular emissions (12 %) and shipping (2 %).

1 Introduction

Exposure models vary from simple relations of the health aspects with the outdoor air concentrations up to comprehensive deterministic exposure models (e.g. Kousa et al., 2002; Ashmore and Dimitripoulou, 2009). Most of the epidemiological studies have been conducted based on relations between pollution concentrations measured at fixed ambient air quality monitoring sites, or modelled values using land-use regression models, and community-level health indicators, such as mortality (Pope and Dockery, 2006).

Since the urban population spends typically 80–95 % of their time indoors (Hänninen et al., 2005; Schweizer et al., 2007), the exposure to particles is dominated by exposure in indoor environments. The most simplistic approaches ignore the differences between indoor and outdoor air. Indoor air quality is determined by infiltration, ventilation and indoor pollution sources. Infiltration of outdoor particles indoors can be significant even in tight buildings that use mechanical ventilation systems and efficient air intake filters. Infiltration can also occur due to the operation of windows and doors, and cracks in the building envelope and window and door frames (Hänninen et al., 2005). Population exposure can therefore be significantly different, depending on the structure and ventilation of buildings.

If one only takes into consideration concentration levels at measurement sites, fine-scale spatial variability is disregarded. However, the concentrations of pollutants in urban areas may vary by an order of magnitude on a scale of tens of metres. This is particularly important for traffic-originated

pollution. Moreover, most of the simplistic models ignore the activity patterns of individuals, i.e. people's day-to-day movements from one location to another, which is known to cause significant variations in exposure (Beckx et al., 2009).

The assessment of exposure with a deterministic approach usually requires application of integrated model chains starting from estimation of emissions to atmospheric dispersion and transformation of air pollutants. This can be complemented with time–microenvironment–activity models, an essential part of exposure assessment, and indoor to outdoor (i / o) concentration ratios. Microenvironment is defined by a location in which human exposure takes place, containing a relatively uniform concentration, such as, e.g. home or workplace. The average personal or population exposure is then estimated as a linear combination of concentrations in different microenvironments, weighted by the time spent in each of them.

Probabilistic models of population exposure distributions such as EXPOLIS (Hänninen et al., 2003, 2005) and INDAIR (Dimitroulopoulou et al., 2006) provide the frequency distribution of exposure within a population, rather than mean or individual exposures. The population exposure can also be obtained by combining time activity, dispersion modelling, and Geographical Information Systems techniques; this approach has been adopted in the models developed by Jensen (1999), Kousa et al. (2002), Gulliver and Briggs (2005), Beckx et al. (2009) and Borrego et al. (2009). These models can evaluate the individual or population exposure in different microenvironments during the day. In particular, the deterministic modelling system EXPAND (EXposure model for Particulate matter And Nitrogen oxiDes; Kousa et al., 2002) can be applied to continuous time segments ranging from 1 h to several years, and for various urban spatial domains, as the time activity and emission data are temporally and spatially resolved. The city-scale resolution allows taking into consideration small-scale (street and neighbourhood scales) spatial variability. The EXPAND model can also consider exposure pathways, by evaluating population intake fractions (Loh et al., 2009).

The EXPAND model was developed for the determination of human exposure to ambient air pollution in an urban area. The aims of this paper are to describe a substantially improved version of this model and to present selected illustrative numerical results. Numerical results were computed for human exposure to fine particulate matter ($PM_{2.5}$) in the Helsinki Metropolitan Area for 2008 and in Helsinki for 2009. The Helsinki Metropolitan Area is located by the Baltic Sea and is comprised of four cities: Helsinki, Espoo, Vantaa and Kauniainen; the total population is slightly over 1.0 million. The population of Helsinki is over 600 000. We have evaluated the exposure of the population in terms of both various microenvironments and the main source categories. This study also presents for the first time quantitative evaluations of the influence of shipping emissions on concentrations and population exposure in Helsinki.

2 Methodology

2.1 Modelling of vehicular traffic flows

We have modelled the traffic flows in the street network of the Helsinki Metropolitan Area using the EMME/2 interactive transportation planning package (INRO, 1994). The model generates a treatment for the traffic demand on the basis of given scenarios, and allocates the activity over the links (i.e. segments of road or street) of this network, according to a predetermined set of rules and individual link characteristics (Elolähde, 2006). The traffic demand generated by the model is governed by the assumed socio-economic urban structure and location of the main activities, such as residential areas and workplaces, as well as the usage rate of public transport. Both the urban bus routes and the incoming and outgoing coach traffic are included in the model.

According to the link characteristics and the number of vehicles, the software is used to compute the average speed of vehicular traffic for each link on a given hour of the day. Furthermore, both weekly and seasonal variations of the traffic density are taken into account. The profiles of vehicle speed and vehicle numbers are then computed for each link for each hour of the day (separately for weekdays, Saturdays and Sundays), and further aggregated over the year.

In this study, approximately 4300 road and street links were included in the computations. The model also allows for the activities at all the major ports in Helsinki – which increase heavy duty vehicle traffic, in particular. In this study, the traffic flow modelling was based on the traffic data for 2008 and 2009, for the corresponding dispersion computations for 2008 and 2009, respectively. It was pertinent to use up-to-date traffic data, due to recent substantial changes of traffic flows, caused especially by a recently constructed major cargo harbour in the easternmost part of Helsinki at Vuosaari. This new harbour is located further away from the Helsinki city centre, and it has been active since November 2008. The container terminals of the harbours at Sörnäinen and at the western harbour (which are located in central Helsinki) were transferred to the harbour at Vuosaari.

2.2 Modelling of emissions

The emissions of $PM_{2.5}$ were evaluated in the Helsinki Metropolitan Area for 2008, and in a more limited domain, the city of Helsinki for 2009. We have included the emissions originated from urban vehicular traffic for both years, and the emissions from shipping and major stationary sources for 2009. This approach has allowed us to study both the general characteristics of population exposure in the whole of the metropolitan area, and in more detail the influence of two potentially significant local source categories in the capital city.

2.2.1 Exhaust and suspension emissions originated from vehicular traffic

The emissions of $PM_{2.5}$ were computed for each link using average speed-dependent functions, determined separately for each vehicle category (Laurikko et al., 2003). The emission factors were based on European emission factors, and these take into account the age distribution of the Finnish vehicle fleet (Kauhaniemi et al., 2011; Laurikko et al., 2003). A total of 14 vehicle categories were included, divided into petrol cars with or without a catalytic converter, diesel-fuelled vehicles, as well as buses and other heavy duty vehicles. The division of the vehicles within the passenger car category was based on the registration statistics.

We evaluated the vehicular-traffic emissions by scaling a previously compiled detailed inventory for the year 2005, to correspond to the years 2008 and 2009. The national vehicular exhaust emission values are available for 2005, 2008 and 2009 from a calculation system for traffic exhaust emissions and energy consumption, LIPASTO (Mäkelä, 2002). The scaling was performed for each road link, mainly using the ratio of the total vehicular exhaust emissions of $PM_{2.5}$ in Helsinki Metropolitan Area in 2005 to that in 2008 and 2009, respectively. This means that the vehicular exhaust emissions were assumed to vary with a constant percentage from 2005 to 2008 or 2009. In addition, this scaling allows for major changes in traffic flows, such as those caused by the transferred cargo harbours.

In the Nordic countries, the cold start and cold driving emissions of $PM_{2.5}$ can be substantial, especially in winter. These emissions were taken into account, using coefficients based on laboratory emission measurements (Laurikko, 1998). The coefficients were estimated separately for weekdays and weekend, and take into consideration the temperature of ambient air and the fraction of vehicles using a pre-heating of engine (Kauhaniemi et al., 2008).

We also applied a model for the road suspension emissions for $PM_{2.5}$, FORE, described by Kauhaniemi et al. (2011). This model is based on the model presented by Omstedt et al. (2005). The emission factor for suspension of road dust (in units $\mu g\,veh^{-1}\,m^{-1}$) is a product of the so-called reference emission factors, the reduction factor of the moisture content of the street, and a weighted sum of the contribution of particles from the wear of pavement and from the traction sand. The FORE model can be used as an assessment tool for urban $PM_{2.5}$ contributions in various European regions, provided that the model input values are available for local traffic flow, meteorological data and region-specific coefficients. The region-specific coefficients can be determined with fairly simple measurements, as described by Omstedt et al. (2005).

However, the emissions from brake, tyre and clutch wear are not included in the model, due to their small contribution compared to suspension and road wear emissions in the Nordic countries. The baseline values for the suspension emission model were set by the reference emission factors that depend on the period (which may include street sanding or not), the mass fraction of particles (fine and coarse), and the traffic environment (urban or highway).

2.2.2 Emissions originated from shipping

Emissions from ship traffic in the harbours of Helsinki and in the surrounding sea areas were modelled using the Ship Traffic Emissions Assessment Model (STEAM) presented by Jalkanen et al. (2009, 2012). The method is based on using the messages provided by the Automatic Identification System (AIS), which enable the positioning of ship emissions with a high spatial resolution (typically a few tens of metres). The model also takes into account the detailed technical data of each individual vessel. The AIS messages were received from the Finnish AIS network.

The geographical domain of ship emission modelling was selected so that all the major harbours in Helsinki were included. We modelled the emissions (i) from ships cruising in the selected domain in the vicinity of Helsinki; (ii) from ships manoeuvring in harbours; and (iii) from the use of diesel generators at ships while at berth. Emissions from other sources in harbours, such as various harbour machinery, were not included.

The computational domain of the shipping emissions comprises a rectangular area, the extent of which is 21.5 km in the east to west direction, and 25.5 km in the north to south direction. The cell size of the computational grid is 0.001°. This domain is slightly larger than the computational domain for evaluating exposures, as we considered it appropriate to include also the shipping emissions originated from the sea areas in the vicinity of Helsinki.

2.2.3 Emissions originated from stationary sources

The emissions from major stationary sources in the Helsinki Metropolitan Area mainly originated from energy production and other industrial sources. We have allowed for the most widely used methods for heating of residential buildings and domestic water, and for household appliances, namely electricity (33 %) and district heating (29 %) (Statistics Finland, 2012).

The third most important source of energy for households is small-scale combustion, which mainly consists of the burning of wood (23 %). However, small-scale combustion was not included in this study, as the spatial distribution of the emission data was not known with sufficient accuracy.

2.3 Dispersion modelling

The urban atmospheric dispersion modelling system utilized in this study combines the road network dispersion model CAR-FMI (Contaminants in the Air from a Road) for vehicular traffic and shipping, and the UDM-FMI model (Urban Dispersion Model) for stationary sources. These models have

been addressed in detail by, e.g. Karppinen et al. (2000a) and Kukkonen et al. (2001). Both of these models are multiple-source Gaussian urban dispersion models.

The dispersion parameters are modelled as a function of Monin–Obukhov length, friction velocity and boundary layer height, which are computed with meteorological pre-processing model MPP-FMI (Karppinen, 2001). This model has been used with input data from the three nearest synoptic weather stations and the nearest sounding station, to evaluate an hourly meteorological time series for the dispersion modelling computations.

In the urban-scale computations, $PM_{2.5}$ was treated as a tracer contaminant, i.e. no chemical reactions or aerosol processes were included in the calculations. The computations included approximately 5000 line sources for vehicular traffic and shipping for both years, and in addition, 40 stationary sources (power plants and industrial facilities) for 2009. All shipping emissions were treated as line sources with an injection height of 30 m above the sea level. The value of 30 m is a weighted average value of the injection heights of all ships considered (including also their estimated average plume rise); as relative weighting coefficients we used the magnitudes of emissions provided by the STEAM model. The STEAM model includes a detailed database that contains technical properties of all major ships that travel in the Baltic Sea.

For 2008, the regional and long-range transported (LRT) background concentrations were based on the concentrations computed with the LOTOS-EUROS model (Schaap et al., 2008). We selected as the LRT background values the predicted hourly $PM_{2.5}$ concentrations at a model grid square (approximately of the size of $7 \times 7\,km^2$) that includes the regional background station Luukki. This site has previously been found to represent well the LRT background concentrations for the Helsinki Metropolitan Area; the influence of local sources on the $PM_{2.5}$ concentrations at this station has been estimated to be on average less than 10 %. The reason for using the predictions of the LOTOS-EUROS model was the harmonization of regional background computations in the EU-funded TRANSPHORM project (www.transphorm.eu). However, for 2009, we used as the LRT background concentrations the measured values at the measurement site in Luukki.

The computations of the LOTOS-EUROS model on a European scale included the formation of secondary inorganic aerosol, including sulfates, nitrates and ammonia, but these did not include the formation of secondary organic aerosol. The contributions from sea salt, wild-land fires and elemental carbon have also been included. The secondary $PM_{2.5}$ has therefore been modelled with a reasonable accuracy in the regional background concentration values; however, there is an underprediction, caused presumably mainly by the missing secondary organic aerosol fraction.

The local contribution of sea salt aerosol in $PM_{2.5}$ is on average smaller than $0.2\,\mu g\,m^{-3}$ in Helsinki; the low value is mainly due to the low salinity of the Baltic Sea (Sofiev et al., 2011). The wind-blown dust concentrations are also low on an annual average level, emitted by distant sources (Franzen et al., 1994). Hence, the urban-scale computation included only the LRT contribution of these natural aerosols.

The concentrations were computed in an adjustable grid. The receptor grid intervals ranged from approximately 20 m in the vicinity of the major roads to 500 m on the outskirts of the area. The number of receptor points was more than 18 000 and more than 6000 for the computations of vehicular traffic and shipping, and for the stationary sources, respectively.

The CAR-FMI model has previously been evaluated against the measured data of urban measurement networks in Helsinki Metropolitan Area and in London both for gaseous pollutants (e.g. Karppinen et al., 2000b; Kousa et al., 2001; Hellén et al., 2005) and for $PM_{2.5}$ (Kauhaniemi et al., 2008; Sokhi et al., 2008; Singh et al., 2014). The performance of the CAR-FMI model has also been evaluated against the results of a field measurement campaign and other roadside dispersion models (Kukkonen et al., 2001; Öttl et al., 2001; Levitin et al., 2005). The UDM-FMI has been evaluated against the measured data of urban measurement networks in Helsinki Metropolitan Area (Karppinen et al., 2000b; Kousa et al., 2001) and the tracer experiments of Kincaid, Copenhagen and Lilleström. The main limitation of Gaussian dispersion models is that they do not allow for the detailed structure of buildings and obstacles.

2.4 Modelling of human activities

We obtained the information on the location of the population from the data set that has been collected annually by the municipalities of the Helsinki Metropolitan Area. The human activity data within the EXPAND model are based on this data set. The data set contains information on the dwelling houses, enterprises and agencies located in the area in 2009. The data set provides geographic information on the total number and age distribution of people living in a particular building, and the total number of people working at a particular workplace. The data also include information on the number and location of customers in shops and restaurants, and individuals in other recreational activities.

The location of people in traffic was evaluated using the computed traffic flow information. This information is available separately for buses, cars, trains, trams, metro, pedestrians and cyclists for each street and rail section on an hourly basis. Neither this information nor the above-mentioned information from the municipalities identifies individual persons. Time activity of people in harbours was based on the numbers of travellers in each ship line and the timetables of ships arriving to and departing from Helsinki.

The time–microenvironment activity data for both years considered (2008 and 2009) is based on the time use survey by Statistics Finland. The time activity data were collected

from 532 randomly selected over-10-year-old inhabitants in the Helsinki Metropolitan Area for the years 2009 and 2010 (OSF, 2013). There was no detailed information on the time activities of children that are younger than or equal to 10 years old; it was therefore assumed in the activity modelling that such children stay at home all the time. This assumption will probably result in only moderate inaccuracies, as most of the childcare facilities and schools are located within a radius of three kilometres of a child's home.

Population time activity data were divided into four microenvironments: home, workplace, traffic and other activities. The category "other activities" includes customers in shops, restaurants and other locations; however, it does not include the personnel working at such places (they are included in the category "workplace"). The time activity data are updated by the municipalities once in every 10 years. The data that we have used in this study (corresponding to the year 2009) are therefore better representative for the last few years than the data used in the previous EXPAND model version (Kousa et al., 2002). The previously applied time–microenvironment activity data were provided for Helsinki in the EXPOLIS study. The EXPOLIS activity data included only adult urban populations, from 25 to 55 years of age, whereas the new activity data include all population age groups.

2.5 The infiltration of outdoor air indoors

Indoor air quality is determined by the efficiency of infiltration of outdoor air indoors, ventilation and indoor air pollution sources. An infiltration factor (F_{inf}) for pollutant species a is defined as

$$F_{\mathrm{inf}} = \frac{C_{\mathrm{ai}}}{C_{\mathrm{a}}}, \tag{1}$$

where C_{ai} is the indoor air concentration of species a originating from ambient air, and C_{a} is the outdoor air concentration of species a. By definition $0 \leq F_{\mathrm{inf}} \leq 1$.

The infiltration rates of ambient air particles in the previous version of the EXPAND model were estimated using data based on the EXPOLIS study. This was a population representative study on working age people, conducted in 1996–1997. It included measurements of indoor and outdoor $PM_{2.5}$ concentrations, and X-ray fluorescence analysis of elemental markers (Hänninen et al., 2004; Jantunen et al., 1998; Rotko et al., 2000). Elemental sulfur was used as a marker of the outdoor originating particles in 84 residences. The i/o ratios of sulfur in particles were also corrected to allow for the particle size distributions (Hänninen et al., 2004).

The infiltration factors at workplaces of the same subjects were also analysed. The workplaces are distributed following a random population sample, but differences between different types of workplaces could not be evaluated, due to the limited number of subjects. Data on infiltration factors in public buildings are scarce; it has therefore been assumed that the values determined in the EXPOLIS project correspond to all workplaces.

In this study, the previous EXPOLIS infiltration estimates were updated, using also aerosol measurements in the ULTRA-2 study. These aerosol samples were collected in Helsinki in 1999, including a sample of homes of 47 cardiovascular patients, with 4–5 repeated measurements (Lanki et al., 2008). The set of homes is smaller in this sample, but the methods were updated to include a treatment of particle-size-dependent behaviour. The comparison of the results obtained using sulfur-based and aerosol methods revealed significant differences in the aerosol parameters – in particular, regarding the deposition rate and the estimation of the air exchange rates. Nevertheless, the $PM_{2.5}$ infiltration factor distributions of residences were almost identical and were not affected by the improved methods.

In this study, we have evaluated only the impact of outdoor air pollution on the population exposure. We have considered neither the influence of indoor sources of $PM_{2.5}$ nor the impact of particulate matter transformation and deposition in the indoor environments on the population exposure. In order to account for the indoor concentrations, the EXPAND model could be used to consider the ratio between indoor and outdoor concentrations. However, the detailed value of this ratio depends on numerous factors, in particular the influence of indoor sources.

The infiltration factors in the present study are based on the results that are summarized in Table 1. These $PM_{2.5}$ infiltration rates were estimated based on residential and workplace measurements using two relatively large population-based data sets (EXPOLIS and ULTRA-2). We therefore evaluate that the residential infiltration rates have been fairly reliably estimated for the 1996–1999 building stock. The corresponding values for workplaces, representing partly public buildings and partly private occupational businesses, are available only from the EXPOLIS study. The infiltration estimates for non-residential buildings therefore contain more substantial uncertainties.

For simplicity, a weighted average of the presented results, i.e. the value of 0.57, was assumed to represent both the home and work environments. As the information in the case of traffic and other microenvironments was very scarce, it was assumed that the infiltration factor would be equal to one for those microenvironments.

The Finnish building code (EP, 2002) was updated in 2002 and 2010, setting new requirements for improved energy efficiency and improved filtration in ventilation. The infiltration rates will therefore be lower in buildings that have been built after the two above-mentioned studies. Hänninen et al. (2005) estimated that there was a 20 % reduction of infiltration factors in the building stock that was built in the 1990s, in comparison with older buildings. The same long-term trend has continued in the 2000s. Considering all buildings, the impact on infiltration factors of improved energy efficiency and filtration in ventilation is much smaller, due to

Table 1. Compilation of available results on the $PM_{2.5}$ infiltration factors in the building stocks in the Helsinki Metropolitan Area, based on the results from the EXPOLIS and ULTRA-2 studies. In the case of the EXPOLIS study, the main references are listed. For the ULTRA-2 study, the methods are mentioned; these infiltration factors have not been previously published. SD = standard deviation.

Acronym of study	Year	Type of buildings	Number of buildings	Infiltration factor (mean ± SD)	References method
EXPOLIS	1996–1997	Residences	84	0.59 ± 0.17	Hänninen et al. (2004, 2011)
EXPOLIS	1996–1997	Workplaces	94	0.47 ± 0.24	Hänninen et al. (2005)
ULTRA-2	1999	Residences	47 (180)*	0.58 ± 0.15	Sulfur-based method (Hänninen et al., 2013)
ULTRA-2	1999	Residences	47 (180)*	0.55 ± 0.13	Aerosol-based method (Hänninen et al., 2013)

* Number of daily measurements in parentheses.

the slow renewal rate of the building stock, estimated to be of the order of 1–2 % annually.

2.6 Modelling of exposure

Exposure to air pollutants can be represented as the sum of the products of time spent by a person in different locations and the averaged air pollutant concentrations prevailing in those locations. These locations are commonly categorized into microenvironments, which are assumed to have homogeneous pollutant concentrations. Exposure can therefore be written as

$$E_i = \sum_{j=1}^{m} T_{ij} C_{ij} E_i = \sum_{j=1}^{m} T_{ij} C_{ij}, \quad (2)$$

where E_i is the total exposure of person i in various microenvironments [μg m^{-3} s], m is the number of different microenvironments, T_{ij} is the time spent in microenvironment j by person i [s] and C_{ij} is the air pollutant concentration that person i experiences in microenvironment j [μg m^{-3}]. Equation (2) can also be interpreted as a weighted sum of concentrations, in which the weights are equal to the time spent in each microenvironment.

The main objective of this study was to evaluate the average exposure of the population with reasonable accuracy, instead of the personal exposures of specific individuals. The exposure modelling in the case of homes is done by combining residential coordinates with the information on the number of inhabitants at each building and the time spent at home during each day. Correspondingly, for the workplace coordinates, the number of the personnel and the time spent at the workplace are combined.

The population activities at other locations (such as shops, restaurants, cafes, pubs, cinemas, libraries and theatres) are evaluated using statistical information of leisure time (CHUF, 2009). The number of persons in traffic is evaluated based on the predicted traffic flows. In the case of buses, trains, metro, trams and pedestrians and cyclists, the number of persons and the time they spend in each street or rail section is estimated using the traffic-planning model EMME/2. In the case of private cars, the EMME/2 model predicts the number of cars; we assumed that the number of passengers in each car is equal to the average value in the area, i.e. 1.31 (Hellman, 2012).

The concentrations are interpolated on to a rectangular grid in the model. The data regarding population activities (number of persons × hour) is also converted to the same grid. For this study, the grid size was selected as $50 \times 50\,m^2$. The GIS system MapInfo is subsequently utilized in the post-processing and visualization of this information.

The model has also been extended to be able to use various internationally used coordination systems; details are reported in Appendix A.

2.7 Modelling of intake fractions

The EXPAND model was refined to calculate not only exposures, but also intake fractions (iF) for the available substances. The iF is defined as intake by humans via relevant exposure pathways, divided by the emissions of the pollutant. For instance, an intake fraction of one in a million (10^{-6}) means that for every tonne of a pollutant emitted, 1 g is inhaled by the exposed population. The iF concept provides a measure of the portion of a source's emissions that is, e.g. inhaled by an exposed population over a defined period of time. The iF concept can be useful in both screening-level order-of-magnitude estimates and more detailed policy modelling of non-reactive compounds (Bennett et al., 2002).

The model allows for the estimation of the spatial and temporal distribution of iFs, by combining and processing different input values: time–microenvironment activity data, the spatial location of the population, microenvironmental population breathing rates and pollutant concentration distributions (Loh et al., 2009). The emissions can be considered for one source only, or for a selected source category. The iF can be calculated using exposure estimates for the microenvironments of interest and the average breathing rate of a population, while in each microenvironment.

3 Results and discussion

We address results computed for two years, 2008 and 2009. The computations in 2008 address the Helsinki Metropolitan Area, whereas the computations in 2009 focus on the city of Helsinki. Both computations include the LRT pollution, and the vehicular emissions. However, the computations for 2009 additionally include the emissions from major stationary sources and the emissions from shipping in the vicinity and in the harbours of Helsinki. The computations for 2008 can therefore be used for examining the population exposure within a wider area (the whole of the Helsinki Metropolitan Area), whereas those for 2009 are useful for investigating, in particular, the influence of major stationary sources and shipping on the population exposure within the more limited area of the Finnish capital.

3.1 Predicted emissions of $PM_{2.5}$

The total emissions of $PM_{2.5}$ originated from vehicular traffic were 322 tonnes for the Helsinki Metropolitan Area in 2008, and 202 tonnes for Helsinki in 2009. The vehicular emissions include exhaust emissions (these include also cold start and driving) and road suspension emissions. The emissions of $PM_{2.5}$ originated from ships were estimated to be 204 tonnes in Helsinki in 2009. The PM emissions originated from major stationary sources were 225 tonnes in Helsinki in 2009, according to Lappi et al. (2008). In summary, the total annual emissions from vehicular sources and from shipping were approximately the same in Helsinki in 2009, and the emissions from major stationary sources were slightly higher than those from vehicular or shipping sources.

The emissions of $PM_{2.5}$ originated from shipping in 2009 are presented in Fig. 1b. There are three main harbours in central Helsinki, listed from north to south: the Kulosaari harbour, the southern harbour and the western harbour. The emissions per unit area are largest within these three harbour areas. One reason for the relatively high shipping emissions in harbours is that auxiliary diesel engines are used for power generation while at berth; these engines have relatively high emissions per power output, compared with the main engines (Jalkanen et al., 2012). The second largest emissions occur along the main shipping routes from Helsinki to Tallinn (the southward ones) and to other major cities.

The small-scale combustion emissions were not included in the dispersion computations, due to insufficient information regarding the spatial distribution and magnitudes of these emissions. The contribution of small-scale combustion to the total $PM_{2.5}$ emissions in Helsinki Metropolitan Area has been estimated to be 15 %; this fraction is slightly lower than the corresponding one for stationary sources (21 %) (Niemi et al., 2009; Gröndahl et al., 2013). In the present study, allowing also for the emissions of small-scale combustion as reported in the above-mentioned studies, the contributions of the different emission source categories for $PM_{2.5}$ in Helsinki in 2009 are 36 % for vehicular traffic, 23 % for major stationary sources, 23 % for shipping and 18 % for small-scale combustion.

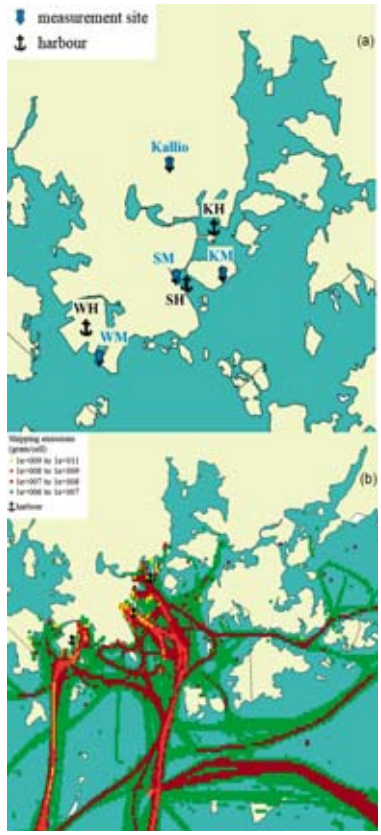

Figure 1. (a) Location of the harbours and the measurement sites in their vicinity in 2009. The notation for harbours: Katajanokka harbour (KH), southern harbour (SH), western harbour (WH); and for the measurement sites: Eteläranta (EM), Katajanokka (KH), western harbour (WM). The urban background measurement site at Kallio is also marked in the figure. **(b)** The predicted emissions of $PM_{2.5}$ originated from shipping ($g\,cell^{-1}$) in Helsinki in 2009; the size of each grid cell is 0.001°.

3.2 Predicted concentrations of $PM_{2.5}$

The predicted concentrations for vehicular emissions and LRT in 2008 are presented in Fig. 2. The centre of Helsinki is on a peninsula that is located approximately in the middle of the southern part of Fig. 2. The LRT is responsible for a substantial fraction of the total $PM_{2.5}$ concentrations. The concentrations are highest in the vicinity of the main roads and streets, and in the centre of Helsinki. Figure 2 shows also the distinct influence of the ring roads number 1 (situated at a distance of about 8 km from the city centre) and number 3

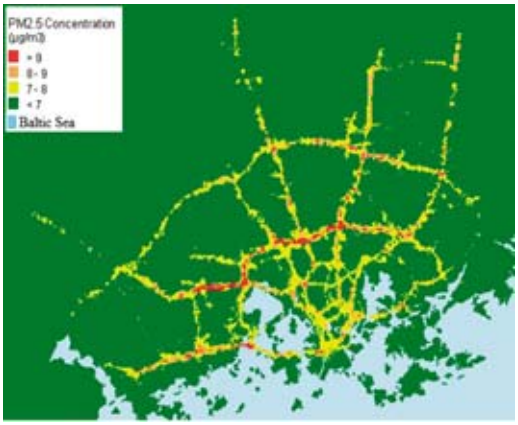

Figure 2. Predicted annual average concentrations of $PM_{2.5}$ ($\mu g\,m^{-3}$) in the Helsinki Metropolitan Area in 2008. The grid size is 50 m × 50 m and the size of the depicted area is 20 km × 16 km.

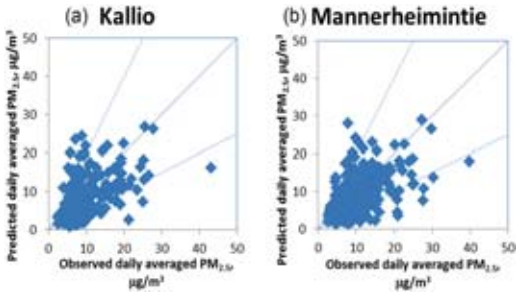

Figure 3. Predicted daily averaged against observed $PM_{2.5}$ concentrations ($\mu g\,m^{-3}$) at the stations of **(a)** Kallio (urban, background) and **(b)** Mannerheimintie (urban, traffic) in 2008.

(situated about 15 km from the city centre), the major roads leading to the Helsinki city centre, and the junctions of major roads and streets. The overall characteristics of the spatial distribution of the predicted concentrations in 2009 were very similar to those in 2008, and are therefore not presented here.

Averaging the results, for 2008, over all receptor grid locations, shows that LRT, vehicular traffic and shipping contribute 86, 11 and 3 % to the $PM_{2.5}$ concentrations, respectively. Although the average contribution of shipping to the total $PM_{2.5}$ concentrations within the whole of the modelled domain was modest, this contribution can be higher than 20 % in the vicinity of the harbours (within a distance of approximately one kilometre).

The computations for 2008 have been evaluated against the measurement data from the air quality monitoring network at the Helsinki Metropolitan Area; selected example results are presented in Fig. 3. In general, the agreement of the measured and predicted values was good or fairly good. For instance, the index of agreement that corresponds to the comparison of predicted and measured hourly time series of the $PM_{2.5}$ concentrations varied from 0.72 to 0.73 at the available three stations, whereas the fractional bias varied from −0.16 to −0.22.

It is appropriate to evaluate whether the above-mentioned values on the contribution of shipping and harbours on the $PM_{2.5}$ concentrations are correct. We therefore compared the predicted annual average concentration values with the available measurements of the Helsinki Region Environmental Services Authority in the vicinity of harbours from 2008 to 2010 (Table 2). For two stations, the year of measurement was not the same as the predicted year (2009); these comparisons are therefore only qualitative. The measured data included from 95 to 97 % of the hourly values for all these stations.

Regarding the values at the stations in the vicinity of the harbours, the agreement of the predicted and measured annual means ranged from 5 to 9 %. This adds some confidence that the predicted contributions from shipping are probably approximately correct. The annual averages of the measured and predicted urban background values also differed only slightly. However, for the computations in 2009 we have used the measured regional background concentration values, which constitute a substantial fraction of the predicted concentrations.

3.3 Predicted time activities

The time activity of the population was divided into four categories: home, workplace, traffic and other activities. The diurnal variation of population activities in various microenvironments in the Helsinki Metropolitan Area is presented in Fig. 4. Children that are younger than or equal to 10 years have been excluded from the data of this figure; however, they are included in the subsequent exposure computations. In the data presented in Fig. 4, we have combined indoor and outdoor time activity in each microenvironment.

On average people spend most of their time in the home environment. As expected, in the late afternoon and early evening, people spend a substantial fraction of their time in traffic and in other activities (these include shopping and various recreational activities). The results presented in Fig. 4 can be compared with the previously applied time activity data for the adult population presented by Kousa et al. (2002). As expected, the more comprehensive sample of the population presented in Fig. 4 (including population of all ages larger than 10 years) includes a substantially larger fraction of home activities, and a smaller fraction of work activities.

The spatial and temporal distributions of the time activity were modelled separately for each microenvironment. The annually averaged results are presented in Fig. 5a–e.

Table 2. Comparison between measured and predicted annual average $PM_{2.5}$ concentrations ($\mu g\,m^{-3}$) at the measurement sites in the vicinity of harbours, and at an urban background site in Helsinki. All modelled values are for 2009. SD = standard deviation based on the hourly values.

Name of the measurement site	Classification of the measurement site	Annual mean ± SD, modelled	Year of measurements	Annual mean ± SD, measured
Eteläranta	In the vicinity of a harbour	8.7 ± 3.3	2010	9.8 ± 9.9
Katajanokka	In the vicinity of a harbour	8.0 ± 2.9	2009	7.7 ± 6.0
Western harbour	In the vicinity of a harbour	8.2 ± 3.2	2008	8.7 ± 8.7
Kallio	Urban background	8.2 ± 3.0	2009	8.4 ± 5.7

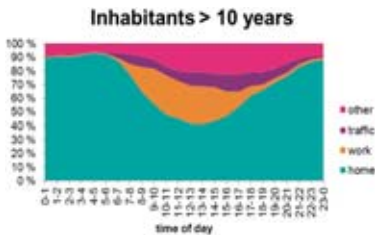

Figure 4. The diurnal variation of the activity of the population in the Helsinki Metropolitan Area in four microenvironments, based on the data for 2009 and 2010. Children that are younger than or equal to ten years old have not been included in the statistics of this figure.

Table 3. Contribution in each microenvironment to total time activity and exposure.

Microenvironment	Contribution to total time activity (%)	Contribution to total exposure (%)
Home	61	60
Work	18	17
Traffic	2	4
Other activity	18	19

As expected, the population density values are highest in the centre of Helsinki (Fig. 5a). There are also elevated levels of population density in the vicinity of the district centres of the other major cities in the area (Espoo and Vantaa), and in the vicinity of major roads and streets. The work-time activities are focused in some regions of central Helsinki, in the district centres, and in some industrial areas, whereas the home activities, and partly also the other activities, are much more evenly dispersed throughout the area.

3.4 Predicted exposures to $PM_{2.5}$

3.4.1 Exposures in various microenvironments in 2008

The population exposures were computed based on the predicted $PM_{2.5}$ concentrations and time activities. The predicted concentration and population data were interpolated on to a rectangular grid with a grid size of 50 m. The population exposures were computed for each hour of the year, at 18.7×10^3 receptor grid squares, separately for the selected four microenvironments.

Population exposure is a combination of both the concentration and activity (or population density) values. The fractions of exposure in various microenvironments compared with the total population exposure to $PM_{2.5}$ are presented in Fig. 6a These values include all age groups (including also children younger than 10 years). The exposure at home is responsible for most of the exposure, 60 %, whereas the work and other activities exposures are responsible for most of the rest of the exposure, i.e. 19 and 17 %, respectively.

We have compared the shares of time activity and exposure in each microenvironment in Table 3, according to the computations. The contributions to the total time activity and exposure are similar for home, work and other activity microenvironments; this indicates that there are no major relative differences in the average concentrations prevailing at those microenvironments. However, for traffic the contribution to exposure is substantially higher than the corresponding contribution to time activity. This is mainly caused by the relatively higher concentrations on the roads and streets and in their vicinity.

We have presented the spatial distributions of the predicted annual average population exposures in the Helsinki Metropolitan Area in 2008 in Fig. 7a–e, for the total exposure and separately for all microenvironments. These distributions exhibit characteristics of both the corresponding spatial concentration distributions and time activities. There are elevated values in the Helsinki city centre, along major roads and streets, and in the vicinity of urban district centres. The high home and work exposures in the centre of Helsinki are caused both by the relatively high concentrations and the highest population and workplace densities in the area.

The spatial distributions of the population exposures at home and work correlate poorly (see Fig. 7b–c). The reason is that while most of the work environments are located either in the centre of Helsinki and in district centres, or in

Figure 5. The predicted density of population (no. persons), evaluated as an average for 2009 and 2010, for **(a)** all microenvironments, **(b)** home, **(c)** work, **(d)** traffic and **(e)** other activities. The grid size is 50 m × 50 m.

major industrial, service and commercial regions, a substantial fraction of residences are also located in suburban areas.

As expected, the exposure while in traffic is focused along the main network of roads and streets, and in their immediate vicinity. These exposures may be under-predicted for three main reasons. First, the traffic flow and emission modelling does not completely allow for all the effects of traffic congestion. The traffic flow modelling does take into account the slowing down of traffic in certain regions and streets, and the emission modelling takes into account the dependency of emissions on the travel speed. However, the emission modelling does not take into account the effects of idling, and the

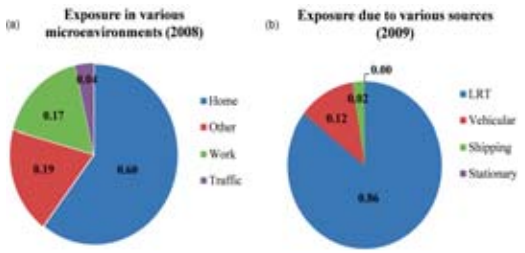

Figure 6. Contribution to the total population exposures to $PM_{2.5}$: **(a)** in each microenvironment in the Helsinki Metropolitan Area in 2008, and **(b)** originated from various source categories in Helsinki, in 2009.

deceleration and acceleration of vehicles. Traffic congestion occurs frequently in the centre of Helsinki, and also along the main roads and streets, especially during rush hours. Second, the dispersion modelling and the spatial averaging does not allow for the very fine-scale (< 50 m) highest peak concentrations above the roads and streets. The dispersion modelling also does not include any treatment for dispersion in street canyons, which tends to result in an under-prediction of concentrations. Third, by assuming no indoor sources (the infiltration factor for vehicles is equal to one) the indoor concentrations are neglected.

We have allowed for only the influence of outdoor air pollution on the population exposure. We have not addressed the indoor sources and sinks of pollution; however, indoor sources such as, e.g. tobacco smoking, cooking, heating and cleaning can cause additional short-term concentration maxima. We have also assumed that the infiltration factor is temporally constant. The temporal variation of indoor concentrations would be expected to be smoother than our assessments, due to the delay associated with the infiltration of outdoor air pollution to indoors. Such a delay would mainly affect shorter term exposure assessments; we consider only annual average exposures in the present study.

3.4.2 Exposures originated from various source categories in 2009

The population exposures from various source categories were also computed for each hour of the year. The contribution of each source category to the total population exposure to $PM_{2.5}$ concentrations in Helsinki are presented in Fig. 6b. The population exposure originated from the LRT background concentrations is responsible for a major fraction, 86 %, of the total exposure. The next largest contributors are vehicular emissions (12 %) and shipping (2 %). The exposure originated from major stationary sources is negligible, caused by the dispersion of pollutants to wide regions due to high stacks for most of these installations. However, the above-mentioned percentage values include some uncertainties, due to excluding the small-scale combustion from these computations. The contribution of small-scale combustion on the population exposure will be higher than its contribution to the total emissions, due to the low injection heights.

We have presented in Fig. 8a–c the spatial distributions of annually averaged predicted population exposures to $PM_{2.5}$ in Helsinki in 2009, originated from various source categories. The population exposure caused by shipping is focused in central Helsinki, near the main harbours and within some densely inhabited parts of the city. As expected, the population exposure is relatively substantially lower within the main park areas (e.g. Central Park, and the parks of Kaisaniemi and Kaivopuisto) and a cemetery (Hietaniemi). In the harbours and their vicinity (approx. 1 km from the harbour), the contribution of shipping to total exposure can reach up to 20 %.

4 Conclusions

We have presented a refined version of a mathematical model for the determination of human exposure to ambient air pollution. A review of the main characteristics of the previous and current versions of the EXPAND model are presented in Table 4. The revisions of the modelling system include the following: (i) the treatment of the time use of population has been extended to include all the age groups and a wide range of activities, including detailed treatments of the various traffic modes, and a wide range of recreational activities; (ii) the infiltration coefficients from outdoor to indoor air have been updated based on new information from the ULTRA-2 study; (iii) the revised model version can also be used for evaluating intake fractions, and the model can be applied using several internationally applied coordinate systems. The model can be used for evaluating specific population exposures, e.g. in terms of population age groups, microenvironments, source categories or individual sources.

Numerical results are presented on the spatial concentrations, the time activity and the population exposures to $PM_{2.5}$ in the Helsinki Metropolitan Area for 2008 and in Helsinki for 2009. The computations included the regionally and long-range transported pollution and the vehicular emissions both for 2008 and 2009. In addition, the emissions from major stationary sources and the emissions from shipping in the sea areas and in the harbours of Helsinki have been considered in the simulations for 2009. The above-mentioned emission source categories contain all the most important sources in the area, except for small-scale combustion (such as residential heating). It has been estimated that small-scale combustion contributes 18 % to the total $PM_{2.5}$ emissions in the Helsinki Metropolitan Area. It was not possible to take into account those residential sources, due to scarcity of spatially resolved emission data.

We have conducted an unprecedentedly detailed and accurate emission inventory of $PM_{2.5}$ originated from shipping in 2009, using the STEAM emission model. The emissions

Figure 7. Predicted population exposure per year ($\mu g\,m^{-3} \cdot$ no. people) to regionally and long-range transported pollution and the emissions originated from the urban vehicular traffic $PM_{2.5}$ in the Helsinki Metropolitan Area in 2008: **(a)** all microenvironments, **(b)** home, **(c)** work, **(d)** traffic and **(e)** other activities.

per unit area were largest within three major harbour areas in Helsinki; the second largest emissions occurred along the main shipping routes. This study presents for the first time for this capital region quantitative evaluations of the influence of shipping emissions on the concentrations and population exposure.

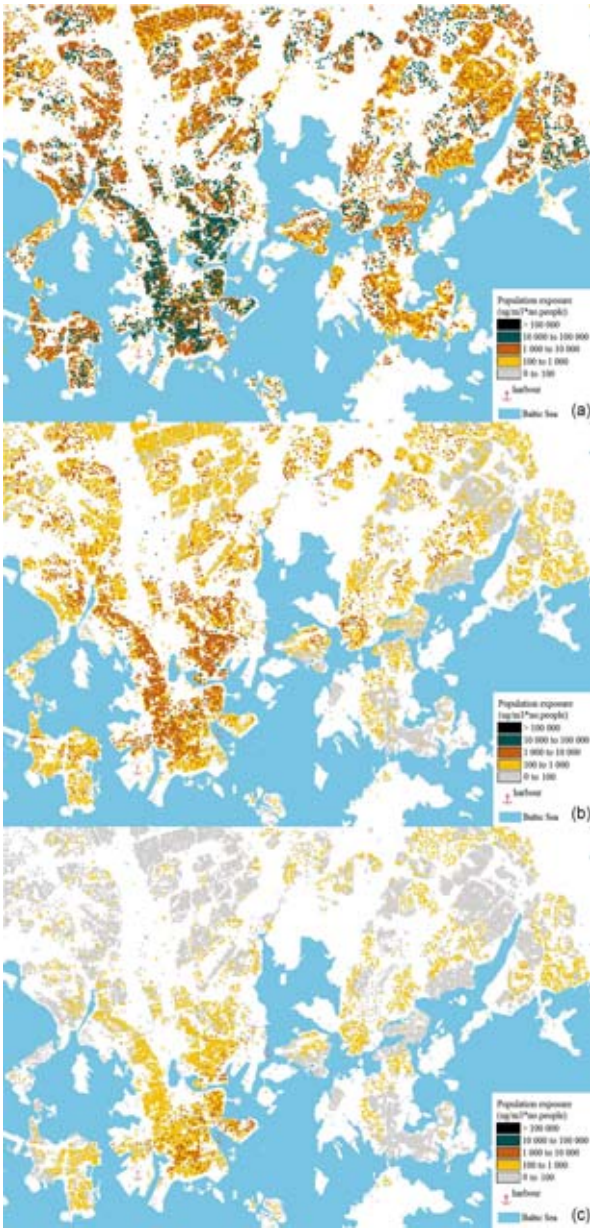

Figure 8. Predicted population exposure per year ($\mu g\,m^{-3} \cdot$ no. people) to $PM_{2.5}$ in Helsinki in 2009. The unit is number of people $\cdot\,\mu g\,m^{-3}$. The computations included regionally and long-range transported background, and the emissions originated from vehicular traffic, shipping and major stationary sources: **(a)** total exposure, **(b)** only emissions from vehicular traffic and **(c)** only emissions from shipping.

A comprehensive and up-to-date inventory was compiled of the time activity of the population of approximately 1.0 million inhabitants. This inventory included the fine-scale spatial distributions of hourly time activity of all the age groups of the population during a year, classified into four microenvironmental categories: home, workplace, traffic and other activities. On average, people spend most of their time at home. As expected, in the late afternoon and early evening, people spend a substantial fraction of their time in traffic and in other activities (these include, e.g. shopping and various

Table 4. A summary of the refinements of the EXPAND model in this study.

	Previous version (Kousa et al., 2002)	Current version (this study)
Emissions	Vehicular (exhaust), major stationary sources	Vehicular (exhaust and suspension), major stationary sources, shipping
Pollutants addressed	NO_x and NO_2	$PM_{2.5}$
Dispersion models	CAR-FMI, UDM-FMI, measured regional background	CAR-FMI, UDM-FMI, LOTOS-EUROS, measured regional background
Time activity data	Working age population (25–65 years), year 2000	All age groups, wider range of activities for various traffic modes and recreational activities, year 2010
Infiltration rates	Based on the EXPOLIS project	Based on the EXPOLIS and ULTRA2 projects
Model results	Population exposure, microenvironment- and source-specific	Population exposure and intake fractions, microenvironment-, source- and population group-specific
Coordinate systems	Finnish coordinate system	Several international and national coordinate systems

recreational activities). The work-time activities are focused in some regions of central Helsinki, in the district centres, and in some industrial areas, whereas the home activities are much more evenly dispersed throughout the area.

Finally, we evaluated the population exposures both in terms of the microenvironments and the main source categories. Approximately 60 % of the total exposure occurred at home, 17 % at work, 4 % in traffic and 19 % in other microenvironments. The spatial distributions of the population exposures exhibit characteristics of both the corresponding spatial concentration distributions and time activities. There were elevated exposure values in the Helsinki city centre, along major roads and streets, and in the vicinity of urban district centres. The high home and work exposures in the centre of Helsinki were caused both by the relatively high concentrations and the highest population and workplace densities in the area.

As expected, the exposure while in traffic was focused along the main network of roads and streets, and in their immediate vicinity. However, the exposures in traffic may be under-predicted in this study for three main reasons. First, the emission modelling does not explicitly allow for traffic congestion. Second, the dispersion modelling and the spatial averaging do not allow either for the dispersion in street canyons or the very fine-scale concentration distributions above the roads and streets. Third, the indoor concentrations are neglected.

The population exposure originated from the LRT background concentrations was responsible for a major fraction, 86 %, of the total exposure. The second largest contributors were vehicular emissions (12 %) and shipping (2 %). The exposure originated from major stationary sources was marginally small. In the harbour areas and their vicinity (approximately at the distance of 1 km), the contribution of shipping to total exposure can reach up to 20 %.

The values for the infiltration factors were updated based on the best available information, from the ULTRA-2 study. However, the assumed infiltration values are averages for residential and workplace buildings, and do not take into account the specific characteristics of individual buildings, such as the efficiency of ventilation and the filtering of pollutants, or pollution sources and sinks within the indoor microenvironments. The relevant information regarding the whole of the building stock was not sufficient for conducting such assessments.

This model has been designed to be utilized by municipal authorities in evaluating the impacts of traffic planning and land use scenarios. It has been used, for instance, as an assessment tool in the revision of the transportation system plan for the Helsinki Metropolitan Area. Such detailed population exposure models can also be a valuable tool of assessment to estimate the adverse health effects caused to the population by air pollution, both for the present and in the future. The model, including the GIS-based methodology, could also be applied on a regional scale in the future.

The methodologies developed, and the EXPAND model itself, are available to be utilized also for other urban areas worldwide, and within other integrated modelling systems, providing that sufficiently detailed concentration fields and time activity surveys will be available. The data that are commonly the most difficult to find and process to a suitable format are the detailed time activity information. This data should include at least a survey regarding the temporally varying location of the population in residential and workplace environments. Whenever possible, this information should be accompanied with time activity information of the population in traffic and at recreational activities. The location of the population in traffic can commonly be estimated mainly based on traffic flow information, combined with information on the number of passengers in private cars, buses and other vehicles.

The executable program of the EXPAND model for Windows operating system for evaluating human exposure to air pollution in an urban area is available upon request from the authors.

Appendix A: The coordinate systems of the model

The EXPAND model was refined to be able to compute exposures and intake fractions internationally using the following coordinate systems:

1. ETRS-GKn, in which GK refers to the Gauss–Krüger projection and *n* stands for the zone of the projection (in total 13 projections),
2. longitude and latitude (WGS84) and
3. Universal Transverse Mercator (UTM) coordinate system.

In addition, the new model version can use the national Finnish coordinate system (abbreviated as KKJ) in all the defined zones.

Acknowledgements. The study was supported by the EU Contract FP7-ENV-2009-1-243406 (TRANSPHORM); EU Health Programme projects HEALTHVENT, Grant No. 2009 12 08; Academy of Finland Contracts 133792 (PM Sizex) and "The Influence of Air Pollution, Pollen and Ambient Temperature on Astma and Allergies in Changing Climate (APTA)". European Regional Development Fund, Central Baltic INTERREG IV A Programme within the project SNOOP; EU contract ENV4-CT95-0205 (ULTRA); and EU contract ENV4-CT96-0202 (EXPOLIS, DG12-DTEE).

Edited by: A. Lauer

References

Ashmore, M. R. and Dimitripoulou, C.: Personal exposure of children to air pollution, Atmos. Environ., 43, 128–141, doi:10.1016/j.atmosenv.2008.09.024, 2009.

Beckx, C., Int Panis, L., Arentze, T., Janssens, D., Torfs, R., Broekx, S., and Wets, G.: A dynamic activity-based population modelling approach to evaluate exposure to air pollution: Methods and application to a Dutch urban area, Environ. Impact Assess., 29, 179–185, 2009.

Bennett, D., McKone, T., Evans, J., Nazaroff, W., Smith, K., Margni, M., Jolliet, O., and Smith, K. R.: Defining intake fraction, Environ. Sci. Technol. 36, 206A–211A, doi:10.1021/es0222770, 2002.

Borrego, C., Sá, E., Monteiro, A., Ferreira, J., and Miranda, A.: Forecasting Human Exposure to atmospheric Pollutants – A modelling approach, Atmos. Environ., 43, 5796–5806, doi:10.1016/j.atmosenv.2009.07.049, 2009.

City of Helsinki Urban Facts (CHUF): Statistical Yearbook of the City of Helsinki, Gummerrus Kirjapaino Oy, Jyväskylä, 2009.

Dimitroulopoulou, C., Ashmore, M. R., Hill, M. T. R., Byrne, M. A., and Kinnersley, R.: INDAIR: a probabilistic model of indoor air pollution in UK homes, Atmos. Environ., 40, 6362–6379, doi:10.1016/j.atmosenv.2006.05.047, 2006.

Elolähde, T.: Traffic model system and emission calculations of the Helsinki Metropolitan Area Council, 20th International Emme Users' Conference, Montreal, available at: www.inro.ca/en/pres_pap/international/ieug06/1-3_Timo_Elolahde_report.pdf (last access: 18 December 2013), 2006.

European Parliament (EP): Directive 2002/91/EC of the European Parliament and of the Council of 16 December 2002 on the Energy Performance of Buildings, available at: http://eur-lex.europa.eu/legal-content/EN/TXT/?uri=CELEX:32002L0091 (last access: 25 August 2014), 2002.

Franzen, L. G., Hjelmroos, M., Kallberg, P., Brorstrom-Lunden, E., Juntto, S., and Savolainen, A.-L.: The "yellow snow" episode of northern Fennoscandia, March 1991 – a case study of long-distance transport of soil, pollen and stable organic compounds, Atmos. Environ., 28, 3587–3604, 1994.

Gulliver J. and Briggs, D.: Time-space modelling of journey-time exposure to traffic-related air pollution using GIS, Environ. Res., 97, 10–95, doi:10.1016/j.envres.2004.05.002, 2005.

Gröndahl, T., Makkonen, J., Myllynen, M., Niemi, J., and Tuomi, S.: Tulisijojen käyttö ja päästöt pääkaupunkiseudun pientaloista (The use of residential fireplaces and their emissions in the Helsinki Metropolitan Area), Helsingin seudun ympäristöpalvelut -kuntayhtymä, HSY, Helsinki, 2013 (in Finnish).

Hänninen, O., Kruize, H., Lebret, E., and Jantunen, M.: EXPOLIS simulation model: $PM_{2.5}$ application and comparison with measurements in Helsinki, J. Exp. Anal. Environ. Epidem., 13, 74–85, doi:10.1038/sj.jea.7500260, 2003.

Hänninen, O., Lebret, E., Ilacqua, V., Katsouyanni, K., Künzli, N., Sram, R., and Jantunen, M.: Infiltration of ambient $PM_{2.5}$ and levels of indoor generated non-ETS $PM_{2.5}$ in residences of four European cities, Atmos. Environ., 38, 6411–6423, doi:10.1016/j.atmosenv.2004.07.015, 2004.

Hänninen, O., Palonen, J., Tuomisto, J., Yli-Tuomi, T., Seppänen, O., and Jantunen, M. J.: Reduction potential of urban $PM_{2.5}$ mortality risk using modern ventilation systems in buildings, Indoor Air, 15, 246–256, doi:10.1111/j.1600-0668.2005.00365.x, 2005.

Hänninen, O., Hoek, G., Mallone, S., Chellini, E., Katsouyanni, K., Kuenzli, N., Gariazzo, C., Cattani, G., Marconi, A., Molnár, P., Bellander, T., and Jantunen, M.: Seasonal patterns of outdoor PM infiltration into indoor environments: review and meta-analysis of available studies from different climatological zones in Europe, Air Qual. Atmos. Health., 4, 221–233, doi:10.1007/s11869-010-0076-5, 2011.

Hänninen, O., Sorjamaa, R., Lipponen, P., Cyrys, J., Lanki, T., and Pekkanen, J.: Aerosol-based modelling of infiltration of ambient $PM_{2.5}$ and evaluation against population-based measurements in homes in Helsinki, Finland, J. Aerosol Sci., 66, 111–122, doi:10.1016/j.jaerosci.2013.08.004, 2013.

Hellén, H., Kukkonen, J., Kauhaniemi, M., Hakola, H., Laurila, T., and Pietarila, H.: Evaluation of atmospheric benzene concentrations in the Helsinki Metropolitan Area in 2000–2003 using diffusive sampling and atmospheric dispersion modelling, Atmos. Environ., 39, 4003–4014, doi:10.1016/j.atmosenv.2005.03.023, 2005.

Hellman, T.: Henkilöautojen Keskikuormitus Niemen Rajalla Helsingissä Vuonna 2012 (The average number of people in the personal cars in Helsinki year 2012), City of Helsinki, City Planning Department, Traffic Planning, Publications on Air Quality, 23, 2012 (in Finnish).

INRO: EMME/2 User's manual, INRO Consultants Inc., Montreal, Canada, 1994.

Jalkanen, J.-P., Brink, A., Kalli, J., Pettersson, H., Kukkonen, J., and Stipa, T.: A modelling system for the exhaust emissions of marine traffic and its application in the Baltic Sea area, Atmos. Chem. Phys., 9, 9209–9223, doi:10.5194/acp-9-9209-2009, 2009.

Jalkanen, J.-P., Johansson, L., Kukkonen, J., Brink, A., Kalli, J., and Stipa, T.: Extension of an assessment model of ship traffic exhaust emissions for particulate matter and carbon monoxide, Atmos. Chem. Phys., 12, 2641–2659, doi:10.5194/acp-12-2641-2012, 2012.

Jantunen, M., Hänninen, O., Katsouyanni, K., Knöppel, H., Künzli, N., and Lebret, E.: Air pollution exposure in European cities: The EXPOLIS-study, J. Expo. Anal. Env. Epid., 8, 495–518, 1998.

Jensen, S. S.: A Geographic Approach to Modelling Human Exposure to Traffic Air Pollution using GIS, PhD Thesis. National Environ. Res. Institute, Denmark, 1999.

Kauhaniemi, M., Karppinen, A., Härkönen, J., Kousa, A., Alaviippola, B., Koskentalo, T., Aarnio, P., Elolähde, T., and Kukkonen, J.: Evaluation of a modelling system for predicting the concentrations of $PM_{2.5}$ in an urban area, Atmos. Environ. 42, 4517–4529, doi:10.1016/j.atmosenv.2008.01.071, 2008.

Kauhaniemi, M., Kukkonen, J., Härkönen, J., Nikmo, J., Kangas, L., Omstedt, G., Ketzel, M., Kousa, A., Haakana, M., and Karppinen, A.: Evaluation of a road dust suspension model for predicting the concentrations of PM_{10} in a street canyon, Atmos. Environ., 45, 3646–3654, doi:10.1016/j.atmosenv.2011.04.055, 2011.

Karppinen, A.: Meteorological pre-processing and atmospheric dispersion modelling of urban air quality and applications in the Helsinki Metropolitan Area. Finnish Meteorological Institute, Contributions No. 33, ISBN 951-697-552-6, University Press, Helsinki, 2001.

Karppinen, A., Kukkonen, J., Elolähde, T., Konttinen, M., Koskentalo, T., and Rantakrans, E.: A modelling system for predicting urban air pollution, Model description and applications in the Helsinki Metropolitan Area, Atmos. Environ., 34, 3723–3733, doi:10.1016/S1352-2310(00)00074-1, 2000a.

Karppinen, A., Kukkonen, J., Elolähde, T., Konttinen, M., and Koskentalo, T.: A modelling system for predicting urban air pollution, Comparison of model predictions with the data of an urban measurement network, Atmos. Environ., 34, 3735–3743, doi:10.1016/S1352-2310(00)00073-X, 2000b.

Kousa, A., Kukkonen, J., Karppinen, A., Aarnio, P., and Koskentalo, T.: Statistical and diagnostic evaluation of a new-generation urban dispersion modelling system against an extensive dataset in the Helsinki Area, Atmos. Environ., 35, 4617–4628, doi:10.1016/S1352-2310(01)00163-7, 2001.

Kousa, A., Kukkonen, J., Karppinen, A., Aarnio, P., and Koskentalo, T.: A model for evaluating the population exposure to ambient air pollution in an urban area, Atmos. Environ., 36, 2109–2119, doi:10.1016/S1352-2310(02)00228-5, 2002.

Kukkonen, J., Härkönen, J., Walden, J., Karppinen, A., and Lusa, K.: Evaluation of the dispersion model CAR-FMI against data from a measurement campaign near a major road, Int. J. Environ. Pollut., 35, 949–960, 2001.

Lanki, T., Hoek, G., Timonen, K. L., Peters, A., Tiittanen, P., and Vanninen, E.: Hourly variation in fine particle exposure is associated with transiently increased risk of ST segment depression, Occup. Environ. Med., 65, 782–786, doi:10.1136/oem.2007.037531, 2008.

Lappi, S., Lovén, K., Rasila, T., and Pietarila, H.: Pääkaupunkiseudun päästöjen leviämismalliselvitys. Energiantuotannon, satamatoiminnan, laivaliikenteen, lentoliikenteen, lentoasematoiminnan ja autoliikenteen typenoksidi-, rikkidioksidi- ja hiukkaspäästöjen leviämislaskelmat, Finnish Meteorological Institute, Helsinki, 2008.

Laurikko, J.: On exhaust emissions from petrol-fuelled passenger cars at low ambient temperatures, VTT Publications 348, Technical Research Centre of Finland, Espoo, 210 pp., 1998.

Laurikko, J., Kukkonen, J., Koistinen, K., and Koskentalo, T.: Integrated modelling system for the evaluation of the impact of Transport-related measures to urban air quality, 2th symposium "Transport and Air Pollution", Avignon, France, 2003.

Levitin, J., Härkönen, J., Kukkonen, J., and Nikmo, J.: Evaluation of the CALINE4 and CAR-FMI models against measurements near a major road, Atmos. Environ., 39, 4439–4452, doi:10.1016/j.atmosenv.2005.03.046, 2005.

Loh, M. M., Soares, J., Karppinen, A., Kukkonen, J., Kangas, L., Riikonen, K., Kousa, A., Asikainen, A., and Jantunen, M. J.: Intake fraction distributions for benzene from vehicles in the Helsinki Metropolitan Area, Atmos. Environ., 43, 301–310, doi:10.1016/j.atmosenv.2008.09.082, 2009.

Mäkelä, K.: "LIPASTO calculation model: unit emissions of traffic", VTT Technical Research Centre of Finland, Espoo, Finland, available at: http://lipasto.vtt.fi/info.htm (last access: 9 April 2014), 2002.

Official Statistics of Finland (OSF): Time use survey [e-publication], Helsinki: Statistics Finland, available at: http://www.stat.fi/til/akay/index_en.html, last access: 1 January 2013.

Niemi, J., Malkki, M., Myllynen, M., Lounasheimo, J., Kousa, A., Julkunen, A., and Koskentalo, T.: Air Quality in the Helsinki Metropolitan Area in 2008, YTV Publications 15/2009, 128, Finland, available at: http://www.hsy.fi/seututieto/Documents/YTV_julkaisusarja/15_2009_vuosiraportti2008.pdf (last access: 12 June 2014), 2009 (in Finnish)

Omstedt, G., Bringfelt, B., and Johansson, C.: A model for vehicle-induced non-tailpipe emissions of particles along Swedish roads, Atmos. Environ., 39, 6088–6097, doi:10.1016/j.atmosenv.2005.06.037, 2005.

Öttl, D., Kukkonen, J., Almbauer, R. A., Sturm, P. J., Pohjola, M., and Härkönen, J. H.: Evaluation of a Gaussian and a Lagrangian model against a roadside dataset, with focus on low wind speed conditions, Atmos. Environ., 35, 2123–2132, doi:10.1016/S1352-2310(00)00492-1, 2001.

Pope, C. A. and Dockery, D. W.: Health effects of fine particulate air pollution: Lines that connect, J. Air Waste Manage., 56, 709–742, 2006.

Rotko, T., Koistinen, K., Hänninen, O., and Jantunen, M.: Sociodemographic descriptors of personal exposure to fine particles ($PM_{2.5}$) in EXPOLIS Helsinki, J. Expo. Anal. Env. Epid., 10, 385–393, doi:10.1038/sj.jea.7500104, 2000.

Schaap, M. F. S., Timmermans, R. M. A., Roemer, M., Velders, G., Beck, J., and Builtjes, P. J. H.: The LOTOS-EUROS model: description, validation and latest developments, Int. J. Environ. Pollut., 32, 270–290, 2008.

Schweizer, C., Edwards, R. D, Bayer-Oglesby, L., Gauderman, W. J., Ilacqua, V., Juhani, M., Lai, H. K., Nieuwenhuijsen, M., and Künzl, N.: Indoor time-microenvironment-activity patterns in seven regions of Europe, J. Expo. Sci. Env. Epid., 17, 170–181, doi:10.1038/sj.jes.7500490, 2007.

Singh, V., Sokhi, R., and Kukkonen, J.: $PM_{2.5}$ concentrations in London for 2008 – A modeling analysis of contributions from road traffic, J. Air Waste Manage., 64, 509–518, doi:10.1080/10962247.2013.848244, 2014.

Sofiev, M., Soares, J., Prank, M., de Leeuw, G., and Kukkonen, J.: A regional-to-global model of emission and transport of sea salt particles in the atmosphere, J. Geophys. Res., 116, D21302, doi:10.1029/2010JD014713, 2011.

Sokhi, R., Mao, H., Srimath, S. T. G., Fan, S., Kitwiroon, N., Luhana, L., Kukkonen, K., Haakana, M., van den Hout, K.

D., Boulter, P., McCrae, I. S., Larssen, S., Gjerstad, K. I., San Jose, R., Bartzis, J., Neofytou, P., van den Breemer, P., Neville, S., Kousa, A., Cortes, B. M., Karppinen, K., and Myrtveit, I.: An integrated multi-model approach for air quality assessment: Development and evaluation of the OSCAR Air Quality Assessment System, Environ. Modell. Softw., 23, 268–281, doi:10.1016/j.envsoft.2007.03.006, 2008.

Statistics Filand: Energy consumption in households [e-publication], ISSN = 2323-329X, 2012, Appendix Figure 1, Energy consumption in households by energy source in 2012, Helsinki: Statistics Finland, available at: http://www.stat.fi/til/asen/2012/asen_2012_2013-11-13_kuv_001_en.html (last access: 30 June 2014), 2012.

V

Atmospheric Environment 43 (2009) 301–310

Contents lists available at ScienceDirect

Atmospheric Environment

journal homepage: www.elsevier.com/locate/atmosenv

Intake fraction distributions for benzene from vehicles in the Helsinki metropolitan area

Miranda M. Loh [a,*], Joana Soares [b], Ari Karppinen [b], Jaakko Kukkonen [b], Leena Kangas [b], Kari Riikonen [b], Anu Kousa [c], Arja Asikainen [a], Matti J. Jantunen [a]

[a] National Public Health Institute (KTL), P.O. Box 95, 70701 Kuopio, Finland
[b] Finnish Meteorological Institute (FMI), Helsinki, Finland
[c] Helsinki Metropolitan Area Council (YTV), Helsinki, Finland

ARTICLE INFO

Article history:
Received 30 April 2008
Received in revised form
2 September 2008
Accepted 15 September 2008

Keywords:
Intake fraction
Benzene
Traffic
Air pollution
Exposure

ABSTRACT

The intake fraction (iF) gives a measure of the portion of a source's emissions that is inhaled by an exposed population over a defined period of time. This study examines spatial and population-based iF distributions of a known human carcinogen, benzene, from a ubiquitous urban source, local vehicular traffic, in the Helsinki Metropolitan Area using three computational methods. The first method uses the EXPAND model (EXPosure to Air pollution, especially to Nitrogen Dioxide and particulate matter), which incorporates spatial and temporal information on population activity patterns as well as urban-scale and street canyon dispersion models to predict spatial population exposure distributions. The second method uses data from the personal monitoring study EXPOLIS (Air Pollution Exposure Distributions of Adult Urban Populations in Europe) to estimate the intake fractions for individuals in the study. The third method, a one-compartment box model provides estimates within an order-of-magnitude or better for non-reactive agents in an urban area. Population intake fractions are higher using the personal monitoring data method (median iF 30 per million, mean iF 39 per million) compared with the spatial model (annual mean iF 10 per million) and the box model (median iF 4 per million, mean iF 7 per million). In particular, this study presents detailed intake fraction distributions on several different levels (spatial, individual, and generic) for the same urban area.

1. Introduction

Benzene is one of the few chemicals established as known human carcinogens. Among organic air pollutants, benzene has been found to have relatively high population risks in various countries. It was identified as a high priority pollutant by the Critical Appraisal of the Setting and Implementation of Indoor Exposure Limits in the EU (INDEX) assessment, with median cancer risks estimated to be between 8 per million and 48 per million for various areas in Europe (Kotzias et al., 2005). Higher risks were found for people living in highly trafficked urban areas.

In urban environments, traffic is the most important source for ambient air benzene concentrations. Other outdoor sources of benzene include fossil fuel and wood combustion and biomass burning (Hedberg et al., 2002; Hellén et al., 2005). The annual average concentrations of benzene in European cities range from less than 10 $\mu g\,m^{-3}$ to almost 25 $\mu g\,m^{-3}$ (Cocheo et al., 2000). Benzene traffic emissions depend on several factors, such as vehicle category, fuel composition, vehicle speed and ambient temperature.

The relationship between a pollutant's source and the subsequent exposure of a population depends on the ability of the released pollutant to reach individuals in specific atmospheric conditions. The intake fraction (iF) gives a measure of the portion of a source's emissions that is inhaled by the exposed population over a defined period of time. The iF is defined as intake via relevant exposure pathways divided by the emissions of the pollutant and source (or source category) of interest. For instance, an intake fraction of 1 in a million (10^{-6}) means that for every tonne of a pollutant emitted, 1 g is inhaled by the exposed population. The iF can be useful in both screening-level order-of-magnitude estimates and more detailed policy modelling (Bennett et al., 2002a). So far, the iF has most successfully been applied for non-reactive and persistent compounds.

Intake fraction has been used in life cycle assessment (Bennett et al., 2002b; Nigge, 2001; Nishioka et al., 2002), for ranking sources (Wang et al., 2006), and in comparisons of different control policies (Stevens et al., 2005). These studies have modelled iF using atmospheric dispersion or multimedia modelling. Intake fractions have

* Corresponding author. Tel: +358 17 201 394; fax: +358 17 201 184.
E-mail address: miranda.loh@ktl.fi (M.M. Loh).

1352-2310/$ – see front matter © 2008 Elsevier Ltd. All rights reserved.
doi:10.1016/j.atmosenv.2008.09.082

been most frequently calculated for whole populations, rather than for individuals. Population intake fraction, iF, however, is the sum of individual intake fractions, iF_i. Understanding the spatial and temporal variability across a population for individual intake fractions provides useful information about which exposure factors drive the inter-individual iF variation. The spatial distribution of intake fractions can also inform patterns of exposure from a particular source.

Few studies have examined the spatial variation of iF on an urban or smaller scale. For pollutants that originate near the ground level, a substantial fraction of the emissions would be expected to affect the near field population. Greco et al. modelled the impact of a county's mobile source fine particulate matter ($PM_{2.5}$) emissions on neighbouring counties, and found that half of total exposure for primary $PM_{2.5}$ occurred within a median distance of 150 km from the source county (Greco et al., 2007a). In a separate analysis, Greco et al. (2007b) examined iF for primary $PM_{2.5}$ along road segments in Boston, USA, using a line source dispersion model and found an annual average iF of 12 per million with half of total exposure occurring within 200 m of the roadway, over twice the values found in the larger scale study (Greco et al., 2007a). The substantially smaller median distance is caused by different spatial scales and methodologies (regional scale versus local scale dispersion modelling).

None of the above analyses included population microenvironment time-activity information, i.e. the population was assumed to stay permanently in their residential addresses. Additionally, only one of the models used in these studies incorporated fine-resolution information on pollutant dispersion from line sources (Greco et al., 2007b). In particular, street level calculations have been shown to result in a more descriptive distribution of iF in terms of height (different floors of a building) and along the street, when information about the number of people and their diurnal distribution is available. Marshall et al. (2003) combined ambient concentration modelling with individual time-activity data and microenvironmental exposure factors to determine individual intake fractions in the South Coast Basin of California, USA, estimating an aggregate intake fraction of 48 per million for benzene. Despite this, no study has yet included a time-series depiction of the number of people in various activities at specific locations or examine the gradients from street canyon pollution concerning the number of people at various times on different floors in buildings.

While iF has been extensively calculated with modelled estimates, measured environmental samples have rarely been used. Margni et al. (2004) compared dioxin iFs using both measured and modelled data, and Juraske et al. (2007) compared modelled estimates of intake fraction for Captan, a pesticide, with measurements. Both found that iFs using measured and modelled data generally agreed within an order-of-magnitude. Marshall and Behrentz (2005) examined the potential iF of non-reactive (i.e. where the half-life of pollutant in air is greater than residence time of air in the modelled compartment) pollutants from buses using a tracer gas to estimate how much of a bus' own emissions would be inhaled by the bus' passengers compared to inhabitants of the surrounding region of the bus (in this case, the South Coast area of California). They determined that passengers would inhale up to five or six orders of magnitude more of the emissions from the bus than average South Coast residents not on the bus.

This paper analyses and compares the results obtained using three methods of evaluating intake fraction from mobile sources; these methods also provide information about fine-resolution spatial and inter-personal variation in intake fractions. Benzene was chosen because it has a relatively long half-life in air and has been shown to be a human carcinogen.

First, the spatial distribution of intake fractions was calculated using a modified version of the EXPAND model (Kousa et al., 2002), that has the added benefit of incorporating street canyon dispersion and exposure. Second, individual intake fractions were calculated using personal, residential (indoor and outdoor), and workplace concentrations as well as time-activity data from the Air Pollution Exposure Distributions of Adult Urban Populations in Europe (EXPOLIS) study. Third, population intake fractions were modelled using a simple box model approach, in which hourly meteorological variables are used as input values. In the cases that were evaluated by Lai et al. (2000) and Marshall et al. (2003, 2005), this method was found to be accurate within a factor of two for predicting the annual averages of non-reactive pollutants. We compare the results computed in this study for mobile sources with previously calculated intake fractions for benzene.

2. Methods

Intake fraction is defined as the incremental intake of a pollutant by the exposed population per unit of emissions.

$$\mathrm{iF} = \frac{\sum_{\text{people, time}} \text{mass intake of pollutant by an individual}}{\text{mass release into the environment}} \quad (1)$$

The numerator can be calculated using exposure estimates for the microenvironments of interest and the average breathing rate of a population while in each microenvironment. We address the Helsinki Metropolitan Area, as extensive datasets on population exposure to benzene are available, and an exposure modelling framework has already been implemented for this area, including detailed time-activity distributions for both stationary and moving populations.

2.1. Experimental data

2.1.1. Personal exposure measurement data from the EXPOLIS study

Detailed descriptions of the EXPOLIS study design and methods have been published previously (Edwards and Jantunen, 2001; Jantunen et al., 1998; Saarela et al., 2003). Personal exposure, residential indoor and outdoor, and workplace concentrations were measured for 201 randomly selected adult (aged 25–55 years) participants in Helsinki during fall 1996 to winter 1997. The monitored population sample represents well the total working-aged population of the Helsinki Metropolitan Area (Rotko et al., 2000). Sampling occurred during the workdays over a 48 h period, generally with up to three participants monitored during the same days. Samples were taken inside the participants' homes, outside the homes, and in their workplace during the periods for which the participant reported being in those locations. This analysis uses the data of 129 persons, for which matched home, work, and personal measurements were available.

2.1.2. Evaluation of the long-range transported background concentrations

For calculating iF, the sampled outdoor residential benzene concentrations were assumed to be dominated by local mobile source emissions. According to both the measurements and the emission and dispersion computations for benzene by Hellén et al. (2005), the most important source categories in the Helsinki Metropolitan Area were exhaust emissions from local vehicular traffic, and the regionally and long-range transported background. The average contribution of the long-range transported fraction can be estimated from monitoring data measured at a regional background station (Luukki) in the vicinity of Helsinki. These measurements started in 2000 and give an annual average background level of 0.7 $\mu g\,m^{-3}$, while the urban ambient air average is around

1.6 μg m^{-3}, similar to that of EXPOLIS residential outdoor air in Helsinki.

Essentially, benzene is only removed from the atmosphere by its reaction with the hydroxyl radical (Atkinson, 1994). During summer in Finland, the atmospheric lifetime of benzene in relation to the above-mentioned reaction is approximately one week; benzene can therefore be transported from the source over a long-range. The transport distances are even longer in winter, as during this time hydroxyl radical concentrations are low at high latitudes (Hakola et al., 2003).

2.1.3. Evaluation of concentrations in traffic based on the EXPOLIS data

Since EXPOLIS did not measure in-traffic and in-vehicle benzene concentrations, we assume that the residual personal benzene exposure, or balance (B), not accounted for by residential indoor, outdoor, and workplace exposures is due primarily to exposure while in traffic:

$$B = C_p - \frac{C_{hi}t_{hi} + C_o t_{ho} + C_w t_w}{T} \quad (2)$$

where C_p is the measured time-weighted average personal exposure over 48 h (μg m^{-3}); C_{hi}, the concentration measured inside the participant's home when the participant was expected to be there (generally during the evenings); t_{hi}, the amount of time spent indoors at home; C_o, the concentration measured outside the participant's home while the participant was at home (concurrent with C_h); t_{ho}, the time spent outdoors while at home; C_w, the concentration measured inside the participant's workplace while the participant was at work; t_w, the time spent at work; T, the total monitoring time for personal exposure, including all activities and microenvironments visited (in this study 48 h). By definition $T = t_{hi} + t_{ho} + t_w + t_t + t_r$, where t_t, the time spent while travelling and t_r, the time spent in all other microenvironments. Shown in Table 1, C_{hi}, C_w, and C_o were measured during the times when the participant reported he/she would be at those locations, resulting in an average of two sampling sessions over the 48 h.

Using Eq. (2), we can calculate the non-time-weighted residual benzene concentration (Table 1) to which the participant would have been exposed when not at home, work, or outdoors. We assume that time at home, work, and travel account for almost all of participants' time-activity (on average >90% of activity for the EXPOLIS-Helsinki sample). For benzene, we assume that mobile sources are the primary contributor to the concentrations in all microenvironments (except where cigarette smoke is present). The residual benzene concentration (C_b) is then defined as:

$$C_b = \max\left\{0, \frac{B}{1 - ((t_{hi} + t_w + t_{ho})/T)}\right\} \quad (3)$$

where B is the time-weighted balance exposure concentration (i.e. not attributable to home indoor, workplace, or home outdoor exposure). The second term in the parenthesis is derived mathematically from Eq. (2) and the definitions and assumptions mentioned above, and the first term has been added in order to avoid possibly occurring non-realistic negative values (that could be caused, e.g., by measurement inaccuracies). Approximately 25% of C_b values were found to be 0 or below. C_b is used as a proxy for the concentration a person is exposed to while in traffic.

Table 1
Measured benzene concentrations in various microenvironments from the EXPOLIS study for samples used in this analysis.

Microenvironment	N	Concentration (ug/m^3)		
		Mean	Median	SD
Home indoor	129	2.13	1.90	1.91
Home outdoor	129	1.80	1.58	1.52
Work indoor	129	4.05	2.10	16.34
Personal	129	3.34	2.57	6.18
Balance concentration	128	3.45	2.65	5.88

2.2. Modelling of traffic flows, emissions and atmospheric dispersion in the EXPAND modelling approach

2.2.1. Modelling of traffic flows and emissions

The traffic information for each line source is obtained from the Helsinki Metropolitan Area Council (YTV). YTV utilizes a traffic planning model, EMME/2 (INRO, 2002), combined with an emission model (Laurikko, 1998) to obtain the traffic flows and emissions separately for each road and street link. Traffic volume and speed can be assessed in terms of diurnal and daily variation for each road segment. These estimations are based on traffic demand matrices that describe the vehicle trips from every spatial zone to all the other zones within the area considered. For more detailed explanation of these matrices the reader is referred to Elolähde and Koskentalo (1996) and Karppinen et al. (2000a,b).

For dispersion in street canyons, we used the operational street pollution model (OSPM) developed by Hertel and Bertowicz (1989), which calculates the concentrations based on emission factors that are modelled separately for each vehicle category. The intrinsic total hydrocarbon (THC) emission factors have been estimated by Laurikko (1998) based on European emission factors produced in the COST 319 action and in the MEET project (TRL, 1999). These data consist of emission factors for the different vehicle categories for the years 2000 and 2025.

Since direct measurements of benzene emissions are not available, they were estimated using measured emissions of THC. According to Friedricht and Schwarz (1998), 2.97% of traffic-emitted THC is benzene, therefore the benzene emissions were estimated simply to be 0.03 times the emissions of total hydrocarbons.

2.2.2. Atmospheric dispersion modelling

Concentrations of benzene emitted from traffic were modelled using CAR-FMI, Contaminants in the Air from a Road – Finnish Meteorological Institute (Härkönen et al., 1996; Härkönen, 2002). This Gaussian finite line source model consists of an emission model and a dispersion model. CAR-FMI dispersion parameters are evaluated using the stability data produced by the meteorological preprocessing model developed at FMI (MPP-FMI) (Karppinen et al., 1997). This modelling system also includes statistical and graphical analysis of the hourly concentrations at each receptor point (Härkönen, 2002). The CAR-FMI results were used as input for the EXPAND model and for the calculation of iF in the whole Helsinki Metropolitan Area (HMA). The modelling of traffic flows, emissions and atmospheric dispersion has previously been evaluated against measured benzene concentrations by Hellén et al. (2005).

The OSPM is a semi-empirical model that calculates concentrations of exhaust gases in a street canyon assuming three different contributions to the kerbside levels: the contribution from the direct flow of pollutants from the source to the receptor, the recirculation component due to the flow of pollutants around a horizontal wind vortex generated within the so-called recirculation zone of the canyon, and the urban background contribution (Berkowicz et al., 1997; Berkowicz, 2000).

One of the main streets in downtown Helsinki, Hämeentie Street, was chosen as the main reference point for the smaller scale computations. To predict the dispersion of benzene traffic emission in a street canyon in Helsinki, a segment from Hämeentie between the Viides Linja and Neljäs Linja Streets was chosen (Fig. 1). This segment can be considered a regular street canyon by definition of having an aspect ratio (height/width) between the so-called avenue

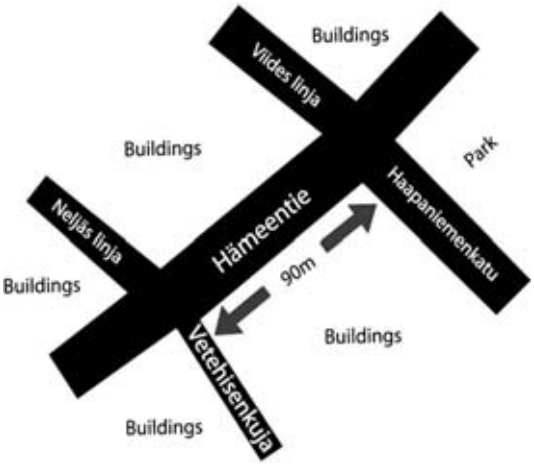

Fig. 1. Map of the segment of Hämeentie Street and immediate surroundings that was selected for the street canyon computations using the OSPM model.

canyon ($H/W < 0.5$) and regular canyon ($H/W \approx 1$) with no openings in the canyon walls (Vardoulakis et al., 2003). A vertical cross-section of the street segment is depicted in Fig. 2. This segment was also chosen because the population density and distribution data were available and air quality measurements were made with a mobile measurement station in 2005 (Aarnio et al., 2005), allowing for model evaluation.

Meteorological data were provided by the meteorological pre-processing model MPP-FMI (Karppinen et al., 1997). This model uses as input data three-hourly synoptic weather observations and meteorological soundings performed twice each day. We used data from the Helsinki-Vantaa weather station and from the Helsinki-Isosaari observatory, and the sounding observations from the station of Jokioinen. The model predicts hourly time-series of all the meteorological parameters needed for dispersion modelling. We have computed the hourly pre-processed meteorological input data for 2000 and 2005.

2.3. Modelling of intake fractions

2.3.1. Evaluation of the spatial distributions of iFs using the EXPAND model

The spatial distribution of iF for benzene from traffic sources in the Helsinki Metropolitan Area (HMA) was evaluated by the exposure model EXPAND ("EXPosure to Air pollution, especially to Nitrogen Dioxide and particulate matter"; Kousa et al., 2002) for the years 2000 and 2005. The basic model framework has been presented in Fig. 3. This model was refined to calculate not only exposures, but also iFs for several substances. This adjustable scale model allows for the estimation of the spatial and temporal distribution of iF by combining and processing different input values: time-microenvironment activity data, the spatial location of the population, and pollutant concentration distributions. The activity patterns available for EXPAND are for the HMA working-age population (25–55 years old), representing 46% of the whole HMA population (Kousa et al., 2002). However, the EXPAND model cannot be used to calculate an individual's personal intake fraction. Rather, it calculates the intake fraction per unit area, averaged over the number of people that are located within that area for all or some portion of the averaging time.

The spatial locations of population and activity data were obtained from the EXPOLIS project (Edwards and Jantunen, 2001). In EXPAND, the microenvironment activity data is divided into four categories: home, workplace, traffic and other activities (Table 2). The traffic activities rely on the traffic flow information for the road and street network. The 'other' microenvironment data represent activities that take place outside of homes and work (e.g., recreational activities) (Kousa et al., 2002).

Although several activities are included in the EXPOLIS database, the EXPAND model used a constant breathing rate of 1 $m^3 h^{-1}$, the light activity breathing rate according to the U.S. Environmental Protection Agency's (USEPA's) Exposure Factors Handbook (U.S. EPA, 1997). In order to reflect the contribution of outdoor benzene to indoor concentrations, an infiltration efficiency of 0.8 for buildings (JRC, 2003) was used to calculate iFs for indoor environments and 4 for vehicles (Marshall et al., 2003), acknowledging that concentrations inside vehicles are higher (Marshall and Behrentz, 2005).

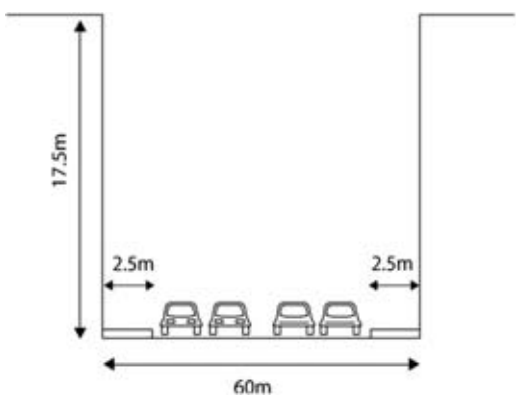

Fig. 2. Vertical cross-section of the street canyon showing the dimensions of the street segment used for the OSPM model calculations.

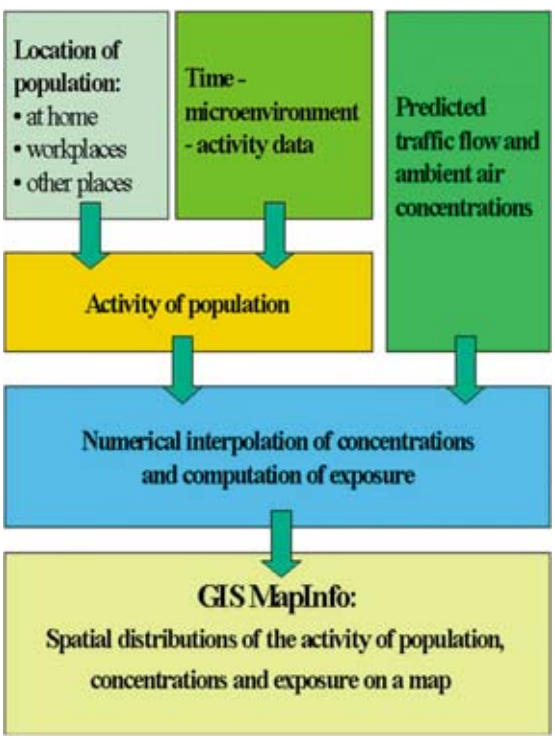

Fig. 3. A schematic presentation of the EXPAND model framework (Kousa et al., 2002).

Table 2
Comparison of time-activity and breathing rate inputs per microenvironment and analysis level for EXPOLIS-based and EXPAND intake fraction calculations.

EXPOLIS sample						EXPAND model		
Microenvironment	Time-activity (hours)					Microenvironment	Breathing rate ($m^3 h^{-1}$)	Activity rate
	Mean	Median	SD	Breathing rate ($m^3 h^{-1}$)	Activity rate			
Home indoor	27.81	26.75	5.8	0.4	Resting	Home	1	Light
Home outdoor	0.57	0.13	1.05	1.6	Moderate			
Work indoor	12.3	14.25	5.58	1	Light	Work	1	Light
Work outdoor	0.33	0	0.92	1.6	Moderate			
Other indoor	2	1.08	2.68	1	Light	Other	1	Light
Other outdoor	0.32	0	0.65	1.6	Moderate			
Traffic	3.29	3.17	1.74	1	Light	Traffic	1	Light
Indoor/outdoor infiltration efficiency	0.8					Indoor/outdoor infiltration efficiency	0.8	
In-traffic/ambient	na					In-traffic/ambient	4	
Level of analysis	Individual					Level of analysis	100 × 100 m	

The hourly concentrations of traffic-related benzene were provided by the dispersion model. The hourly averaged iFs for each grid square are computed directly from Eq. (1), based on the predicted concentrations and activity of population (number of persons × hour) values, using the GIS MapInfo (Kousa et al., 2002).

2.3.2. Evaluation of iF_i's of individuals based on EXPOLIS

An individual's iF is computed from:

$$iF = \frac{\sum_{i=1}^{m} C_{v,k} t_k Q_k}{E_v} \tag{4}$$

where $C_{v,k}$ is the benzene concentration in microenvironment k due to vehicular sources ($\mu g\, m^{-3}$); t_k, the time spent in microenvironment k (h), Q_k, the breathing rate while in microenvironment k ($m^3 h^{-1}$), and E_v, vehicle benzene emissions (μg) over the time evaluated. In the EXPOLIS study, the only outdoor air measurements were taken outside each home. Therefore, we have to assume that this value (C_o) is representative of the outdoor concentration for a specific person in general (i.e. at all times and for all places that they visit). Therefore the contribution to the indoor environment from the outdoors is defined as this concentration (C_o) multiplied by the infiltration efficiency of 0.8.

We assume that the outdoor contribution is predominantly from vehicular emissions and that other sources (including long-range transport) are negligible. The times spent in each microenvironment were taken from participants' time-activity diaries and breathing rates (see Table 2) were from the U.S. EPA's Exposure Factors Handbook (U.S. EPA, 1997).

Each EXPOLIS participant's intake fraction (iF_i) is:

$$iF_i = \frac{C_b t_t Q_l + pC_o t_{hi} Q_r + pC_o t_w Q_l + pC_o t_r Q_l + C_o t_o Q_m}{E_{v,y}} \tag{5}$$

where C_b is the residual benzene concentration ($\mu g\, m^{-3}$); C_o, the concentration measured outside the participant's home while the participant was at home; t_t, the time spent in traffic (h); t_{hi}, the time spent indoors at home (h); t_w, the time spent at work; t_r, the time spent in other indoor microenvironments; t_o, the time spent in all outdoor microenvironments; p, the infiltration efficiency for benzene from outdoor air into the indoors; Q_l, the light activity breathing rate ($m^3 h^{-1}$); Q_r, the resting breathing rate; Q_m, the moderate activity breathing rate; $E_{v,y}$, the emissions from vehicles in the Helsinki metropolitan area in y = year 1996 or 1997, depending on when the participant was sampled (Myllynen et al., 2006). The terms in the right-hand-side of Eq. (5) represent exposure while travelling, at home, at work, in other indoor microenvironments and in all outdoor microenvironments. The same values of concentration and breathing rate are applied for all travel, regardless of mode. However, the actual concentrations tend to be higher for drivers while breathing rates are higher for walkers and bikers.

2.3.3. Evaluation of iFs based on the one-compartment model

The one-compartment box model used as input values the sequential hourly meteorological time-series data from 1996, extracted from the archives of FMI, to calculate an average intake fraction for that year. The model is based on the equation (Lai et al., 2000):

$$iF_{box} = \frac{QP}{uH\sqrt{A}} \tag{6}$$

where iF_{box} is the urban intake fraction estimated using the box model; Q, the average adult population breathing rate (m^3 person^{-1} h^{-1}); P, the working-age population in the Helsinki metropolitan area (persons); u, the average wind speed ($m\, h^{-1}$); H, the atmospheric mixing height (m); A, the surface area (m^2).

The parameter data for the box model (summarized in Table 3) come from the MPP-FMI model mentioned earlier. We first computed a sequential hourly time-series of iF values using the hourly meteorological values (using Eq. (6)), and then computed annual averages of those iF values. This method assumes a uniform concentration throughout the compartment, providing no resolution on spatial variability, although it can provide some indication of temporal variability, as driven by meteorology. This implies that the near-ground concentrations (and iFs) tend to be underpredicted within the whole region, and especially in the vicinity of the main sources.

3. Results

The annual average benzene iF for the working-age population within the Helsinki Metropolitan Area (HMA) during 2000 and

Table 3
Description of the input parameters used for the box model calculations and the final results.

	Mean	Median	SD
W.A. population	494,000		
Breathing rate ($m^3 h^{-1}$)	0.83		
Wind speed ($m\, s^{-1}$)	4.15	3.91	1.99
Mixing height (m)	435	265	500
Area (km^2)	745		
Intake fraction (per million)	7	4	8

The following are constant values: working-age population in the Helsinki Metropolitan Area (in the table 'W.A. population'), breathing rate and geographical area. The wind speed and mixing height values are hourly averaged for the year 1996. The intake fraction results are shown as the statistics for the hourly box model calculations for the working-age population. Data from MPP-FMI (Karppinen et al., 1997).

2005 were computed using the EXPAND model. Henceforward, the iF concerning the HMA will be denoted as urban iF. The urban iF values presented use concentrations originating from traffic in the HMA for the intake calculation. Only results for 2005 are shown in Fig. 4, as the results for both years were almost identical. The values in the figure have been computed separately for each numerical grid cell, and are therefore called 'geographically partial' or simply 'partial' iF. These correspond to exposures in each particular grid cell, but traffic emissions from the whole HMA.

Higher values of the partial urban iFs range between 0.001 per million and 0.1 per million, and are concentrated in residential and commercial areas, where people spend most of their time. Both the number of receptors and the concentrations are relatively higher in these areas. Box plots of the distributions of the partial urban iFs for each microenvironment resulting from EXPAND calculations are presented in Fig. 5. The population exposure was relatively higher while in traffic, due to the higher concentrations of benzene inside vehicles and in the vicinity of the main roads and streets. There is an order-of-magnitude difference in the concentrations between the immediate vicinity of the roads and streets compared with other areas.

People are also exposed to benzene traffic-related emissions in the home and work environments, where people spend almost 90% of their time. The urban iFs for each microenvironment, i.e., the intake fraction resulting from summing up the partial urban intake fractions due to exposure in home, work, traffic, and other microenvironments for the working-age population within the HMA calculated with the EXPAND model, are 2.5 per million, 1.4 per million, 5.9 per million and 0.2 per million, respectively. The urban iF corresponding to the exposure of the HMA working-age population, summed across these different microenvironments, is 10 per million.

About 20% of the subjects have an intake fraction of zero from combined exposure in traffic and outdoor microenvironments.

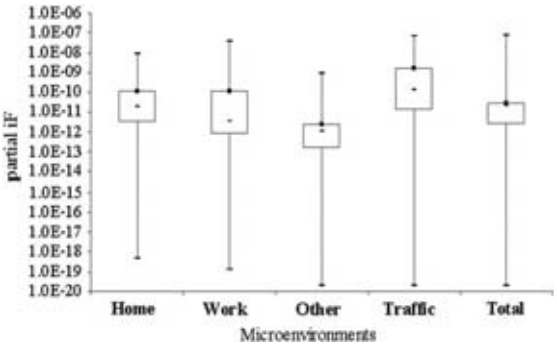

Fig. 5. Distribution of partial urban intake fractions for various microenvironments for benzene originating from mobile sources for the working-age population in the Helsinki Metropolitan Area in 2005, computed by the EXPAND model. The values have been computed separately for each numerical grid cell ($100 \times 100\ m^2$) of the domain (partial intake fractions). The boxes show the 25th and 75th percentiles, and whiskers indicate 5th and 95th percentiles. Median is indicated by the line inside the box, and mean is indicated by the circle.

These null values can be attributed to either no reported time spent in these microenvironments or nonexistent traffic-related benzene concentrations, according to the dispersion computations. These null values were excluded when performing the statistical analysis.

We also computed iFs for a street canyon segment of Hämeentie Street (local iF). The computations with OSPM were based on data on the number of inhabitants and workers and the time-activity patterns of people in that area. Urban background concentrations were excluded. The local iF from the vehicle emissions in the Hämeentie segment includes exposures to inhabitants, workers

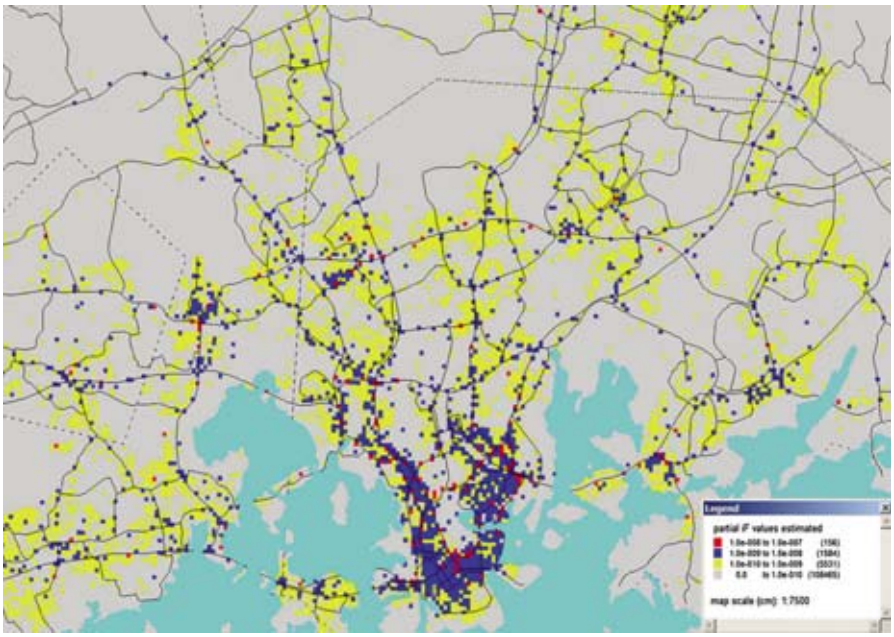

Fig. 4. Spatial distribution of partial urban intake fraction for benzene originating from mobile sources for the working-age population in the Helsinki Metropolitan Area in 2005, computed by the EXPAND model. The light blue in the figure represents the Baltic Sea; the centre of Helsinki is located in the peninsula in the middle of the lower part of the figure. The values in the figure have been computed separately for each numerical grid cell ($100 \times 100\ m^2$) of the domain (partial intake fractions). For each grid cell presented, the numerical values of the intake fractions correspond to emissions within the whole area, and population in each particular grid cell.

and customers, and persons in traffic in the street segment. The local iF was 37 per million.

Using measured data from EXPOLIS (Fig. 6), the average intake fraction of benzene from traffic sources for an individual over a 48-h period was 0.00008 per million (median = 0.00006 per million), with an intake fraction for all 129 people of 0.01 per million. If we extrapolate from the EXPOLIS group to the entire working-age population (i.e., by dividing the average iF from EXPOLIS by the total working-age population within the HMA; Kousa et al., 2002), we estimate an urban intake fraction of 39 per million. Using the concentrations evaluated by the simple box model, the average hourly urban intake fraction for the HMA working adult population was 7 per million (median = 4 per million). The box model results showed that urban iF tends to be lower in the afternoon hours rather than the night and morning hours. Median monthly values were lowest in May–July, and highest in January–April, particularly in March.

Fig. 6 shows box plots of intake fraction for the EXPOLIS participants in each microenvironment corresponding to the EXPAND categories. Median exposures are similar in all microenvironments, but 'other' and traffic have long tails at the higher ends of the distributions. This implies that traffic may have a higher iF in some cases compared to home and work exposures.

4. Discussion

None of the models was able to account for all dimensions over which intake fraction varies. Looking at all three of our methods, we were able to elucidate different properties of iF. From EXPAND, we could see spatially how iF is dependent on the time-averaged population density in a given year across all areas of the HMA. From EXPOLIS, we could see the impact of emissions in the HMA on an individual in the population, and how that impact varies between people as well as within a person (from the patterns of microenvironmental exposure). Finally, we were able to use a simple, yet informative box model to examine temporal iF variations due to meteorology.

The intake fraction values computed using the EXPAND model and based on EXPOLIS data are not directly comparable, as the location distributions of the populations and the years considered are different, and because the EXPOLIS population was not sampled during the weekends, July or the Christmas holiday period. Consequently the traffic benzene iF derived from the EXPOLIS population sampling may result in a small overestimation in comparison to the iF modelled from the EXPAND data, which represents all days of the year. However, they both provide useful information about the patterns of exposures across space and individuals. The EXPAND model addresses the iF of the entire working-age population within the whole HMA, while EXPOLIS examines iF_i's for single persons out of a subset of working-age persons in the same area.

Further, the analysis of EXPOLIS data does not differentiate long-range transported contributions versus local sources. On the other hand, these can be derived from dispersion model computations, and therefore we were able to present the EXPAND results that correspond to local source contributions only. The long-range transported fraction for benzene in residential areas is around 0.4 and approaches 1.0 at the outskirts of the metropolitan area (Hellén et al., 2003). In analyzing the EXPOLIS data, we used different breathing rates depending on the microenvironment, while in the EXPAND model, we used only one breathing rate.

As can be seen in Fig. 4, the highest annual urban iFs for the working-age population are centred in the downtown of Helsinki, where most of the commercial areas are located and where the majority of people live and work; and in other residential areas of the metropolitan area, with partial urban iFs between 0.001 per million and 0.1 per million. In other words, between 1.0 ng and 0.1 μg are inhaled in each $100 \times 100\ m^2$ grid cell per gram of benzene emitted from mobile sources in the whole HMA. For the Hämeentie street segment modeled in Table 4, the iF of approximately 40 μg per gram of benzene emitted on that particular segment (not the entire HMA) is inhaled by the people who spend time in that segment. Due to the longer amount of time spent in the area, the local intake fraction for residents is largest and the in-traffic local intake fraction is smallest (Table 4). However, the intake fraction per unit time and per individual in traffic is actually larger compared to that of residents and others. Thus, if the time spent in each of these microenvironments was equal per person, exposure in traffic would be responsible for the greater part of the intake fraction.

The average 48-h individual iF_i, based on the EXPOLIS study's personal monitoring data is 0.00008 per million. The EXPOLIS data show that at the median, the urban iF due to time spent indoors at home and work was greater in comparison to other microenvironments, although at the higher end of the distribution, traffic iF is larger than home and work iF (Fig. 6).

Extrapolated to the entire working-age HMA population, the urban iF (39 per million) based on EXPOLIS data is slightly lower than the population annual average estimated by Marshall et al. (2003), 48 per million, using a personal modelling approach (Table 5). The range of iFs evaluated by Marshall et al. (2003) was from 34 to 85 per million. Benzene iF from traffic in Helsinki would be expected to be lower by about a factor of 2 than that in

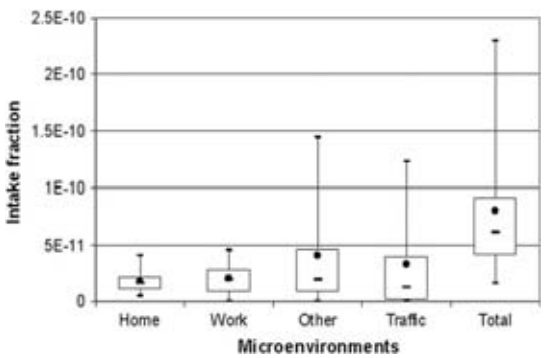

Fig. 6. Distribution of individual intake fractions of the EXPOLIS population sample ($n = 129$) in the Helsinki Metropolitan Area, presented separately for various microenvironments. The boxes show the 25th and 75th percentiles, and whiskers indicate 5th and 95th percentiles. Median is indicated by the line inside the box, and mean is indicated by the circle.

Table 4
Predicted intake fractions by inhalation in the street canyon in the selected segment of the Hämeentie Street, year 2000.

Group	Breathing rate ($m^3\ h^{-1}$)[a]	No. of people[b]	Time of exposure (fraction of day)[c]	iF_{local} (per million)
Inhabitants	1	176	0.56	16
Workers & customers	1	113	0.37	20
In traffic	1	20,380	0.000104	1.1
Total iF				37

The numbers of inhabitants, workers and customers correspond to the selected street segment. The number of persons in traffic is defined as the number of people who have transported through this street segment daily. The local iF is the sum of the contributions in the first three rows in the table. Emissions correspond to the street segment only.

[a] U.S. EPA (1997).
[b] Kousa et al. (2002).
[c] Schweizer et al. (2007).

Table 5
Comparison of mobile source intake fraction studies.

Reference/pollutant	Region/population	Modelling method	Breathing rate	Result (mean value, per million)
This study	Helsinki Metropolitan Area	CAR-FMI/EXPAND	$1\ m^3\ h^{-1}$	10
		EXPOLIS data	Varied	39
		Box model	$0.83\ m^3\ h^{-1}$	7
Marshall et al. (2003)/benzene	South Coast Air Basin, CA, USA/15 million people	Microenvironment benzene concentrations, time-activity patterns, EMFAC2000 emissions model	$12.2\ m^3\ d^{-1}$	48
			$20\ m^3\ d^{-1}$	79
Marshall et al. (2003)/benzene	South Coast Air Basin, CA, USA/15 million people	Ambient monitored benzene concentrations	$12.2\ m^3\ d^{-1}$	33
Marshall et al. (2005)/non-reactive pollutants	US urban areas	Box model	$12.2\ m^3\ d^{-1}$	21
Marshall et al. (2005)/non-reactive pollutants	US urban areas	Empirical model comparing CO with meteorological factors and MOBILE5 emission factors	$12.2\ m^3\ d^{-1}$	10 (summer), 15 (winter)
Marshall et al. (2005)/benzene	US urban areas	NATA concentrations	$12.2\ m^3\ d^{-1}$	7
Greco et al. (2007a)/primary PM2.5	All US counties	S-R matrix	$20\ m^3\ d^{-1}$	1.6
Evans et al. (2000)/primary PM2.5	Urban road segments	CALPUFF		9.4
Evans et al. (2000)/primary PM2.5	Rural road segments	CALPUFF		8.8

Los Angeles, as the population density in the HMA is approximately half that reported by Marshall et al. in their article. Methodological differences as well as a possible overestimate of individual iFs from EXPOLIS may explain these discrepancies, particularly since we only included about half the total population (only ages 25–55).

The box model provides an urban iF estimate within a factor of six of the EXPOLIS results, and within less than a factor of 2 of the EXPAND results, but does not have any spatial resolution. This method is a substantially simpler screening-type tool of assessment, compared with the EXPAND and EXPOLIS approaches. The box model calculation showed a lower annual average compared to the same model for U.S. urban areas (Marshall et al., 2005; Table 5). On the other hand, if we sum up the partial urban iFs across the whole HMA, the EXPAND model provides a urban iF of 10 per million, a factor of four less than the intake fraction calculated using the measured personal and microenvironment concentrations from the working population of HMA, according to the EXPOLIS data. However, these values are not directly comparable, and EXPAND values actually should be lower, considering the physical differences of these procedures (e.g. inclusion of only vehicular emissions). Interestingly, the box model and EXPAND urban iF estimates are more similar than with EXPOLIS.

The EXPOLIS calculation can be expected to result in an overestimate, since it does not subtract out the contributions of long-range transported background benzene or those from other sources. Background benzene has been found to be relatively constant across time in Helsinki, with an average value of about $0.7\ \mu g\ m^{-3}$ (Hellén et al., 2005). We chose not to subtract out this value in the analysis of EXPOLIS data, as that procedure would likely introduce random inaccuracies into the calculation (only a measured annual average regional background concentration was available, not sequential hourly data). As an estimate of the potential effect of removing the background benzene concentration, if we subtract the effect of the $0.7\ \mu g\ m^{-3}$ from the numerator of the average individual iF_i, the population iF evaluated based on EXPOLIS data would be reduced by up to two-thirds. The years addressed are also different, and thus benzene emissions are not exactly the same. This is not expected, however, to lead to significant differences, as the intake fraction is, as a first approximation, independent of the emission rate (assuming a linear relationship between emissions and concentrations).

In EXPAND, we have assumed an infiltration efficiency of 4.0 in vehicles; however, the information on in-vehicle concentrations in relation to ambient concentrations is scarce and uncertain (Marshall et al., 2003). Clearly, this factor will significantly influence the iF values while people are travelling.

National scale assessments that include a greater number of urban areas or entire counties, such as the National Air Toxics Assessment (NATA) in the United States (Marshall et al., 2005) and Greco et al. (2007a), provide slightly lower estimates for non-reactive pollutants (means of 7 per million and 1.6 per million, respectively). These differences are explained by the fact that the lower average population density resulting from averaging entire counties rather than urban areas probably reduces the average iF more than its value is increased by including a larger target area and population. Also, differences between models can influence the final outcomes. For example, more local scale modeling, such as the use of street canyon models, are likely to result in higher values. The difference between results in the national and city scale assessments by Greco et al. (2007a,b) are one demonstration of this. In the analysis using NATA data, Marshall points out that the dispersion model used was shown to underpredict monitored values by about 40% for non-reactive pollutants. Additionally, the lack of time-microenvironment activity data may in part explain the differences between national and local scale models.

Overall, the average iFs calculated for Helsinki using both modelled and measured data are within an order-of-magnitude range of those found in most of the previous mobile source iF studies for benzene or other pollutants that can be considered non-reactive on an urban-scale.

Within this analysis, several inherent uncertainties regarding the modelling assumptions should be acknowledged. In the calculation using EXPOLIS concentrations, our assumption that the balance of exposure not attributable to indoor and outdoor residential and in-workplace concentrations is representative of the in-traffic exposure may lead to an overestimate of the in-traffic concentration. The range of these concentrations spanned two orders of magnitude. While the effect of tobacco smoke exposure is already accounted for in homes and workplaces, other microenvironments with tobacco smoke were not distinguished. However, there did not appear to be a statistically significant difference in the balance concentration for participants that reported exposure to tobacco smoke compared to those who did not. One outlying concentration, however, did fall under the smoke-exposed category, and was also associated with use of a grill. Otherwise, other activities such as use of paint, solvents, time spent in garages and visits to gas stations did not show marked influences on the balance concentration.

The indirect computation of the balance concentration term can also be influenced by measurement inaccuracies, compared with the computation of the other terms. Additionally, we assumed that the outdoor residential concentration was representative of traffic-related benzene ambient concentrations throughout the

day. This may bias the exposure to traffic benzene downwards, since night-time concentrations are generally lower than daytime.

The EXPOLIS population sample, although small, has been shown to represent well the working-age (aged 25–55) population of the HMA. Most had indoor jobs and only few worked in what might be called high exposure jobs. Because only a part of the exposed population within the HMA was – and no populations outside of the HMA were – considered, the estimated population iF and individual iF levels and distributions do not include the entire population exposed to benzene from traffic within the HMA, only the working-age population.

The total HMA population size (940,000 in 1999) is about two times the size of our target population (494,000) (http://cem.jrc.it/expofacts). The unaccounted HMA population consists of children, students and other young adolescents and the elderly. We can assume that its area residential distribution is not systematically different from the working-age population. It spends about the same amount of time indoors, but less time in traffic (on avg. 1.31 h d^{-1} for 19 y, and 0.82 h d^{-1} for 65 y, vs. 1.42 h d^{-1} for 20–64 y, http://cem.jrc.it/expofacts). The traffic benzene iF for the total HMA population would therefore be about 1.5–2.0 times the HMA working-age population iF, i.e. 20, …, 60 per million, very similar to the other values in Table 5. The respective distribution of individual iF_i's would be expected to shift and spread somewhat towards lower values.

Uncertainties grow as we attempt to expand our results to cover the whole exposed population. The nearest major population centres outside of the HMA are Lahti, 80 km North-East with 80,000, Tallin 80 km South with 420,000 and St. Petersburg 300 km East with 4,800,000 inhabitants. Other population centres are either much smaller or more distant. Consequently a rather large fraction, in the order of half of the total population iF can be assumed to accumulate within the HMA. This would increase the total population iF from the HMA traffic-emitted benzene to somewhere between 40 and 120 per million – with considerable uncertainty. As for the distribution of individual iF_i's, this increase would accumulate from very low individual iF_i's of millions of people.

A source apportionment of non-methane hydrocarbons found that traffic was responsible for about 50% of ambient concentrations, while long-range transport was responsible for 37% (Hellén et al., 2003). This finding was similar to a factor analysis of EXPOLIS data by Edwards, who found that long-range transport was a significant contributor to the variance of benzene concentrations (Edwards and Jantunen, 2001). Thus, the personal intake fractions evaluated based on EXPOLIS data are most likely over-estimates, and the actual values might be more in line with those calculated by the EXPAND model.

Another area of uncertainty is in the emissions estimates. In particular, the emission inventory did not contain the contributions from small-scale combustion. The overall influence of acceleration and deceleration, and that of traffic congestion is taken into account in YTV's traffic model, but the emissions are assumed to be evenly distributed along each line source in the numerical computations. The concentrations near major junctions and during severe congestion therefore tend to be underpredicted.

Due to the lack of measurements of benzene concentrations, few studies have compared model results to measured values. Predictions of CAR-FMI have been shown to slightly overpredict (by approximately 5%) the measured annual average benzene values at the urban background station of Kallio. At the stations of Tikkurila and Lintuvaara, the measured values were underpredicted by approximately 40% and 30%, respectively. The station of Lintuvaara is located in a residential area with single-family houses, where benzene emissions of small-scale wood-burning, which were not taken into account in model calculations, are significant. This also explains part of the discrepancy between modelled and predicted values at Tikkurila.

Beyond the case-specific uncertainties and limitations described above, the application of the concept of the intake fraction also has inherent limitations. It has been found to be most reliable for non-reactive substances, although it has been used for secondary sulphate and nitrate particles in the United States (Levy et al., 2002, 2003). Due to the complexities of modelling reactive pollutants, however, results for such substances are less consistent. The use of the intake fraction also always implies user-selected spatial and temporal integration (averaging) of data. The total uncertainty of modelling the intake fraction contains the uncertainties of several sequential potentially complex models (traffic flows, emission, dispersion, time-activity, indoor-outdoor infiltration and breathing rate models).

Despite the limitations and uncertainties inherent in intake fraction estimation and modelling in general, the intake fraction provides a flexible tool for risk assessment that summarizes quantitatively the relationship between a source and the exposed population. The application of intake fractions can provide novel perspectives on the source–exposure relationships, especially regarding the fine-resolution spatial distributions, microenvironment-specific iFs and distribution of individual iF_is in a population.

Acknowledgements

This research was supported by the European Chemical Industry Council (CEFIC) agreement LRI-B3.3-KTLE-0511. The authors would like to thank Kari Mäkelä of the Technical Research Centre of Finland (VTT) for the traffic data.

References

Aarnio, P., Myllynen, M., Koskentalo, M., 2005. Ilmanlaatu pääkaupunkiseudulla vuonna 2004. Helsinki Metropolitan Area Council (YTV).

Atkinson, R., 1994. Gas-phase tropospheric chemistry of organic compounds. Journal of Physical and Chemical Reference Data, Monograph 2, 1–216.

Bennett, D., McKone, T., Evans, J., Nazaroff, W., Smith, K., Margni, M., et al., 2002a. Defining intake fraction. Environmental Science and Technology 36, 206A–211A.

Bennett, D., Margni, M., McKone, T., Jolliet, O., 2002b. Intake fraction for multimedia pollutants: a tool for life cycle analysis and comparative risk assessment. Risk Assessment 22 (5), 905–918.

Berkowicz, R., Hertel, O., Larsen, S., Sørensen, N., Nielsen, M., 1997. Modelling Traffic Pollution in Streets. Ministry of Environment and Energy, National Environmental Research Institute, Denmark.

Berkowicz, R., 2000. A simple model for urban background pollution. Environmental Monitoring and Assessment 65, 259–267.

Cocheo, V., Paolo Sacco, P., Boaretto, C., De Saeger, E., Ballesta, P., Skov, H., Goelen, E., Gonzalez, N., Caracena, A., 2000. Urban benzene and population exposure, brief communication. Nature 404, 141.

Edwards, R.D., Jantunen, M.J., 2001. Benzene exposure in Helsinki, Finland. Atmospheric Environment 35 (8), 1411–1420.

Elolähde, T., Koskentalo, T., 1996. Calculating emissions of a transport network. Magazine of the Finnish Air Pollution Prevention Society 5–6, 26–28.

Evans, J., Thompson, K., Hattis, D., 2000. Exposure efficiency: concept and application to perchloroethylene exposure from dry cleaners. Journal of the Air and Waste Management Association 50, 1700–1703.

Friedricht, R., Schwarz, U., 1998. Emission inventories. In: Fenger, J., Hertel, O., Palmgren, F. (Eds.), Urban Air Pollution-European Aspects. Kluwer Academic Publishers, Dordrecht, The Netherlands, p. 95.

Greco, S.L., Wilson, A.M., Spengler, J.D., Levy, J.I., 2007a. Spatial patterns of mobile source particulate matter emissions-to-exposure relationships across the United States. Atmospheric Environment 41 (5), 1011–1025.

Greco, S.L., Wilson, A.M., Hanna, S.R., Levy, J.I., 2007b. Factors influencing mobile source particulate matter ernissions-to-exposure relationships in the Boston urban area. Environmental Science and Technology 41 (22), 7675–7682.

Hakola, H., Tarvainen, V., Laurila, T., Hiltunen, V., Hellén, H., Keronen, P., 2003. Seasonal variation of VOC concentrations above a boreal coniferous forest. Atmospheric Environment 37, 1623–1634.

Härkönen, J., 2002. Regulatory dispersion modelling of traffic-originated pollution. Ph.D. thesis, Faculty of Science, University of Helsinki, Helsinki, Finland.

Härkönen, J., Valkonen, E., Kukkonen, J., Rantakrans, E., Lahtinen, K., Karppinen, A., Jalkanen, L., 1996. A model for the dispersion of pollution from a road network. In: Publications on Air Quality 23. Finnish Meteorological Institute, Helsinki.

Hedberg, E., Kristensson, A., Ohlsson, M., Johansson, C., Johansson, P.A., Swietlicki, E., et al., 2002. Chemical and physical characterization of emissions

from birch wood combustion in a wood stove. Atmospheric Environment 36 (30), 4823–4837.

Hellén, H., Kukkonen, J., Kauhaniemi, M., Hakola, H., Laurila, T., Pietarila, H., 2005. Evaluation of atmospheric benzene concentrations in the Helsinki Metropolitan Area in 2000–2003 using diffusive sampling and atmospheric dispersion modelling. Atmospheric Environment 39 (22), 4003–4014.

Hellén, H., Hakola, H., Laurila, T., 2003. Determination of source contributions of NMHCs in Helsinki (60 degrees N, 25 degrees E) using chemical mass balance and the Unmix multivariate receptor models. Atmospheric Environment 37 (11), 1413–1424.

Hertel, O., Bertowicz, R., 1989. Operational Street Pollution Model (OSPM). Evaluation of the model on data from St. Olavs Street in Oslo, DMU Luft A-135.

INRO, 2002. The EMME/2 transportation planning software: modelling and analysis features. Available from: http://www.inro.ca/en/products/emme2/e2fea.pdf:27.

Jantunen, M.J., Hanninen, O., Katsouyanni, K., Knoppel, H., Kuenzli, N., Lebret, E., et al., 1998. Air pollution exposure in European cities: the "EXPOLIS" study. Journal of Exposure Analysis and Environmental Epidemiology 8 (4), 495–518.

Joint Research (JRC), 2003. Draft EU risk assessment report on benzene (Human Health Part March 2003). Available from: http://ecb.jrc.it/existing-chemicals/.

Juraske, R., Anton, A., Castells, F., Huijbregts, M.A.J., 2007. Human intake fractions of pesticides via greenhouse tomato consumption: comparing model estimates with measurements for Captan. Chemosphere 67 (6), 1102–1107.

Karppinen, A., Joffre, S., Vaajama, P., 1997. Boundary layer parameterization for Finnish regulatory dispersion models. International Journal of Environment and Pollution 8, 557–564.

Karppinen, A., Kukkonen, J., Elolähde, T., Konttinen, M., Koskentalo, T., 2000a. A modelling system for predicting urban air pollution: comparison of model predictions with the data of an urban measurement network in Helsinki. Atmospheric Environment 34 (22), 3735–3743.

Karppinen, A., Joffre, S., Kukkonen, J., 2000b. The refinement of a meteorological preprocessor for the urban environment. International Journal of Environment and Pollution 14, 565–572.

Kotzias, D., Koistinen, K., Schlitt, C., Carrer, P., Maroni, M., Jantunen, M., 2005. Final Report for Critical Appraisal of the Setting and Implementation of Indoor Exposure Limits in the EU: The INDEX Project. Institute for Health and Consumer Protection, European Commission Joint Research Centre, Ispra, Italy.

Kousa, A., Kukkonen, J., Karppinen, A., Aarnio, P., Koskentalo, T., 2002. A model for evaluating the population exposure to ambient air pollution in an urban area. Atmospheric Environment 36 (13), 2109–2119.

Lai, A.C.K., Thatcher, T.L., Nazaroff, W.W., 2000. Inhalation transfer factors for air pollution health risk assessment. Journal of the Air and Waste Management Association 50 (9), 1688–1699.

Laurikko, J., 1998. On exhaust from petrol-fuelled passenger cars at low ambient temperatures. In: VTT Publications 348. Technical Research Centre of Finland, Espoo, Finland. 210–347.

Levy, J.I., Wolff, S.K., Evans, J.S., 2002. A regression-based approach for estimating primary and secondary particulate matter intake fractions. Risk Analysis 22 (5), 895–904.

Levy, J.I., Wilson, A.M., Evans, J.S., Spengler, J.D., 2003. Estimation of primary and secondary particulate matter intake fractions for power plants in Georgia. Environmental Science and Technology 37 (24), 5528–5536.

Margni, M., Pennington, D.W., Amman, C., Jolliet, O., 2004. Evaluating multimedia/multipathway model intake fraction estimates using POP emission and monitoring data. Environmental Pollution 128 (1–2), 263–277.

Marshall, J.D., Behrentz, E., 2005. Vehicle self-pollution intake fraction: children's exposure to school bus emissions. Environmental Science and Technology 39 (8), 2559–2563.

Marshall, J.D., Riley, W.J., McKone, T.E., Nazaroff, W.W., 2003. Intake fraction of primary pollutants: motor vehicle emissions in the South Coast Air Basin. Atmospheric Environment 37 (24), 3455–3468.

Marshall, J.D., Teoh, S.K., Nazaroff, W.W., 2005. Intake fraction of nonreactive vehicle emissions in US urban areas. Atmospheric Environment 39 (7), 1363–1371.

Myllynen, M., Aarnio, P., Kostkentalo, T., Malkki, M., 2006. Air Quality in Helsinki Metropolitan Area Year 2005. Helsinki Metropolitan Area Council (YTV), Helsinki.

Nigge, K.M., 2001. Generic spatial classes for human health impacts, part I: methodology. International Journal of Life Cycle Assessment 6 (5), 257–264.

Nishioka, Y., Levy, J.I., Norris, G.A., Wilson, A., Hofstetter, P., Spengler, J.D., 2002. Integrating risk assessment and life cycle assessment: a case study of insulation. Risk Analysis 22 (5), 1003–1017.

Rotko, T., Oglesby, L., Kunzli, N., Jantunen, M.J., 2000. Population sampling in European air pollution exposure study, EXPOLIS: comparisons between the cities and representativity of the samples. Journal of Exposure Analysis and Environmental Epidemiology 10 (4), 355–364.

Saarela, K., Tirkkonen, T., Laine-Ylijoki, J., Jurvelin, J., Nieuwenhuijsen, M.J., Jantunen, M., 2003. Exposure of population and microenvironmental distributions of volatile organic compound concentrations in the EXPOLIS study. Atmospheric Environment 37 (39–40), 5563–5575.

Schweizer, C., Edwards, R.D., Bayer-Ogesby, L., Gauderman, W.J., Ilcqua, V., Jantunen, M.J., Lai, H.K., Nieuwenhuijsen, M., Kűnzli, N., 2007. Indoor time-microenvironment-activity patterns in seven regions of Europe. Journal of Exposure Science and Environmental Epidemiology 17, 170–181.

Stevens, G., Wilson, A., Hammitt, J.K., 2005. A benefit-cost analysis of retrofitting diesel vehicles with particulate filters in the Mexico City metropolitan area. Risk Analysis 25 (4), 883–899.

Transport Research Laboratory (TRL), 1999. Methodology for calculating transport emissions and energy consumption. Deliverable 22 for the Project MEET. European Commission. SE/491/98:362.

U.S. EPA, 1997. Exposure Factors Handbook. National Center for Environmental Assessment, Office of Research and Development, Washington, D.C.

Vardoulakis, S., Fisher, B.E.A., Pericleous, K., Gonzalez-Flesca, N., 2003. Modelling air quality in street canyons: a review. Atmospheric Environment 37 (2), 155–182.

Wang, S.X., Hao, J.M., Ho, M.S., Li, J., Lu, Y.Q., 2006. Intake fractions of industrial air pollutants in China: estimation and application. Science of the Total Environment 354 (2–3), 127–141.

FINNISH METEOROLOGICAL INSTITUTE
Erik Palménin aukio 1
P.O. Box
FI-00101 HELSINKI
tel. +358 29 539 1000
WWW.FMI.FI

FINNISH METEOROLOGICAL INSTITUTE
CONTRIBUTIONS No. 121
http://en.ilmatieteenlaitos.fi/research
ISBN I978-951-697-882-9 (paperback)
ISBN 978-951-697-883-6 (pdf)
ISSN 0782-6117
Erweko
Helsinki 2016